

## ABSTRACT

FOX, WILLIAM CARR. Investigating Nucleosynthesis in Massive AGB Stars with Transfer Reactions. (Under the direction of Richard Longland).

The asymptotic giant branch (AGB) phase of stellar evolution involves complex nucleosynthesis processes responsible for the production of many chemical elements observed in the universe. The signatures of active AGB nucleosynthesis have been discovered through the observation of both enhanced rubidium abundance in the atmospheres of massive O-rich AGB stars and abundance anticorrelations of light-element pairs in low-mass globular cluster stars. Massive AGB stars have even been considered a candidate nucleosynthesis host for the extreme potassium enrichment and magnesium depletion observed in the red giant stars of the globular cluster NGC 2419. Slow neutron capture during AGB thermal instabilities (the s-process) and hydrogen burning at the base of the convective hydrogen envelope (hot-bottom burning) have been shown to be sites of the nucleosynthesis for these abundance patterns. These sites are investigated in this thesis through nuclear reaction network calculations involving the reaction rates of all relevant nuclei. The discrepancy between observed and predicted rubidium abundance in massive AGB stars is investigated with a Monte Carlo reaction network. All reaction rates in the network are varied within their uncertainties to determine the rates most correlated with rubidium abundance. The discrepancy is determined to be unlikely a result of reaction rate uncertainties, but the  $^{86}\text{Rb}(n, \gamma)^{87}\text{Rb}$  reaction rate is found to be one of the most in need of constraint. The Mg–K anticorrelation in the globular cluster NGC 2419 is investigated by constraining the key potassium-destroying reaction  $^{39}\text{K}(p, \gamma)^{40}\text{Ca}$  using nuclear structure input from the  $^{39}\text{K}(^3\text{He}, d)^{40}\text{Ca}$  proton-transfer reaction measurement at the Triangle Universities Nuclear Laboratory. This measurement has resolved a key  $^{39}\text{K} + p$  resonance, 154 keV, for the first time, among others, leading to a significant impact on the  $(p, \gamma)$  reaction rate at temperatures  $T \lesssim 110$  MK. Potassium production is found to decrease at these temperatures as a result, and the temperatures and densities of the hydrogen-burning candidate sites responsible for the Mg–K anticorrelation are mildly constrained.

© Copyright 2023 by William Carr Fox

All Rights Reserved

Investigating Nucleosynthesis in Massive AGB Stars with Transfer Reactions

by  
William Carr Fox

A dissertation submitted to the Graduate Faculty of  
North Carolina State University  
in partial fulfillment of the  
requirements for the Degree of  
Doctor of Philosophy

Physics

Raleigh, North Carolina  
2023

APPROVED BY:

---

Christian Iliadis

---

Carla Fröhlich

---

Matthew Green

---

John Classen

---

Richard Longland  
Chair of Advisory Committee

## **DEDICATION**

To Mom, Dad, Grandma, Lindsay, and Alex.

## BIOGRAPHY

William Fox was born in Raleigh, N.C. in 1993 to his parents Daniel and Tammy Fox, who were both the inspiration for his academic pursuits. He attended Sanderson High School, where he was first exposed to physics in his senior year, unknowingly shaping his entire career. As an undergraduate at the University of North Carolina at Wilmington, he developed a deep connection with both physics and mathematics, studying general relativity and astrophysics. He conducted research in gravitational wave theory in the midst of the first gravitational wave detection by LIGO, inspiring him to pursue graduate studies. As a graduate student at North Carolina State University, he discovered a newfound interest in experimental nuclear physics and has been drawn to its connection with astrophysics ever since.

## ACKNOWLEDGEMENTS

First, I would like to thank my wonderful wife, Alex. She has been a relentless encouragement through my entire graduate studies, and I am eternally grateful for her support. Being an expert in literature, she has provided an artistic perspective in my life not often encountered in this field. I cannot thank her enough for her countless hours listening to me ramble on about the latest figure or paragraph in my thesis. She always enthusiastically discussed the material with me and helped me perfect it, regardless of whether I provided context. She has been an inspiration to me through her own career, and I look forward to supporting her as she has certainly done for me.

Richard Longland has been an exceptional advisor, mentor, and friend over the last five years. His advising style has coupled well with my own researching style, giving me the freedom to create my own path toward solutions. He truly brings out the creativity in his students by allowing them to develop their own analysis pipelines, distinguishing themselves from each other. I am grateful for Richard taking me in, even with minimal experimental background. Through his guidance, I now have the skills and mindset of an experimental physicist, something I never thought I would achieve. For this and much more, I could not be more grateful.

Working closely with Christian Iliadis has been one of the highlights of my time as a graduate student. He has been an outstanding mentor and friend since my early days at TUNL. Even brief encounters with Christian are always memorable due to his personable nature. He has made my time at TUNL not only academically rewarding, but also enjoyable. I have referenced his nuclear astrophysics book and course notes countless times in my research, and this thesis would not exist without him.

I am very grateful for the rest of my committee members, Carla Fröhlich, Matthew Green, and John Classen, who have taken the time to read my thesis and provided constructive feedback during my defense. From our discussions, many positive changes have been implemented into the thesis.

I would have pursued a different career if not for Russell Herman. As my undergraduate advisor and mentor, he inspired me to be a physicist. I look back on those days learning general relativity and gravitational wave theory from him with complete awe at how he could make such complicated subjects so simple. He is one of the greatest physics and mathematics educators I have ever known, and I owe him lifetimes of gratitude for getting me to where I am today.

Caleb Marshall, Federico Portillo Chaves, and Kiana Setoodehnia comprised Richard's research group when I joined, and they were each essential to my assimilation into the group.

Caleb taught me everything I needed to know about the quirks of the tandem accelerator and the Direct Extraction Negative Ion Source (DENIS) at TUNL. Federico taught me how to make evaporated targets, how to perform maintenance on the focal plane detector, and how to use FRESCO for distorted-wave Born approximation (DWBA) calculations. I only briefly got to know Kiana before she left the group, but she has helped me immensely whether she knows it or not. Her meticulous notes on the focal plane detector, the Enge Split-Pole Spectrograph, and the Enge beamline were vital to the success of the  $^{39}\text{K}(^3\text{He}, d)^{40}\text{Ca}$  experiment presented in this thesis, among many other experiments performed at TUNL.

The Nuclear Astrophysics group at TUNL has provided me with a sense of community unlike any other. Its informal nature has helped ease the everyday stress of being a graduate student and allowed me to create many new friendships among colleagues. Sharing my research with students, postdocs, and professors via countless presentations and research updates has also greatly enhanced my communication skills. I am very grateful for this close group of people, and I expect to remain close to each of them throughout my career.

Finally, I would like thank the TUNL staff, without whom the  $^{39}\text{K}(^3\text{He}, d)^{40}\text{Ca}$  experiment presented in this thesis would not have been possible. In particular, I would like to thank Chris Westerfeldt, John Dunham, Bret Carlin, and Tom Calisto for each working closely with me and others in Richard's group on various technical concerns in the lab. Chris has worked tirelessly to maintain our cryopumps, allowing us to achieve excellent vacuum in the Enge beamline, target chamber, and Enge magnet. He has also been crucial in maintaining the evaporation chamber in the physics department at Duke, used for the evaporated potassium iodine targets in this thesis. John has been the "go-to" expert for the tandem accelerator and DENIS at TUNL, and has trained our entire group on their operation and maintenance. Bret has been the expert on the electronic components in our experimental setup at the Enge, as well as for the LabView graphical user interface used to operate the tandem beamline components. Finally, Tom has used his engineering expertise to tackle countless projects and issues with our experimental setup at the Enge for us.

## TABLE OF CONTENTS

<b>List of Tables . . . . .</b>	<b>ix</b>
<b>List of Figures . . . . .</b>	<b>x</b>
<b>Chapter 1 Introduction . . . . .</b>	<b>1</b>
1.1 Asymptotic Giant Branch Stars . . . . .	2
1.2 s-Process Nucleosynthesis . . . . .	5
1.3 Hot-Bottom Burning . . . . .	10
1.4 Globular Cluster Abundance Anomalies . . . . .	11
<b>Chapter 2 Nuclear Reactions in Stars . . . . .</b>	<b>16</b>
2.1 Introduction . . . . .	16
2.2 Nuclear Reaction Networks . . . . .	16
2.3 Reaction Rates . . . . .	18
2.3.1 Narrow Resonances . . . . .	21
2.3.2 Particle Partial Widths . . . . .	22
2.3.3 $\gamma$ -ray Partial Widths . . . . .	23
2.4 Transfer Reactions . . . . .	24
2.4.1 Optical Model . . . . .	24
2.4.2 Distorted Wave Born Approximation . . . . .	25
<b>Chapter 3 Rubidium Production in Massive AGB Stars . . . . .</b>	<b>28</b>
3.1 Introduction . . . . .	28
3.2 Rubidium Abundance . . . . .	28
3.2.1 The s-Process Branching at $^{86}\text{Rb}$ . . . . .	29
3.2.2 The Rubidium Problem . . . . .	31
3.3 s-Process Reaction Network Methodology . . . . .	33
3.3.1 The Reaction Network . . . . .	33
3.3.2 Abundance Evolution . . . . .	34
3.3.3 Monte Carlo Procedure . . . . .	37
3.3.4 Measuring Correlations with Mutual Information . . . . .	38
3.4 Reaction Rate Sensitivities . . . . .	39
3.4.1 Correlations . . . . .	39
3.4.2 The [Rb/Zr], [Rb/Sr], and [Rb/Fe] Ratios . . . . .	43
3.4.3 Discussion . . . . .	46
3.5 Conclusions . . . . .	47
<b>Chapter 4 <math>^{39}\text{K}(p, \gamma)^{40}\text{Ca}</math> Constraints for Globular Cluster NGC 2419 . . . . .</b>	<b>48</b>
4.1 Introduction . . . . .	48
4.2 NGC 2419 and the Mg–K Anticorrelation . . . . .	48
4.3 The Previous $^{39}\text{K}(p, \gamma)^{40}\text{Ca}$ Reaction Rate . . . . .	53
4.3.1 Longland <i>et al.</i> (2018) Evaluation . . . . .	53
4.3.2 Contributing Resonances . . . . .	55

4.3.3	Previous Proton-Transfer Measurements . . . . .	57
4.4	The $^{39}\text{K}(^3\text{He}, d)^{40}\text{Ca}$ Experiment . . . . .	57
4.4.1	Targets . . . . .	58
4.4.2	Focal-Plane Spectra . . . . .	60
4.4.3	Energy Shifts . . . . .	61
4.4.4	Silicon Detector Telescope . . . . .	64
4.4.5	Oxidized Spectra . . . . .	67
4.5	Bayesian Peak Fitting and Target Oxidation . . . . .	67
4.5.1	Bayesian Peak Fitting . . . . .	68
4.5.2	Fitting Peaks with Target Oxidation . . . . .	71
4.6	Cross Sections . . . . .	77
4.6.1	Yield to Cross Section Conversion . . . . .	78
4.6.2	Rutherford Scattering . . . . .	79
4.6.3	Cross Sections in the Center-of-Mass System . . . . .	79
4.6.4	Si Detector Normalization . . . . .	81
4.6.5	Optical Model Normalization . . . . .	83
4.7	$^{39}\text{K}(^3\text{He}, d)^{40}\text{Ca}$ Analysis . . . . .	87
4.7.1	Energy Calibrations . . . . .	87
4.7.2	DWBA Calculations . . . . .	95
4.7.3	Angular Distribution Results . . . . .	100
4.7.4	Spectroscopic Factors . . . . .	111
4.7.5	Proton Partial Widths and Resonance Energies . . . . .	114
4.8	New $^{39}\text{K}(p, \gamma)^{40}\text{Ca}$ Reaction Rate . . . . .	116
4.8.1	The Reaction Rate . . . . .	116
4.8.2	Resonance Contributions . . . . .	119
4.9	New Constraints for the Mg–K Anticorrelation . . . . .	121
4.10	Conclusions . . . . .	125
<b>Chapter 5</b>	<b>Development of a New Digital Data Acquisition System . . . . .</b>	<b>126</b>
5.1	Introduction . . . . .	126
5.2	Background and Motivation . . . . .	126
5.3	Overview of the CAEN V1730 Digitizer . . . . .	129
5.3.1	Digital Pulse-Processing Parameters . . . . .	129
5.3.2	Time Stamp Determination . . . . .	132
5.3.3	Event Readout Format . . . . .	133
5.4	Frontend DAQ Software . . . . .	136
5.5	Testing the Digital Data Acquisition System . . . . .	137
5.5.1	Energy Resolution Tests with $^{152}\text{Eu}$ . . . . .	137
5.5.2	Timing Resolution Tests with $^{60}\text{Co}$ . . . . .	140
5.5.3	Development of Coincidence Logic in EngeSpec . . . . .	142
5.6	Conclusions . . . . .	142
<b>Chapter 6</b>	<b>Summary and Conclusions . . . . .</b>	<b>144</b>
<b>APPENDIX</b>	<b>. . . . .</b>	<b>154</b>



## LIST OF TABLES

Table 3.1	The top eight most correlated reaction rates with the $X(^{87}\text{Rb})/X(^{86}\text{Sr})$ and $X(^{87}\text{Rb})/X(^{90}\text{Zr})$ mass fraction ratios, ranked according to mutual information (MI). Spearman's correlation coefficient $r_s$ is also provided, to indicate the polarity of the correlation. . . . .	40
Table 3.2	Percentiles from $-2\sigma$ (2.5%) to $+2\sigma$ (97.5%) of the [Rb/Sr], [Rb/Zr], and [Rb/Fe] probability densities from the present Monte Carlo reaction network calculation. . . . .	45
Table 4.1	Information on each run of the $^{39}\text{K}(^3\text{He}, d)^{40}\text{Ca}$ experiment, including the angle of the Enge, the target used, the magnetic field of the Enge, and the sort group (see text). . . . .	63
Table 4.2	Global optical model potential parameters for $^{39}\text{K} + ^3\text{He}$ at $E_{\text{lab}} = 21$ MeV from Ref. [Lia09]. . . . .	84
Table 4.3	Excitation energies $E_x$ determined through a Markov Chain Monte Carlo (MCMC) energy calibration for the $^{40}\text{Ca}$ states observed in the present experiment. For comparison, the ENSDF [Che17] excitation energies and $J^\pi$ values are also given, unless otherwise indicated. Brackets represent states from ENSDF too close in energy to resolve via the energy calibration alone. Calibration states are shown in italics. . . . .	94
Table 4.4	Global optical model potential parameters for $^{39}\text{K} + ^3\text{He}$ and $^{40}\text{Ca} + d$ and the proton bound-state parameters. . . . .	97
Table 4.5	The states resolved in the present experiment for the first time in the indicated regimes. Parentheses denote ambiguous $\ell$ assignments. . . . .	111
Table 4.6	Spectroscopic factors compared with Refs. [Ers66, Set67, For70, Cag71, Fuc69]. . . . .	113
Table 4.6	(continued) . . . . .	114
Table 4.7	Center-of-mass resonance energies $E_r$ , angular momentum assignments, and proton partial-widths obtained for proton-unbound $^{40}\text{Ca}$ states in this experiment. The total proton partial-width uncertainty is reported, including a 30% systematic uncertainty. The last column shows proton partial-width upper limits calculated by Ref. [Lon18b]. . . . .	115
Table A.1	Initial abundances, in terms of mass fractions $X_{\text{init}}$ , in the s-process reaction network model of Chapter 3. Relative solar system abundances from Ref. [Lod09] are applied to the remaining nuclei after modifications to $^1\text{H}$ , $^4\text{He}$ , $^{12}\text{C}$ , $^{13}\text{C}$ , $^{14}\text{N}$ , $^{16}\text{O}$ , and $^{56}\text{Fe}$ . . . . .	156
Table A.1	(continued) . . . . .	157

## LIST OF FIGURES

- Figure 1.1 Evolution of a  $5 M_{\odot}$  star represented on the Hertzsprung-Russell (HR) diagram. The two stages of the asymptotic giant branch (AGB) are highlighted in red. See text for definitions of acronyms. Figure adapted from Ref. [Car07]. . . . . 3
- Figure 1.2 The evolution and structure of a thermally pulsing AGB star. Three thermal pulses are depicted in blue, extinguishing the hydrogen burning shell. The neutron sources  $^{13}\text{C}(\alpha, n)^{16}\text{O}$  and  $^{22}\text{Ne}(\alpha, n)^{25}\text{Mg}$  are shown to be active between pulses and during pulses, respectively. Figure adapted from Ref. [Rei14]. . . . . 4
- Figure 1.3 The s-process path from iron to arsenic. The stable nuclei in black undergo neutron capture, while the unstable nuclei in blue ( $\beta^-$ -decay) and red ( $\beta^+$ -decay or electron capture) either decay or undergo neutron-capture depending on their half-lives and the neutron density  $N_n$ . At s-process branchings, e.g.  $^{59}\text{Fe}$ , the probability for neutron-capture and decaying is approximately equal, hence the path is split into two branches. Figure adapted from Ref. [Rei14]. . . . . 6
- Figure 1.4 A simple s-process path initiating from the nucleus with mass number  $A - 1$ , where shaded nuclei are stable, and unshaded nuclei are unstable. Case (a) is shown by the solid arrows, where only  $\beta$ -decays occur on unstable nuclei. Case (b), indicated by the addition of dashed arrows, treats  $A'$  as a branching point nucleus. . . . . 7
- Figure 1.5 The temperature evolution at the bottom of the convective hydrogen envelope during the TP-AGB phase for a  $6M_{\odot}$  star with  $Z = 0.02$ . Several thermal pulses are shown, each rapidly decreasing the temperature in this region, which extinguishes hydrogen burning. Adapted from Ref. [Kar14]. . . . . 10
- Figure 1.6 The O–Na anticorrelation of 1,200 red giants among all 19 globular clusters observed in the survey of Ref. [Car10]. Blue arrows indicate upper limits in O abundances, while lines separate different populations of red giants based on their relative O and Na richness. Primordial (P), extreme (E), and intermediate (I) populations are labeled in the first panel. See text for definitions of these populations. Adapted from Ref. [Car10]. . . . . 12
- Figure 1.7 The hydrogen burning mechanism driving the O–Na anticorrelation. Nuclei in blue are destroyed overall in the various cycles, while nuclei in red are produced. Shaded nuclei are stable. The first two stages of the CNO cycle (left), distinguished by the temperature-dependent branch at  $^{15}\text{N}$ , lead to an overall depletion of oxygen. The  $^{15}\text{N}(p, \gamma)^{16}\text{O}$  reaction is activated at about 40 MK. The Ne–Na cycle (right), occurring simultaneously at about the same activation temperature, leads to an overall production of sodium. The  $^{23}\text{Na}(p, \gamma)^{24}\text{Mg}$  reaction activates at about 70 MK. . . . . 14

Figure 2.1 The Gamow window, $E_0 \pm \Delta/2$ , for the $^{39}\text{K}(p, \gamma)^{40}\text{Ca}$ reaction at 100 MK. The Gamow factor $e^{-2\pi\eta}$ is shown in red; the Maxwell-Boltzmann factor $e^{-E/kT}$ is shown in green, and the Gamow peak $e^{-2\pi\eta}e^{-E/kT}$ is shown in blue. The resonances that contribute significantly to the reaction rate at this temperature will have energies within the Gamow window, between about 140 keV and 230 keV. . . . .	20
Figure 3.1 The $^{85}\text{Kr}$ and $^{86}\text{Rb}$ s-process branchings, highlighted in red, along the s-process path from Kr to Zr. The dashed arrows extending from these branchings indicate the path dependence on the neutron density. The $N = 50$ closed-shell nuclei are represented by the vertical dashed line, which have low neutron-capture cross sections. The relative abundance of $^{87}\text{Rb}$ to nearby nuclei such as $^{86}\text{Sr}$ and $^{90}\text{Zr}$ is expected to be an indicator of neutron density. . . . .	30
Figure 3.2 The AGB model predictions of $[\text{Rb}/\text{Fe}]$ (top) and $[\text{Rb}/\text{Zr}]$ (bottom) as a function of stellar mass from Refs. [Kar12, Raa12, Kar16, Pig16]. The dots and triangles represent abundances from the last computed thermal pulse and from synthetic calculations, respectively. The number of nuclei $n$ in the corresponding network is provided in the legend, as well as the delay superwind parameter $P$ (see text), if applicable, and the metallicity $z$ . The range of observed $[\text{Rb}/\text{Fe}]$ and $[\text{Rb}/\text{Zr}]$ values from Ref. [Per17] are shown by the shaded blue background. Adapted from Ref. [Per17]. . . . .	32
Figure 3.3 The abundance evolution of key nuclei related to the s-process branching at $^{86}\text{Rb}$ for a single network calculation simulating the conditions during a single AGB thermal pulse. The $T$ , $\rho$ , and $X_{\text{last}}(^4\text{He})$ parameters are 300 MK, $10^3$ g/cm $^3$ , and 0.7, respectively, with $X_{\text{init}}(^4\text{He}) = 0.75$ . . . . .	35
Figure 3.4 The network flux plot for a single network calculation simulating the conditions during a single AGB thermal pulse. The $T$ , $\rho$ , and $X_{\text{last}}(^4\text{He})$ parameters are 300 MK, $10^3$ g/cm $^3$ , and 0.7, respectively, with $X_{\text{init}}(^4\text{He}) = 0.75$ . The arrow thickness corresponds to the magnitude of the integrated flux from one nucleus to another, with three levels of relative magnitude shown. The reactions with the largest net flux are the triple- $\alpha$ reaction, the $^{13}\text{C}$ neutron source sequence $^{12}\text{C}(p, \gamma)^{13}\text{N}(\beta^+\nu)^{13}\text{C}(\alpha, n)^{16}\text{O}$ , and the neutron poison $^{14}\text{N}(n, p)^{14}\text{C}$ . . . . .	36
Figure 3.5 The largest reaction rate correlations with the final mass fraction ratio $X(^{87}\text{Rb})/X(^{86}\text{Sr})$ , ranked by mutual information, given in the top-right corner of each plot. On the $x$ -axis is the gaussian rate variation factor $p$ (see text). The $T$ , $\rho$ , and $X_{\text{last}}(^4\text{He})$ parameters for each sample are 300 MK, $10^3$ g/cm $^3$ , and 0.7, respectively, with $X_{\text{init}}(^4\text{He}) = 0.75$ . The Monte Carlo reaction network calculation was performed for $5 \times 10^4$ samples, and the density of these samples is represented by color, with yellow being the most dense region. . . . .	41

Figure 3.6	The largest reaction rate correlations with the final mass fraction ratio $X(^{87}\text{Rb})/X(^{90}\text{Zr})$ , ranked by mutual information. See Fig. 3.5 caption for details.	42
Figure 3.7	Probability densities of the [Rb/Sr] (green), [Rb/Zr] (blue) and [Rb/Fe] (red, dashed) abundance ratios resulting from the Monte Carlo reaction network calculation for $5 \times 10^4$ samples at $T = 300$ MK, $\rho = 10^3$ g/cm <sup>3</sup> , and $X_{\text{last}}(^4\text{He}) = 0.7$ , with $X_{\text{init}}(^4\text{He}) = 0.75$ . The solid red probability density was obtained by correcting [Rb/Fe] for its enhanced $^{56}\text{Fe}$ initial mass fraction relative to solar system abundance. In the legend, “init” refers to the initial value of [Rb/Fe] before the network calculation (see text).	44
Figure 3.8	The [Rb/Fe] and [Rb/Zr] probability densities from the present Monte Carlo nuclear reaction network calculation plotted with the AGB model data of Refs. [Kar12, Raa12, Kar16, Pig16] and the (blue) observation scatter of Ref. [Per17]. The median probability densities are shown by the dotted lines, while the $1\sigma$ and $2\sigma$ bands are represented by the dark and light bands, respectively. The $+1\sigma$ and $+2\sigma$ [Rb/Zr] probability density values are shown added to the model with the largest [Rb/Zr] value. This depicts the likelihood of reaction rate uncertainties alone being responsible for reproducing the largest observed [Rb/Zr] ratios.	46
Figure 4.1	The observed Mg and K elemental abundances of red giants in NGC 2419 from Refs. [Muc12] (red) and [Coh12] (blue). Figure adapted from [Ili16].	49
Figure 4.2	The hydrogen burning mechanism driving the Mg–K anticorrelation in the globular cluster NGC 2419. The nucleosynthesis chain for the Mg depletion is the Mg–Al cycle, shown on the left-hand side. Whether the $^{26}\text{Al}^m$ isomer or the $^{26}\text{Al}^g$ ground state is populated, the result is $^{27}\text{Al}$ production, which repeats the cycle with $^{27}\text{Al}(p, \alpha)^{24}\text{Mg}$ . The main nucleosynthesis chain for the K enrichment is shown on the right-hand side with solid arrows. The $^{37}\text{Ar}(p, \gamma)^{38}\text{K}$ reaction proceeds at a much higher rate than $^{37}\text{Ar}(e^-, \nu)^{37}\text{Cl}$ electron capture at the stellar densities of interest. Nuclides in blue are destroyed and nuclides in red are produced in the overall nucleosynthesis. Shaded nuclides are stable.	50
Figure 4.3	Temperature-density conditions reproducing the Mg–K anticorrelation and other abundance patterns in NGC 2419, obtained by sampling $T$ , $\rho$ , $X_{\text{H}}$ , reaction rate probability densities, and initial abundances from a nuclear reaction network (see text). The $T$ – $\rho$ conditions for several polluter star candidates are represented by the black curves. Adapted from Ref. [Ili16].	52

Figure 4.4	Systematic effects of the $^{39}\text{K}(p, \gamma)^{40}\text{Ca}$ rate influencing temperature and density conditions. The indicated variation factors ( $\alpha = 1/10, 1/5, 5, 10$ ) are applied to the reaction rate in each panel, and the black dots show the resulting temperature-density conditions that provide an acceptable match with observed abundances. The red dots represent the case where no systematic effects ( $\alpha = 1$ ) have been added. Figure adapted from Ref. [Der17]. . . . .	53
Figure 4.5	The recent $^{39}\text{K}(p, \gamma)^{40}\text{Ca}$ reaction rate probability density calculation of [Lon18b] as a function of temperature. The median, recommended rate is shown as the dotted normalization line. The thick and thin black lines represent the 68% ( $1\sigma$ ) and 95% ( $2\sigma$ ) uncertainty bands, respectively. The color scale shows the continuous nature of the probability density, with darker red colors closer to the recommended rate. The green line represents the previous calculation of Ref [Che81]. . . . .	54
Figure 4.6	The individual resonance contributions to the $^{39}\text{K}(p, \gamma)^{40}\text{Ca}$ reaction rate from Ref. [Lon18b] as a fraction of unity. Measured resonances are represented with shading or hatched lines and are shown with their $1\sigma$ uncertainty bands. Resonances from upper limits are represented by dashed lines and show their 84% ( $+1\sigma$ ) value. The black line represents the total resonance contribution of all resonances that individually contribute less than 20% to the total reaction rate. . . . .	56
Figure 4.7	The evaporation chamber before the production of KI targets. The 3 targets shown in position become the KI #1, KI #2, and KI #3 targets after evaporation. The thickness monitor is also shown in position around a fourth opening in the 16-slot target holder. . . . .	59
Figure 4.8	A 2D histogram of the focal-plane $\Delta E$ vs E detector signals. Different groups correspond to different particles depending on their mass and charge. The deuteron group, highlighted in red, is being gated on in the figure. . . . .	60
Figure 4.9	A histogram spectrum of the front (P1) focal-plane detector position section at $\theta_{\text{lab}} = 5^\circ$ and $E_{\text{lab}} = 21$ MeV with the KI #6 target (in red) and the carbon target (in black), both gated on the deuteron group from the the $\Delta E$ vs. E spectrum. Overlapping peaks indicate contaminants. . . . .	61
Figure 4.10	A 2D histogram of the front (P1) focal-plane position section vs event number over all $^{39}\text{K}(^3\text{He}, d)^{40}\text{Ca}$ runs (#23 – #27) at $\theta_{\text{lab}} = 9^\circ$ with the KI #5 target. Both axes are compressed to 512 channels. The P1 section is zoomed in on the $^{13}\text{N}$ ground state to show the effect of energy shifts due to beam retunes. A beam retune after run #25 caused the shift in the P1 spectrum shown at event (bin) number 320. The unknown phenomenon at event (bin) number 100 occurred during run #23, which caused a reduction in counts but no energy shift. . . . .	62
Figure 4.11	A 2D histogram of the Si $\Delta E$ vs Si E detector signals. Different groups correspond to different particles depending on their mass and charge. The $^3\text{He}$ group, highlighted in red, is being gated on in the figure. . . . .	65

Figure 4.12 A 2D histogram of the Si $\Delta E$ vs Si total E detector signals, gated on the $^3\text{He}$ group and at $\theta_{\text{lab}} = 45^\circ$ . This is similar to Fig. 4.11, except the total Si energy has been calculated based on the slope of the peaks in the Si $\Delta E$ vs Si E spectrum (see Eqn. 4.1). Each peak is labeled with its corresponding elastic scattering element. . . . .	65
Figure 4.13 A histogram spectrum of Si Total E gated on the $^3\text{He}$ group at $\theta_{\text{lab}} = 45^\circ$ , obtained by projecting Fig. 4.12 onto its $x$ -axis. Each peak is labeled with its corresponding elastic scattering element. The individual $^{39}\text{K}$ and $^{41}\text{K}$ isotopes are unresolvable. . . . .	66
Figure 4.14 A histogram spectrum of the focal-plane P1 section at $\theta_{\text{lab}} = 7^\circ$ with the KI #1 target, gated on the deuteron group. The peaks are clearly not gaussian because of the presence of high-energy (low-channel) tails, a result of oxidation in the KI #1 target. . . . .	68
Figure 4.15 A Bayesian multi-gaussian fit with <b>BayeSpec</b> for the $^{40}\text{Ca}$ excited states (in red) 6025 keV and 5903 keV from $^{39}\text{K}(^3\text{He}, d)^{40}\text{Ca}$ and the $^{14}\text{N}$ excited states (in orange) 5106 keV and 4915 keV from $^{13}\text{C}(^3\text{He}, d)^{14}\text{N}$ at $\theta_{\text{lab}} = 5^\circ$ . In red and orange are 50 random samples of the gaussian distributions from the $\sigma$ , $\mu$ , and $A$ posteriors for each peak. The $^{40}\text{Ca}$ peaks share an identical $\sigma$ posterior, while the $^{14}\text{N}$ peaks share their own as well. In blue are the sums of the peaks plus the background line for each of those 50 samples. . . . .	71
Figure 4.16 The constructed priors for $\mu - x_m$ (left) and $A/y_m$ (right) from 10,000 samples of the $\sigma$ and $\lambda$ priors of Eqns. 4.11 and 4.12. The gaussian (blue) approximations were derived from the mean and standard deviation of the samples. The lognormal (red) approximations were derived from the mean and standard deviation of the natural logarithm of those samples. . . . .	74
Figure 4.17 A Bayesian exponentially-modified gaussian fit with <b>BayeSpec</b> for the 6285 keV $^{40}\text{Ca}$ state from $^{39}\text{K}(^3\text{He}, d)^{40}\text{Ca}$ at $\theta_{\text{lab}} = 5^\circ$ with an oxidized potassium iodine target (KI #1). In blue are 50 random samples of the exponentially-modified gaussian distribution from the $\sigma$ , $\lambda$ , $\mu$ , and $A$ posteriors, plus the background line. In green are the gaussian components of the exponentially-modified gaussian samples. The new mode and peak intensity are represented by the black lines, where the solid line represents their mean and the dashed lines represent their standard deviation. . . . .	75
Figure 4.18 A Bayesian exponentially-modified gaussian fit with <b>BayeSpec</b> for the $^{40}\text{Ca}$ excited states (left to right, in red) 7694 keV, 7658 keV, 7623 keV, and 7532 keV from $^{39}\text{K}(^3\text{He}, d)^{40}\text{Ca}$ and the $^{14}\text{N}$ excited state (in orange) 6446 keV from $^{13}\text{C}(^3\text{He}, d)^{14}\text{N}$ at $\theta_{\text{lab}} = 5^\circ$ with an oxidized potassium iodine target (KI #1). In red and orange are 50 random samples of the exponentially-modified gaussian distributions from the $\sigma$ , $\lambda$ , $\mu$ , and $A$ posteriors for each peak. The $^{40}\text{Ca}$ peaks share identical $\sigma$ and $\lambda$ posteriors, whereas the $^{14}\text{N}$ peak has its own. In blue are the sums of the peaks plus the background line for each of those 50 samples.	76

Figure 4.19 The variations from the average differential cross-section ratio $R$ , normalized to unity, for each sort group over all $^{40}\text{Ca}$ states measured at $\theta_{\text{lab}} = 13^\circ$ . The colored lines correspond to each $^{40}\text{Ca}$ state up to $E_x = 8935$ keV. The variations are typically within 10% of the average, which is true for the other angles as well. The average deviation for a given angle is used as an additional scatter uncertainty, as described in the text. . . . .	83
Figure 4.20 The differential cross-section, as a ratio to Rutherford scattering, of the global $^3\text{He}$ optical model potential of Ref. [Lia09] for $^{39}\text{K}$ (black line) and that of the present relative $^{39}\text{K}(^3\text{He}, ^3\text{He})^{39}\text{K}$ measurements (red data). The scaling factor $N_{\text{ES}}$ is illustrated, which is also applied to the transfer data to establish an absolute scale. . . . .	85
Figure 4.21 The same as Fig. 4.20, except the differential cross-section of the global $^3\text{He}$ optical model potential has been scaled by $N_{\text{ES}}$ to match the experimental measurements, as described in the text. . . . .	86
Figure 4.22 The calibration states for the MCMC energy calibration, represented by red vertical lines for the $\theta_{\text{lab}} = 5^\circ$ focal plane position spectrum. Their ENSDF [Che17] energies are labeled in keV. The 8425 keV state uses the energy of the recent measurement from Ref. [Gri22] instead. The 8484 keV and 9136 keV alternative calibration states are used when the 8425 keV and 9454 keV states were obscured at $\theta_{\text{lab}} = 5, 7^\circ$ and $20^\circ$ , respectively. The $^{17}\text{F}$ contaminant appears in exactly the same position as the 8425 keV state in the figure. . . . .	88
Figure 4.23 Residuals between the excitation energies predicted from the MCMC energy calibration and that of the median calibration line at $\theta_{\text{lab}} = 5^\circ$ (sort group #3) for the calibration states (in red) and the test states (in black). The 68% ( $1\sigma$ ) and 95% ( $2\sigma$ ) confidence intervals for the fit are represented by the dark and light shading, respectively. See text for details. . . . .	90
Figure 4.24 Excitation energies and their uncertainties of the 8551 keV state from the MCMC energy calibration for each sort group, excluding sort groups #1 and #2 that used an oxidized target. The ENSDF energy and its uncertainty are given as the red line and red band, respectively. A simple average and a weighted average of the energies are given by the black and orange lines, respectively. The uncertainty propagated from the simple average and from the weighted average are given by the blue and orange bands, respectively. The simple average of the MCMC uncertainties is represented by the green band, which best captures the range of the individual uncertainties for each state. . . . .	91

Figure 4.25 Residuals between the final reported energies for each state from the MCMC energy calibration and that of ENSDF [Che17]. The residuals and uncertainties for each state result from a simple average of the MCMC energies and uncertainties of each sort group, respectively. The residuals in red represent the astrophysical region, from 8359 keV to 8995 keV. The $x$ -axis values correspond to the following states in keV; 1: 5903, 2: 6285, 3: 6582, 4: 6750, 5: 6950, 6: 7113, 7: 7623, 8: 7658, 9: 7694, 10: 7973, 11: 8113, 12: 8188, 13: 8271, 14: 8359, 15: 8484, 16: 8551, 17: 8665, 18: 8748, 19: 8764, 20: 8851, 21: 8935, 22: 8995, 23: 9092, 24: 9136, 25: 9227, 26: 9405, 27: 9419, 28: 9432, 29: 9538, 30: 9603. . . . .	92
Figure 4.26 The energy-calibrated focal plane position spectrum, focused on the $^{40}\text{Ca}$ states above the proton separation energy at $\theta_{\text{lab}} = 5^\circ$ (sort group #3). The average width of the energy bins is approximately 1.6 keV in this region. The $^{40}\text{Ca}$ states are labeled with their ENSDF [Che17] energies in keV, and contaminants at this angle are indicated. The red vertical line indicates the proton separation energy, $S_p = 8328.18(2)$ keV from Ref. [Wan21]. . . . .	95
Figure 4.27 Normalization between the relative transfer differential cross section of the 7532 keV state and that of all possible DWBA models based on the current ENSDF $J^\pi = 2^-$ assignment. The normalization $N_{\text{ES}}$ between elastic scattering and the global $^3\text{He}$ OMP is shown to scale, as is the $C^2 S$ normalization. . . . .	98
Figure 4.28 The DWBA models of Fig. 4.27 scaled down to the 7532 keV data to compare angular distributions. The $l = 1$ models are a clear match for this state. . . . .	99
Figure 4.29 Differential cross sections for 4491 keV through 6582 keV. See text for details. . . . .	101
Figure 4.30 Differential cross sections for 6750 keV through 7658 keV. See text for details. . . . .	102
Figure 4.31 Differential cross sections for 7694 keV through 8271 keV. See text for details. . . . .	103
Figure 4.32 Differential cross sections for 8935 keV through 9227 keV. See text for details. . . . .	104
Figure 4.33 Differential cross-sections of proton-unbound $^{40}\text{Ca}$ states observed in the present experiment below the lowest directly measured $(p, \gamma)$ resonance at 8935 keV. The left panel shows the $l = 1$ distributions, while the right panel shows all other distributions. . . . .	105
Figure 4.34 A Bayesian Monte Carlo fit for the 9405–9432 keV multiplet at $\theta_{\text{lab}} = 5^\circ$ , including the clearly distinguishable 9454 keV state. The multiplet is fit with 3 peaks in this experiment, with calibrated energies of 9403.7(31) keV, 9416.7(32) keV, and 9431.7(32) keV. This is better resolution than $(d, n)$ [Fuc69] was able to achieve, where only 2 peaks in the multiplet were fit at energies of 9408 keV and 9431 keV. . . . .	110

Figure 4.35 Comparison between the $^{39}\text{K}(p, \gamma)^{40}\text{Ca}$ reaction rate using the proton partial-widths and resonance energies of the present experiment (solid line, blue band) and the most recent evaluation of Ref. [Lon18b] (dotted line, gray band). The reaction rate ratio is taken with respect to the median, recommended rate of Ref. [Lon18b] for both calculations. The $1\sigma$ uncertainty bands are shown. . . . .	117
Figure 4.36 Comparison between the $^{39}\text{K}(p, \gamma)^{40}\text{Ca}$ reaction rate uncertainty using the proton partial-widths and resonance energies of the present experiment (solid band) and the most recent evaluation of Ref. [Lon18b] (dotted band). Each reaction rate ratio is taken with respect to their own median, recommended rate. The $1\sigma$ uncertainty bands are shown. . . . .	118
Figure 4.37 Individual resonance contributions to the $^{39}\text{K}(p, \gamma)^{40}\text{Ca}$ reaction rate, where a value of 1.0 implies that the given resonance contributes 100% to the reaction rate at that temperature. The labels correspond to center-of-mass resonance energies in keV. Resonances with shading or hatched lines have been measured and are shown with their $1\sigma$ uncertainty bands. Resonances with a single, dashed line are upper limit calculations and show their 84% $1\sigma$ value, for clarity. The resonances displayed are those that individually account for at least 10% of the total reaction rate at their corresponding temperatures. The remaining summed resonance contributions are represented by the dotted line. . . . .	120
Figure 4.38 The $T$ - $\rho$ conditions that match the observed Mg-K anticorrelation in the globular cluster NGC 2419, using both the new and previous $^{39}\text{K}(p, \gamma)^{40}\text{Ca}$ reaction rates. Solutions for both rates are shown in gray as the overlap region, while solutions unique to one rate are indicated with red (new) or blue (old). An $X_{\text{last}}(^1\text{H})$ value of 0.2 is used here. . . . .	122
Figure 4.39 The maximum change in potassium abundance when using the new $^{39}\text{K}(p, \gamma)^{40}\text{Ca}$ reaction rate compared to that of Ref. [Lon18b]. All other reaction rates are provided by <b>Starlib</b> [Sal13]. A maximum decrease in $[\text{K}/\text{Fe}]$ of 0.23 dex (a factor of 1.7 decrease) occurs at $T = 100$ MK, $\rho = 4 \times 10^7$ g/cm <sup>3</sup> , and $X_{\text{last}}(^1\text{H}) = 0.2$ . This configuration now reproduces the Mg-K anticorrelation in NGC 2419, whereas the rate of Ref. [Lon18b] does not. . . . .	124
Figure 5.1 The traditional method of converting detected particles or $\gamma$ -rays into numerical data using analog pulse-processing modules and an analog-to-digital converter (ADC). . . . .	127
Figure 5.2 The new method of converting detected particles and $\gamma$ -rays into numerical data with a digitizer, replacing analog modules and the need for an ADC. . . . .	128
Figure 5.3 The CAEN V1730 Digitizer (pictured on the right), along with its associated DPP firmware and custom frontend DAQ software, is replacing the need for the unportable analog pulse-processing modules (pictured on the left) associated with the Enge focal-plane detector package at TUNL. . . . .	129

Figure 5.4	A signal sampled by the V1730 digitizer, summarizing the parameters used by the DPP algorithms. When the signal crosses the threshold value, the trigger fires, which primes the system for data acquisition.. .	130
Figure 5.5	The dynamic baseline calculation using the mean value of a user-defined number of samples in a moving time window. The baseline freezes during the energy integration of a signal that has been triggered. . . . .	131
Figure 5.6	The data format for the first two events in a channel aggregate. Each memory location is 32-bits and is accessed during readout. Individual samples are not saved by our digitizer, so every 32-bit line that contains a sample, $S_1$ , $S_2$ , etc., is omitted. Each event therefore contains up to three memory locations. The channel aggregate itself has a header consisting of the first two memory locations, SIZE and FORMAT. . .	134
Figure 5.7	The data format for a board aggregate, consisting of up to 8 channel aggregates and 4 memory locations making up the header. Each memory location is 32-bits and is accessed during readout. . . . .	135
Figure 5.8	The settings file, settings-DPP.dat, where the most common user-defined DPP parameters are adjusted. It is unlikely any other internal setting is needed, but implementing new V1730 register settings has been made simple. . . . .	137
Figure 5.9	The $^{152}\text{Eu}$ $\gamma$ -ray spectrum as a result of $\beta$ -decay. The raw $Q_{long}$ value is given on the $x$ -axis and the number of counts in each bin is given on the $y$ -axis. The largest four $\gamma$ -ray peaks are shown, where the right-most one is the 1408 keV peak used for the energy resolution analysis. . .	138
Figure 5.10	Resolution tests of the long gate (left) and gate offset (right) DPP parameters for the 1408 keV $^{152}\text{Eu}$ calibration state. . . . .	139
Figure 5.11	The $^{60}\text{Co}$ $\gamma$ -ray spectrum shown with the EngeSpec GUI. . . . .	140
Figure 5.12	The coincidence histogram using the LED time stamp determination mode. The channels on the $x$ -axis span from 0 to 8196, where the $\Delta t = 0$ condition has been shifted to the center, at channel 4096. The FWHM is found to be 10.7 ns for this case. . . . .	141
Figure 5.13	The coincidence histogram using the CFD time stamp determination mode. The FWHM is 4.75 ns for this case. . . . .	141

## CHAPTER

# 1

## INTRODUCTION

Understanding the origin of the elements has been the primary goal of nuclear astrophysics since its conception. Through the work of Burbidge, Burbidge, Fowler, and Hoyle [Bur57], and independently Cameron [Cam57], it was established that the chemical elements observed in our solar system were synthesized through nuclear burning in stars. Indeed, all but the lightest elements in our observable universe (hydrogen through boron) are the ashes of stellar burning. Consequently, in the quest to discover the nature of the elemental origins, we must understand the nature of stellar processes. From birth to death, stars undergo nuclear reactions in their interiors. With sufficient temperatures, the reaction products themselves undergo subsequent nuclear reactions. An evolutionary stage is reached at which point the star either explodes or simply ejects its material outward. This nuclear-processed material is mixed together with the ashes from neighboring stars, forming new stars with new compositions and therefore new nucleosynthesis. One of the most complex evolutionary stages of a star is known as the asymptotic giant branch (AGB) phase, and stars that we currently observe on this phase are known as AGB stars. This thesis focuses on these complex nucleosynthesis processes in massive AGB stars, including s-process nucleosynthesis resulting from thermal pulses, as well as hot-bottom burning at the base of the convective hydrogen envelope. These stellar processes are investigated through laboratory nuclear reaction experiments here on earth. In particular, transfer reaction experiments are used in this thesis as a surrogate for the direct reactions occurring in the stellar processes. These experiments provide information on the nuclear structure of the nuclei involved in the key reactions, and therefore they constrain the reaction rates that are crucial to nucleosynthesis.

The present chapter will provide an overview of the nuclear astrophysics topics addressed in this thesis. Chapter 2 will introduce the mathematical formalism for quantifying nucleosynthesis with reaction rates, as well as the formalism for transfer reactions. Chapter 3 will address the “rubidium problem” in massive AGB stars, a discrepancy between observed and theoretical rubidium abundances from s-process nucleosynthesis. The s-process branching at  $^{86}\text{Rb}$  is investigated through a Monte Carlo reaction network approach, identifying the most important reactions affecting rubidium abundance. Chapter 4 will address the Mg–K abundance anomaly observed in the globular cluster NGC 2419, which may have originated from hot-bottom burning in massive AGB stars. The  $^{39}\text{K}(\text{He}, d)^{40}\text{Ca}$  proton-transfer reaction is measured at high resolution, and new constraints are placed on the key potassium-destroying reaction  $^{39}\text{K}(p, \gamma)^{40}\text{Ca}$ . Finally, Chapter 5 will introduce the development of a new digital data acquisition system (DAQ) for the focal-plane detector package at the Enge Split-Pole Spectrograph, which will replace the current analog system for future transfer reaction experiments.

## 1.1 Asymptotic Giant Branch Stars

Asymptotic giant branch (AGB) stars produce about half of all elements heavier than iron in our galaxy [Bus99], and they are one of the leading candidates for the origin of abundance anomalies in globular clusters [Pra07]. An understanding of these stars therefore provides insight into the origin of the elements. The asymptotic giant branch refers to the evolutionary track that these stars follow on a typical Hertzsprung-Russell (HR) diagram, which asymptotically approaches that of the red giant branch. HR diagrams show the luminosity of a star as a function of its effective temperature. These properties are often cataloged for observed stars, and the current evolutionary phase of a star can be determined from its relative position on the diagram. A theoretical example of the evolutionary track of a  $5 M_{\odot}$  star is represented on the HR diagram of Fig. 1.1. Starting from the zero-age main sequence (ZAMS), where the star first begins to burn hydrogen, the evolutionary track passes through the sub-giant branch (SGB), the red-giant branch (RGB), the horizontal branch (HB), the early (E-) and thermally-pulsing (TP-) asymptotic giant branch (AGB) phases, and the post-AGB branch. It then undergoes planetary nebula (PN) formation, before eventually becoming a white dwarf. Each of these branches represents a unique evolutionary phase of the star, many of which are described in the figure at key transitional points. As mentioned above, this thesis focuses on AGB stars, the evolutionary track of which is highlighted in red in the figure.

It is clear from Figure 1.1 that AGB stellar evolution is separated into two stages. The

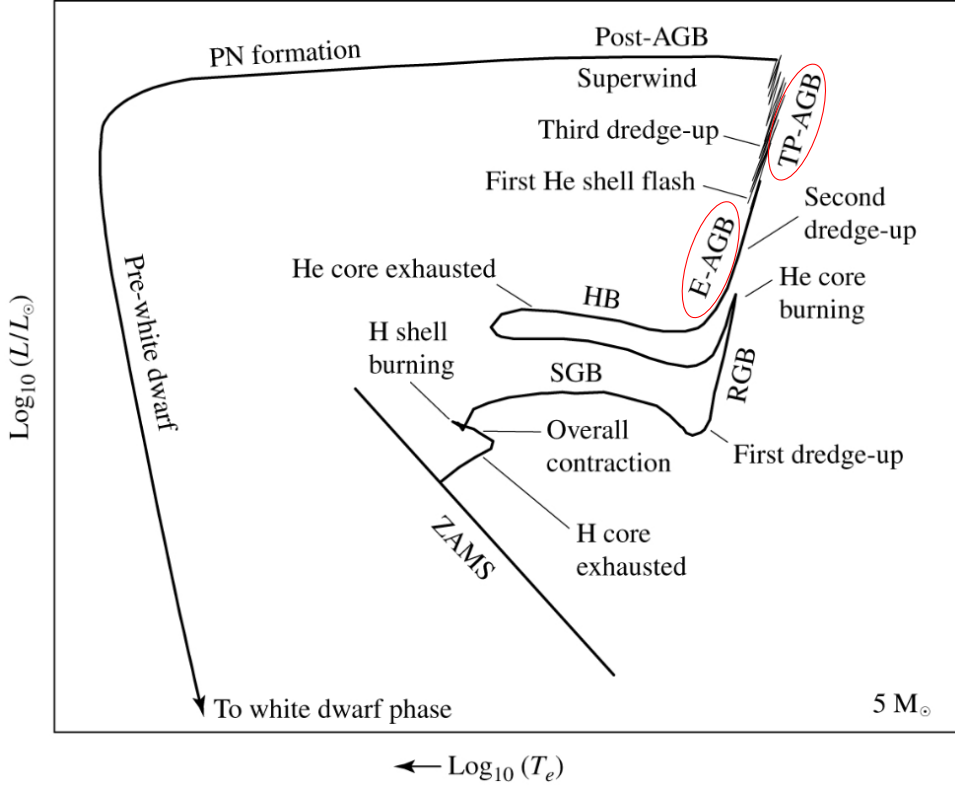


Figure 1.1: Evolution of a  $5 M_{\odot}$  star represented on the Hertzsprung-Russell (HR) diagram. The two stages of the asymptotic giant branch (AGB) are highlighted in red. See text for definitions of acronyms. Figure adapted from Ref. [Car07].

*early-AGB* (e-AGB) stage occurs after both hydrogen and helium have been exhausted in the core of a star, leaving behind mostly inert carbon and oxygen. Hydrogen and helium burning is still active in separate shells around the core, with a helium-rich intershell region in between. The far more active hydrogen-burning shell perpetually increases the density and temperature of the intershell region, until the rate of energy generated by the helium-burning shell is greater than the rate at which energy can be transported outward through radiative diffusion [Ili15a]. A thermal instability, called a *thermal pulse*, occurs as a result, initiating the *thermally pulsing AGB* (TP-AGB) stage, shown in Figure 1.2. This pulse causes the helium-burning shell to extend into the intershell region and ignite the hydrogen-burning shell, rendering it inactive for a brief period. The nuclei inside the intershell region get carried outward through the convective hydrogen envelope toward the surface of the star, in what is known as a *third dredge-up* (3DUP) event<sup>1</sup>, where they are ejected by stellar winds. The

<sup>1</sup>The first two dredge-ups are depicted in Figure 1.1, occurring at the start of the RGB and during the e-AGB stage, respectively. For stars with  $M \lesssim 4 M_{\odot}$ , the second dredge-up does not occur because the convective hydrogen envelope cannot penetrate the intershell region at this point.

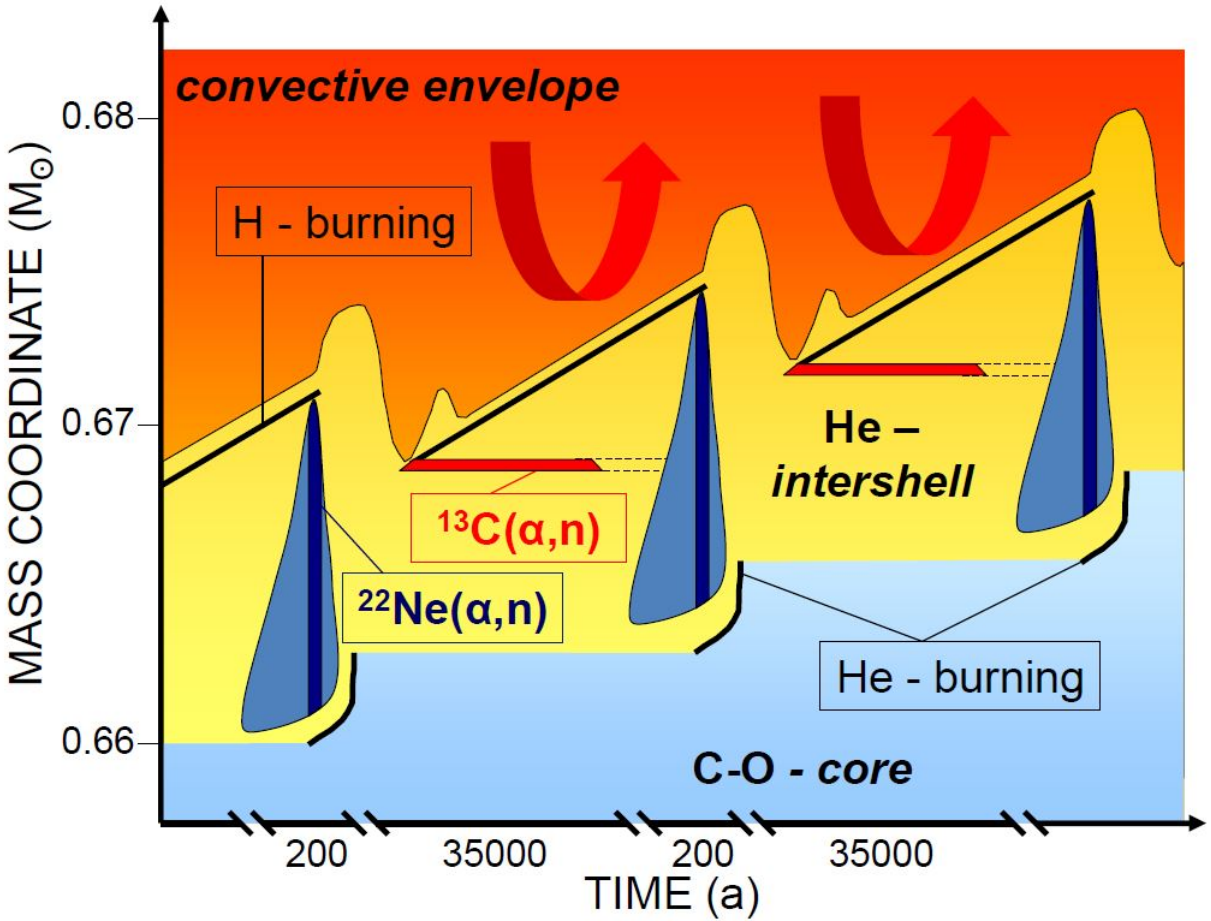


Figure 1.2: The evolution and structure of a thermally pulsing AGB star. Three thermal pulses are depicted in blue, extinguishing the hydrogen burning shell. The neutron sources  $^{13}\text{C}(\alpha, n)^{16}\text{O}$  and  $^{22}\text{Ne}(\alpha, n)^{25}\text{Mg}$  are shown to be active between pulses and during pulses, respectively. Figure adapted from Ref. [Rei14].

hydrogen-burning shell takes over once again as the dominant energy-producer after the thermal pulse, and this cycle repeats for on the order of tens to hundreds of pulses [Hab04].

Helium burning during each thermal pulse produces  $^{12}\text{C}$  as a result of the triple- $\alpha$  reaction, followed by  $^{16}\text{O}$  from  $^{12}\text{C}(\alpha, \gamma)^{16}\text{O}$ , which get accumulated mostly in the core, increasing its mass. However, some  $^{12}\text{C}$  accumulates in the intershell region. After a 3DUP event resulting from a thermal pulse, some protons from the convective hydrogen envelope mix into the intershell region, initiating the reaction sequence  $^{12}\text{C}(p, \gamma)^{13}\text{N}(\beta^+ \nu)^{13}\text{C}(p, \gamma)^{14}\text{N}$ . The effect of these additional proton-capture reactions is the formation of a  $^{13}\text{C}$  pocket and a  $^{14}\text{N}$  pocket at the top of the intershell region. During the interpulse period, when temperatures are between  $100 \text{ MK} \lesssim T \lesssim 300 \text{ MK}$ , the  $^{13}\text{C}(\alpha, n)^{16}\text{O}$  reaction is activated, producing a large neutron density of  $N_n \approx 10^7 \text{ cm}^{-3}$ . During thermal pulses, when temperatures are

$T \gtrsim 300$  MK, the reaction sequence  $^{14}\text{N}(\alpha, \gamma)^{18}\text{F}(\beta^+ \nu)^{18}\text{O}(\alpha, \gamma)^{22}\text{Ne}$  proceeds. As a result, the  $^{22}\text{Ne}(\alpha, n)^{25}\text{Mg}$  reaction is activated, producing an even larger neutron density of  $N_n \approx 10^{10} \text{ cm}^{-3}$ . Nucleosynthesis occurs in the intershell region from these two neutron sources via a series of neutron-captures and  $\beta$ -decays, known as the s-process, described in Section 1.2. The heavy nuclei produced from the s-process are brought to the surface by subsequent thermal pulses and 3DUP events.

In the case of AGB stars with  $M \gtrsim 4 M_\odot$ , the convective hydrogen envelope reaches down to the top of the hydrogen-burning shell during the interpulse period, where temperatures are  $T \gtrsim 50$  MK [Ili15a], but can theoretically reach as high as  $T \approx 150$  MK for *Super-AGB* (SAGB) stars with  $M \gtrsim 7 M_\odot$  [Ven12]. The resulting hydrogen burning nucleosynthesis is known as hot-bottom burning, detailed in Section 1.3, and the products of this burning are brought to the surface by the convective hydrogen envelope. This process is one of the leading candidates for the recent abundance anticorrelations observed in globular clusters, detailed in Section 1.4.

## 1.2 s-Process Nucleosynthesis

Most light nuclei below the iron-peak at mass number  $A \approx 60$  are formed through charged-particle fusion reactions in stars, where temperatures are sufficient for transmission through the repulsive Coulomb barrier via quantum tunneling. The synthesis of nuclei heavier than the iron-peak, however, cannot be explained by these charged-particle fusion reactions. At low temperatures, the transmission probability through the large Coulomb barrier of heavy nuclei becomes prohibitively small, while at high temperatures, nuclear statistical equilibrium favors the production of iron-peak nuclei due to their large binding energy per nucleon. Nuclei with  $A \gtrsim 60$  must be formed instead by neutron capture, where Coulomb repulsion is no longer a factor. Neutron capture will generate neutron-rich isotopes of a given element, some of which eventually undergo  $\beta$ -decay if they are unstable. The stable daughter nuclei will then capture neutrons until another unstable isotope is reached, and the process continues this way up to some of the heaviest nuclei.

When the neutron density in the astrophysical environment is sufficiently small such that unstable nuclei preferentially  $\beta$ -decay, the ensuing nucleosynthesis is referred to as the *s-process*. This is a relatively slow process (hence the *s-*), as the nucleosynthesis can only proceed based on the half-lives of the unstable nuclei. If, on the other hand, the neutron density is sufficiently large such that unstable nuclei preferentially neutron-capture, the ensuing nucleosynthesis is referred to as the *r-process* because this happens at a much more (*r*-apid pace. These two processes occur in different astrophysical sites and are equally

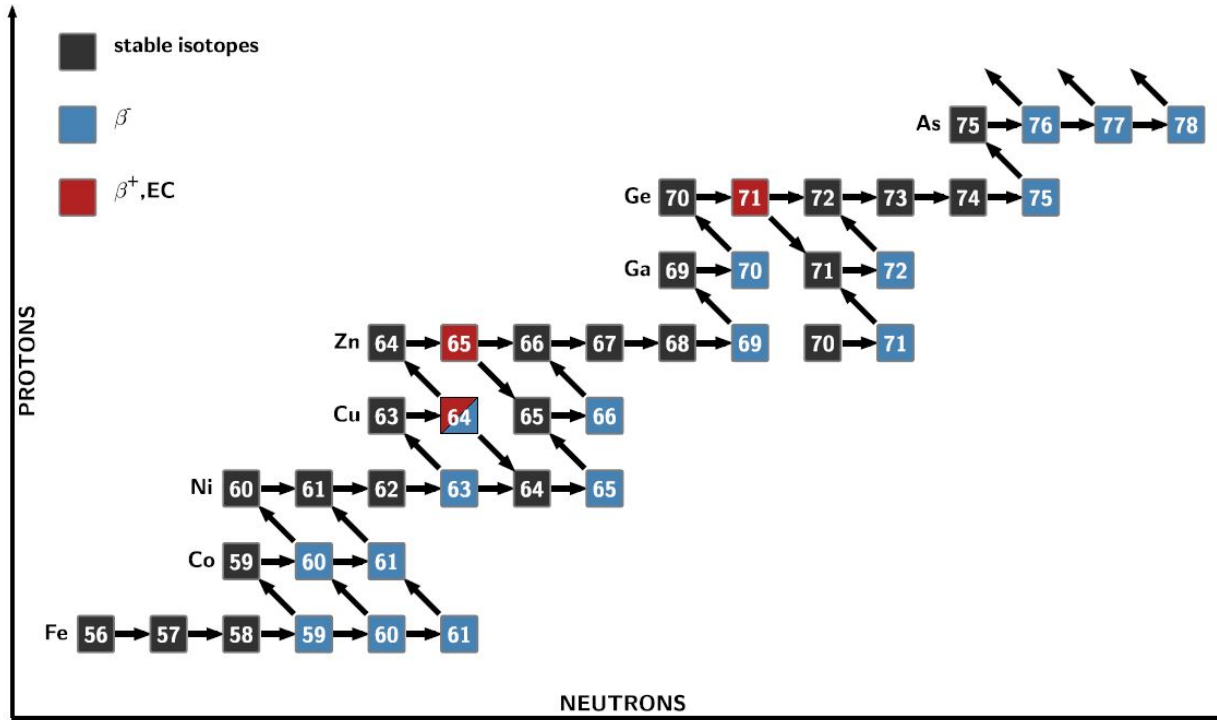


Figure 1.3: The s-process path from iron to arsenic. The stable nuclei in black undergo neutron capture, while the unstable nuclei in blue ( $\beta^-$ -decay) and red ( $\beta^+$ -decay or electron capture) either decay or undergo neutron-capture depending on their half-lives and the neutron density  $N_n$ . At s-process branchings, e.g.  $^{59}\text{Fe}$ , the probability for neutron-capture and decaying is approximately equal, hence the path is split into two branches. Figure adapted from Ref. [Rei14].

responsible for almost all of the heavy nuclei in the observable universe. Some heavy nuclei are referred to as s-only or r-only nuclei because only one of these processes accounts for their abundance. The research presented in Chapter 3 is based on s-process nucleosynthesis occurring in AGB stars.

To illustrate how the s-process works, consider the chain of reactions shown in Figure 1.3, starting with the most abundant nucleus in the iron peak,  $^{56}\text{Fe}$ . This is referred to as a *seed nucleus* because it is the nucleus that initiates the s-process reaction chain. Stable nuclei are shown in black in the figure, nuclei unstable to  $\beta^-$ -decay are shown in blue, and nuclei unstable to  $\beta^+$ -decay or electron capture (EC) are shown in red. As is typical of a chart of the nuclides, neutron number increases to the right and proton number increases upward. Neutron-capture is therefore represented by an arrow to the right, while  $\beta$ -decays and electron capture are represented by diagonal arrows due to the conversion of a neutron to a proton, or vice versa. If there is a sufficient neutron density  $N_n$  in the astrophysical environment, the neutron-capture of  $^{56}\text{Fe}$ ,  $^{56}\text{Fe}(n, \gamma)^{57}\text{Fe}$ , leads to the stable nucleus  $^{57}\text{Fe}$ .

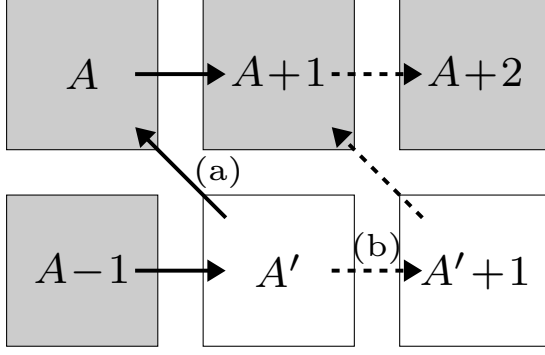


Figure 1.4: A simple s-process path initiating from the nucleus with mass number  $A - 1$ , where shaded nuclei are stable, and unshaded nuclei are unstable. Case (a) is shown by the solid arrows, where only  $\beta$ -decays occur on unstable nuclei. Case (b), indicated by the addition of dashed arrows, treats  $A'$  as a branching point nucleus.

The two subsequent neutron-captures,  $^{57}\text{Fe}(n, \gamma)^{58}\text{Fe}$  and  $^{58}\text{Fe}(n, \gamma)^{59}\text{Fe}$ , on the stable  $^{57}\text{Fe}$  and  $^{58}\text{Fe}$  nuclei, respectively, leads to the unstable  $^{59}\text{Fe}$  nucleus. The nucleosynthesis path has now lead to an *s-process branching*, and  $^{59}\text{Fe}$  is referred to as a *branching point nucleus*. At these branchings, the decay constant for  $\beta$ -decay,  $\lambda_\beta$ , is approximately equal to the decay constant for neutron capture,  $\lambda_{n\gamma}$ . That is,  $\lambda_\beta \approx \lambda_{n\gamma}$ , and the path splits into two branches with approximately equal probability. These branchings are sensitive to neutron density  $N_n$  and the neutron-capture cross section  $\sigma_{n\gamma}$  of the unstable branching point nucleus, described below. After the s-process branching, the path continues in this way up to some of the heaviest nuclei.

Now consider the simple s-process path shown in Figure 1.4, starting from a stable nucleus with mass number  $A - 1$ . In case (a), represented by solid arrows, the unstable nucleus with mass number  $A'$  will  $\beta$ -decay to nucleus  $A$ , which will then neutron-capture to nucleus  $A + 1$ , and so on. The more complicated case (b) is represented by both solid and dashed arrows, where the nucleus  $A'$  is a branching point nucleus, and it can undergo neutron-capture and  $\beta$ -decay at roughly equal probability. We will first consider case (a), where  $\lambda_\beta \gg \lambda_{n\gamma}$ , such that the path does not lead through the dashed arrows. In this case, the abundance at each mass number exists in only one (unprimed) nucleus. Therefore the abundance evolution of any stable nucleus  $A$  only depends on the neutron-capture reaction rates of the  $A - 1$  and  $A$  nuclei, as in

$$\frac{dN_s(A)}{dt} = N_n(t)N_s(A - 1)\langle\sigma v\rangle_{A-1} - N_n(t)N_s(A)\langle\sigma v\rangle_A, \quad (1.1)$$

where  $N_s(A)$  and  $N_n(t)$  are the time-dependent number densities of the  $A$  nucleus and the

neutron, respectively, and  $\langle\sigma v\rangle_A$  is the neutron-capture reaction rate per particle pair of the  $A$  nucleus. The first term in Eqn 1.1 represents the rate of production of the  $A$  nucleus, while the second term represents its rate of destruction. We will assume that the temperature is constant while the neutron source is active, so that the neutron-capture reaction rates are also constant. The neutron-capture reaction rate is frequently expressed in terms of a Maxwellian-averaged cross section  $\langle\sigma\rangle_A \equiv \langle\sigma v\rangle_A/v_T$ , where  $v_T = \sqrt{2kT/\mu_{An}}$  is the thermal velocity, or in other words, the maximum of the velocity distribution;  $\mu_{An}$  is the reduced mass between the  $A$  nucleus and the neutron, which is approximately equal to the neutron mass. That is,  $\mu_{An} = M_AM_n/(M_A + M_n) \approx M_n$ , which makes  $v_T$  approximately independent of target mass. The abundance evolution of the nucleus  $A$  can then be written as

$$\frac{dN_s(A)}{dt} = v_T N_n(t) [N_s(A-1)\langle\sigma\rangle_{A-1} - N_s(A)\langle\sigma\rangle_A]. \quad (1.2)$$

Far from any s-process branchings or closed neutron-shell nuclei, an approximate equilibrium is obtained where the abundance of the  $A$  nucleus increases until its production rate and destruction rate are approximately equal. This is known as the *local equilibrium approximation*, and it is expressed as  $N_s(A, \tau)\langle\sigma\rangle_A \approx N_s(A-1, \tau)\langle\sigma\rangle_{A-1}$ , where  $\tau$  is the neutron exposure, in units of neutrons per area. The neutron exposure is proportional to the time-integrated neutron flux  $\Phi$ , as in  $\tau = (\sqrt{\pi}/2)\Phi$ . The local equilibrium approximation has been shown to hold for the s-only isotopes of tellurium ( $Z = 52$ ), as well as for many other s-only nuclei with adjacent mass numbers between  $90 \lesssim A \lesssim 205$  [Ili15a]. However, there is a distinct separation of observed solar system  $N_\odot(A)\langle\sigma\rangle_A$  values at  $A \approx 90$ , and the approximation does not hold at all near the closed neutron-shell nuclei. Refs. [Cla61, See65] have shown that better agreement with solar system  $N_\odot(A)\langle\sigma\rangle_A$  values is achieved when considering not just a single neutron exposure  $\tau$ , but an exponential distribution of  $\tau$ -values. Indeed, it is reasonable to assume that the number of  $^{56}\text{Fe}$  seed nuclei decreases with increased exposure to neutrons. With this additional constraint, the solar system  $N_\odot(A)\langle\sigma\rangle_A$  values are reproduced to a remarkable accuracy for  $90 \lesssim A \lesssim 205$ , when also accounting for s-process branchings, discussed below. The region between  $60 \lesssim A \lesssim 90$  is also reproduced with an exponential distribution of neutron exposures, but different parameters are required between the two cases. These two components are referred to as the *main s-process component* ( $90 \lesssim A \lesssim 205$ ) and the *weak s-process component* ( $60 \lesssim A \lesssim 90$ ). A third component, called the *strong s-process component* is needed to explain the solar system  $N_\odot(A)\langle\sigma\rangle_A$  values at  $A \gtrsim 205$ .

These components originate from different astrophysical environments, where the total number of  $^{56}\text{Fe}$  seed nuclei and the exponential neutron exposure differ. The main s-process

component is from thermally-pulsing AGB stars with  $1.5M_{\odot} \lesssim M \lesssim 3M_{\odot}$ , while the weak s-process component is thought to originate from core helium burning and shell carbon burning in massive stars with  $M \gtrsim 13M_{\odot}$  [Ili15a]. The primary neutron source for the main component is  $^{13}\text{C}(\alpha, n)^{16}\text{O}$ , with the  $^{22}\text{Ne}(\alpha, n)^{25}\text{Mg}$  neutron source only marginally activated. This latter source acts to enhance the efficiency of s-process branchings. The weak s-process component, however, relies on  $^{22}\text{Ne}(\alpha, n)^{25}\text{Mg}$  as its primary neutron source, since temperatures are significantly higher for these massive stars.

If we now consider case (b), where the nucleus  $A'$  in Figure 1.4 is at an s-process branching, we can see that only a fraction of the path reaches the nucleus  $A$ , but the entire path reaches the nucleus  $A + 1$ . In this case, the local equilibrium approximation becomes  $N_s(A, \tau)\langle\sigma\rangle_A + N_s(A', \tau)\langle\sigma\rangle_{A'} \approx N_s(A + 1, \tau)\langle\sigma\rangle_{A+1}$ . We can now define the *branching ratio*  $B$  as

$$\begin{aligned} B &\equiv \frac{N_s(A, \tau)\langle\sigma\rangle_A}{N_s(A + 1, \tau)\langle\sigma\rangle_{A+1}} = \frac{\lambda_{\beta}(A')}{\lambda_{\beta}(A') + \lambda_{n\gamma}(A')} \\ &= \frac{\ln 2/T_{1/2}(A')}{\ln 2/T_{1/2}(A') + N_n\langle\sigma\rangle_{A'}v_T}. \end{aligned} \quad (1.3)$$

Solving for the neutron number density  $N_n$ , we obtain

$$N_n = \left( \frac{1 - B}{B} \right) \frac{1}{\langle\sigma\rangle_{A'}v_T} \frac{\ln 2}{T_{1/2}(A')}. \quad (1.4)$$

Even though Eqn. 1.4 is just one of many examples of possible s-process branching configurations, it shows the only inputs necessary to calculate the neutron density, which is a key parameter in stellar models of the s-process. From this equation, a connection is made between the study of s-process branchings and the neutron density.

In order to extract the neutron density with a reasonable uncertainty, it is crucial to have precise experimental neutron-capture cross sections of the  $A$ ,  $A + 1$ , and  $A'$  nuclei. Since the  $A$  and  $A + 1$  nuclei are stable, these are usually readily available. However,  $A'$  is unstable, and it is typically not feasible to perform neutron-capture cross section measurements on unstable nuclei. In cases where data is not available, the cross sections have to be estimated using Hauser-Feshbach theory. It is possible to experimentally constrain neutron-capture cross sections on unstable nuclei by performing photoabsorption reactions on the recoil nucleus, if it is stable. The dipole response of the recoil nucleus via nuclear resonance fluorescence (NRF) and the  $(\gamma, n)$  reaction can be used to determine the photoabsorption cross section of the recoil nucleus, which can in turn be used to determine its photon strength function (PSF). The PSF is a crucial input for statistical model calculations constraining Maxwellian-averaged

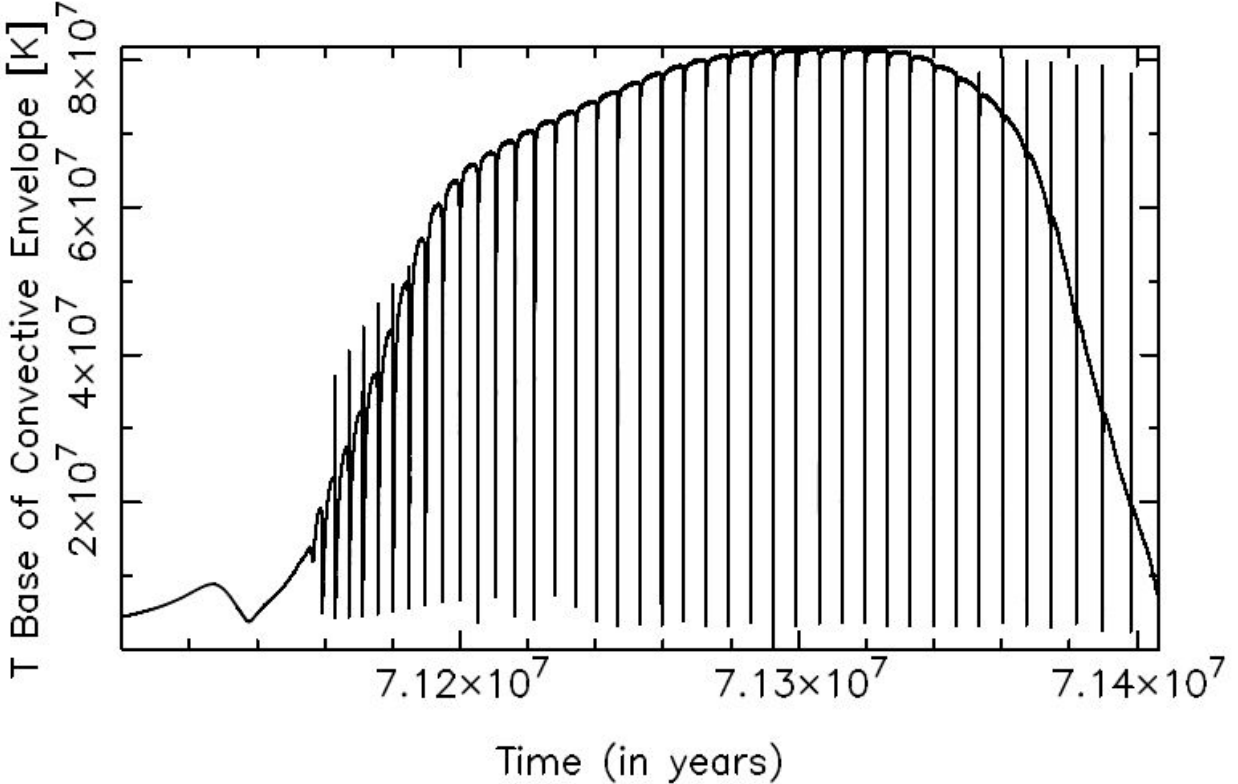


Figure 1.5: The temperature evolution at the bottom of the convective hydrogen envelope during the TP-AGB phase for a  $6M_{\odot}$  star with  $Z = 0.02$ . Several thermal pulses are shown, each rapidly decreasing the temperature in this region, which extinguishes hydrogen burning. Adapted from Ref. [Kar14].

cross sections of neutron-capture on unstable nuclei [Wil20].

### 1.3 Hot-Bottom Burning

Hot-bottom burning (HBB) occurs in AGB stars when the bottom of the convective hydrogen envelope reaches sufficiently high temperatures for nuclear processing. The onset of HBB is highly dependent upon the AGB mass and metallicity, with a minimum mass of  $\sim 5M_{\odot}$  at solar metallicity  $Z_{\odot}$ , to even theoretically as low as  $\sim 2M_{\odot}$  at  $Z = 0$  [Hab04]. Temperatures can exceed 50 MK during HBB, which is sufficient to activate the CNO cycle, as well as the Ne-Na chain. For super-AGB stars and the most massive and lowest-metallicity AGB stars, temperatures can exceed 100 MK, which is sufficient to activate the Mg-Al and Ar-K chains [Kar14]. HBB is only active during the interpulse period because thermal pulses act to cool down this region by about an order of magnitude. Figure 1.5 shows the temperature at the base of the convective hydrogen envelope for a  $6M_{\odot}$  TP-AGB star with  $Z = 0.02$ . The

temperature reaches a maximum of 82 MK at the 28th thermal pulse, and eventually HBB is no longer active due to mass loss slowly eroding the convective hydrogen envelope [Kar14].

Hot-bottom burning in AGB stars is one of the leading mechanisms responsible for globular cluster abundance anomalies, described in more detail in Section 1.4. The AGB stars from the first stellar generation of globular cluster formation eject the products of HBB into the inter-cluster medium, where mixing occurs with the unprocessed gas left behind from star formation. New stars forming in this mixed material have enhanced abundances from nuclear processing, while other stars may form in the absence of AGB ejecta. Discrepancies in abundance between otherwise similar stars is the result. There are other candidates for hydrogen burning besides HBB in AGB stars which have been proposed to explain these abundance anomalies, such as classical novae and supermassive stars. In some cases it has been shown that more than one mechanism may be responsible for the observed abundances [Gra19]. However, mixing between processed and unprocessed material is a common requirement regardless of the hydrogen burning origin.

## 1.4 Globular Cluster Abundance Anomalies

Globular clusters are compact conglomerates of stars associated with all types of galaxies. They are typically on the order of 1 pc to a few tens of pc in radius, and they are very old, in most cases having an age of about 10 Gyr. Peak globular cluster formation is thought to pre-date most stellar formation in galaxies, and they may have played a crucial role in early galaxy formation [Gra19]. In the Milky Way galaxy, they often have low metallicity and are distributed throughout the halo, the thick disk, and the bulge. These properties, while interesting, are not what have made globular clusters garner considerable interest in the last few decades.

A characteristic recently attributed to globular clusters, which distinguishes them from similar objects such as open clusters, is the presence of chemical inhomogeneities among their low-mass stars. Once labeled *abundance anomalies*, these inhomogeneities take the form of anticorrelations among the abundances of light element pairs, such as O–Na and Mg–Al. A new definition of globular clusters that includes this characteristic was suggested by Ref. [Car10], since almost every globular cluster in which abundances have been observed has exhibited an O–Na anticorrelation. The only exceptions are Terzan 7 and Pal 12, where the simultaneous Na and O abundances of only 7 [Sbo07] and 4 [Coh04] stars were observed, respectively. Other anticorrelations and correlations are exhibited in some, but not all globular clusters, making each cluster distinguishable by the combination and extent of their abundance inhomogeneities. These cluster-to-cluster differences are primarily driven by differences in

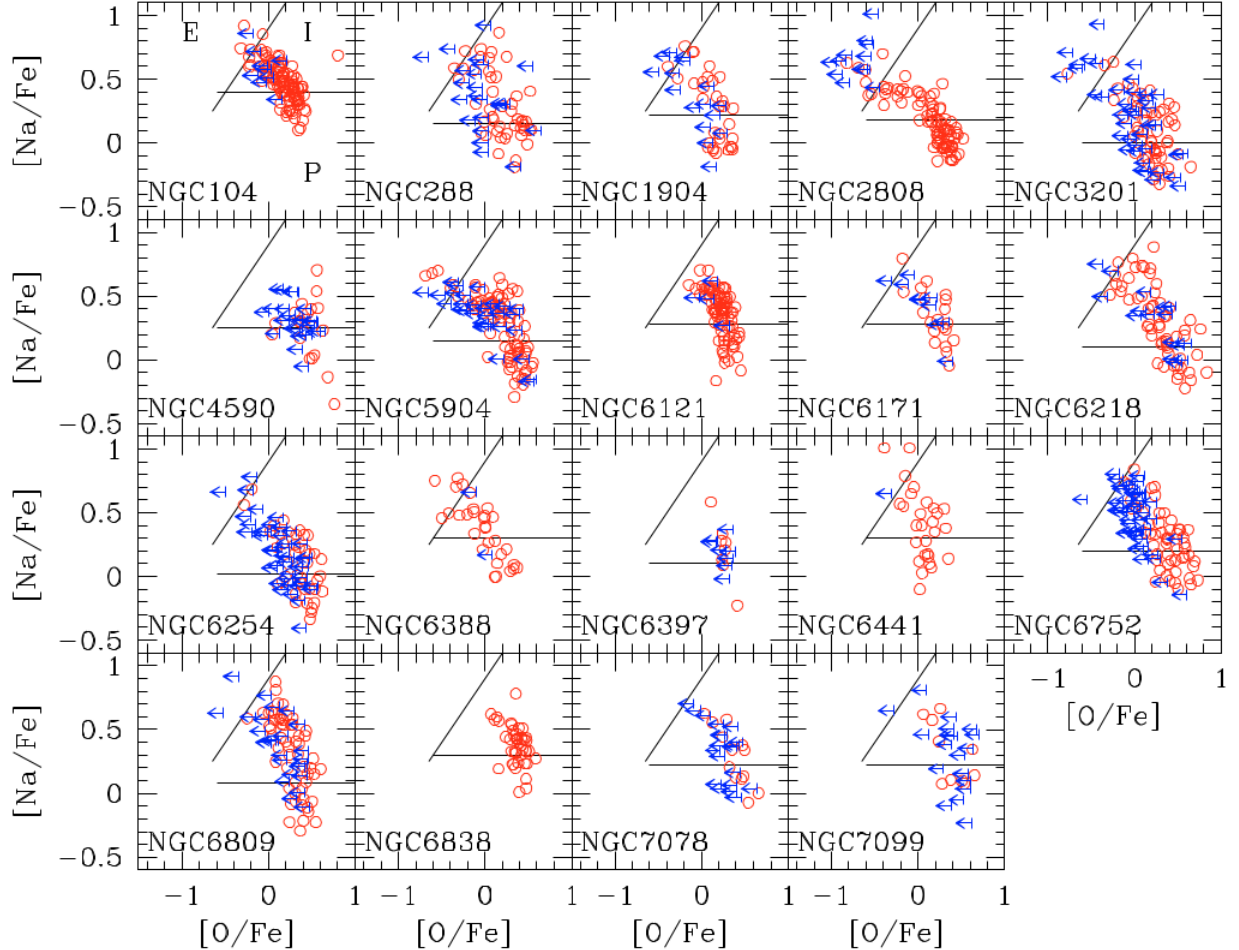


Figure 1.6: The O–Na anticorrelation of 1,200 red giants among all 19 globular clusters observed in the survey of Ref. [Car10]. Blue arrows indicate upper limits in O abundances, while lines separate different populations of red giants based on their relative O and Na richness. Primordial (P), extreme (E), and intermediate (I) populations are labeled in the first panel. See text for definitions of these populations. Adapted from Ref. [Car10].

luminosity and metallicity. Meanwhile, no abundance anticorrelations have ever been observed in open clusters [Gra19].

Fig. 1.6 shows the ubiquitous O–Na anticorrelation in 1,200 red giants among all 19 globular clusters sampled by Ref. [Car10]. The red giants with an enhanced Na abundance are associated with a depletion in O abundance, and vice versa. The populations of red giants are split into 3 categories based on the extent of their Na enrichment, and associated O depletion. These populations are the primordial (P), extreme (E), and intermediate (I) components, as indicated in the first panel of Fig. 1.6. The primordial population is Na-poor/O-rich, the extreme population is Na-rich/O-poor, and the intermediate population is in-between. The

primordial population is so-called because the same abundance pattern is typical of field stars with a similar metallicity. However, the Na and O abundances of the intermediate and extreme populations indicates that these red giants went through an unknown process. Low-mass stars like red giants and main sequence stars do not reach the high temperatures necessary for the nucleosynthesis chains that produce the observed Na and O abundances. This reasoning also applies to the other observed anticorrelations in globular clusters [Pra07].

The most likely scenario explaining these inhomogeneities is that the currently observed stars are part of a second generation which formed from the ashes of an older, first generation of stars. The material ejected from these more-massive first generation stars upon their death likely polluted the inter-cluster medium where the second generation stars began to form. Hence, these first generation stars are sometimes called *polluter stars*, a class of massive, extinct stars that are the origin of the apparent abundance anomalies. Different generations of stars existing in a given globular cluster would provide evidence for *multiple stellar populations*. This premise has been widely debated over the last few decades, with most research supporting it at present [Gra04, Gra12, Gra19].

Polluter stars are likely the site of the nucleosynthesis that gives rise to the currently observed abundance patterns in globular clusters. Their exact nature is unknown, but the nucleosynthesis mechanism driving the inhomogeneities in the vast majority of globular clusters is well established as proton-capture reactions in high temperature hydrogen-burning environments [Den89, Lan93]. The ubiquitous O–Na anticorrelation, for example, is exhibited in the hydrogen burning of the CNO and Ne–Na cycles at about 40 MK [Gra19]. Fig. 1.7 shows the nucleosynthesis chains that lead to an overall oxygen depletion and sodium production. The first stage of the CNO cycle involves a series of  $(p, \gamma)$  and  $(\beta^+ \nu)$  reactions on stable and radioactive nuclei, respectively, starting from  $^{12}\text{C}$ . This stage occurs at fusion temperatures of about 10 MK. Once  $^{15}\text{N}$  is reached,  $^{15}\text{N}(p, \alpha)^{12}\text{C}$  closes the cycle if the temperature is less than about 40 MK. Otherwise, the second stage of the CNO cycle will be activated from  $^{15}\text{N}(p, \gamma)^{16}\text{O}$ . This eventually leads to  $^{17}\text{O}$ , which closes the second stage of the cycle via  $^{17}\text{O}(p, \alpha)^{14}\text{N}$ . This second stage leads to an overall destruction of oxygen. Meanwhile, the Ne–Na cycle activates at about 40 MK as well, starting from  $^{20}\text{Ne}(p, \gamma)^{21}\text{Na}$ . Once  $^{23}\text{Na}$  is reached, it will close the cycle via  $^{23}\text{Na}(p, \alpha)^{20}\text{Ne}$  if temperatures are less than about 70 MK, otherwise  $^{23}\text{Na}(p, \gamma)^{24}\text{Mg}$  is activated. These destruction reactions on  $^{23}\text{Na}$  are slow enough such that sodium is produced overall.

Although nucleosynthesis via hydrogen burning is what drives the observed abundance patterns, it is not the only mechanism responsible for them. The majority of second generation stars must be composed of a mixture of nuclear-processed ejecta and matter with a pristine composition, in order for nuclear reaction network models to reproduce the observed globular

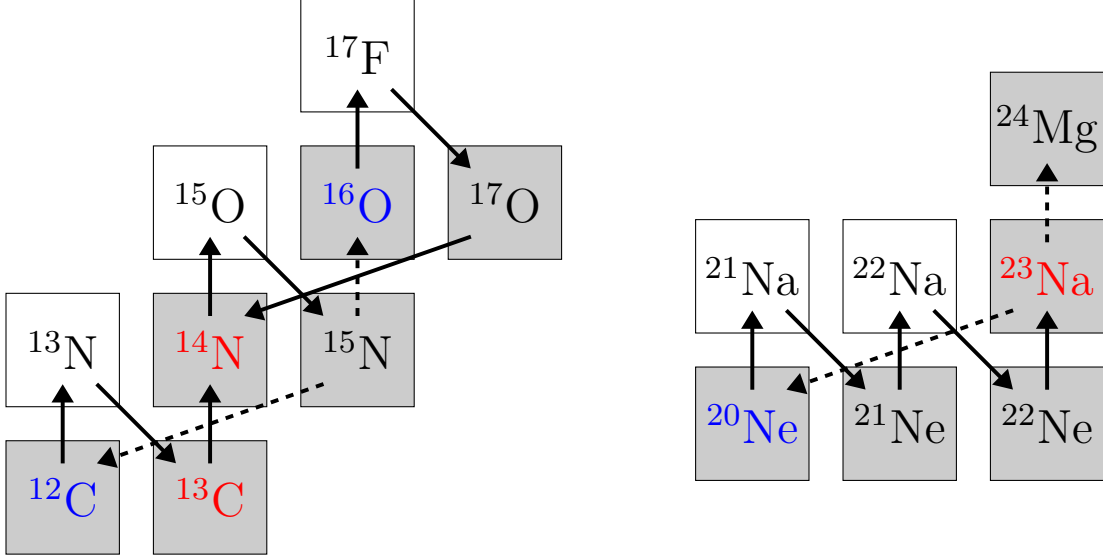


Figure 1.7: The hydrogen burning mechanism driving the O–Na anticorrelation. Nuclei in blue are destroyed overall in the various cycles, while nuclei in red are produced. Shaded nuclei are stable. The first two stages of the CNO cycle (left), distinguished by the temperature-dependent branch at  $^{15}\text{N}$ , lead to an overall depletion of oxygen. The  $^{15}\text{N}(p, \gamma)^{16}\text{O}$  reaction is activated at about 40 MK. The Ne–Na cycle (right), occurring simultaneously at about the same activation temperature, leads to an overall production of sodium. The  $^{23}\text{Na}(p, \gamma)^{24}\text{Mg}$  reaction activates at about 70 MK.

cluster abundance patterns [Pra07]. The nuclear-processed ejecta is the matter resulting from nucleosynthesis via hydrogen burning in the first generation polluter stars, while pristine matter refers to the unprocessed gas left behind from the first burst of star formation. Many polluter star sites such as AGB stars, fast-rotating massive stars, and supermassive stars require dilution with unprocessed gas in order to convert their correlated O and Na abundances into the observed anticorrelation [Erc10, Erc11, Erc12]. The observed, mixed abundances in a typical dilution model are obtained by diluting one part of processed matter with  $f$  parts of pristine matter, as in

$$X_{\text{mix}} = \frac{X_{\text{proc}} + f X_{\text{pris}}}{1 + f}, \quad (1.5)$$

where  $X$  is the mass fraction of a given nucleus among its overall composition and  $f$  is the dilution factor [Pra07, Car09]. A very small dilution factor represents nearly pure processed matter, while a very large dilution factor results in mostly pristine matter. The dilution model works very well for most globular clusters, but often a single dilution model does

not simultaneously reproduce the abundances of the extreme and intermediate populations. In these cases, more than one class of polluter stars is required to match the observations, suggesting that the multiple populations premise may be more complex than previously considered [Gra19].

## CHAPTER

# 2

## NUCLEAR REACTIONS IN STARS

### 2.1 Introduction

This chapter introduces the formalism for quantifying stellar nucleosynthesis with reaction rates, which is an important foundation for the rest of this thesis. Section 2.2 introduces the concept of a nuclear reaction network, involving the abundance evolution of each nucleus given all possible reactions in the network. Section 2.3 describes the formalism for reaction rate calculations, with a focus on resonant reactions. Finally, Section 2.4 will describe the theory of transfer reactions, and their use in obtaining experimental information on the key nuclear structure inputs for reaction rates.

### 2.2 Nuclear Reaction Networks

Nuclei in a high temperature stellar plasma are constantly undergoing nuclear processes, changing the overall composition of the stellar region. Each nucleus has several possible ways in which it can be destroyed and produced, depending on the environmental conditions and stellar composition at any given time. To quantify the change in abundance of a given nuclear species, we track its number density  $N(t)$  over time, as introduced in Equation 1.1. Here, we will obtain a general expression for the abundance evolution of any nuclear species. To derive the expression, first consider the reaction between two nuclei 0 and 1. The rate at

which this reaction proceeds is related to the mean lifetime  $\tau$ , or inversely, the decay constant  $\lambda \equiv 1/\tau$  of the nuclear species in the stellar plasma. The rate of change of  $N_0(t)$  over time from reactions with nucleus 1 is expressed as

$$\left( \frac{dN_0}{dt} \right)_1 = -\lambda_1(0)N_0 = -\frac{N_0}{\tau_1(0)} = N_0N_1\langle\sigma v\rangle_{01}, \quad (2.1)$$

where  $\langle\sigma v\rangle_{01}$  is the reaction rate for a single pair of particles 0 and 1. The number density for species  $i$  can also be written as  $N_i = \rho X_i N_A / M_i$ , where  $\rho$  is the mass density of the stellar plasma,  $X_i$  and  $M_i$  are the mass fraction and mass of species  $i$ , respectively, and  $N_A$  is Avogadro's number. Hence, the decay constant for nucleus 1 can also be expressed as

$$\lambda_1(0) = \frac{1}{\tau_1(0)} = N_1\langle\sigma v\rangle_{01} = \rho \frac{X_1}{M_1} N_A \langle\sigma v\rangle_{01}. \quad (2.2)$$

Eqn. 2.2 is used frequently to determine the preferred reaction by which a nucleus is destroyed in a stellar plasma [Ili15a]. In the s-process, for example, it can be used to determine which branch of an s-process branching will be preferred, or if the paths have roughly equal probability. In hydrogen-burning nucleosynthesis, it can be used to determine if a burning cycle will be closed or if it will be escaped. Note that the decay constant depends on both the stellar mass density and temperature, the latter of which through  $\langle\sigma v\rangle$ .

Now consider every nuclear process that can occur on a given nuclear species  $i$ , including nuclear reactions, photoabsorptions, and decays. In the absence of mixing and expansion, its net abundance evolution is expressed by the differential equation<sup>1</sup>

$$\begin{aligned} \frac{dN_i}{dt} = & \sum_{j,k} N_j N_k \langle\sigma v\rangle_{jk \rightarrow i} + \sum_l \lambda_{\text{dec},l \rightarrow i} N_l + \sum_m \lambda_{\gamma,m \rightarrow i} N_m \\ & - \sum_n N_n N_i \langle\sigma v\rangle_{ni} - \sum_o \lambda_{\text{dec},i \rightarrow o} N_i - \sum_p \lambda_{\gamma,i \rightarrow p} N_i. \end{aligned} \quad (2.3)$$

The terms in the first and second lines represent all possible production and destruction processes, respectively, for the nuclear species  $i$ . The first term includes all reactions between nuclei  $j$  and  $k$  producing nucleus  $i$ ; the second term includes all nuclei  $l$  decaying to nucleus  $i$  through  $\beta$ -decay,  $\alpha$ -decay, fission, etc.; the third term includes all photoabsorption reactions on nuclei  $m$  leading to nucleus  $i$ , and the remaining terms represent the analogous, reverse destruction processes.

In order to properly describe nucleosynthesis in a stellar plasma, we must account for the

---

<sup>1</sup>If nonidentical particles  $j$  and  $k$  produce two nuclei  $i$ , then the first term in Eqn. 2.3 must be replaced by  $2N_j N_k \langle\sigma v\rangle_{jk \rightarrow i}$ . If identical particles ( $j = k$ ) produce only one nucleus  $i$ , then that term must instead be replaced by  $N_j^2 \langle\sigma v\rangle_{jj \rightarrow i}/2$ . Analogous arguments apply to the fourth term.

abundance evolution of all relevant nuclei in the environment, each described by Eqn. 2.3. This system of coupled, nonlinear ordinary differential equations is known as a *nuclear reaction network*. In most realistic scenarios, this system of equations must be solved numerically. The number density  $N_i(t)$  of each nucleus in the network is typically given in terms of the mass fraction  $X_i(t)$ , where  $\sum_i X_i(t) = 1$ , as it is much simpler to conceptualize relative mass fractions than number densities. Solutions to the nuclear reaction network at some final time  $t_f$  are therefore reported as final mass fractions  $X_f$  and are nominally referred to as final abundances. From  $N_i = \rho X_i N_A / M_i$ , the mass fraction normalization can be expressed as

$$\sum_i X_i = \sum_i \frac{N_i M_i}{\rho N_A} = 1. \quad (2.4)$$

Hence,  $\rho N_A = \sum_i N_i M_i$ , and the mass fraction can therefore be written as

$$X_i = \frac{N_i M_i}{\sum_i N_i M_i} \approx \frac{N_i A_i}{\sum_i N_i A_i}, \quad (2.5)$$

where the nuclear mass  $M_i$  can usually be approximated by the mass number  $A_i$ . Eqn. 2.5 is especially convenient when considering, for example, a network consisting of initial solar system abundances, such as that of Ref. [Lod09]. These solar system number densities  $N$  are normalized to  $10^6$  Si atoms, and relative isotopic abundances are taken into account. When putting these  $N$ -values into Eqn. 2.5, this normalization cancels. Often the network is selected from a subset of solar system nuclei, in which case it is a simple matter of adjusting the mass fractions so that their sum remains unity. Even in cases where some of the solar system abundances should be modified to represent a specific stellar environment, as will be the case in Chapter 3, Eqn. 2.5 makes this scenario trivial.

## 2.3 Reaction Rates

The reaction rate per particle pair in a stellar medium is given by

$$\langle \sigma v \rangle_{01} = \sqrt{\frac{8}{\pi \mu_{01}}} \frac{1}{(kT)^{3/2}} \int_0^\infty E \sigma(E) e^{-E/kT} dE, \quad (2.6)$$

where  $\mu_{01}$  is the reduced mass of particle 0 and particle 1,  $\mu = M_0 M_1 / (M_0 + M_1)$ ;  $k$  is the Boltzmann constant;  $T$  is the stellar temperature;  $E$  is the center-of-mass energy between the particles; and  $\sigma(E)$  is the reaction cross section evaluated at  $E$ . The energy dependence of the cross section determines whether numerical integration must be performed. The formalism for reaction rate calculations therefore depends on whether  $\sigma(E)$  is smoothly varying over

energy (for non-resonant reactions) or if it can be described by isolated resonances (for resonant reactions). It can be described by both in principle, in which case the cross section is separated into non-resonant and resonant components, assuming interference effects are negligible. Regardless of the nature of  $\sigma(E)$ , it can be separated into a Coulomb factor and a factor resulting only from nuclear structure, called the astrophysical S-factor  $S(E)$ . That is, the cross section can be rewritten as

$$\sigma(E) = \frac{1}{E} e^{-2\pi\eta} S(E), \quad (2.7)$$

where  $\eta$  is the Sommerfeld parameter defined by  $2\pi\eta = \sqrt{2\mu_{01}/E} Z_0 Z_1 e^2 / \hbar$ ;  $Z_0$  and  $Z_1$  are the atomic numbers of the nuclei. The  $1/E$  factor is included to cancel with the  $E$  factor in the reaction rate. Substituting Eqn. 2.7 into Eqn. 2.6, we have

$$\langle \sigma v \rangle_{01} = \sqrt{\frac{8}{\pi\mu_{01}}} \frac{1}{(kT)^{3/2}} \int_0^\infty e^{-2\pi\eta} e^{-E/kT} S(E) dE. \quad (2.8)$$

The integrand in Eqn. 2.8 is composed of the Gamow factor  $e^{-2\pi\eta}$ , the Maxwell-Boltzmann factor  $e^{-E/kT}$ , and the astrophysical S-factor  $S(E)$ . The former two factors have a combined energy dependence of  $e^{-\sqrt{1/E}} e^{-E}$ , while the  $S(E)$  energy dependence is based on the nuclear structure of the specific reaction. The overlap between the Gamow and Maxwell-Boltzmann factors is called the *Gamow peak*,  $e^{-2\pi\eta} e^{-E/kT}$ . This peak determines the energies at which the reaction will proceed in the stellar environment at the given temperature<sup>2</sup>. It has a maximum at

$$E_0 = \left[ \left( \frac{\pi}{\hbar} \right)^2 (Z_0 Z_1 e^2)^2 \left( \frac{m_{01}}{2} \right) (kT)^2 \right]^{1/3} \\ = 0.1220 \left( Z_0^2 Z_1^2 \mu_{01} T_9^2 \right)^{1/3} [\text{MeV}] \quad (2.9)$$

where  $T_9$  is the temperature in units of GK. The energy  $E_0$  is the most probable energy for non-resonant reactions, where  $S(E)$  varies smoothly. For resonant reactions, where  $S(E)$  is described by a sharp Lorentzian function, the Gamow peak can still be a useful indicator of which resonances contribute significantly to the total reaction rate, particularly at lower resonance energies ( $E_r^{\text{c.m.}} \lesssim 0.5$  MeV). The Gamow peak can be approximated by a Gaussian

---

<sup>2</sup>This is a slight oversimplification. For resonant reactions at high stellar temperatures, the resonances that contribute significantly to the reaction rate may occur below the Gamow peak [Ili15a].

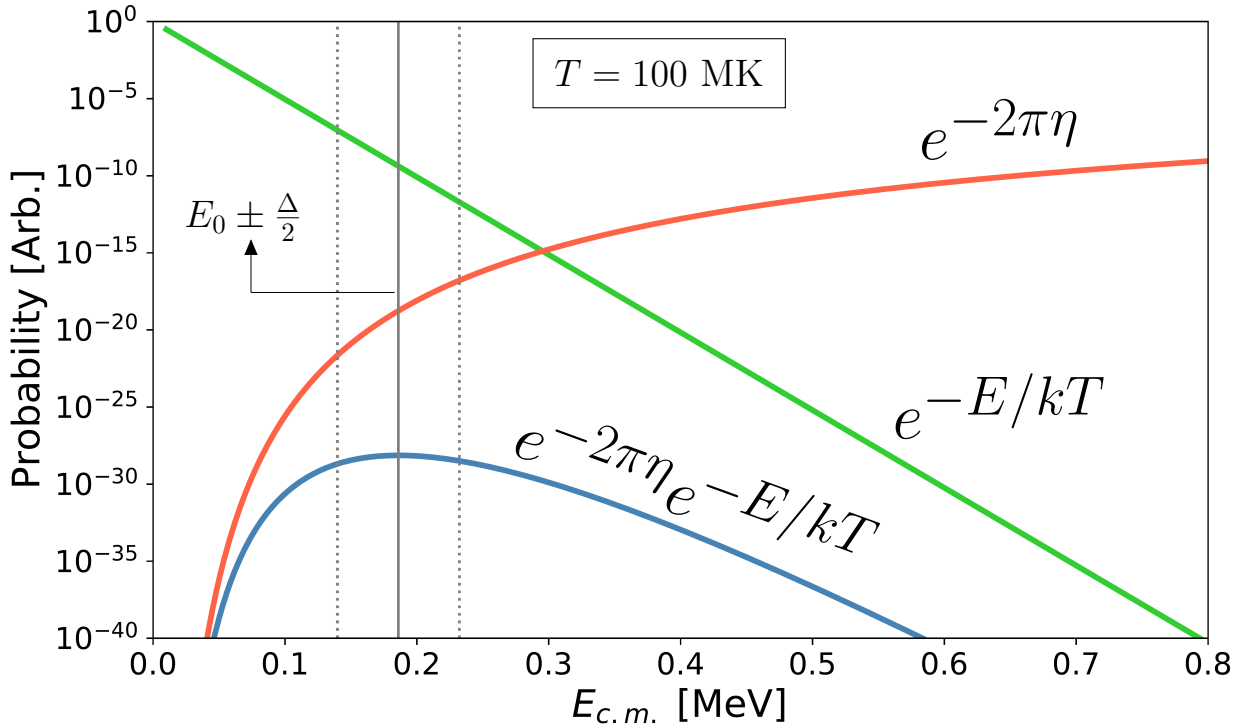


Figure 2.1: The Gamow window,  $E_0 \pm \Delta/2$ , for the  $^{39}\text{K}(p, \gamma)^{40}\text{Ca}$  reaction at 100 MK. The Gamow factor  $e^{-2\pi\eta}$  is shown in red; the Maxwell-Boltzmann factor  $e^{-E/kT}$  is shown in green, and the Gamow peak  $e^{-2\pi\eta}e^{-E/kT}$  is shown in blue. The resonances that contribute significantly to the reaction rate at this temperature will have energies within the Gamow window, between about 140 keV and 230 keV.

function with a mean of  $E_0$  and a  $1/e$  width of

$$\Delta = \frac{4}{\sqrt{3}} \sqrt{E_0 kT} = 0.2368 \left( Z_0^2 Z_1^2 \mu_{01} T_9^5 \right)^{1/6} [\text{MeV}]. \quad (2.10)$$

Thermonuclear reactions therefore mainly occur in the energy window from  $E_0 - \Delta/2$  to  $E_0 + \Delta/2$ , known as the *Gamow window*.

For the  $^{39}\text{K}(p, \gamma)^{40}\text{Ca}$  reaction, discussed in Chapter 4, the Gamow window at temperatures of 100 MK occurs between about 140 keV and 230 keV, centered on about 185 keV. This situation is depicted in Figure 2.1. The Gamow and Maxwell-Boltzmann factors are shown in red and green, respectively, while the combined Gamow peak is shown in blue. The Gamow window centered on  $E_0$  is shown between the vertical dotted lines. As will be clear in Section 4.8.2, the  $^{39}\text{K}(p, \gamma)^{40}\text{Ca}$  reaction rate is dominated by isolated resonances in the temperature range of astrophysical interest, 80–260 MK, occurring between about 120 keV and 450 keV.

### 2.3.1 Narrow Resonances

An isolated resonance at the resonance energy  $E_r$  is described by the Breit-Wigner cross-section [Bre36]

$$\sigma_{\text{BW}}(E) = \frac{\lambda^2}{4\pi} \omega \frac{\Gamma_a(E) \Gamma_b(E)}{(E - E_r)^2 + \Gamma(E)^2/4}, \quad (2.11)$$

where  $\lambda$  is the deBroglie wavelength, defined by  $\lambda^2/2 = (\pi\hbar)^2/(\mu_{01}E)$ ;  $\Gamma_a(E)$  and  $\Gamma_b(E)$  are the entrance channel and exit channel partial widths, respectively;  $\Gamma(E)$  is the total width, and  $\omega$  is the spin factor, defined as

$$\omega = \frac{(2J+1)}{(2J_0+1)(2J_1+1)}, \quad (2.12)$$

where  $J$  is the resonance spin, and  $J_0$  and  $J_1$  are the spins of the interacting particles. Substituting Eqn. 2.11 into Eqn. 2.6, the reaction rate per particle pair arising from an isolated resonance becomes

$$\langle\sigma v\rangle_{01} = \frac{\sqrt{2\pi}\hbar^2}{(\mu_{01}kT)^{3/2}} \omega \int_0^\infty \frac{\Gamma_a(E) \Gamma_b(E)}{(E - E_r)^2 + \Gamma(E)^2/4} e^{-E/kT} dE. \quad (2.13)$$

Consider the partial widths  $\Gamma_i$  and the Maxwell-Boltzmann factor  $e^{-E/kT}$  varying slowly with energy over the width of the resonance. In this situation, the resonance is considered narrow, and these factors can be treated as being independent of energy over this energy range. The reaction rate is then written as

$$\begin{aligned} \langle\sigma v\rangle_{01} &= \frac{\sqrt{2\pi}\hbar^2}{(\mu_{01}kT)^{3/2}} \omega \Gamma_a \Gamma_b e^{-E_r/kT} \int_0^\infty \frac{dE}{(E - E_r)^2 + \Gamma(E)^2/4} \\ &= \frac{\sqrt{2\pi}\hbar^2}{(\mu_{01}kT)^{3/2}} \omega \Gamma_a \Gamma_b e^{-E_r/kT} \frac{2}{\Gamma} \arctan\left(\frac{E - E_r}{\Gamma/2}\right) \Big|_0^\infty \\ &= \left(\frac{2\pi}{\mu_{01}kT}\right)^{3/2} \hbar^2 \omega \frac{\Gamma_a \Gamma_b}{\Gamma} e^{-E_r/kT}, \end{aligned} \quad (2.14)$$

where the last line results from the further approximation of narrow resonances,  $E_r \gg \Gamma$ , which makes the lower bound of integration effectively  $-\infty$ . The quantity

$$\omega\gamma \equiv \omega \frac{\Gamma_a \Gamma_b}{\Gamma} \quad (2.15)$$

is defined as the *resonance strength* because it is proportional to the maximum cross section multiplied by the total resonance width,  $\omega\gamma \propto \sigma_{\max}\Gamma$ . The reaction rate per particle pair for

multiple isolated, narrow resonances forms an incoherent sum,

$$\langle \sigma v \rangle_{01} = \left( \frac{2\pi}{\mu_{01} kT} \right)^{3/2} \hbar^2 \sum_i (\omega\gamma)_i e^{-E_{r,i}/kT}. \quad (2.16)$$

The calculation of partial widths differs between particles and  $\gamma$ -rays. The following discussion will consider charged-particles and  $\gamma$ -rays only. For a discussion of neutron partial widths, see Ref. [Ili15a].

### 2.3.2 Particle Partial Widths

The charged-particle partial width for channel  $c$  is

$$\Gamma_c(E) = \frac{2\hbar^2}{\mu_{01} R^2} P_c(E) C^2 S \theta_{sp,c}, \quad (2.17)$$

where the channel radius  $R$  is defined by  $R = R_0 (A_0^{1/3} + A_1^{1/3})$ ; the penetration factor  $P_c(E)$  can be calculated as

$$P_c(E) = \frac{\rho}{F^2(E) + G^2(E)}, \quad (2.18)$$

where  $\rho = 0.21874 R \sqrt{\mu_{01} E}$  and  $F$  and  $G$  are the energy dependent Coulomb wave functions;  $C^2 S$  is the spectroscopic factor, sometimes simply referred to as  $S$ , where  $C$  is the isospin Clebsch-Gordon coefficient, and  $\theta_{sp,c}$  is the dimensionless single-particle reduced width. The charged-particle partial width can be thought of as being proportional to the probability of the particle being emitted from the compound nucleus. Each of the latter three quantities in Eqn. 2.17 contribute to this probability. The penetration factor  $P_c(E)$  represents the probability of overcoming or tunneling through the Coulomb barrier to reach the nuclear surface. The dimensionless single-particle reduced width  $\theta_{sp,c}$  represents the probability that the particle occupies the exact single-particle shell-model state of the resonance at the nuclear surface. Finally, the spectroscopic factor  $C^2 S$  is a measure of how much the populated state resembles that single-particle shell-model state. Although  $C^2 S$  is model-dependent, it is the only quantity in Eqn. 2.17 that is based on measurement, as will be clear in Section 2.4.2.

The dimensionless single-particle reduced width is given by

$$\theta_{sp,c} = \frac{R}{2} |u_{sp,c}(R)|^2, \quad (2.19)$$

where  $u_{sp,c}(R)$  is the single-particle radial wavefunction evaluated at the channel radius,

which is normalized to unity as in

$$\int_0^R |u_{\text{sp},c}(R)|^2 r^2 dr = 1. \quad (2.20)$$

One method of numerically calculating  $\theta_{\text{sp},c}$  is to vary the parameters of the single-particle potential until a resonance is produced at the binding energy. This is performed, for example, by the code **BIND**, detailed in Ref. [Ili97]. Another procedure, performed for  $^{39}\text{K}(p,\gamma)^{40}\text{Ca}$  in Sec. 4.7.5, is to use the weak binding approximation. This approximation is required if the nuclear reaction code used in the determination of  $C^2S$  only handles bound states, as is the case with **Fresco** [Tho88, Tho06]. This method assumes unbound states are weakly bound (by  $\lesssim 50$  keV), and therefore  $u_{\text{sp},c}(R)$  is the bound state radial wavefunction evaluated at the channel radius. The channel radius  $R$  is selected to represent the nuclear surface, where the wavefunctions for the bound state and unbound state are equivalent.

A fact that appears troubling for the weak binding approximation at first glance is that both  $C^2S$  and  $\theta_{\text{sp},c}$  depend linearly on the binding energy, assuming  $R$  is chosen at the nuclear surface. Therefore, both quantities will diverge from unbound calculations at high binding energies. However, as Ref. [Har23] has shown for the proton-transfer reaction  $^{30}\text{Si}(^3\text{He},d)^{31}\text{P}$ ,  $C^2S$  decreases as a function of binding energy at roughly the same rate as  $\theta_{\text{sp},c}$  increases, such that their product is balanced. The only significant energy dependence from Eqn. 2.17 therefore comes from the penetration factor  $P_c(E)$ , which can easily be evaluated for unbound energies without the use of the weak binding approximation.

### 2.3.3 $\gamma$ -ray Partial Widths

The  $\gamma$ -ray partial width for a single transition is

$$\Gamma_\gamma(\bar{\omega}, E_\gamma) = \frac{8\pi(L+1)}{L [(2L+1)!!]^2} \left( \frac{E_\gamma}{\hbar c} \right)^{2L+1} B(\bar{\omega}L), \quad (2.21)$$

where  $\bar{\omega}$  represents either electric or magnetic radiation;  $E_\gamma$  is the  $\gamma$ -ray transition energy;  $L$  is the  $\gamma$ -ray multipolarity, and  $B$  is the branching ratio. The  $\gamma$ -ray partial width at the incoming particle energy  $E$  can be scaled with respect to that of the resonance energy  $E_r$  as in

$$\Gamma_\gamma(E) = \Gamma_\gamma(E_r) \left( \frac{E + Q - E_f}{E_r + Q - E_f} \right)^{2L+1}, \quad (2.22)$$

where  $Q$  is the  $Q$ -value, or equivalently, the particle separation energy, and  $E_f$  is the final excitation energy of the  $\gamma$ -decay.

## 2.4 Transfer Reactions

It is clear from the previous sections that there is an intimate connection between astrophysics and nuclear structure. Astrophysical reaction rates depend on resonance strengths and resonance energies, both of which can be obtained through experimental investigation of nuclear reactions in the laboratory. Transfer reaction measurements can provide these key nuclear ingredients and are often better suited to investigate the low energy resonances important for astrophysical environments than the direct reactions themselves.

Transfer reactions occur when either a single nucleon or cluster of nucleons  $x$  are transferred between the projectile system  $a$  and the target system  $A$ . The reaction  $A(a, b)B$  proceeds, where, assuming  $x$  is transferred from  $a = b + x$  to  $A$ , a new composite nucleus  $B = A + x$  is formed. This is known as a stripping reaction. If  $x$  were instead transferred from the target to the projectile, it would be considered a pickup reaction. Stripping reactions will be the focus of the current section, as this type of reaction is performed in this thesis.

### 2.4.1 Optical Model

The scattering of  $a+A$  or  $b+B$  can be described in general by coupling every available reaction channel. In practice, however, this is far too complex because it would require specifying the  $N$ -body Hamiltonian. The optical model can be applied instead, where interactions are averaged over, and the scattering problem reduces to considering a single particle interacting with a complex potential  $U(r) = V(r) + iW(r)$ . The real part  $V(r)$  describes the elastic scattering process, while the imaginary part  $W(r)$  is responsible for absorption, or the loss of flux due to the other available reaction channels [Kra87].

The optical model potential (OMP)  $U(r)$  is typically described by a real volume term, imaginary volume and surface absorption terms, real and imaginary spin-orbit coupling terms, and a Coulomb potential term  $V_c(r)$ . The real ( $r$ ) and imaginary ( $v$ ) volume potentials have a Woods-Saxon form  $f(r)$ , and the surface ( $s$ ) and spin-orbit ( $so$ ) potentials have a Woods-Saxon derivative form  $df(r)/dr$ , where

$$f_i(r) = \left[ 1 + \frac{\exp(r - R_i)}{a_i} \right]^{-1} \quad (i = r, v, s, so), \quad (2.23)$$

with the radii calculated from  $R_i = r_i A_t^{1/3}$  for  $i = r, v, s, so, c$ . The parameters  $r_i$  and  $a_i$  are referred to as the radius and diffusiveness parameters, respectively, and  $A_t$  is the target mass.

The full potential is written as [Lia09]

$$U(r) = -V_r f_r(r) - iW_v f_v(r) + i4a_s W_s \frac{d f_s(r)}{dr} + \lambda_\pi^2 \frac{V_{so} + iW_{so}}{r} \frac{d f_{so}(r)}{dr} \vec{\sigma} \cdot \vec{\ell} + V_c(r), \quad (2.24)$$

where  $\lambda_\pi^2 = 2.0 \text{ fm}^2$  and the Thomas form for the spin-orbit coupling is chosen.

In general, there are 14 parameters that make up the OMP of Eqn. 2.24,  $V_r$ ,  $r_r$ ,  $a_r$ ,  $W_v$ ,  $r_v$ ,  $a_v$ ,  $W_s$ ,  $r_s$ ,  $a_s$ ,  $V_{so}$ ,  $r_{so}$ ,  $a_{so}$ ,  $W_{so}$ , and  $r_c$ . For a given pair of nuclei, these parameters must be chosen carefully, as systematic uncertainties in quantities derived from the OMP are usually large. The parameters are often determined from local experimental elastic scattering data, which are relevant only for the specific target nucleus and beam energy used. They can also be extracted globally, from exhaustive studies of experimental elastic scattering data for several target nuclei over a wide range of energies [An06, Lia09]. In the case of global OMPs, the potential parameters are usually expressed as functions of beam energy and target mass. These global OMPs are used for the transfer reaction experiment of Chapter 4.

### 2.4.2 Distorted Wave Born Approximation

The optical model is a useful way to simplify the  $N$ -body scattering problem for  $a + A$  and  $b + B$ , but the information about the available reaction channels, such as a transferred particle  $x$ , is lost to the imaginary absorption term. Particle transfer can be treated as a perturbation to the elastic scattering of  $a + A$  and  $b + B$ , each described by an OMP [Sat83]. This perturbation is implemented by the Distorted Wave Born Approximation (DWBA). DWBA can be applied under the assumption that the transfer process is weak enough to be treated as a first order perturbation and that transfer occurs directly between  $a + A$  and  $b + B$ , with no rearrangement of the core configuration [Ham21].

The transfer process is governed by the perturbing interaction potential  $V_{\text{tr}}$ . The initial and final wavefunctions are represented by the distorted waves  $\chi_i^{(+)}(\mathbf{k}_i)$  and  $\chi_f^{(-)*}(\mathbf{k}_f)$ , respectively, where  $\mathbf{k}$  is the associated wave number. The transition amplitude for the transfer process can be written as

$$T_{i \rightarrow f}^{\text{DWBA}} = \langle \chi_f^{(-)*}(\mathbf{k}_f) | V_{\text{tr}} | \chi_i^{(+)}(\mathbf{k}_i) \rangle. \quad (2.25)$$

Coordinate transformation is performed on the  $a + A$  and  $b + B$  systems, leading to

$$T_{i \rightarrow f}^{\text{DWBA}} = J \int d\mathbf{r}_a \int d\mathbf{r}_b \chi_b^{(-)*}(\mathbf{k}_b, \mathbf{r}_b) \langle B, b | V_{\text{tr}} | A, a \rangle \chi_a^{(+)}(\mathbf{k}_a, \mathbf{r}_a), \quad (2.26)$$

where  $J$  is the Jacobian of the transformation. The term  $\langle B, b | V_{\text{tr}} | A, a \rangle$  is called the *form*

*factor*, which contains information about the nuclear structure and selection rules of the transition.

The full transition amplitude involves evaluating a six-dimensional integral over the two relative coordinates  $\mathbf{r}_a$  and  $\mathbf{r}_b$ . This full evaluation is known as a *finite-range* (FR) calculation. With modern computers, this calculation can be performed quite easily. However, it is still possible to make an additional approximation to reduce the number of integrals evaluated. This can be useful if Monte Carlo methods are employed for transfer reaction calculations. An assumption can be made, called the *zero-range* (ZR) *approximation*, that the form factor has a small range. This effectively means that the ejectile is emitted at the same point as the projectile is absorbed. With this assumption, the transition amplitude reduces to a three-dimensional integral and only the  $A + x$  interaction needs to be considered. In general, the integrand of the transition amplitude is proportional to the projectile internal wavefunction  $\phi_{b+x}$  and the  $b + x$  interaction potential  $V_{b+x}$ . That is,  $D(\mathbf{r}_{b+x}) = \phi_{b+x} V_{b+x}$ . Under the ZR approximation, this becomes

$$D(\mathbf{r}_{b+x}) \approx D_0 \delta(\mathbf{r}_b - \mathbf{r}_x), \quad (2.27)$$

where  $D_0$  is the ZR coupling constant, which can be calculated theoretically for  $(a, b)$  transfer reactions. For the  $(^3\text{He}, d)$  reaction performed in Chapter 4, the ZR approximation is assumed, and the value  $D_0 = -172.8 \text{ MeV F}^{3/2}$  from Ref. [Bas66] is used.

In order to extract information from the form factor, a particular representation for  $V_{\text{tr}}$  must be chosen. The *prior* or *post* representations refer to whether the interaction is associated with the entrance or exit channel, respectively, and they are equivalent to first order [Sat83]. In the post representation, for example, the reaction will depend on all interactions with the core in the exit channel,  $b$ , including the optical potentials. In other words,

$$V_{\text{post}} = V_{x+b} + U_{A+b} - U_{B+b}, \quad (2.28)$$

where  $V_{x+b}$  is a real, single-particle potential. The approximation  $U_{A+b} - U_{B+b} \approx 0$  is often made, called the *no-remnant approximation*. Applying this approximation, the form factor can be expressed in the post form as

$$\begin{aligned} \langle B, b | V_{\text{post}} | A, a \rangle &= \langle B, b | V_{x+b} | A, a \rangle \\ &= \langle B | A \rangle \langle b | V_{x+b} | a \rangle, \end{aligned} \quad (2.29)$$

where the second line results from factorization, as  $V_{x+b}$  only acts on the projectile. The term  $\langle B | A \rangle$  is called the *overlap function*, which describes a state in the composite nucleus

$B \rightarrow A + x$ . The radial part of the overlap function  $I_{A+x}^B(r)$  can be approximated by a single-particle wave function, usually generated by a Woods-Saxon potential,

$$I_{A+x}^B(r) \approx S_{A+x}^{1/2} \phi_{A+x}(r), \quad (2.30)$$

where  $\phi_{A+x}(r)$  is the bound state radial wavefunction describing the relative  $A + x$  motion. The square of the coefficient  $S_{A+x} = |S_{A+x}^{1/2}|^2$  is defined as the *spectroscopic factor*. Usually though, it is paired with the isospin Clebsch-Gordan coefficient  $C^2$ , so that  $C^2 S_{A+x}$  is the typical definition of the spectroscopic factor. It can be thought of as the overlap probability between the  $A + x$  wavefunction and the final single-particle configuration  $B$ .

This procedure is repeated for the overlap of  $a \rightarrow b + x$  in the prior representation resulting in  $C^2 S_{b+x}$ . At this point, a theoretical cross section proportional to the square of the transition amplitude can then be computed. Comparing to an experimental differential cross section, the proportionality is the combined spectroscopic factor

$$\frac{d\sigma}{d\Omega}_{\text{Exp}} = C^2 S_{A+x} C^2 S_{b+x} \frac{d\sigma}{d\Omega}_{\text{DWBA}}. \quad (2.31)$$

Recall from Eqn. 2.17 that  $C^2 S$ , referring to  $C^2 S_{A+x}$ , goes directly into the particle partial width calculation. Hence, experimental differential cross sections can be used to obtain  $C^2 S_{A+x}$  and therefore particle partial widths, assuming  $C^2 S_{b+x}$  is known. For small projectile particles  $b$  and  $x$ , these are usually available through ab-initio calculations, such as Ref. [Bri11].

## CHAPTER

# 3

## RUBIDIUM PRODUCTION IN MASSIVE AGB STARS

### 3.1 Introduction

This chapter details my investigation of the key reaction rates constraining rubidium production in massive AGB stars. Section 3.2 introduces the “rubidium problem”, a discrepancy between observed and theoretical [Rb/Zr] abundance ratios of massive AGB stars, which is the motivation of the present investigation. Section 3.3 describes the reaction network methodology used in the present work for investigating the  $^{86}\text{Rb}$  s-process branching. The results of a single network calculation are presented, and the extension to a Monte Carlo reaction network procedure is described. Finally, Section 3.4 showcases the results of the Monte Carlo reaction network calculation, where the effects of reaction rate uncertainties on rubidium production are demonstrated. The reaction rates with the strongest correlation to the  $^{87}\text{Rb}/^{86}\text{Sr}$  and  $^{87}\text{Rb}/^{90}\text{Zr}$  abundance ratios are reported, where these ratios are indicators of the  $^{86}\text{Rb}$  s-process branching efficiency. The [Rb/Zr] probability density is then extracted to address the connection between reaction rate uncertainties and the rubidium problem.

### 3.2 Rubidium Abundance

Many processes occur during the interpulse period in asymptotic giant branch (AGB) stars. Protons from the hydrogen-burning shell are mixed into the intershell region just after

thermal pulses, where  $^{12}\text{C}$  is then destroyed by proton-capture reactions during the sequence  $^{12}\text{C}(p, \gamma)^{13}\text{N}(\beta^+\nu)^{13}\text{C}(p, \gamma)^{14}\text{N}$ . The result is the formation of  $^{13}\text{C}$  and  $^{14}\text{N}$  pockets at the top of the intershell region. The  $^{13}\text{C}(\alpha, n)^{16}\text{O}$  reaction from the  $^{13}\text{C}$  pocket is activated at temperatures of  $100 \text{ MK} \lesssim T \lesssim 300 \text{ MK}$ , producing neutron densities of  $N_n \approx 10^7 \text{ g/cm}^3$ . This reaction is the main source of free neutrons during the interpulse period.

During thermal pulses,  $^{14}\text{N}$  from the  $^{14}\text{N}$  pocket captures  $\alpha$ -particles via the sequence  $^{14}\text{N}(\alpha, \gamma)^{18}\text{F}(\beta^+\nu)^{18}\text{O}(\alpha, \gamma)^{22}\text{Ne}$ , producing  $^{22}\text{Ne}$ . The  $^{22}\text{Ne}(\alpha, n)^{25}\text{Mg}$  reaction is then activated during thermal pulses at temperatures of  $T \gtrsim 300 \text{ MK}$ , producing large neutron densities of  $N_n \approx 10^{10} \text{ g/cm}^3$ . This reaction is the main source of free neutrons during thermal pulses. For massive AGB stars ( $M \gtrsim 4 M_\odot$ ), the  $^{22}\text{Ne}(\alpha, n)^{25}\text{Mg}$  neutron source dominates over  $^{13}\text{C}(\alpha, n)^{16}\text{O}$  in terms of the total neutron production. The free neutrons from both reactions lead to nucleosynthesis of heavy elements such as Rb, Sr, Y, and Zr via the s-process (see Section 1.2). These elements are brought to the surface from subsequent thermal pulses and are ejected into the interstellar medium.

### 3.2.1 The s-Process Branching at $^{86}\text{Rb}$

The  $^{22}\text{Ne}(\alpha, n)^{25}\text{Mg}$  neutron source enhances the efficiency of s-process branchings, altering the relative abundance of nearby nuclei. Hence, the abundance ratio of nuclei on either side of an s-process branching is an indicator of both the neutron density and the predominant neutron source [Gar06]. The branchings at  $^{85}\text{Kr}$  and  $^{86}\text{Rb}$ , for example, determine whether the production of the closed-neutron shell ( $N = 50$ ) nucleus  $^{87}\text{Rb}$  is favored. This situation is depicted in Figure 3.1, where stable nuclei are shaded, and unstable nuclei are unshaded. The  $^{85}\text{Kr}$  and  $^{86}\text{Rb}$  s-process branchings are highlighted in red, and their corresponding neutron captures or  $\beta^-$ -decays are illustrated with dashed arrows. A complication arises with  $^{85}\text{Kr}$ , since the  $^{84}\text{Kr}(n, \gamma)^{85}\text{Kr}$  reaction can populate the  $^{85}\text{Kr}^m$  isomeric state at roughly equal probability to that of the  $^{85}\text{Kr}^g$  ground state [Rau13]. The  $^{85}\text{Kr}^m$  state  $\beta^-$ -decays to  $^{85}\text{Rb}$  with about an 80% probability. Otherwise, it  $\gamma$ -decays to the ground state with about a 20% probability. Only the ground state can undergo neutron capture. In the absence of large neutron densities,  $^{85}\text{Kr}$  and  $^{86}\text{Rb}$  will preferentially  $\beta^-$ -decay, bypassing  $^{87}\text{Rb}$  altogether and producing  $^{86}\text{Sr}$ . If, on the other hand, there is a sufficiently large neutron density from the  $^{22}\text{Ne}(\alpha, n)^{25}\text{Mg}$  neutron source,  $^{87}\text{Rb}$  will be accumulated. Since  $^{87}\text{Rb}$  is a closed-shell nucleus, it also has an exceptionally low neutron-capture cross section, enhancing its abundance even more. In the large neutron density scenario, we should expect  $^{87}\text{Rb}$  to be favored over  $^{86}\text{Sr}$  or even  $^{90}\text{Zr}$ .

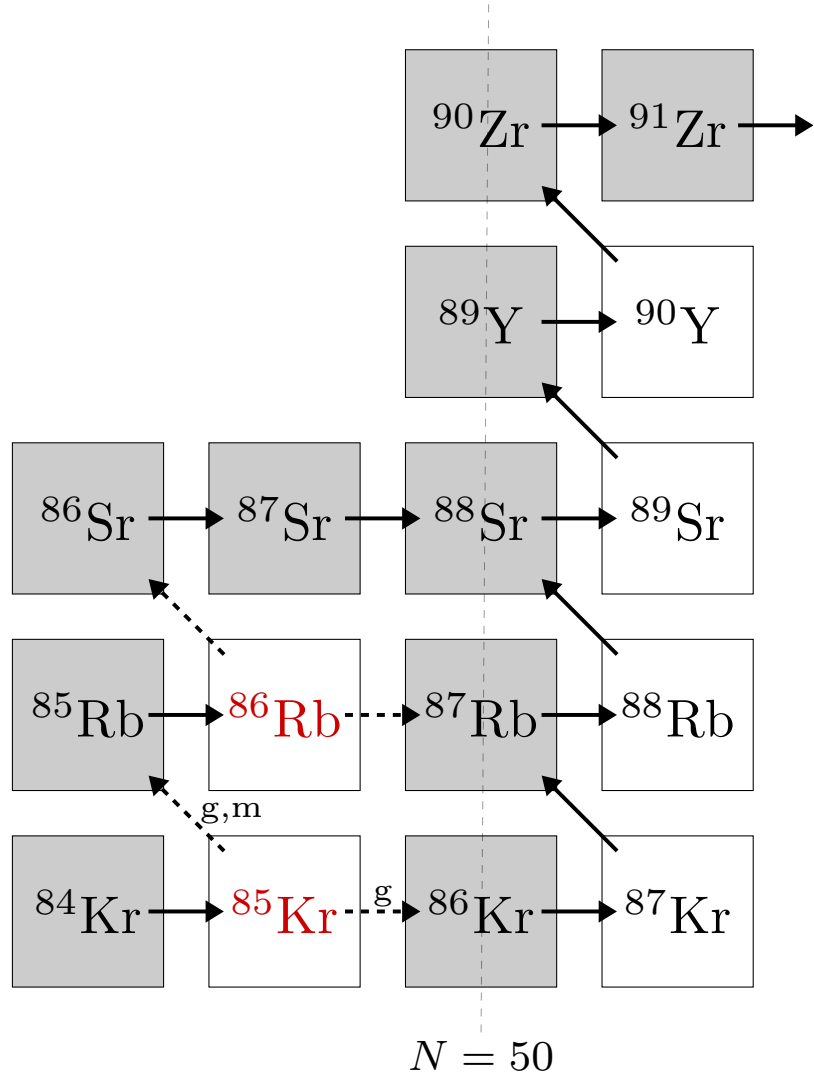


Figure 3.1: The  $^{85}\text{Kr}$  and  $^{86}\text{Rb}$  s-process branchings, highlighted in red, along the s-process path from Kr to Zr. The dashed arrows extending from these branchings indicate the path dependence on the neutron density. The  $N = 50$  closed-shell nuclei are represented by the vertical dashed line, which have low neutron-capture cross sections. The relative abundance of  $^{87}\text{Rb}$  to nearby nuclei such as  $^{86}\text{Sr}$  and  $^{90}\text{Zr}$  is expected to be an indicator of neutron density.

### 3.2.2 The Rubidium Problem

Unfortunately, observing isotopic ratios of  $^{87}\text{Rb}$  to other nearby nuclei in stellar sources is not possible due to the broadness of their isotopic lines in the observed spectra. However, elemental abundances can be observed, and the ratio of nearby elements can also be an indicator of neutron density and the neutron source. Refs. [Gar06, Gar07] sampled 102 massive, Galactic O-rich AGB stars and determined their Rb [Gar06], Li, and Zr [Gar07] abundances. Among them, an accurate abundance analysis of both Rb and Zr could only be achieved for 22 stars due to the difficulty in quantifying the circumstellar contribution to the Rb line. The analysis yielded strong Rb abundances up to  $[\text{Rb}/\text{Fe}] \sim +2.6$  dex, where the abundance of X,  $[\text{X}/\text{Fe}]$ , is defined in terms of number densities  $N$  as

$$[\text{X}/\text{Fe}] = \log \left( \frac{N_{\text{X}}}{N_{\text{Fe}}} \right)_{*} - \log \left( \frac{N_{\text{X}}}{N_{\text{Fe}}} \right)_{\odot}, \quad (3.1)$$

with  $*$  representing the composition of the star and  $\odot$  representing the solar composition. The unitless quantifier dex is therefore logarithmic, indicating that the star with the maximum ratio of Rb atoms to Fe atoms was found to be  $10^{2.6} \approx 400$  times that of solar composition, with an uncertainty of  $\lesssim 0.8$  dex. The total range of abundances was found to be between  $[\text{Rb}/\text{Fe}] \sim -1.0$  to  $+2.6$  dex, with the massive stars associated with the  $^{22}\text{Ne}(\alpha, n)^{25}\text{Mg}$  neutron source determined to have  $\gtrsim +0.6$  dex. The Zr abundances were simultaneously found to have only a mild enrichment with  $[\text{Zr}/\text{Fe}] < 0.5$  dex. Hence, the  $[\text{Rb}/\text{Zr}]$  ratios were determined to be up to  $[\text{Rb}/\text{Zr}] \sim 2.1$  dex ( $\sim 125$  times solar). Neither the high  $[\text{Rb}/\text{Fe}]$  abundances nor the high  $[\text{Rb}/\text{Zr}]$  ratios were predicted by current theoretical models of s-process nucleosynthesis in AGB stars [Raa12, Kar12].

Ref. [Gar09] also observed O-rich AGB stars in the Large and Small Magellanic Clouds (LMC and SMC, respectively), satellite galaxies of the Milky Way. They found an even larger Rb overabundance among the massive AGB stars in their sample between  $[\text{Rb}/\text{Fe}] \sim 3 - 5$  dex, or  $10^3 - 10^5$  times that of the solar composition. The Zr abundance was found to be only marginally enhanced, as before, leading to  $[\text{Rb}/\text{Zr}]$  ratios of  $\sim 3 - 4$  dex ( $10^3 - 10^4$  times solar). This extreme Rb overabundance, which is at odds with current theoretical predictions, is referred to as the *rubidium problem* by Ref. [Gar09].

The analysis that Refs. [Gar06, Gar07, Gar09] performed to obtain the high Rb abundances included the use of a stellar atmospheric model with a classical hydrostatic atmosphere [Gus08]. Ref. [Zam14] developed an updated atmospheric model of AGB stars that incorporated a pseudo-dynamical atmosphere and applied this to a small sample of 5 O-rich AGB stars. They found updated  $[\text{Rb}/\text{Zr}]$  ratios much lower than those obtained with the classical hydrostatic models and in better agreement with the theoretical nucleosynthesis models. Ref. [Per17]

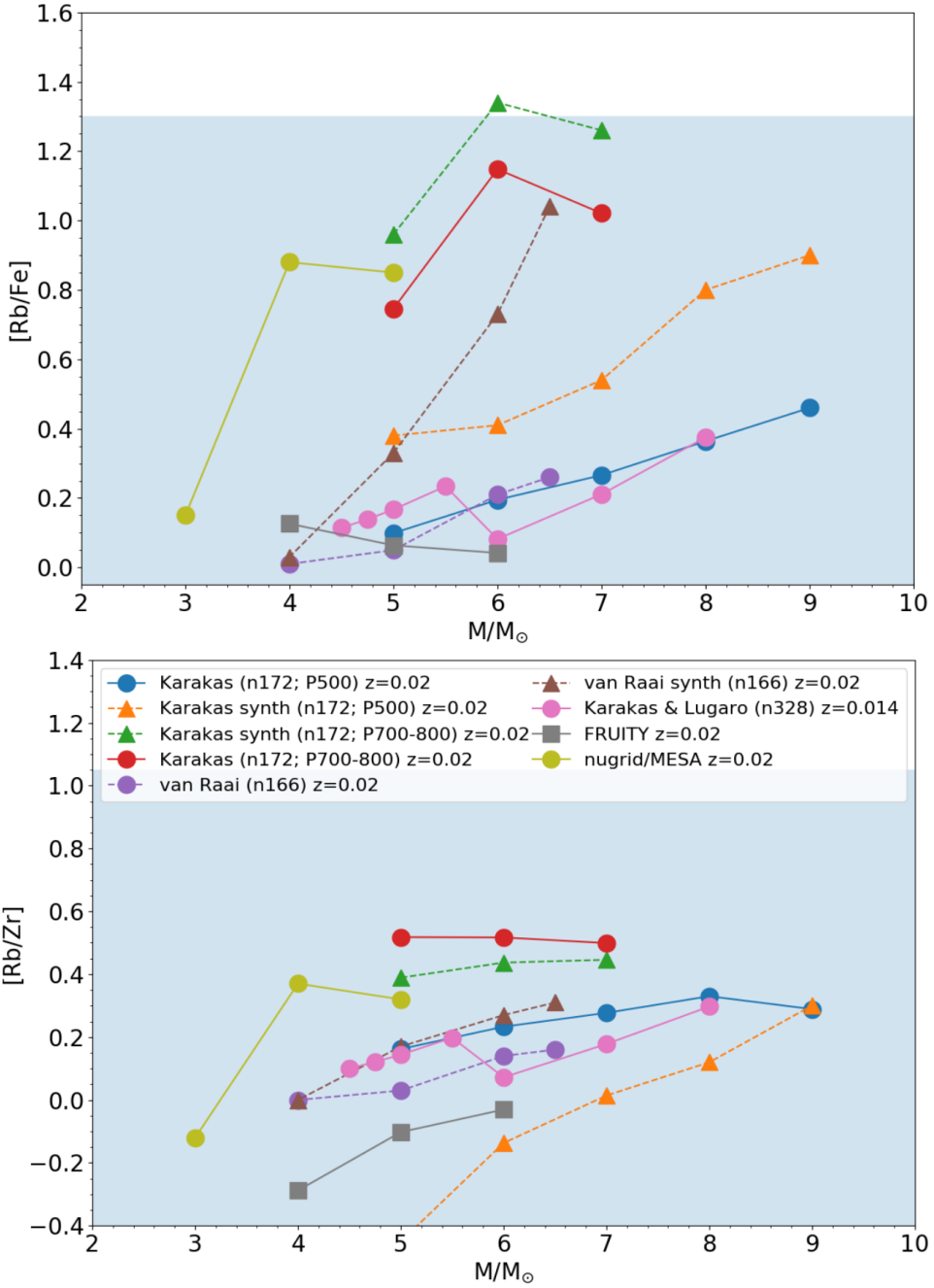


Figure 3.2: The AGB model predictions of  $[Rb/Fe]$  (top) and  $[Rb/Zr]$  (bottom) as a function of stellar mass from Refs. [Kar12, Raa12, Kar16, Pig16]. The dots and triangles represent abundances from the last computed thermal pulse and from synthetic calculations, respectively. The number of nuclei  $n$  in the corresponding network is provided in the legend, as well as the delay superwind parameter  $P$  (see text), if applicable, and the metallicity  $z$ . The range of observed  $[Rb/Fe]$  and  $[Rb/Zr]$  values from Ref. [Per17] are shown by the shaded blue background. Adapted from Ref. [Per17].

expanded this study to investigate the full sample of massive Galactic AGB stars analyzed by Refs. [Gar06, Gar07]. They found a similar decrease in the [Rb/Fe] abundances and [Rb/Zr] ratios, in much better agreement with theoretical models from Refs. [Kar12, Raa12, Kar16, Pig16].

Figure 3.2 shows these theoretical model predictions as a function of AGB mass, compared with the new range of observed [Rb/Fe] abundances (top) and [Rb/Zr] ratios (bottom) from the updated pseudo-dynamical atmospheric models, shaded in blue [Per17]. The dots and triangles represent abundances from the last computed thermal pulse and from synthetic calculations, respectively. The models with a modified mass-loss prescription (green and red points), indicated with  $P = 700 - 800$  shown in the legend, delay the beginning of the superwind phase until the pulsation period  $P$  reaches the indicated number of days. The effect of these models is to intentionally increase the Rb abundance, hence the red and green models show much higher Rb production than the others, which all use the standard  $P = 500$  days. The full range of the [Rb/Fe] abundances can now be reproduced by the theoretical models, but the largest [Rb/Zr] ratios are still not reproduced. The largest [Rb/Zr] ratio found by Ref. [Per17] is 1.05 dex, and the largest of any theoretical model is 0.52 dex, a difference of 0.53 dex. Therefore, despite the better agreement with moderate [Rb/Zr] ratios, the largest observed [Rb/Zr] ratios have still not been reproduced for Galactic O-rich AGB stars. This is true even for the modified AGB models, where Rb abundance is artificially enhanced. In conjunction with this remaining discrepancy, the extreme [Rb/Fe] and [Rb/Zr] observations for O-rich AGB stars in the LMC and SMC [Gar09] have yet to be reconciled.

The rubidium problem is investigated in the remainder of this chapter by considering the reaction rate uncertainties of all reactions relevant to the s-process in AGB stars. Some of these reactions are essential to rubidium production in the models presented in this section. In particular, the s-process branching at  $^{86}\text{Rb}$  is investigated with a nuclear reaction network (see Section 2.2) by considering the relative abundance of  $^{87}\text{Rb}$  to the nearby nuclei  $^{86}\text{Sr}$  and  $^{90}\text{Zr}$ . If these ratios are significantly altered when sampling a given reaction rate within its own uncertainty, the reaction is considered significant to rubidium production.

## 3.3 s-Process Reaction Network Methodology

### 3.3.1 The Reaction Network

An s-process reaction network of 769 nuclei and 7,571 reactions from  $^1\text{H}$  to  $^{212}\text{Bi}$  is considered, where nucleosynthesis is simulated during a single thermal pulse in the intershell region of an AGB star at constant temperature  $T$  and density  $\rho$ . The system of differential equations

described by Eqn. 2.3 is computed numerically, given the reaction rate probability densities tabulated in the **Starlib** [Sal13] library, truncated for the nuclei in the network. The median, recommended reaction rates are used for the single calculation described in Section 3.3.2, while the full probability densities are sampled in Section 3.4. The abundances at each time step are reported in terms of mass fractions  $X$ . The final time is determined by the amount of helium that has been exhausted, such that a final mass fraction of  $X_{\text{last}}(^4\text{He})$  stops the evolution. Helium is not expected to be completely exhausted during a thermal pulse, so this condition is chosen to be slightly less than the initial  ${}^4\text{He}$  mass fraction  $X_{\text{init}}(^4\text{He})$ .

The intershell region consists of about 75%  ${}^4\text{He}$ , 22%  ${}^{12}\text{C}$ , and a small amount of  ${}^{16}\text{O}$  [Hab04], with the remainder roughly approximated in terms of relative solar system abundances [Lod09]. A complication to consider is how to address proton-mixing because it is not inherently described by Eqn. 2.3, yet it is the origin of the neutron sources  ${}^{13}\text{C}(\alpha, n){}^{16}\text{O}$  and  ${}^{22}\text{Ne}(\alpha, n){}^{25}\text{Mg}$  via the  ${}^{13}\text{C}$  and  ${}^{14}\text{N}$  pockets, respectively. Additionally, no protons are expected to exist in the intershell region during thermal pulses, as they get consumed in the formation of the  ${}^{13}\text{C}$  and  ${}^{14}\text{N}$  pockets. This issue is rectified by enhancing the initial mass fractions of  ${}^{13}\text{C}$  and  ${}^{14}\text{N}$  from their relative solar system abundances to simulate the  ${}^{13}\text{C}$  and  ${}^{14}\text{N}$  pockets and having an initial  ${}^1\text{H}$  mass fraction of zero. The abundance of the  ${}^{56}\text{Fe}$  s-process seed nucleus is also slightly enhanced from its relative solar system abundance, to achieve a more efficient s-process. The initial abundances used in the present reaction network are provided in Table A.1.

The constant temperature  $T$  and density  $\rho$  for the reaction network are chosen as 300 MK and  $10^3$  g/cm $^3$ , respectively, indicative of the conditions in the intershell region during a thermal pulse at which the  ${}^{22}\text{Ne}(\alpha, n){}^{25}\text{Mg}$  neutron source is expected to activate [Hab04]. The  $X_{\text{last}}(^4\text{He})$  parameter is chosen as 0.7, where  $X_{\text{init}}(^4\text{He}) = 0.75$ .

### 3.3.2 Abundance Evolution

The abundance evolution for a single s-process nuclear reaction network calculation is shown in Fig. 3.3. It is apparent that  ${}^{13}\text{C}$  and  ${}^{14}\text{N}$  suddenly drop just after  $10^3$  s, corresponding with a burst of neutrons  $n$ .  ${}^{16}\text{O}$  and  ${}^{25}\text{Mg}$  production occur simultaneously, indicating that the neutron sources  ${}^{13}\text{C}(\alpha, n){}^{16}\text{O}$  and  ${}^{22}\text{Ne}(\alpha, n){}^{25}\text{Mg}$  are active, respectively. This burst of neutrons leads to a production of  ${}^{87}\text{Rb}$  and a destruction of the initial  ${}^{86}\text{Sr}$ , indicating that the neutron density is sufficient to active the  ${}^{85}\text{Kr}$  and  ${}^{86}\text{Rb}$  s-process branchings.

The flux plot of Fig. 3.4 tells a slightly more nuanced story. In the plot, arrows indicate the reactions that have occurred in the network, producing a net abundance flow from one nucleus to another. The arrow thickness is associated with the magnitude of the integrated flux, with

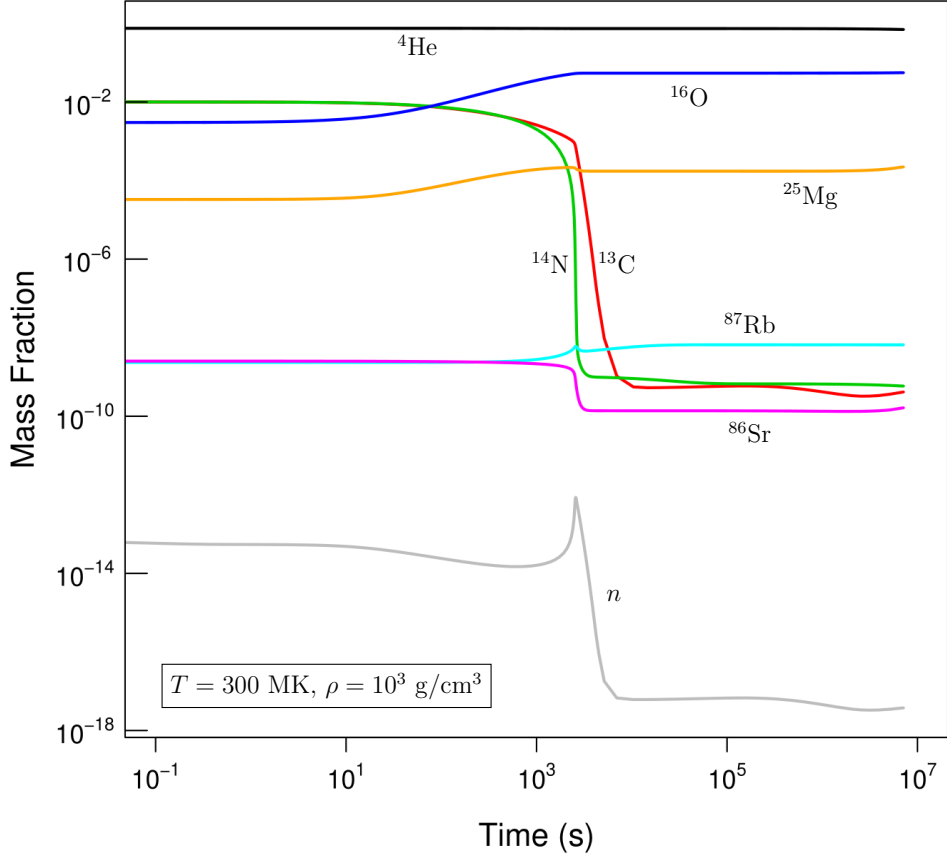


Figure 3.3: The abundance evolution of key nuclei related to the s-process branching at  $^{86}\text{Rb}$  for a single network calculation simulating the conditions during a single AGB thermal pulse. The  $T$ ,  $\rho$ , and  $X_{\text{last}}(^4\text{He})$  parameters are 300 MK,  $10^3 \text{ g/cm}^3$ , and 0.7, respectively, with  $X_{\text{init}}(^4\text{He}) = 0.75$ .

three levels of relative magnitude depicted. The reactions with the largest net flux are the triple- $\alpha$  reaction, the  $^{13}\text{C}$  neutron source sequence  $^{12}\text{C}(p, \gamma)^{13}\text{N}(\beta^+\nu)^{13}\text{C}(\alpha, n)^{16}\text{O}$  and the neutron poison  $^{14}\text{N}(n, p)^{14}\text{C}$ . The  $^{22}\text{Ne}$  neutron source sequence  $^{14}\text{N}(\alpha, \gamma)^{18}\text{F}(\beta^+\nu)^{18}\text{O}(\alpha, \gamma)^{22}\text{Ne}$  is present, but it is associated with the middle tier of relative magnitude. Hence, the  $^{13}\text{C}$  neutron source appears to be the dominant one, even though the s-process branchings clearly favor  $^{87}\text{Rb}$  from the abundance evolution of Fig. 3.3. Interestingly, the  $^{13}\text{N}(n, p)^{13}\text{C}$  net flux, overlapping with that of  $^{13}\text{N}(\beta^+\nu)^{13}\text{C}$ , is also quite large, destroying neutrons along with  $^{14}\text{N}(n, p)^{14}\text{C}$ . The protons produced from these reactions likely contribute to the  $^{12}\text{C}(p, \gamma)^{13}\text{N}$  reaction, giving rise to more  $^{13}\text{C}$ , even though no initial protons were provided.

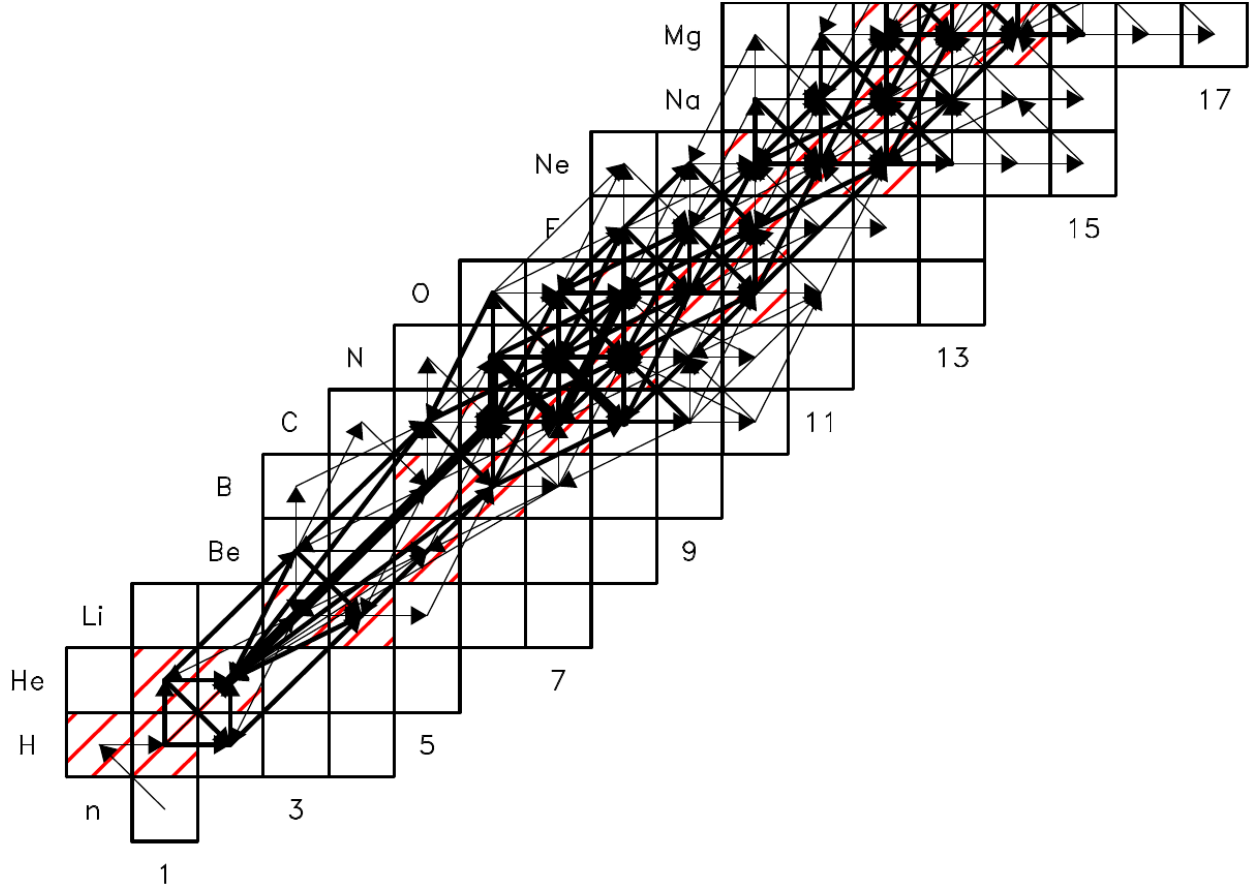


Figure 3.4: The network flux plot for a single network calculation simulating the conditions during a single AGB thermal pulse. The  $T$ ,  $\rho$ , and  $X_{\text{last}}(^4\text{He})$  parameters are 300 MK,  $10^3$  g/cm $^3$ , and 0.7, respectively, with  $X_{\text{init}}(^4\text{He}) = 0.75$ . The arrow thickness corresponds to the magnitude of the integrated flux from one nucleus to another, with three levels of relative magnitude shown. The reactions with the largest net flux are the triple- $\alpha$  reaction, the  $^{13}\text{C}$  neutron source sequence  $^{12}\text{C}(p, \gamma)^{13}\text{N}(\beta^+\nu)^{13}\text{C}(\alpha, n)^{16}\text{O}$ , and the neutron poison  $^{14}\text{N}(n, p)^{14}\text{C}$ .

A test of the initial abundances was performed where the enhanced value of  $X_{\text{init}}(^{13}\text{C}) = 0.01$  was swapped with the solar system value of  $X_{\text{init}}(^{22}\text{Ne}) = 6.34 \times 10^{-5}$ , in order to see if the  $^{22}\text{Ne}(\alpha, n)^{25}\text{Mg}$  neutron source could be maximized and the  $^{13}\text{C}(\alpha, n)^{16}\text{O}$  neutron source could be minimized. Indeed, the net flux of  $^{22}\text{Ne}(\alpha, n)^{25}\text{Mg}$  increases, but not as significantly as one might expect, since the two neutron sources have roughly equivalent flux in this scenario. In addition, the final  $X(^{87}\text{Rb})/X(^{86}\text{Sr})$  ratio decreases with these initial abundances, presumably from the drop in neutron density as a result of the weaker  $^{13}\text{C}(\alpha, n)^{16}\text{O}$  flux. Increased temperatures were also tested, but the abundance evolution is considerably more complicated, yet the fluxes remained more or less consistent, with only slight enhancements in the  $^{14}\text{N}(\alpha, \gamma)^{18}\text{F}(\beta^+\nu)^{18}\text{O}(\alpha, \gamma)^{22}\text{Ne}$  sequence. The topic of  $X_{\text{init}}$ ,  $T$ , and  $\rho$  variations merits

further investigation, but the simple s-process model described in Figs. 3.3 and 3.4 is sufficient for the present purpose of investigating reactions important to rubidium production, as the  $^{85}\text{Kr}$  and  $^{86}\text{Rb}$  s-process branchings are clearly activated.

### 3.3.3 Monte Carlo Procedure

The reaction rate probability densities from the **Starlib** library [Sal13], calculated with the **RatesMC** code [Lon10, Lon23], are sampled in the remaining analysis of this chapter. The reaction rates in the s-process network are simultaneously sampled within their own uncertainties, and a single network calculation is performed with the sampled rates to obtain final abundances of the nuclei in the network. This procedure is performed for several thousand reaction rate samples, and the final abundances therefore form probability densities of their own. These reaction rates are calculated given nuclear physics inputs, which can contain large uncertainties. To properly sample these uncertainties, a Monte Carlo sampling procedure is the most efficient. This procedure is described by Ref. [Lon12], and a summary is presented here.

The rate probability densities in **Starlib** are described by the lognormal shape parameters  $\mu$  and  $\sigma$  (not to be confused with the gaussian mean and standard deviation),

$$\begin{aligned} \mu &= \ln x_{\text{med}}, \\ \sigma &= \ln \sqrt{\frac{x_{\text{high}}}{x_{\text{low}}}}, \end{aligned} \quad (3.2)$$

where  $x_{\text{med}}$ ,  $x_{\text{high}}$ , and  $x_{\text{low}}$  are the median (recommended), 84th percentile, and 16th percentile rates, respectively. Reaction rate samples  $x(T)_i$  are drawn from a given reaction  $j$  at the temperature  $T$  and are represented by

$$\begin{aligned} x(T)_{ij} &= e^{\mu(T)_j} e^{p(T)_{ij}\sigma(T)_j} \\ &= x(T)_{\text{med},j} [f.u.(T)]_j^{p(T)_{ij}}, \end{aligned} \quad (3.3)$$

where  $p(T)$  is a gaussian-distributed random variable with a mean of zero and a standard deviation of unity, known as the *rate variation factor*, and the factor  $f.u.(T) \equiv e^{\sigma(T)}$  is known as the *factor uncertainty*. The parametrization of  $p(T)$  can be treated as independent of temperature to an excellent approximation [Lon12], known as a flat parametrization,  $p(T) = p$ . In this scenario,  $p$  is sampled from a normal distribution, while  $f.u.(T)$  remains a temperature-dependent quantity due to the lognormal  $\sigma(T)$  parameter. Since the present reaction network uses a constant  $T = 300$  MK, only the rate uncertainty at this temperature needs to be

sampled. Additionally, forward and reverse reaction rates are not sampled independently, as the same value of  $p$  is applied to both rates.

### 3.3.4 Measuring Correlations with Mutual Information

One of the primary goals in performing Monte Carlo reaction network calculations is to determine which reaction rates would benefit from experimental constraint for the given nucleosynthesis model. If the abundances of key nuclei are significantly altered when varying a reaction rate within its uncertainty, that rate is likely significant to the present nucleosynthesis. The reaction rate sensitivity of a given reaction  $j$  on the abundance of a given nucleus can be determined by analyzing the scatter plot between the rate variation factor  $p_j$  and the final mass fraction  $X$  over all network samples [Ili15b]. This can also be performed for an abundance ratio of nuclei 1 and 2 with the mass fraction ratio  $X_1/X_2$ . The random variables  $p_j$  and  $X$  are recorded after each network sample, and correlations are determined during post-processing using one of a variety of statistical metrics. For a given key mass fraction  $X$  or mass fraction ratio  $X_1/X_2$ , the correlations are then ranked according to this metric to determine the most important reaction rates governing the nucleosynthesis.

Pearson's correlation coefficient  $r$  has been used by Ref. [Coc14] to determine the linearity of these two random variables for reactions sensitive to  $^6\text{Li}$  production in big bang nucleosynthesis. However, this metric is not effective when the correlation is nonlinear. Spearman's correlation coefficient  $r_s$  was used by Ref. [Ili15b] for a similar nucleosynthesis network. It is more effective at quantifying nonlinear correlations because it measures the relationship between two variables described by a monotonic function. However, often these correlations are found exhibiting nonlinear behavior and are non-monotonic. A metric that is suitable for a general range of correlations is *mutual information*, recently used by Ref. [Ili20], which measures the amount of information about one random variable contained in another random variable [Cov06]. For the discrete random variables  $x$  and  $y$  containing the values  $\{x_1, x_2, \dots\}$  and  $\{y_1, y_2, \dots\}$  their mutual information MI is defined as

$$\text{MI} = \sum_x \sum_y P(x, y) \log \left[ \frac{P(x, y)}{P(x)P(y)} \right], \quad (3.4)$$

where  $P(x)$  and  $P(y)$  are the marginal probability distributions of  $x$  and  $y$ , respectively, and  $P(x, y)$  is their joint probability distribution. Mutual information between  $x$  and  $y$  is zero if, and only if, they are independent of each other. This metric has no finite upper limit, meaning the effective use of MI is to compare between relative magnitudes. That is all that is required for the purpose of ranking reaction rate correlations, and I therefore adopt MI as

the correlation metric in the present analysis.

## 3.4 Reaction Rate Sensitivities

### 3.4.1 Correlations

The Monte Carlo reaction network calculation was performed for  $5 \times 10^4$  samples. Correlations between every reaction in the network and the mass fraction ratios  $X(^{87}\text{Rb})/X(^{86}\text{Sr})$  and  $X(^{87}\text{Rb})/X(^{90}\text{Zr})$  were computed using the mutual information (MI) metric. The correlations were ranked according to their relative MI values, and the top 8 most correlated reaction rates with each ratio are listed in Table 3.1. Spearman's correlation coefficient  $r_s$  is provided to indicate the signature (positive or negative) of the correlation, assuming it is at least linear or monotonic. In many cases, the MI and  $|r_s|$  values are not consistent among the ranks, which is indicative of nonlinear, non-monotonic correlations. The top 3 most correlated reaction rates for both ratios, ranked by MI, are  $^{86}\text{Rb}(n, \gamma)^{87}\text{Rb}$ ,  $^{13}\text{N}(n, p)^{13}\text{C}$ , and  $^{14}\text{N}(n, p)^{14}\text{C}$ .

Beyond roughly the 8th largest MI values, the correlations slowly approach a minimum, as the reaction rates become increasingly uncorrelated with the mass fraction ratios. For both ratios, the least correlated reaction rate is that of  $^{49}\text{V}(\alpha, p)^{52}\text{Cr}$ , which has MI = 0.0468 and 0.0311 for  $X(^{87}\text{Rb})/X(^{86}\text{Sr})$  and  $X(^{87}\text{Rb})/X(^{90}\text{Zr})$ , respectively. Hence, the decrease between the top 8 MI values is much sharper than any subsequent decrease, and those reaction rates in Table 3.1 are the only ones that have a significant impact when sampling their uncertainties.

The correlation plots for the top 8 reaction rates are shown in Fig. 3.5 for  $X(^{87}\text{Rb})/X(^{86}\text{Sr})$  and in Fig. 3.6 for  $X(^{87}\text{Rb})/X(^{90}\text{Zr})$ . Each reaction is labeled with its MI rank, and its MI value is given in the top-right corner of each panel. The gaussian-distributed rate variation factor  $p$  is given on the  $x$ -axis, while the indicated mass fraction ratio (logarithm) is given on the  $y$ -axis. Each point is a sample corresponding to a single reaction network calculation, and the density of samples is indicated by the color gradient, with yellow corresponding to the most dense region. It is clear that the vertical scatter in each panel of Fig. 3.5 is quite large, indicative of the fact that all rates are sampled simultaneously to obtain a given mass fraction ratio sample. Despite the scatter, clear correlations are shown. These correlation plots will be analyzed in detail in the following discussion.

### Neutron Capture and $\beta^-$ -Decay

The  $^{86}\text{Rb}(n, \gamma)^{87}\text{Rb}$  reaction produces  $^{87}\text{Rb}$  directly from the  $^{86}\text{Rb}$  s-process branching, which also prevents  $^{86}\text{Sr}$  from accumulating, explaining its rank as the strongest correlation with the  $X(^{87}\text{Rb})/X(^{86}\text{Sr})$  ratio. Even for the  $X(^{87}\text{Rb})/X(^{90}\text{Zr})$  ratio, it has the third strongest

Table 3.1: The top eight most correlated reaction rates with the  $X(^{87}\text{Rb})/X(^{86}\text{Sr})$  and  $X(^{87}\text{Rb})/X(^{90}\text{Zr})$  mass fraction ratios, ranked according to mutual information (MI). Spearman's correlation coefficient  $r_s$  is also provided, to indicate the polarity of the correlation.

$X(^{87}\text{Rb})/X(^{86}\text{Sr})$				$X(^{87}\text{Rb})/X(^{90}\text{Zr})$			
Rank	Reaction	MI	$r_s$	Rank	Reaction	MI	$r_s$
1	$^{86}\text{Rb}(n, \gamma)^{87}\text{Rb}$	0.1967	0.4347	1	$^{13}\text{N}(n, p)^{13}\text{C}$	0.1921	-0.4822
2	$^{13}\text{N}(n, p)^{13}\text{C}$	0.1718	-0.4450	2	$^{14}\text{N}(n, p)^{14}\text{C}$	0.1331	0.1574
3	$^{14}\text{N}(n, p)^{14}\text{C}$	0.1341	0.1518	3	$^{86}\text{Rb}(n, \gamma)^{87}\text{Rb}$	0.1046	0.1405
4	$^{85}\text{Kr}(\beta^- \nu)^{85}\text{Rb}$	0.1102	-0.2433	4	$^{90}\text{Y}(n, \gamma)^{91}\text{Y}$	0.1039	0.3222
5	$^{86}\text{Rb}(\beta^- \nu)^{86}\text{Sr}$	0.1045	-0.2421	5	$^{87}\text{Kr}(n, \gamma)^{88}\text{Kr}$	0.0741	-0.2138
6	$^{85}\text{Kr}(n, \gamma)^{86}\text{Kr}$	0.0951	0.2176	6	$^{85}\text{Kr}(n, \gamma)^{86}\text{Kr}$	0.0637	0.1973
7	$^{18}\text{O}(\alpha, n)^{21}\text{Ne}$	0.0780	0.1272	7	$^{90}\text{Y}(\beta^- \nu)^{90}\text{Zr}$	0.0561	-0.1191
8	$^{25}\text{Na}(p, \gamma)^{26}\text{Mg}$	0.0660	0.0097	8	$^{18}\text{O}(\alpha, n)^{21}\text{Ne}$	0.0521	0.1103

correlation. This is likely due to the low neutron-capture cross section of  $^{87}\text{Rb}$ , such that it accumulates when the  $^{86}\text{Rb}$  s-process branching is activated, leading also to a reduced path to Zr.

A large portion of the reaction rates in the correlation plots and in Table 3.1 are neutron-captures and  $\beta$ -decays coming directly from the  $^{86}\text{Rb}$  and  $^{85}\text{Kr}$  s-process branchings. These neutron-capture reactions,  $^{86}\text{Rb}(n, \gamma)^{87}\text{Rb}$  and  $^{85}\text{Kr}(n, \gamma)^{86}\text{Kr}$ , are associated with a positive correlation, and the corresponding  $\beta^-$ -decays are associated with a negative correlation. This is the expected behavior, as these reactions are directly responsible for  $^{87}\text{Rb}$  production. Despite the proper Spearman correlation coefficient  $r_s$  signature in Table 3.1 for these reactions, it can already be seen to fail to capture some of the interesting nonlinear features of the correlation plots. This is the case for the  $^{86}\text{Rb}(n, \gamma)^{87}\text{Rb}$  rate in the upper left panel of Fig. 3.5, where positive  $p$ -values are much more positively correlated than negative  $p$ -values. Hence, mutual information is a necessary metric for this analysis.

The  $^{90}\text{Y}(n, \gamma)^{91}\text{Y}$  and  $^{90}\text{Y}(\beta^- \nu)^{90}\text{Zr}$  rates are sensitive only to the  $X(^{87}\text{Rb})/X(^{90}\text{Zr})$  ratio. These rates directly affect  $^{90}\text{Zr}$  abundance in opposing ways. The former reaction acts to bypass  $^{90}\text{Zr}$  along the s-process path, while the latter produces it directly. The  $r_s$  signatures of these rates in Table 3.1 are indicative of this effect. The  $^{87}\text{Kr}(n, \gamma)^{88}\text{Kr}$  reaction rate is also only sensitive to the  $X(^{87}\text{Rb})/X(^{90}\text{Zr})$  ratio, as it acts to bypass  $^{87}\text{Rb}$ , eventually producing  $^{90}\text{Zr}$ . It is clear that the vertical scatter is reduced in Fig. 3.6 for  $X(^{87}\text{Rb})/X(^{90}\text{Zr})$ , likely because  $^{90}\text{Zr}$  is much easier to accumulate than  $^{86}\text{Sr}$ , closing the gap between  $^{87}\text{Rb}$  abundance. It is also a closed-shell ( $N = 50$ ) nucleus, similar to  $^{87}\text{Rb}$ , with a low neutron-capture cross section.

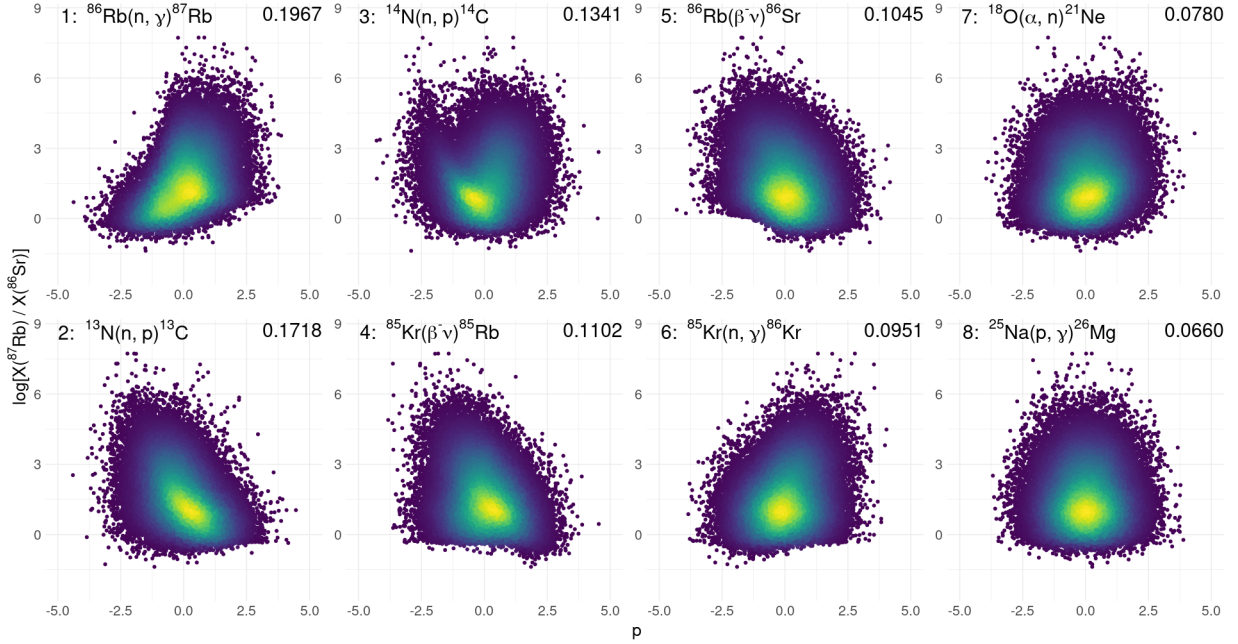


Figure 3.5: The largest reaction rate correlations with the final mass fraction ratio  $X(^{87}\text{Rb})/X(^{86}\text{Sr})$ , ranked by mutual information, given in the top-right corner of each plot. On the  $x$ -axis is the gaussian rate variation factor  $p$  (see text). The  $T$ ,  $\rho$ , and  $X_{\text{last}}(^4\text{He})$  parameters for each sample are 300 MK,  $10^3$  g/cm $^3$ , and 0.7, respectively, with  $X_{\text{init}}(^4\text{He}) = 0.75$ . The Monte Carlo reaction network calculation was performed for  $5 \times 10^4$  samples, and the density of these samples is represented by color, with yellow being the most dense region.

## The Neutron Sources

Interestingly, the main neutron sources  $^{13}\text{C}(\alpha, n)^{16}\text{O}$  and  $^{22}\text{N}(\alpha, n)^{25}\text{Mg}$  do not make an appearance in Table 3.1. In fact, they are mostly uncorrelated with either mass fraction ratio. A possible explanation of this could be that these rates are already well-constrained, and sampling over a small uncertainty may not affect the nucleosynthesis. The  $^{13}\text{C}(\alpha, n)^{16}\text{O}$  and  $^{22}\text{Ne}(\alpha, n)^{25}\text{Mg}$  **Starlib** reaction rates at 300 MK have factor uncertainties of  $f.u. = 18\%$  and  $f.u. = 23\%$ , respectively. Compared to many rate uncertainties, this is quite small and could offer an explanation for the lack of correlation, even if these reactions do inevitably contribute to  $^{87}\text{Rb}$  abundance. Although the main neutron sources are not correlated, the  $^{18}\text{O}(\alpha, n)^{21}\text{Ne}$  rate is mildly correlated with both ratios, according to Table 3.1. This may act as an alternative neutron source.

## The Neutron Poisons

I will now revisit the discussion of the  $^{13}\text{N}(n, p)^{13}\text{C}$  and  $^{14}\text{N}(n, p)^{14}\text{C}$  reactions. The known neutron poison  $^{14}\text{N}(n, p)^{14}\text{C}$  [Hab04] makes an appearance in the top three correlations

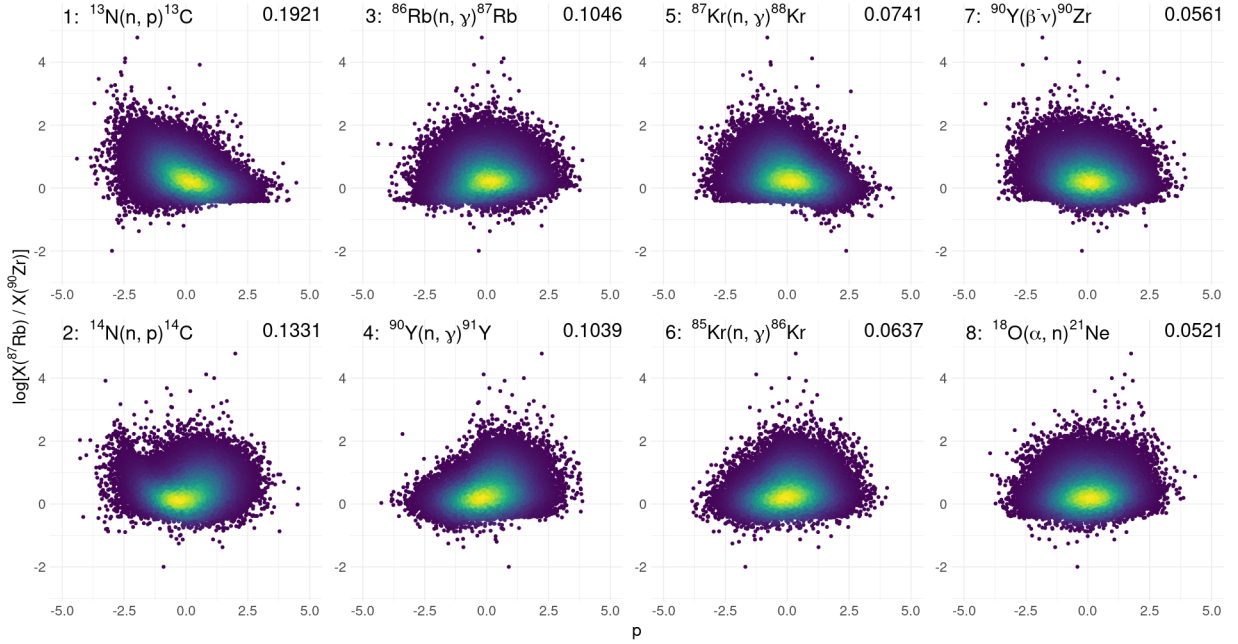


Figure 3.6: The largest reaction rate correlations with the final mass fraction ratio  $X(^{87}\text{Rb})/X(^{90}\text{Zr})$ , ranked by mutual information. See Fig. 3.5 caption for details.

of Table 3.1. However, it is counterintuitively associated with a positive correlation for both ratios from the  $r_s$  signature. One should expect that the  $^{86}\text{Rb}$  and  $^{85}\text{Kr}$  s-process branchings are deactivated with decreasing neutron density. This troublesome situation is resolved when analyzing the  $^{14}\text{N}(n, p)^{14}\text{C}$  correlation density in Figs. 3.5 and 3.6. A nonlinear, non-monotonic correlation is clearly depicted, with a strong negative correlation for negative  $p$ -values and a slightly positive correlation for positive  $p$ -values. This is a prime example of  $r_s$  being potentially misleading. When  $p$  is negative, the reaction rate is reduced such that less neutrons are being consumed by this reaction, leading to more neutrons available for  $^{87}\text{Rb}$  production. Conversely, when  $p$  is positive, the reaction rate is increased such that more neutrons are consumed, but more protons are consequently produced. These protons are consumed by the  $^{12}\text{C}$  sequence leading to  $^{13}\text{C}$ , where neutrons can be produced anyway from  $^{13}\text{C}(\alpha, n)^{16}\text{O}$ .

The strength of the  $^{13}\text{N}(n, p)^{13}\text{C}$  neutron poison correlation is somewhat surprising, as  $^{14}\text{N}(n, p)^{14}\text{C}$  is the more well-documented neutron poison in the literature [Hab04]. It has a strong negative  $r_s$  correlation for both mass fraction ratios, which is not misleading in this case, as is clear in the correlation plots of Figs. 3.5 and 3.6. Although one may think this reaction should have the same effect as  $^{14}\text{N}(n, p)^{14}\text{C}$ , its correlation plot is clearly different. The reason is that  $^{13}\text{N}(n, p)^{13}\text{C}$  happens to compete with  $^{13}\text{N}(\beta^+\nu)^{13}\text{C}$ , leading to equivalent production of the  $^{13}\text{C}$  neutron source, but the former reaction consumes neutrons in the

process. Hence,  $^{13}\text{N}(n, p)^{13}\text{C}$  is always a net neutron-destroyer, since the protons that are produced cycle back to this reaction via  $^{12}\text{C}(p, \gamma)^{13}\text{N}$ .

Eqn. 2.2 can be used to determine the conditions for which the  $^{13}\text{N}(n, p)^{13}\text{C}$  rate is favored over that of  $^{13}\text{N}(\beta^+ \nu)^{13}\text{C}$ . For  $(n, p)$  to be favored, the neutron mass fraction  $X_n$  would have to exceed

$$X_n > \frac{M_n}{\tau_{\beta^+}(^{13}\text{N})\rho N_A \langle \sigma v \rangle(T)} \approx 2.5 \times 10^{-15}, \quad (3.5)$$

where the mass density is  $\rho = 10^3 \text{ g/cm}^{-3}$ ;  $M_n$  is the neutron mass;  $\tau_{\beta^+}(^{13}\text{N}) \approx 863 \text{ s}$  [Aud03] is the mean lifetime for  $\beta^+$ -decay, and the recommended  $(n, p)$  reaction rate from **Starlib** at 300 MK is  $N_A \langle \sigma v \rangle = 4.586 \times 10^8 \text{ cm}^3 \text{ s}^{-1} \text{ mol}^{-1}$ . Referring back to the abundance evolution for the single nucleosynthesis calculation shown in Fig. 3.3,  $X_n$  exceeds this amount initially with a value of  $\approx 5 \times 10^{-14}$ . At this  $X_n$ , the mean lifetime  $\tau_n$  for  $(n, p)$  is about  $\tau_n \approx 43 \text{ s} \ll 863 \text{ s}$ , confirming that  $(n, p)$  is greatly favored. At its peak,  $X_n$  is  $8 \times 10^{-13}$ , corresponding with  $\tau_n \approx 3 \text{ s}$ , an even shorter mean lifetime. Eventually,  $X_n$  drops to about  $5 \times 10^{-18}$  in Figure 3.3, which implies  $\tau_n \approx 4.3 \times 10^5 \text{ s} >> 863 \text{ s}$ . Therefore, the  $\beta^+$ -decay is finally favored at this point. This exercise shows that  $^{13}\text{N}(n, p)^{13}\text{C}$  is surprisingly important for s-process nucleosynthesis and should be investigated further.

### 3.4.2 The [Rb/Zr], [Rb/Sr], and [Rb/Fe] Ratios

The elemental ratios  $X(\text{Rb})/X(\text{Sr})$  and  $X(\text{Rb})/X(\text{Zr})$  can be investigated as well. Analysis of these ratios leads to similar conclusions drawn in Section 3.4.1, and the correlation plots for the elemental ratios are omitted for this reason. The main differences are for specific reactions such as  $^{90}\text{Y}(n, \gamma)^{91}\text{Y}$  and  $^{90}\text{Y}(\beta^- \nu)^{90}\text{Zr}$ , which are no longer as sensitive. Both of these reactions inevitably lead to Zr. Even though the  $(n, \gamma)$  reaction bypasses  $^{90}\text{Zr}$ , it produces  $^{91}\text{Zr}$ , and Zr has several stable isotopes up to  $^{96}\text{Zr}$ . Overall, however, most reaction rates sensitive to the isotopic ratios are also sensitive to the elemental ratios. This is especially true for the  $(n, \gamma)$  reactions and  $\beta^-$ -decays of the  $^{86}\text{Rb}$  and  $^{85}\text{Kr}$  s-process branchings, as well as the  $^{13}\text{N}(n, p)^{13}\text{C}$  and  $^{14}\text{N}(n, p)^{14}\text{C}$  neutron poisons.

An illuminating result comes from the probability densities of the final elemental abundances in the form of Eqn. 3.1, calculated relative to solar system abundances. This equation is used for each reaction network sample to determine the range of possible [Rb/Sr] and [Rb/Zr] ratios, as well as Rb abundances ([Rb/Fe]) resulting from simultaneously sampling every reaction rate uncertainty. Figure 3.7 showcases these results, where the  $x$ -axis is in terms of dex. By definition, 0 dex implies that the ratio consists of relative solar system abundances. The initial Rb, Sr, and Zr isotopic mass fractions were all given relative solar system abundances. The initial [Rb/Sr] and [Rb/Zr] ratios were therefore roughly 0 dex, and

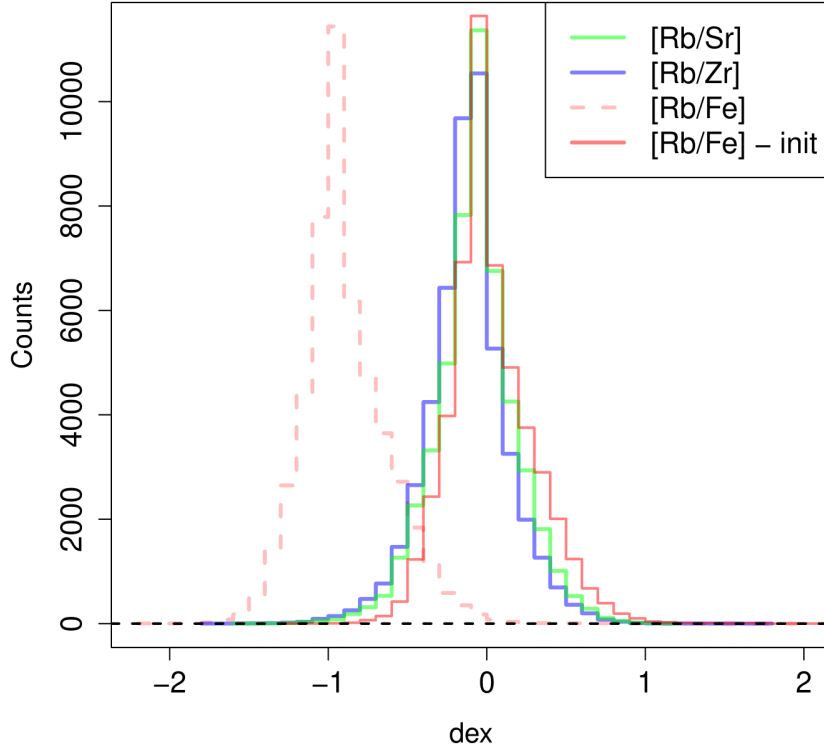


Figure 3.7: Probability densities of the  $[{\rm Rb/Sr}]$  (green),  $[{\rm Rb/Zr}]$  (blue) and  $[{\rm Rb/Fe}]$  (red, dashed) abundance ratios resulting from the Monte Carlo reaction network calculation for  $5 \times 10^4$  samples at  $T = 300$  MK,  $\rho = 10^3$  g/cm $^3$ , and  $X_{\text{last}}({}^4\text{He}) = 0.7$ , with  $X_{\text{init}}({}^4\text{He}) = 0.75$ . The solid red probability density was obtained by correcting  $[{\rm Rb/Fe}]$  for its enhanced  ${}^{56}\text{Fe}$  initial mass fraction relative to solar system abundance. In the legend, “init” refers to the initial value of  $[{\rm Rb/Fe}]$  before the network calculation (see text).

the figure shows that there was little overall change in these relative abundances after the Monte Carlo network calculation.

However, the initial  ${}^{56}\text{Fe}$  mass fraction was enhanced from its solar system value (see Table A.1). The initial  $[{\rm Rb/Fe}]$  abundance before the calculation was -0.918 dex. Assuming this variation from initial solar system abundances did not play a significant role in the nucleosynthesis, the  $[{\rm Rb/Fe}]$  probability density can be corrected to account for its initial -0.918 dex value. This assumption was tested in an additional Monte Carlo network calculation for  $10^3$  samples with an initial solar system  ${}^{56}\text{Fe}$  mass fraction. No significant differences were found in both the elemental and isotopic mass fraction ratio probability densities. Hence, the  $[{\rm Rb/Fe}]$  probability density has been translated by +0.918 dex in Fig. 3.7. This corrected  $[{\rm Rb/Fe}]$  result shows that the Rb abundance has increased slightly ( $\sim +7\%$ ).

Table 3.2: Percentiles from  $-2\sigma$  (2.5%) to  $+2\sigma$  (97.5%) of the [Rb/Sr], [Rb/Zr], and [Rb/Fe] probability densities from the present Monte Carlo reaction network calculation.

	2.5%	16%	50%	84%	97.5%
[Rb/Sr]	-0.594	-0.301	-0.061	0.167	0.468
[Rb/Zr]	-0.667	-0.348	-0.112	0.098	0.418
[Rb/Fe]	-0.442	-0.206	-0.016	0.288	0.622

The median,  $\pm 1\sigma$  percentiles (84% and 16%), and  $\pm 2\sigma$  percentiles (97.5% and 2.5%) of the [Rb/Sr], [Rb/Zr], and [Rb/Fe] probability densities are listed in Table 3.2. Comparing to the s-process nucleosynthesis models of Refs. [Kar12, Raa12, Kar16, Pig16] in Fig. 3.2, the [Rb/Fe] and [Rb/Zr] probability densities of the present analysis span most of these models, within  $\pm 2\sigma$ . This is illustrated in Fig. 3.8, where the median probability densities of the present analysis are represented by the dotted lines, and the  $1\sigma$  and  $2\sigma$  ranges are depicted by the dark and light bands, respectively. For the [Rb/Zr] ratio, the only models with significant tension compared to the present probability density are those that use an artificially delayed superwind (green and red) to enhance the Rb production. These models are also well outside of the bands for the [Rb/Fe] abundance, as are some of the models with very large rubidium production.

The main purpose of Fig. 3.8, however, is not to show how well the present Monte Carlo nuclear reaction network calculation reproduces the other models. Rather, the purpose is to show the approximate uncertainty that is inherent in each model, resulting from reaction rate uncertainties alone. These models were each calculated from a single network calculation using median reaction rates. If the reaction rates were sampled within their uncertainties, as in the present analysis, the resulting [Rb/Fe] and [Rb/Zr] ratios would span a similar range. Assuming the present uncertainties can be applied equally to each model, it becomes difficult to compare between specific models. On top of this, additional uncertainties result from the AGB model parameters as well.

Like the other models, this reaction rate sensitivity study does not reproduce the largest observed [Rb/Zr] ratios, even at the 97.5% ( $+2\sigma$ ) value. However, assuming the uncertainty from the present analysis can be applied to the model with the largest [Rb/Zr] ratio, the red model at  $M = 5M_{\odot}$ , the  $+2\sigma$  uncertainty does reproduce the largest observed [Rb/Zr] ratio at 1.05 dex. This situation is represented by the red uncertainty bars added to this model in Fig. 3.8. Hence, the rubidium problem could be resolved if the most sensitive reaction rates found from this analysis in Table 3.1 were significantly altered within their uncertainty. Although this is unlikely to be the case, the addition of model parameter uncertainties could

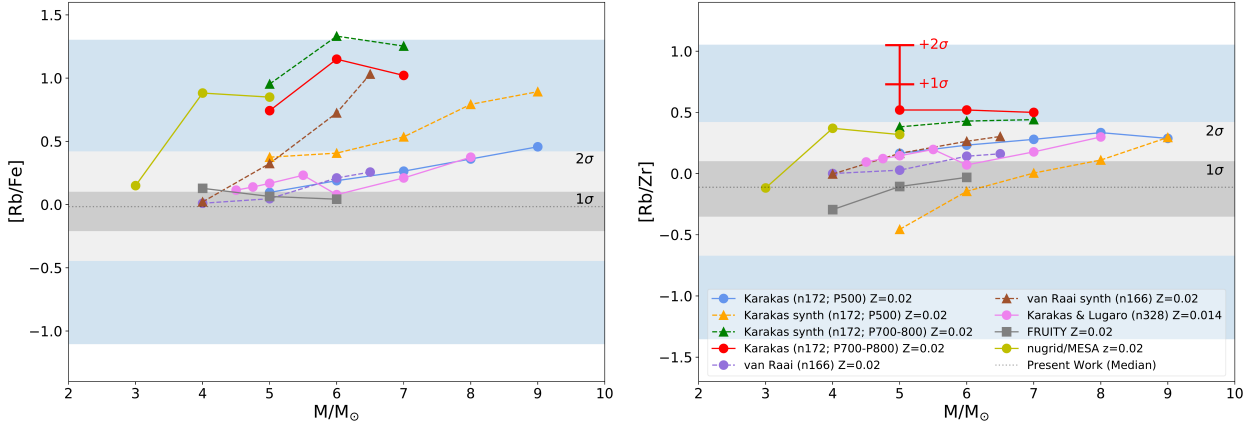


Figure 3.8: The  $[Rb/Fe]$  and  $[Rb/Zr]$  probability densities from the present Monte Carlo nuclear reaction network calculation plotted with the AGB model data of Refs. [Kar12, Raa12, Kar16, Pig16] and the (blue) observation scatter of Ref. [Per17]. The median probability densities are shown by the dotted lines, while the  $1\sigma$  and  $2\sigma$  bands are represented by the dark and light bands, respectively. The  $+1\sigma$  and  $+2\sigma$   $[Rb/Zr]$  probability density values are shown added to the model with the largest  $[Rb/Zr]$  value. This depicts the likelihood of reaction rate uncertainties alone being responsible for reproducing the largest observed  $[Rb/Zr]$  ratios.

make this situation more feasible.

### 3.4.3 Discussion

As mentioned in Refs. [Raa12, Per17], a potential scenario that may offer an explanation for the remaining  $[Rb/Zr]$  discrepancies is that Zr could be condensed into dust in the stellar atmosphere. Observations sample the gas around a star, not the dust. Therefore, if Zr is depleted by condensing into dust, and Rb is not, this could be the mechanism behind these high observed  $[Rb/Zr]$  ratios. In fact, Zr has a condensation temperature over twice as large as Rb [Raa12], making it easier to condense. Models of dust formation could offer a solution.

One area that the present analysis did not cover is the sensitivity of systematic reaction rate variations. Sampling the reaction rates within their uncertainties assumes those uncertainties are properly described. If some of the key rates, e.g. the neutron sources  $^{13}C(\alpha, n)^{16}O$  and  $^{22}Ne(\alpha, n)^{25}Mg$  were systematically altered beyond their established uncertainties, the discrepancy might be explained. Unknown systematic uncertainties are often associated with experimentally constrained reaction rates, so this should be a topic of investigation in the future.

### 3.5 Conclusions

The “rubidium problem” was investigated with the results of a Monte Carlo reaction network calculation, where every reaction rate in the network was sampled simultaneously within its own uncertainty. Final abundance probability densities were extracted for the key nuclei affected by the  $^{86}\text{Rb}$  and  $^{85}\text{Kr}$  s-process branchings. Ratios of  $^{87}\text{Rb}/^{86}\text{Sr}$  and  $^{87}\text{Rb}/^{90}\text{Zr}$ , sensitive to the efficiency of the branchings, were found to be correlated with several key reaction rates. Namely,  $^{86}\text{Rb}(n, \gamma)^{87}\text{Rb}$ ,  $^{13}\text{N}(n, p)^{13}\text{C}$ , and  $^{14}\text{N}(n, p)^{14}\text{C}$  were the 3 reaction rates found to be most correlated with these ratios, indicating that these rates are significant to s-process nucleosynthesis and Rb abundance in particular. The other  $(n, \gamma)$  reactions and  $\beta^-$ -decays associated with the  $^{86}\text{Rb}$  and  $^{85}\text{Kr}$  s-process branchings were also found to be significant. However, the neutron sources  $^{13}\text{C}(\alpha, n)^{16}\text{O}$  and  $^{22}\text{Ne}(\alpha, n)^{25}\text{Mg}$  were found to not be correlated with Rb abundance. This does not mean that neither of these sources were activated, but it does suggest that their rate uncertainties are not significant in altering s-process nucleosynthesis at  $T = 300$  MK, the transition temperature determining the dominant neutron source.

The [Rb/Zr] probability density from the present Monte Carlo reaction network was mostly found to be in agreement with that of the models from Refs. [Kar12, Raa12, Kar16, Pig16], except for the cases where Rb abundance was artificially enhanced. The large width of the [Rb/Zr] probability density shows that comparison between models is difficult, because each model should have a similar uncertainty resulting from reaction rate uncertainties alone. This problem is exacerbated when considering the additional stellar model parameter uncertainties. Assuming the uncertainty from the present analysis can be applied to the model with the largest [Rb/Zr] ratio, its  $+2\sigma$  value would reproduce the largest observed [Rb/Zr] ratio at 1.05 dex. Hence, if the most sensitive reaction rates found from this analysis were significantly altered within their uncertainty, the rubidium problem could be resolved, especially considering model parameter uncertainties and potential condensation of Zr into dust.

## CHAPTER

# 4

## $^{39}\text{K}(p, \gamma)^{40}\text{Ca}$ CONSTRAINTS FOR GLOBULAR CLUSTER NGC 2419

### 4.1 Introduction

This chapter details the original research constraining hydrogen-burning conditions responsible for abundance anomalies in the globular cluster NGC 2419. In particular, the observed potassium enrichment and magnesium depletion of red giants of NGC 2419 is reproduced with nuclear reaction network calculations using new nuclear physics information presented in this chapter. A new reaction rate of the key potassium-destroying reaction,  $^{39}\text{K}(p, \gamma)^{40}\text{Ca}$ , is calculated from the new proton partial-widths and resonance energies of astrophysically-important, proton-unbound  $^{40}\text{Ca}$  states measured in the proton-transfer reaction  $^{39}\text{K}({}^3\text{He}, d)^{40}\text{Ca}$ . The reaction rate is significantly constrained for  $T \lesssim 110$  MK. Reaction network calculations will show new temperature-density constraints for hydrogen-burning, compared with that of the previously calculated reaction rate. Hot-bottom burning in Super-AGB stars is investigated as a polluter candidate driving the Mg–K anticorrelation in NGC 2419.

### 4.2 NGC 2419 and the Mg–K Anticorrelation

The O–Na anticorrelation is ubiquitous in globular clusters, as stated in Section 1.4. However, there are other abundance patterns that are unique to individual or a small subset of globular clusters. The globular cluster NGC 2419 was recently found to exhibit some puzzling

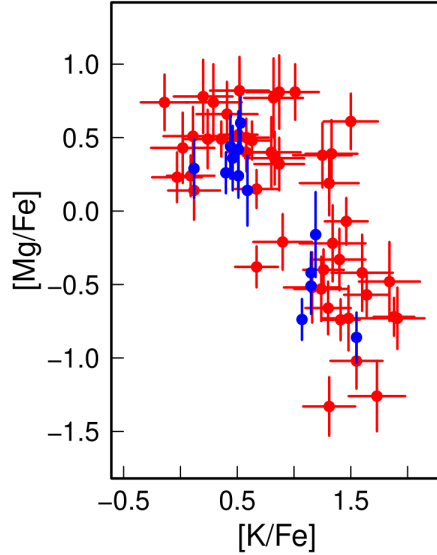


Figure 4.1: The observed Mg and K elemental abundances of red giants in NGC 2419 from Refs. [Muc12] (red) and [Coh12] (blue). Figure adapted from [Ili16].

abundance patterns. About 30% of the red giants observed show a strong K enrichment correlated with a considerable Mg depletion [Muc12, Coh12]. Fig. 4.1 shows the observed elemental potassium and magnesium abundances, with respect to iron, for the red giants in NGC 2419 sampled by Ref. [Muc12] in red and Ref. [Coh12] in blue. This was the first discovery of a Mg–K anticorrelation in any globular cluster. Only one other cluster to date, NGC 2808, has exhibited such an anticorrelation in a small portion of its stars [Muc15, Muc17], but the extent of the K enrichment is about 7 times less than that of NGC 2419. Meanwhile, the extent of the Mg depletion is about 3 times less. The evolutionary history of NGC 2419 must therefore be rather unique for it to exhibit such abundance patterns not seen in other globular clusters.

Just as the nucleosynthesis mechanism for the O–Na anticorrelation involves a series of  $(p, \gamma)$  reactions and radioactive decays, the same is true for the Mg–K anticorrelation. The hydrogen burning schemes are illustrated in Fig. 4.2. The Mg–Al cycle, shown on the left-hand side of the figure, starts from  $^{24}\text{Mg}$  at about 70 MK. After the subsequent  $^{24}\text{Mg}(p, \gamma)^{25}\text{Al}$  and  $^{25}\text{Al}(\beta^+ \nu)^{25}\text{Mg}$  reactions, there is a chance the  $^{26}\text{Al}^m$  isomer is populated. The isomer preferentially  $\beta^+$  decays to  $^{26}\text{Mg}$ , while the ground state  $^{26}\text{Al}^g$  preferentially captures a proton. Either scenario eventually synthesizes  $^{27}\text{Al}$ , which can repeat the cycle with  $^{27}\text{Al}(p, \alpha)^{24}\text{Mg}$  or proceed with  $^{27}\text{Al}(p, \gamma)^{28}\text{Si}$  if the temperature is more than about 80 MK. The overall effect is a depletion of magnesium and an enrichment of aluminum and silicon.

The hydrogen burning scheme for the K enrichment in NGC 2419 is illustrated on the

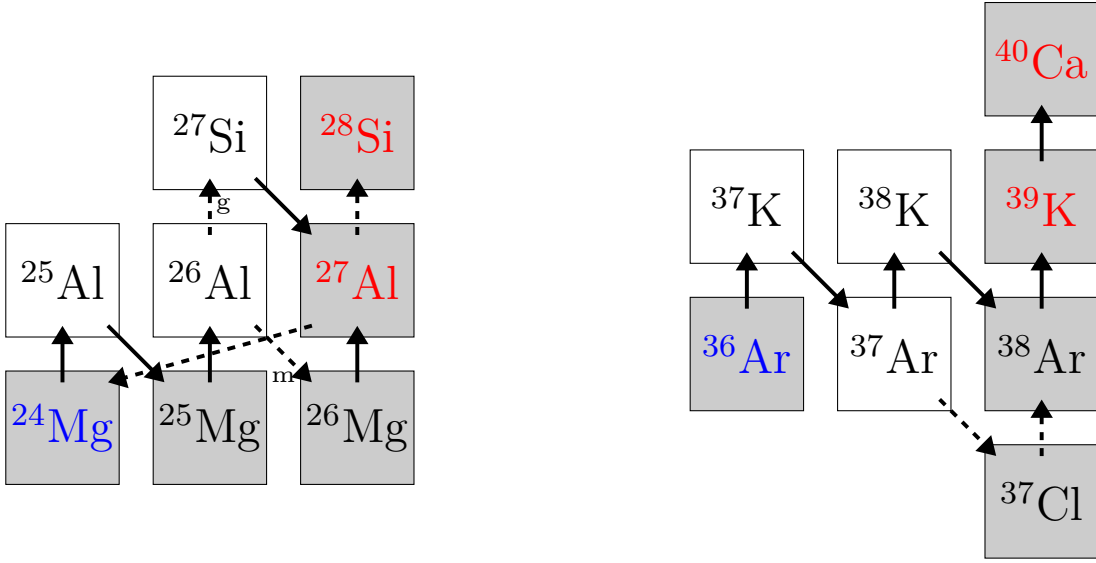


Figure 4.2: The hydrogen burning mechanism driving the Mg–K anticorrelation in the globular cluster NGC 2419. The nucleosynthesis chain for the Mg depletion is the Mg–Al cycle, shown on the left-hand side. Whether the  $^{26}\text{Al}^m$  isomer or the  $^{26}\text{Al}^g$  ground state is populated, the result is  $^{27}\text{Al}$  production, which repeats the cycle with  $^{27}\text{Al}(p, \alpha)^{24}\text{Mg}$ . The main nucleosynthesis chain for the K enrichment is shown on the right-hand side with solid arrows. The  $^{37}\text{Ar}(p, \gamma)^{38}\text{K}$  reaction proceeds at a much higher rate than  $^{37}\text{Ar}(e^-, \nu)^{37}\text{Cl}$  electron capture at the stellar densities of interest. Nuclides in blue are destroyed and nuclides in red are produced in the overall nucleosynthesis. Shaded nuclides are stable.

right-hand side of Fig. 4.2. It has been shown to start from  $^{36}\text{Ar}$ , an  $\alpha$ -nucleus and the most abundant argon isotope at the low metallicities of the first stellar generation [Ven12]. Some authors [Ven12, Muc15] have incorrectly claimed that the main K enrichment chain involves the decay of  $^{37}\text{Ar}$  to  $^{37}\text{Cl}$ , then the subsequent  $^{37}\text{Cl}(p, \gamma)^{38}\text{Ar}$  reaction, indicated by the dashed arrows in Fig. 4.2. However, as Ref. [Ili16] indicates, the  $^{37}\text{Ar}(p, \gamma)^{38}\text{K}$  reaction has a much larger decay constant than the electron capture reaction  $^{37}\text{Ar}(e^-, \nu)^{37}\text{Cl}$  at the stellar densities of interest. Therefore, the main chain must proceed to  $^{38}\text{K}$  before the subsequent  $^{38}\text{K}(\beta^+ \nu)^{38}\text{Ar}$  and  $^{38}\text{Ar}(p, \gamma)^{39}\text{K}$  reactions. The former chain is expected to contribute only marginally to  $^{39}\text{K}$  nucleosynthesis. Additionally, unlike the mechanisms for the O–Na anticorrelation and the Mg depletion, the sequence leading from  $^{36}\text{Ar}$  to  $^{39}\text{K}$  is not a cycle because the  $^{39}\text{K}(p, \alpha)^{36}\text{Ar}$  reaction has a much smaller decay constant than  $^{39}\text{K}(p, \gamma)^{40}\text{Ca}$ . However, as it will become clear in Section 4.2, the  $^{39}\text{K}(p, \gamma)^{40}\text{Ca}$  reaction rate is currently very uncertain in the astrophysical temperature range of interest.

The nucleosynthesis mechanism for the Mg–K anticorrelation may be well-established,

but the site of this nucleosynthesis is much more uncertain. Ref. [Ven12] were the first to propose polluter star candidates for the Mg–K anticorrelation in NGC 2419, as well as the other observed abundance patterns. Of consideration were massive AGB stars and Super-AGB (SAGB) stars of  $\sim 6 M_{\odot}$ , where hydrogen burning occurs during hot-bottom burning (HBB) at the base of the convective hydrogen envelope. Agreement was found with the observed intermediate K-enriched population only in an artificially optimized scenario. The  $^{38}\text{Ar}(p, \gamma)^{39}\text{K}$  reaction rate would need to increase by a factor of 100, and the poorly known mass loss rate in the AGB models would need to simultaneously decrease by a factor of 4. However, Ref. [Ven12] does not investigate the effect of varying other relevant reaction rates, which could have the same effect as increasing the  $^{38}\text{Ar}(p, \gamma)^{39}\text{K}$  rate.

Ref. [Ili16] expanded the search for polluter candidates by performing a Monte Carlo nuclear reaction network calculation that reproduced all of the observed abundances in NGC 2419, including the Mg–K anticorrelation. The parameters that were randomly sampled include the temperature  $T$ , density  $\rho$ , final hydrogen mass fraction  $X_{\text{H}}$ , all reaction rate probability densities in the network, and initial abundances.  $T$  and  $\rho$  were held constant for each network calculation. The reaction rates were obtained by truncating the Starlib [Sal13] library for the relevant rates. The resulting  $T$ – $\rho$  conditions that matched all of the observed abundances are shown by the blue dots in Fig. 4.3. A narrow band of possible  $T$ – $\rho$  conditions was found between  $\approx 80 - 260$  MK and  $\approx 10^{-4} - 10^8$  g/cm<sup>3</sup>, with additional solutions not shown in the figure up to 10<sup>11</sup> g/cm<sup>3</sup>. The black curves represent the  $T$ – $\rho$  hydrogen burning conditions of several polluter star candidates. These include the cores of 15  $M_{\odot}$  and 120  $M_{\odot}$  main sequence (MS) stars, the hydrogen-burning (H) shell of a 1  $M_{\odot}$  red giant star, hot-bottom burning of a 6  $M_{\odot}$  and 8  $M_{\odot}$  thermally-pulsing AGB and SAGB star, respectively, a 1.15  $M_{\odot}$  ONe classical nova (CN), and 0.8  $M_{\odot}$  and 1.0  $M_{\odot}$  CO classical novae. The only candidates that nominally overlap with this band are ONe and CO classical novae. However, another candidate Ref. [Ili16] considers is SAGB stars because of the large uncertainty in AGB stellar model parameters, such as the mass loss rate and the prescription of convective mixing. Adjusting these parameters within their current uncertainties could increase the temperature of HBB enough to match the observed abundances.

While Ref. [Ili16] simultaneously sampled the reaction rate probability densities of all the reactions in the network, they did not investigate the effect of individual reaction rates. Ref. [Der17] investigated the sensitivity of the acceptable  $T$ – $\rho$  conditions for NGC 2419 polluter stars on unknown systematic effects of individual reaction rates. Only 4 reactions were found to make a significant impact on the acceptable  $T$ – $\rho$  conditions,  $^{30}\text{Si}(p, \gamma)^{31}\text{P}$ ,  $^{37}\text{Ar}(p, \gamma)^{38}\text{K}$ ,  $^{38}\text{Ar}(p, \gamma)^{39}\text{K}$ , and  $^{39}\text{K}(p, \gamma)^{40}\text{Ca}$ . If the reaction rate of  $^{39}\text{K}(p, \gamma)^{40}\text{Ca}$ , for example, were systematically larger than its recommended rate, by even as little as a factor of 5, the

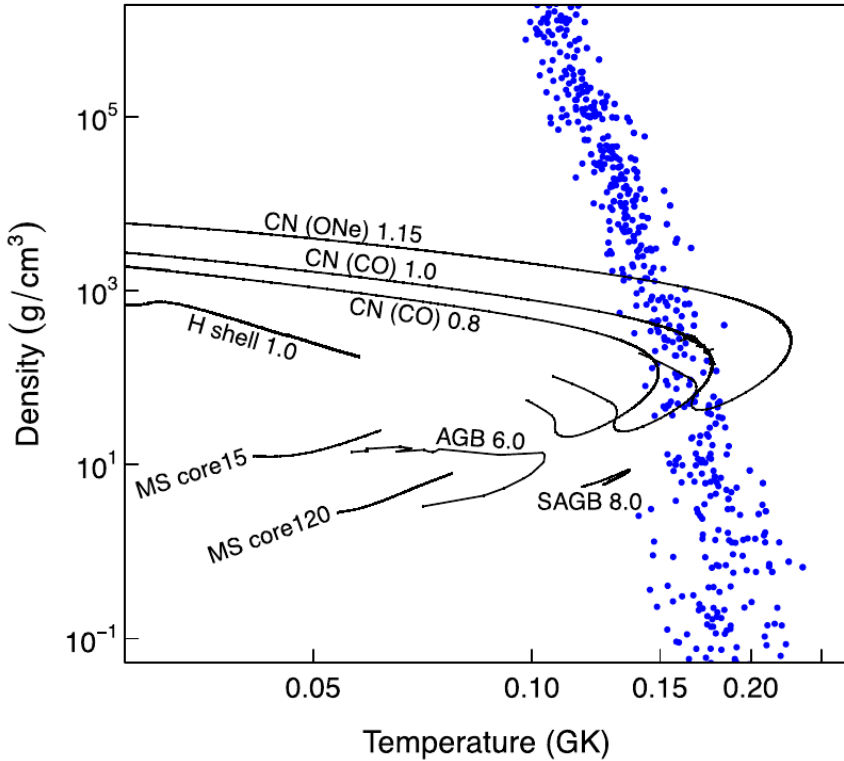


Figure 4.3: Temperature-density conditions reproducing the Mg–K anticorrelation and other abundance patterns in NGC 2419, obtained by sampling  $T$ ,  $\rho$ ,  $X_H$ , reaction rate probability densities, and initial abundances from a nuclear reaction network (see text). The  $T$ – $\rho$  conditions for several polluter star candidates are represented by the black curves. Adapted from Ref. [Ili16].

acceptable  $T$ – $\rho$  band would have significantly reduced scatter and would be constrained to the low-temperature side for all densities. This scenario is shown in Fig. 4.4 on the bottom-left panel, where the black dots represent the new rate multiplied by the indicated variation factor  $\alpha$ , and the red dots represent the recommended rate ( $\alpha = 1$ ). This makes sense in theory because potassium abundance would be reduced if the rate of its primary destruction reaction were increased. The high temperature conditions would therefore destroy too much potassium compared to its observed abundance. In contrast, if the rate were systematically smaller by a factor of 5, the solutions interestingly only have increased scatter. These same effects are also true for  $^{30}\text{Si}(p, \gamma)^{31}\text{P}$ , but the opposite is true for  $^{37}\text{Ar}(p, \gamma)^{38}\text{K}$  and  $^{38}\text{Ar}(p, \gamma)^{39}\text{K}$ , as these latter reactions increase the potassium abundance.

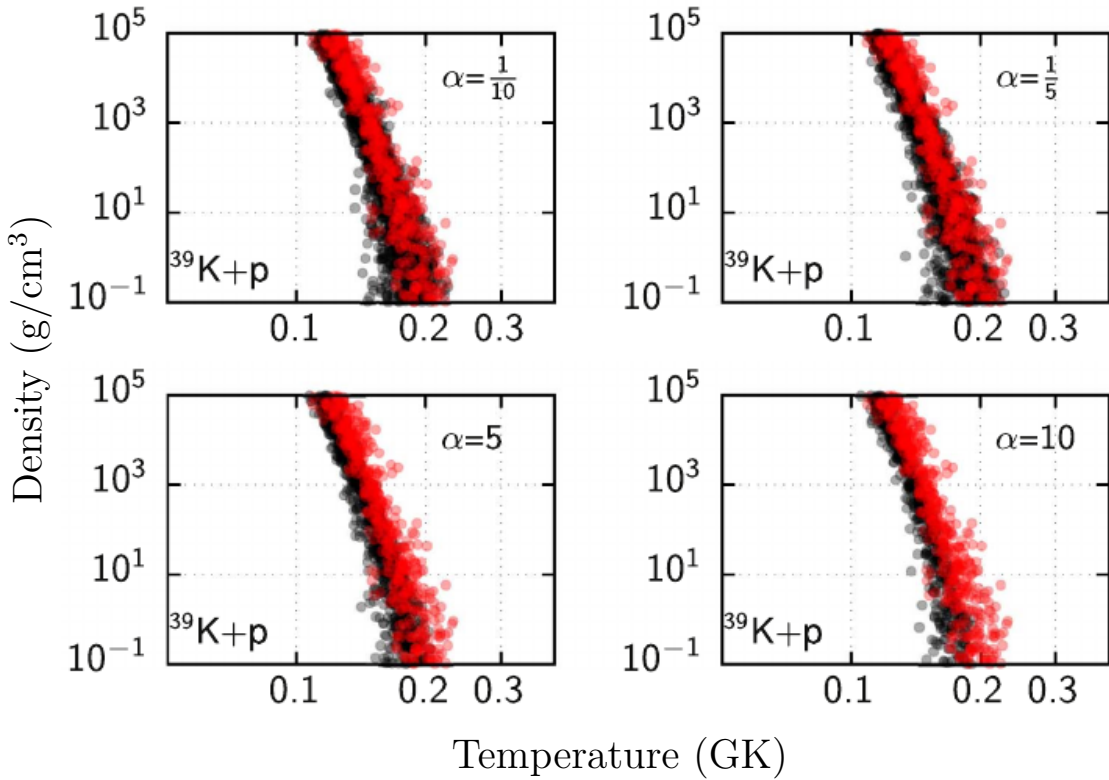


Figure 4.4: Systematic effects of the  $^{39}\text{K}(p, \gamma)^{40}\text{Ca}$  rate influencing temperature and density conditions. The indicated variation factors ( $\alpha = 1/10, 1/5, 5, 10$ ) are applied to the reaction rate in each panel, and the black dots show the resulting temperature-density conditions that provide an acceptable match with observed abundances. The red dots represent the case where no systematic effects ( $\alpha = 1$ ) have been added. Figure adapted from Ref. [Der17].

## 4.3 The Previous $^{39}\text{K}(p, \gamma)^{40}\text{Ca}$ Reaction Rate

The remainder of this chapter will focus specifically on the key potassium-destroying reaction  $^{39}\text{K}(p, \gamma)^{40}\text{Ca}$ , found by Ref. [Der17] to be one of the few important reactions able to constrain the potassium abundance in NGC 2419 and therefore constrain the possible  $T-\rho$  conditions of its polluter stars.

### 4.3.1 Longland *et al.* (2018) Evaluation

The most recent  $^{39}\text{K}(p, \gamma)^{40}\text{Ca}$  reaction rate evaluation is that of Ref. [Lon18b], which Ref. [Der17] used while it was in preparation. Its probability density was calculated using a Monte Carlo reaction rate formalism [Lon10] with resonance strengths and resonance energies provided by the direct measurements of Refs. [Kik90, Che81, Lee66]. The lowest directly measured resonance strength from these experiments is for the resonance at  $E_r^{\text{c.m.}} = 606$

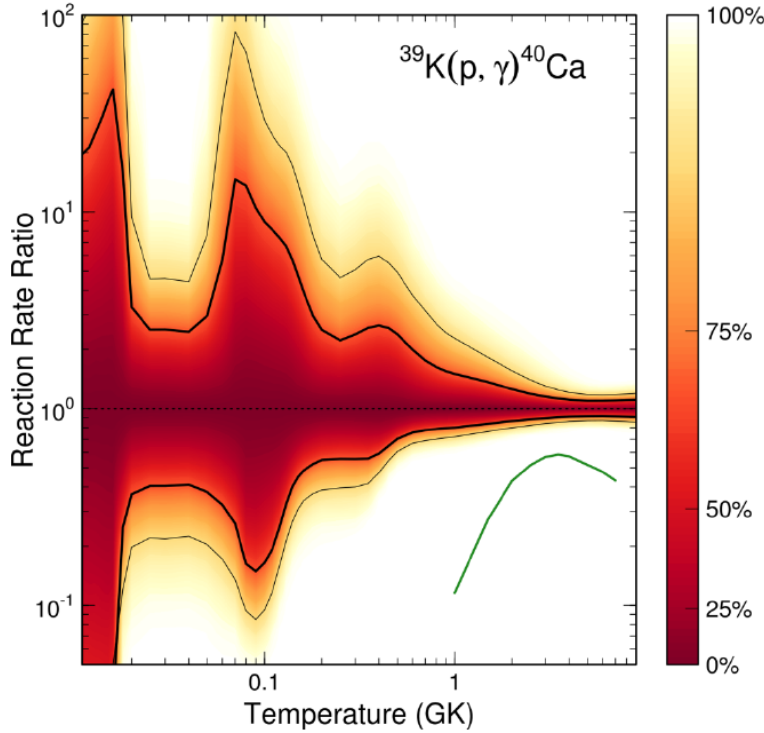


Figure 4.5: The recent  $^{39}\text{K}(p, \gamma)^{40}\text{Ca}$  reaction rate probability density calculation of [Lon18b] as a function of temperature. The median, recommended rate is shown as the dotted normalization line. The thick and thin black lines represent the 68% ( $1\sigma$ ) and 95% ( $2\sigma$ ) uncertainty bands, respectively. The color scale shows the continuous nature of the probability density, with darker red colors closer to the recommended rate. The green line represents the previous calculation of Ref [Che81].

keV. For resonances below this, indirect  $^{39}\text{K}({}^3\text{He}, d)^{40}\text{Ca}$  [Cag71] and  $^{39}\text{K}(d, n)^{40}\text{Ca}$  [Fuc69] proton-transfer measurements provided proton partial-widths, when available. Additionally, the indirect  $^{36}\text{Ar}({}^6\text{Li}, d)^{40}\text{Ca}$   $\alpha$ -transfer measurement of Ref. [Yam94] provided  $\alpha$ -particle partial widths for the  $(p, \alpha)$  channel, when available. Otherwise, measured or theoretical upper limits were given to the single particle reduced widths of the remaining resonances. These upper limits are described by the Porter-Thomas distribution [Por56, Wei09], truncated at the upper limit value in the case of measured upper limits. This provided a physically motivated probability density from which to sample unknown or upper-limit partial widths.

The reaction rate probability density evaluated by Ref. [Lon18b] is shown in Fig. 4.5. The reaction rate uncertainty is represented on the  $y$ -axis as a factor of the mean, recommended rate, which has been normalized to unity. The 68% ( $1\sigma$ ) and 95% ( $2\sigma$ ) uncertainty bands are represented by the thick and thin black lines, respectively, while the color scale indicates the continuity of the probability density. Clearly, the rate uncertainty is very large between about

$0.05 - 0.2$  GK ( $50 - 200$  MK), where the total  $1\sigma$  width peaks at a factor of 84 at about 80 MK. Recall from Section 4.2 that the astrophysically-relevant temperature range spanning the  $T-\rho$  band in Figs. 4.3 and 4.4 is  $\approx 80 - 260$  MK. The most recent  $^{39}\text{K}(p, \gamma)^{40}\text{Ca}$  reaction rate is therefore very uncertain in the astrophysical temperature range of interest. This is concerning, given that Ref. [Der17] found that the  $T-\rho$  conditions are sensitive to systematic variations in the  $^{39}\text{K}(p, \gamma)^{40}\text{Ca}$  rate, by even as little as a factor of 5. This motivates the necessity of constraining the  $^{39}\text{K}(p, \gamma)^{40}\text{Ca}$  rate, particularly for the contributing resonances between  $\approx 50 - 260$  MK.

### 4.3.2 Contributing Resonances

The  $^{39}\text{K} + p$  resonances that contribute to the reaction rate in the  $\approx 50 - 260$  MK range span resonance energies of  $E_r^{\text{c.m.}} \approx 90 - 450$  keV (See Section 2.3) and  $^{40}\text{Ca}$  excited state energies of about  $E_x \approx 8400 - 8800$  keV, where the most recent  $^{40}\text{Ca}$  proton separation energy measurement is  $S_p = 8328.18(2)$  keV from Ref. [Wan21]. This resonance energy range is below the lowest directly measured resonance at  $E_r^{\text{c.m.}} = 606$  keV ( $E_x = 8935$  keV), indicating that this region is entirely described by inferred transfer reaction partial widths or upper limits at present.

The contributing resonances from the reaction rate evaluation of Ref. [Lon18b] are shown in Fig. 4.6. The individual, fractional resonance contribution for each resonance is shown as a function of temperature. Measured resonances are shown with their  $1\sigma$  width, representative of the Monte Carlo formalism [Lon10] and are shaded or have hatched lines for clarity. Upper limit resonances are represented by dashed lines at their 84% ( $+1\sigma$ ) value. All resonances that individually contribute at least 20% to the total reaction rate are shown in the figure with corresponding resonance energy labels, while the remaining resonance contributions sum to the black line. Of note are the 96 keV, 156 keV, and 337 keV resonances, which overwhelmingly contribute to the reaction rate at their respective temperatures. The 337 keV resonance, in particular, is the most important resonance between  $\approx 0.15 - 0.4$  GK ( $150 - 400$  MK), which makes up most of the astrophysical temperature range of interest,  $80 - 260$  MK. However, the discrepancy between the 84% ( $+1\sigma$ ) contribution and the 16% ( $-1\sigma$ ) contribution is very large. The large uncertainty in the reaction rate around  $50 - 200$  MK in Fig. 4.5 is partly due to the uncertainty in this resonance contribution, but it is mostly a result of the many unknown resonances with only upper limit values between the 96 keV resonance and the 337 keV resonance.

Low-lying resonances at astrophysically-important proton energies are difficult to populate for  $^{39}\text{K}(p, \gamma)^{40}\text{Ca}$ , hence why the lowest directly measured resonance strength is that of the

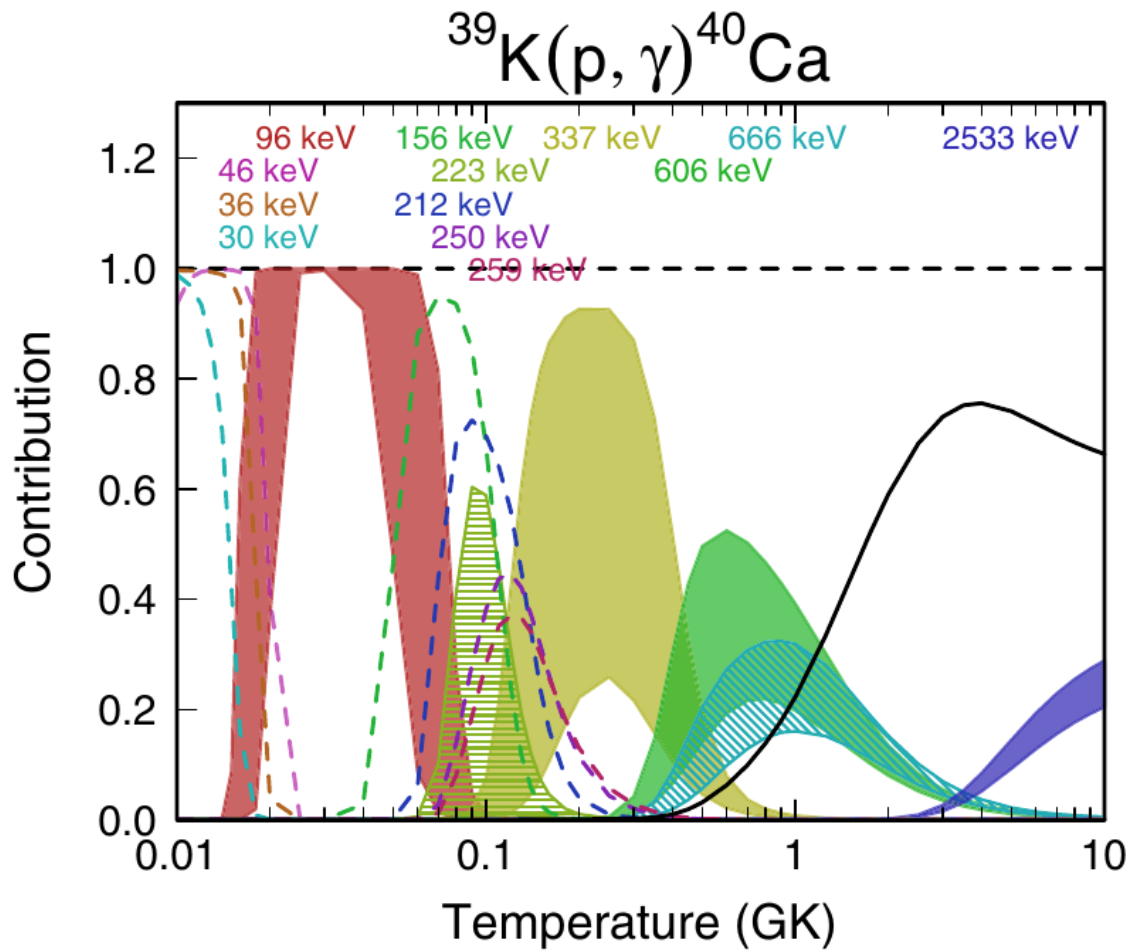


Figure 4.6: The individual resonance contributions to the  $^{39}\text{K}(p, \gamma)^{40}\text{Ca}$  reaction rate from Ref. [Lon18b] as a fraction of unity. Measured resonances are represented with shading or hatched lines and are shown with their  $1\sigma$  uncertainty bands. Resonances from upper limits are represented by dashed lines and show their 84% ( $+1\sigma$ ) value. The black line represents the total resonance contribution of all resonances that individually contribute less than 20% to the total reaction rate.

606 keV resonance. At energies lower than this, an alternative to populating these same states is to use proton-transfer reactions, such as  $(^3\text{He}, d)$  or  $(d, n)$ , which are not constrained by the Coulomb barrier in the same manner as  $(p, \gamma)$ . The  $^{39}\text{K}(^3\text{He}, d)^{40}\text{Ca}$  reaction was measured in this thesis for the purpose of constraining the  $^{39}\text{K}(p, \gamma)^{40}\text{Ca}$  reaction rate.

### 4.3.3 Previous Proton-Transfer Measurements

The previous  $^{39}\text{K}(^3\text{He}, d)^{40}\text{Ca}$  [Ers66, Set67, For70, Cag71] and  $^{39}\text{K}(d, n)^{40}\text{Ca}$  [Fuc69] proton-transfer measurements were not capable of achieving high resolution, particularly for unbound  $^{40}\text{Ca}$  states, i.e. at energies above the proton separation energy. The  $(^3\text{He}, d)$  measurements of Refs. [Ers66, Set67, Cag71] obtained spectroscopic factors ( $C^2S$ ) for only 2 unbound  $^{40}\text{Ca}$  states, with ENSDF [Che17] excitation energies of  $E_x = 8425$  keV ( $E_r^{\text{c.m.}} = 96$  keV) and 8551 keV ( $E_r^{\text{c.m.}} = 223$  keV), which are both below the lowest directly measured resonance at  $E_x = 8935$  ( $E_r^{\text{c.m.}} = 606$  keV). Meanwhile, Ref. [For70] did not observe unbound  $^{40}\text{Ca}$  states due to their focus on lower energy excited states. The  $(d, n)$  measurement of Ref. [Fuc69] obtained  $C^2S$  for 14 unbound  $^{40}\text{Ca}$  states, with only 4 of these states below the lowest directly measured resonance, including 8359 keV ( $E_r^{\text{c.m.}} = 30$  keV), 8425 keV ( $E_r^{\text{c.m.}} = 96$  keV), 8551 keV ( $E_r^{\text{c.m.}} = 223$  keV), and 8665 keV ( $E_r^{\text{c.m.}} = 337$  keV). Hence, there is an overlap between the  $(^3\text{He}, d)$  and  $(d, n)$  measurements of 2 unbound  $^{40}\text{Ca}$  states, 8425 keV ( $E_r^{\text{c.m.}} = 96$  keV) and 8551 keV ( $E_r^{\text{c.m.}} = 223$  keV). The  $^{39}\text{K}(p, \gamma)^{40}\text{Ca}$  reaction rate calculation of Ref. [Lon18b] used the  $C^2S$  measurements of Ref. [Cag71] for these 2 states, due to their more sophisticated coupled-channel DWBA calculations. They used the  $C^2S$  measurement of Ref. [Fuc69] for the 8665 keV ( $E_r^{\text{c.m.}} = 337$  keV) state. However, the reaction rate calculation did not include the 8359 keV ( $E_r^{\text{c.m.}} = 30$  keV)  $C^2S$  measurement of Ref. [Fuc69], as this state has an energy discrepancy with ENSDF [Che17] of 12 keV. This resonance was instead given an upper limit. Several unknown resonances remain below  $E_x = 8935$  keV ( $E_r^{\text{c.m.}} = 606$  keV). Ref. [Lon18b] uses upper limits for 18 resonances in this region. Hence, this was strong motivation to revisit the proton-transfer reaction at modern resolution to potentially resolve the currently unknown resonances.

## 4.4 The $^{39}\text{K}(^3\text{He}, d)^{40}\text{Ca}$ Experiment

The  $^{39}\text{K}(^3\text{He}, d)^{40}\text{Ca}$  experiment was performed in 2019 over 5 days using the Enge Split-Pole Spectrograph at the Triangle Universities Nuclear Laboratory (TUNL). The 10 MV FN tandem Van de Graaff accelerator at TUNL accelerated a fully-ionized  $^3\text{He}$  beam to  $E_{\text{lab}} = 21$  MeV, where the energy was stabilized using a pair of high-resolution slits between two  $90^\circ$

dipole magnets. The  $^{39}\text{K}(\text{He}, d)^{40}\text{Ca}$  proton transfer reaction and  $^{39}\text{K}(\text{He}, \text{He})^{39}\text{K}$  elastic scattering were measured separately between  $\theta_{\text{lab}} = 5 - 20^\circ$  and  $\theta_{\text{lab}} = 15 - 59^\circ$ , respectively, using the focal plane detector package described by Ref. [Mar19]. The  $d$  and  $^3\text{He}$  particles that were ejected from the target at the angle  $\theta_{\text{lab}}$  passed through the magnetic field  $B$  of the Enge Split-Pole Spectrograph, where they were then focused at a position along the focal plane, based on their magnetic rigidity  $B\rho$ . The focal-plane detector was preemptively moved via dual motors to align itself with the focal plane. Meanwhile, for every  $^{39}\text{K}(\text{He}, d)^{40}\text{Ca}$  or  $^{39}\text{K}(\text{He}, \text{He})^{39}\text{K}$  focal-plane measurement, elastic scattering was simultaneously measured with a silicon detector telescope inside the target chamber, positioned at a constant  $45^\circ$  from the beamline to monitor potential target degradation and other target properties.

#### 4.4.1 Targets

A total of 7 natural KI (93.26%  $^{39}\text{K}$ , 6.73%  $^{41}\text{K}$ ) targets were made throughout the course of the experiment, in 2 separate evaporation batches. The targets labeled KI #1, KI #2, and KI #3 were made in the first batch, while those labeled KI #4, KI #5, KI #6, and KI #7 were made in the second batch, on the second day of the experiment. For each batch, the targets were simultaneously produced by evaporating approximately  $75 \mu\text{g}/\text{cm}^2$  of natural KI onto aluminum target frames, each with a  $21 \mu\text{g}/\text{cm}^2$  natural carbon (98.84%  $^{12}\text{C}$ , 0.96%  $^{13}\text{C}$ ) foil backing. The KI target thickness was measured by a thickness monitor inside the evaporation chamber, placed at roughly the same distance from the evaporation material as were the aluminum target frames with carbon backings. Fig. 4.7 shows a photograph of the chamber just before the evaporation process, with 3 natural carbon targets in position. A separate  $21 \mu\text{g}/\text{cm}^2$  natural carbon target was also used in the experiment for calibrations with the  $^{12}\text{C}(\text{He}, d)^{13}\text{N}$ ,  $^{13}\text{C}(\text{He}, d)^{14}\text{N}$ , and  $^{16}\text{O}(\text{He}, d)^{17}\text{F}$  reactions, among other contaminants.

Potassium iodide is hygroscopic, meaning it will eventually oxidize at atmospheric pressure. To prevent this, care was taken to transport the targets from the evaporation chamber to the target chamber in a vacuum-sealed box at rough vacuum ( $\sim 10^{-2}$  torr), where they were then exposed to high vacuum ( $\sim 10^{-6}$  torr) for the remainder of the experiment. However, as will be described later, the first batch of targets (KI #1, KI #2, and KI #3) oxidized at some point during the first day of the experiment, for the  $\theta_{\text{lab}} = 5^\circ$  and  $7^\circ$  ( $^3\text{He}, d$ ) measurements. The focal-plane spectra for these runs, exclusively using the KI #1 target, consisted of peaks with high-energy tails, expected of targets that undergo oxidation [Lan44]. These angles were measured again toward the end of the experiment with the non-oxidized KI #6 target, but the oxidized KI #1 data was not discarded nevertheless. Section 4.5.2 details a novel technique for fitting these spectra, an example of which is shown in Section 4.4.5.



Figure 4.7: The evaporation chamber before the production of KI targets. The 3 targets shown in position become the KI #1, KI #2, and KI #3 targets after evaporation. The thickness monitor is also shown in position around a fourth opening in the 16-slot target holder.

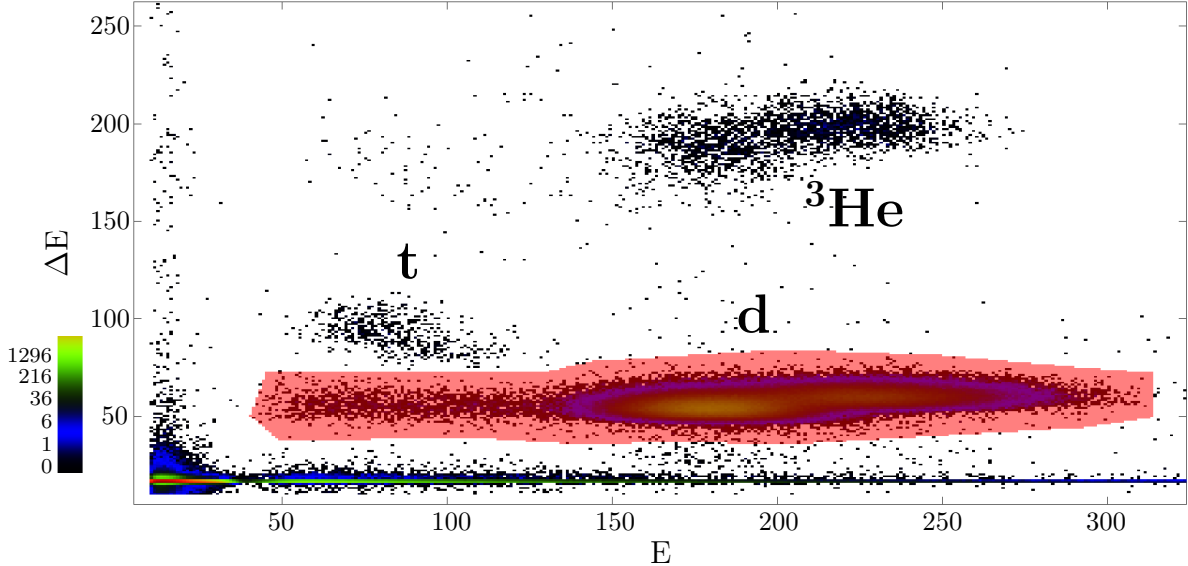


Figure 4.8: A 2D histogram of the focal-plane  $\Delta E$  vs  $E$  detector signals. Different groups correspond to different particles depending on their mass and charge. The deuteron group, highlighted in red, is being gated on in the figure.

#### 4.4.2 Focal-Plane Spectra

The focal-plane detector package (see Ref. [Mar19]) consists of two position-sensitive avalanche counters, one located in the front of the detector (P1 section) and one located near the back (P2 section), a gas proportionality counter ( $\Delta E$  section), and a residual energy scintillator ( $E$  section). The data acquisition system (DAQ) triggers on the  $E$  section, located at the back of the detector, so that coincidences with all sections are established. The combination of the  $\Delta E$  and  $E$  sections enables particle discrimination based on mass and charge, allowing a given particle to be gated on and therefore filtering out undesired particles and detector noise in other spectra. In the  $^{39}\text{K}(^{3}\text{He}, d)^{40}\text{Ca}$  experiment, the  $\Delta E/E$  spectrum was used to gate on the deuteron group for  $^{39}\text{K}(^{3}\text{He}, d)^{40}\text{Ca}$  and the  $^3\text{He}$  group for  $^{39}\text{K}(^{3}\text{He}, ^3\text{He})^{39}\text{K}$ . Figure 4.8 shows an example 2D histogram of  $\Delta E$  vs  $E$  in the offline `Jam` software package [Swa01, Swa02] for the KI #6 target at  $\theta_{\text{lab}} = 5^\circ$  and an Enge magnetic field of  $B = 1.14$  T. The  $d$ ,  $t$ , and  $^3\text{He}$  particles appear in groups, with the  $d$  group highlighted in red to represent a gate. The  $p$  group is joined by noise in the  $\Delta E$  detector below the  $\Delta E$  threshold and are filtered out along with the other particle groups. Both the  $\Delta E$  and  $E$  signals are compressed from their original 4096 channels to 512 channels in the 2D spectrum.

The 1D histogram of the P1 section, gated on the deuteron group of Fig 4.8, is shown in Fig. 4.9 in red. The overlayed black spectrum is from a carbon target to show overlapping peaks, indicating contaminants in the KI target. The deuteron peaks shown only in red were

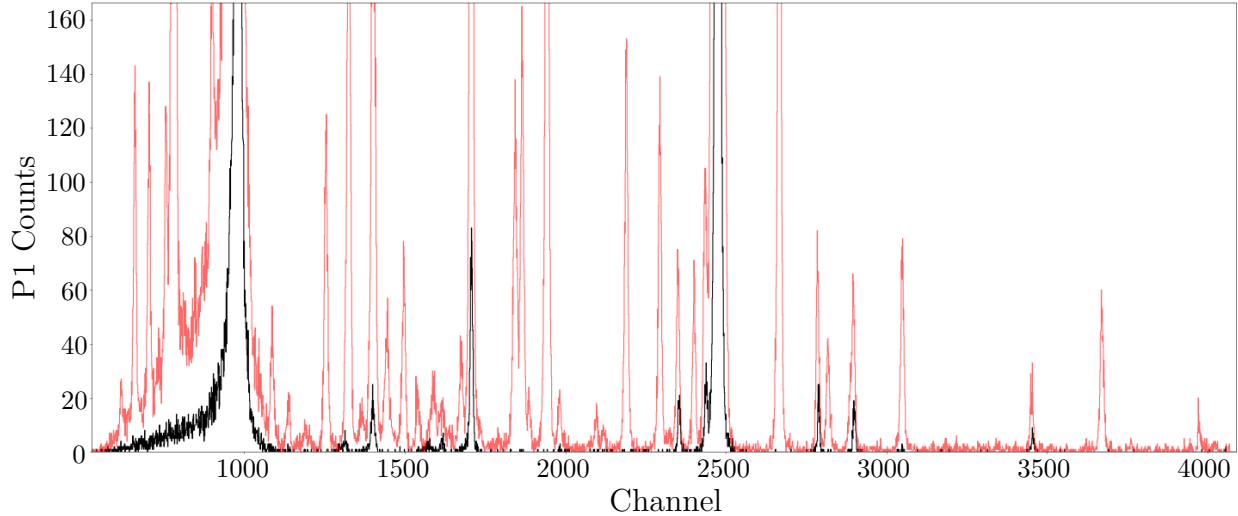


Figure 4.9: A histogram spectrum of the front (P1) focal-plane detector position section at  $\theta_{\text{lab}} = 5^\circ$  and  $E_{\text{lab}} = 21$  MeV with the KI #6 target (in red) and the carbon target (in black), both gated on the deuteron group from the the  $\Delta E$  vs.  $E$  spectrum. Overlapping peaks indicate contaminants.

ejected from  $^{39}\text{K}(^3\text{He}, d)^{40}\text{Ca}$  reactions in the KI target, where different excited states of the  $^{40}\text{Ca}$  recoil nuclei were populated, resulting in different kinematics for each deuteron depending on the excited state. High-energy deuterons are associated with high-energy  $^{40}\text{Ca}$  excited states, and vice versa. The deuterons are momentum-separated by the Enge Split-Pole Spectrograph, focusing the higher energy ones on the left side of the position sections and the lower energy ones on the right side. Thus, the P1 channel number in Fig. 4.9 is inversely related to the  $^{40}\text{Ca}$  excited state energies. The same is true of the excited states from the contaminants.

#### 4.4.3 Energy Shifts

The P1 peak centroid positions typically remain constant over time. However, certain changes in the beam can introduce shifts in these positions, broadening the peaks over more channels than usual. For instance, adjusting the beam steerers or focusing elements at any point along the beamline can cause very slight kinematic differences to occur in the target. This is because the target material is never perfectly uniformly-distributed. Sometimes these differences in kinematics are large enough to cause a noticeable drift in the P1 spectrum. Retuning the beam between runs at the same Engle angle  $\theta_{\text{lab}}$  is the most common example of energy shifts, followed by switching between targets from a different evaporation batch. Any unintentional beam drift can also cause them, albeit usually to a lesser degree.

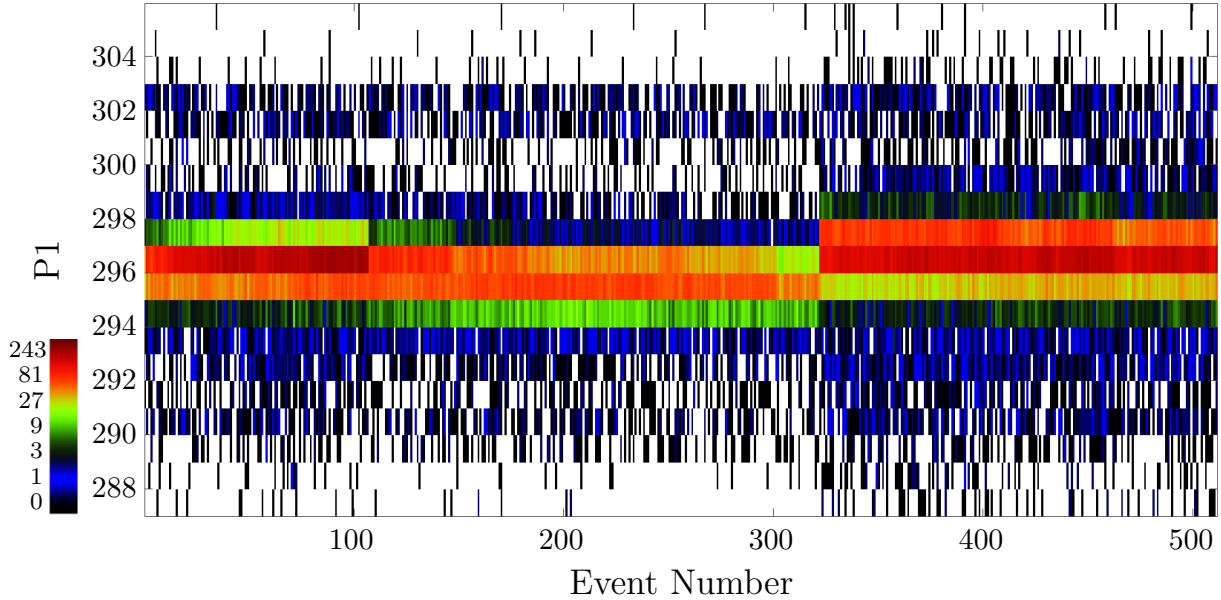


Figure 4.10: A 2D histogram of the front (P1) focal-plane position section vs event number over all  $^{39}\text{K}(^3\text{He}, d)^{40}\text{Ca}$  runs (#23 – #27) at  $\theta_{\text{lab}} = 9^\circ$  with the KI #5 target. Both axes are compressed to 512 channels. The P1 section is zoomed in on the  $^{13}\text{N}$  ground state to show the effect of energy shifts due to beam retunes. A beam retune after run #25 caused the shift in the P1 spectrum shown at event (bin) number 320. The unknown phenomenon at event (bin) number 100 occurred during run #23, which caused a reduction in counts but no energy shift.

To visualize these energy shifts, the P1 spectrum must be traced over time. This feature was recently added to the offline version of the `EngeSpec` [Lon19] graphical user interface (GUI), and I implemented the same feature in my local `Jam` source code. For each event, the P1 data is collected and the event number is recorded during the sort routine. The total number of events is unknown until the end of the sort routine, which unfortunately makes an online version of this feature nearly impossible. The 4096-channel P1 data and the corresponding event numbers are compressed into 512 bins, where they each get incremented into a 2D histogram.

There were a few instances of energy shifts during the  $^{39}\text{K}(^3\text{He}, d)^{40}\text{Ca}$  experiment. One happened due to a necessary beam-retune after a tour group was scheduled to view the tandem accelerator. The low-energy beamline Faraday cup was put in place for about an hour, and tuning was required to get the beam back on target. The runs before and after this retune are represented by the 2D histogram of P1 vs event number in Fig. 4.10. Depicted in the figure are the runs #23 – #27 at  $\theta_{\text{lab}} = 9^\circ$  with the KI #5 target. The P1 section is zoomed in on the  $^{13}\text{N}$  ground state, as it had the most counts and is therefore easiest to visualize

Table 4.1: Information on each run of the  $^{39}\text{K}(\text{He}, d)^{40}\text{Ca}$  experiment, including the angle of the Enge, the target used, the magnetic field of the Enge, and the sort group (see text).

Sort Group	$\theta_{\text{lab}}$ [°]	Run Numbers	Target	Enge Field [T]
1	5	9, 10	KI #1	1.14
2	5	11	KI #1	1.14
3	5	83 – 87	KI #6	1.14
4	7	15 – 20	KI #1	1.14
5	7	72, 75 – 78	KI #6	1.14
6	9	23	KI #5	1.145
7	9	24, 25	KI #5	1.145
8	9	26, 27	KI #5	1.145
9	11	31 – 33	KI #5	1.145
10	13	39 – 41	KI #5	1.145
11	13	42	KI #5	1.145
12	13	43, 44	KI #5	1.145
13	13	45, 47	KI #5, KI #6	1.145
14	15	55 – 59	KI #6	1.145
15	20	60, 61, 64	KI #6	1.145
16	20	65, 66	KI #6	1.145

energy shifts. The  $^{13}\text{N}$  ground state centroid starts at P1 bin number 296, and a clear shift to bin number 297 is seen at event number 320. A 1-bin shift in the 512-bin 2D spectrum corresponds to an 8-channel shift in the 4096-channel P1 spectrum, which was noticeable even during the experiment. Based on the BCI of each run, it was easy to determine that the shift happened between runs #25 and #26, exactly when the retune happened. This is also evident from the shift in counts at this point because more beam current was acquired as a result of the retune. There is also an unknown phenomenon just after event bin number 100, occurring during run #23. The peaks do not appear to be shifted from it, at least not as dramatically as from the retune, but it is clear that the beam current changed abruptly.

It would not be appropriate to sort all runs at  $\theta_{\text{lab}} = 9^\circ$  together for the  $^{39}\text{K}(\text{He}, d)^{40}\text{Ca}$  energy calibration and yield analysis. Because of the presence of energy shifts at some angles, it was necessary to group runs together based on where the energy shifts occurred. I refer to these groups as *sort groups*. All of the runs in the  $^{39}\text{K}(\text{He}, d)^{40}\text{Ca}$  experiment, as well as their sort groups, are shown in Table 4.1. Because there were 7 angles measured in this experiment ( $\theta_{\text{lab}} = 5^\circ, 7^\circ, 9^\circ, 11^\circ, 13^\circ, 15^\circ$  and  $20^\circ$ ), the ideal scenario would be to have 7 sort groups, 1 for each angle. However, there are 16 sort groups for various reasons, including beam retunes, switching targets, and the occasional beam noise from beamline element power supplies failing. In the case of sort group #13 at  $\theta_{\text{lab}} = 13^\circ$ , consisting of runs #45 and #47,

2 different targets are used between them, but they are from the same evaporation batch and therefore did not cause an energy shift. The  ${}^{39}\text{K}({}^3\text{He}, {}^3\text{He}){}^{39}\text{K}$  P1 spectra fortunately did not contain energy shifts because only a single run was needed per angle, and the same target (KI #7) was used for each run.

In the case of the  ${}^{39}\text{K}({}^3\text{He}, d){}^{40}\text{Ca}$  run #23 at  $\theta_{\text{lab}} = 9^\circ$ , and for a few other runs, the energy shift occurred during the run, not between runs. For this reason, it was also necessary to have the ability to gate on the P1 vs Event Number histogram for the entire area before or after a shift. I added this feature to both my local `EngeSpec` and `Jam` source codes. Only the events occurring in the gate are used in a new, event-gated P1 spectrum. Unfortunately, this means that the recorded BCI is no longer accurate. An approximation to the new, reduced BCI is to scale the original BCI by the fraction of events in the gate. This is not exact due to the loss of resolution when compressing the events into 512 bins, but it is more than sufficient considering the much larger uncertainty from the BCI measurement itself. The same fraction can be applied to the time-keeping scalars to correct for the new deadtime. The exact same gate is also used in these cases for the simultaneous silicon detector telescope spectra, as introduced in the next section, to ensure consistency with the reduced BCI and deadtime between the focal-plane and silicon detector spectra. This is essential for a relative measurement between the two detectors, as discussed in Section 4.6.4.

#### 4.4.4 Silicon Detector Telescope

To minimize the effects of uncertainty in the target thickness, non-uniformity in the target, and target degradation after exposure to the beam, the  ${}^{39}\text{K}({}^3\text{He}, {}^3\text{He}){}^{39}\text{K}$  elastic scattering and  ${}^{39}\text{K}({}^3\text{He}, d){}^{40}\text{Ca}$  proton-transfer yields from the focal-plane P1 spectra were normalized to the simultaneous  ${}^{39}\text{K}({}^3\text{He}, {}^3\text{He}){}^{39}\text{K}$  elastic scattering yield of a Si detector telescope positioned at a constant  $\theta_{\text{lab}} = 45^\circ$  inside the target chamber. The scale for the Si-normalized focal-plane differential cross-section measurements was then corrected using the global  ${}^3\text{He}$  optical model potential (OMP) differential cross-section for  ${}^{39}\text{K}$  from Ref. [Lia09] (see Sections 4.6.4 and 4.6.5). The scaling factor was the ratio between the differential cross-section of the global OMP and that of the Si-normalized focal-plane  ${}^{39}\text{K}({}^3\text{He}, {}^3\text{He}){}^{39}\text{K}$  measurements.

The silicon detector telescope consists of a  $\Delta E$  detector and a thicker, residual energy E detector, used in coincidence for particle discrimination in the same way as the  $\Delta E$  and E focal-plane detectors. A representative 2D  $\Delta E$  vs E histogram for the silicon detectors at  $\theta_{\text{lab}} = 45^\circ$  with the KI #6 target is shown in Fig. 4.11. As before, different groups correspond to different particles depending on mass and charge. The highlighted gate is around the  ${}^3\text{He}$  group. There are 4 regions in this group that are more dense than the background and that

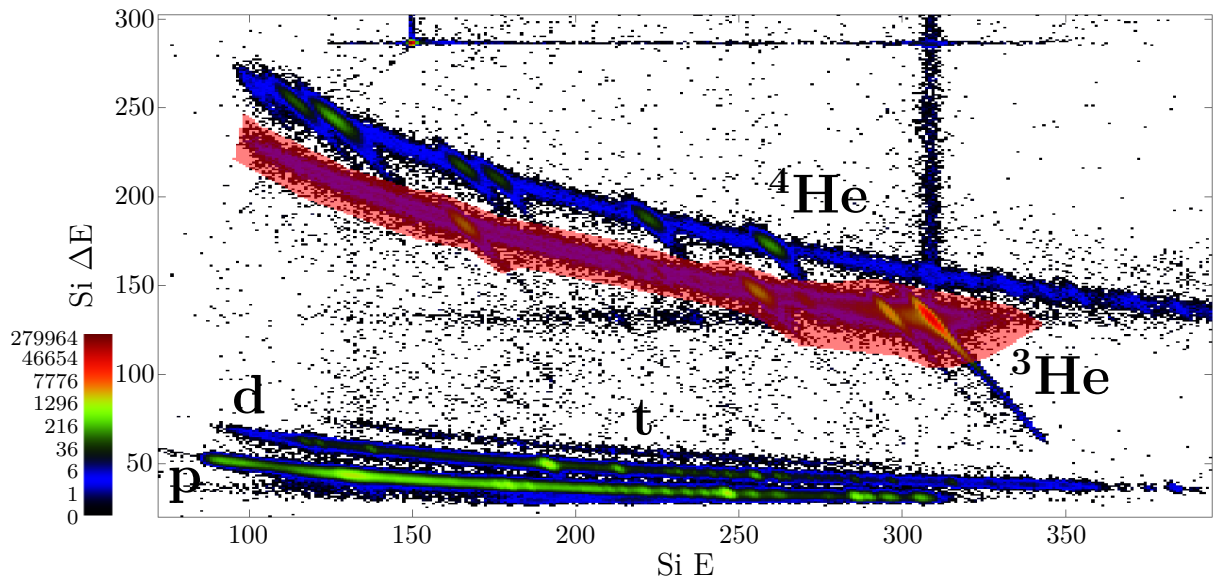


Figure 4.11: A 2D histogram of the Si  $\Delta E$  vs Si E detector signals. Different groups correspond to different particles depending on their mass and charge. The  $^3\text{He}$  group, highlighted in red, is being gated on in the figure.

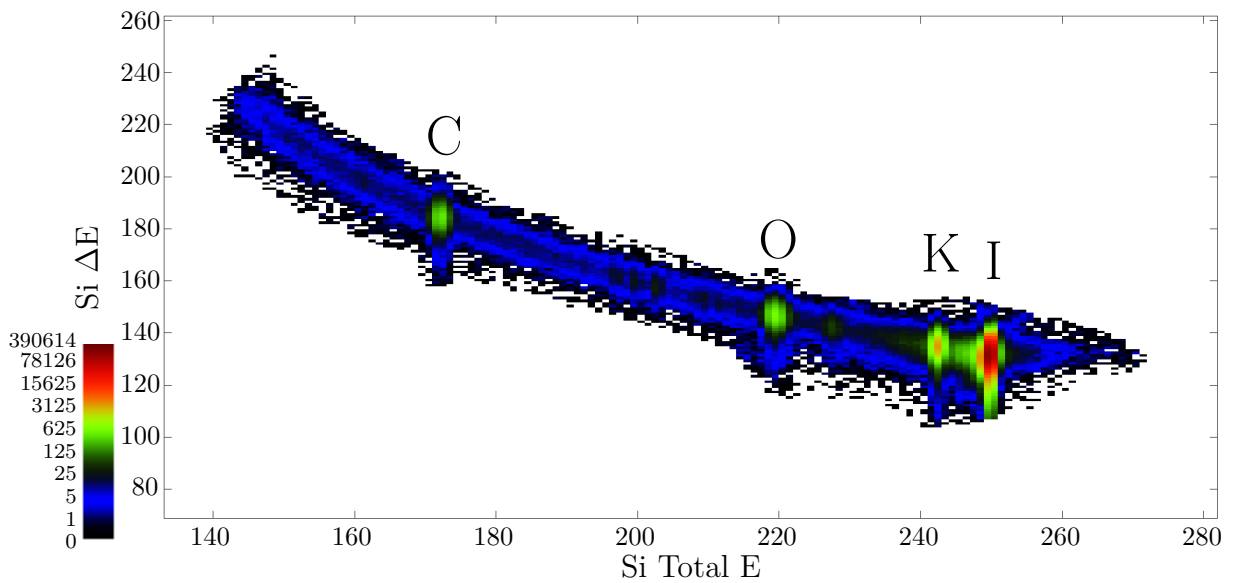


Figure 4.12: A 2D histogram of the Si  $\Delta E$  vs Si total E detector signals, gated on the  $^3\text{He}$  group and at  $\theta_{\text{lab}} = 45^\circ$ . This is similar to Fig. 4.11, except the total Si energy has been calculated based on the slope of the peaks in the Si  $\Delta E$  vs Si E spectrum (see Eqn. 4.1). Each peak is labeled with its corresponding elastic scattering element.

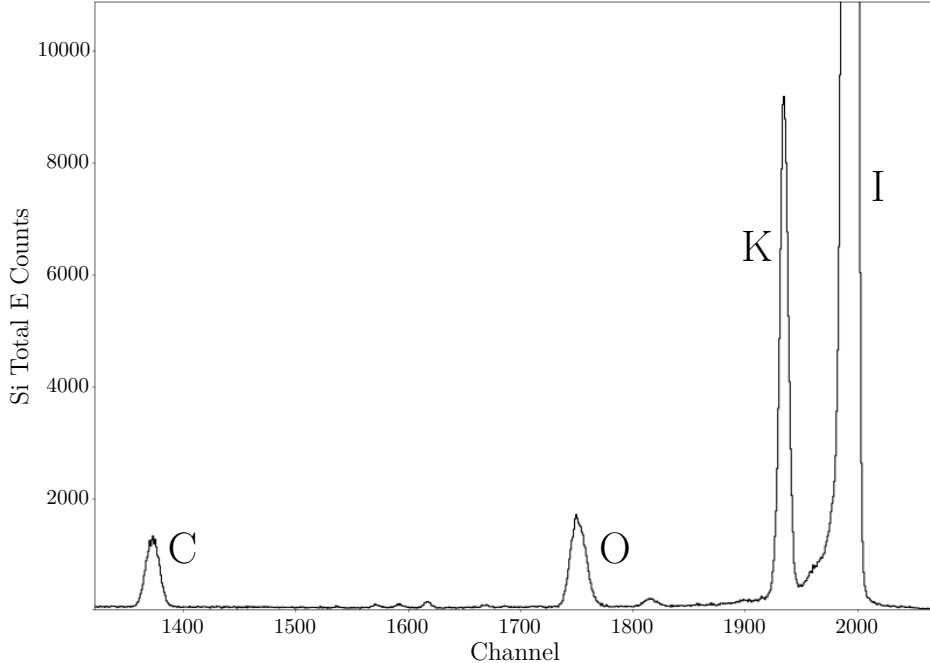


Figure 4.13: A histogram spectrum of Si Total E gated on the  ${}^3\text{He}$  group at  $\theta_{\text{lab}} = 45^\circ$ , obtained by projecting Fig. 4.12 onto its  $x$ -axis. Each peak is labeled with its corresponding elastic scattering element. The individual  ${}^{39}\text{K}$  and  ${}^{41}\text{K}$  isotopes are unresolvable.

have an even more negative slope than the trend of the overall group. These different regions correspond to scattering from different elements in the target. From left to right, they are carbon, oxygen, potassium, and iodine, as the more massive elements will deposit more energy in the Si E detector.

To obtain the  ${}^{39}\text{K}({}^3\text{He}, {}^3\text{He}){}^{39}\text{K}$  Si detector yield, the gated Si  $\Delta E$  vs Si E spectrum is first transformed. The regions corresponding to the individual scattering elements all have the same slope, and by rotating them so that they vertically align with the  $y$ -axis, they can be projected onto the  $x$ -axis to create a new 1D histogram with narrow peaks. This transformation is equivalent to finding the total energy deposited in the silicon detectors,

$$E^{\text{tot}} = \frac{E + p_{\text{Si}}\Delta E}{1 + p_{\text{Si}}}, \quad (4.1)$$

where  $p_{\text{Si}}$  is the Si slope parameter defined by the user in either `Engespec` or `Jam`. The transformed 2D Si  $\Delta E$  vs Si total E spectrum, gated on the  ${}^3\text{He}$  group, is shown in Fig. 4.12. The scattering elements are labeled with their element symbols. Finally, the projected 1D histogram for Si total E is presented in Fig. 4.13, where the potassium (K) peak can be seen on the shoulder of the iodine (I) peak. The yield of the potassium peak ideally remains constant

throughout the experiment, for a given target, since the Si detector telescope is positioned at a constant  $\theta_{\text{lab}} = 45^\circ$ . However, target degradation occurs naturally over time, decreasing the yield of both focal-plane and Si detector measurements. Hence, the normalization corrects for this, as well as the other unknown target properties.

One complication is the poor resolution between different isotopes for elastic scattering, especially at low angles. In the Si detectors, the potassium peak always consisted of  $^{41}\text{K}$  in addition to  $^{39}\text{K}$ , since a natural KI target was used. In the focal-plane P1 detector, which has better energy resolution, the elastic scattering  $^{39}\text{K}$  peak could be resolved only for  $\theta_{\text{lab}} \geq 40^\circ$ . The presence of  $^{41}\text{K}$  was corrected for in the differential cross-section calculations of  $^{39}\text{K}({}^3\text{He}, {}^3\text{He})^{39}\text{K}$  by taking into account both the isotopic abundance ratio of potassium (93.26%  $^{39}\text{K}$ , 6.73%  $^{41}\text{K}$ ) and the relative differential cross-sections of global  ${}^3\text{He}$  OMPs for  $^{39}\text{K}$  and  $^{41}\text{K}$ . The former contribution cancels out in the Si detector normalization for  $\theta_{\text{lab}} < 40^\circ$ , but provides a  $\sim 7\%$  increase in the differential cross section ratio for  $\theta_{\text{lab}} \geq 40^\circ$ . The latter contribution is almost negligible due to the similar theoretical angular distributions of both differential cross sections over the angles of interest.

#### 4.4.5 Oxidized Spectra

The KI #1 target was the first one to be used in the  $^{39}\text{K}({}^3\text{He}, d)^{40}\text{Ca}$  experiment at  $\theta_{\text{lab}} = 5^\circ$  and  $7^\circ$ . It was immediately clear that this target was producing peaks that were not gaussian in the focal-plane P1 spectra, as were the other targets in the first evaporation batch, KI #2 and KI #3. They were transported together and all placed in the target chamber simultaneously. At some point, they were presumably exposed to atmosphere suddenly or for an extended period of time, despite the care taken in transporting them to the target chamber in a sealed box at rough vacuum. The oxidized focal-plane P1 spectrum for all KI #1 runs (#15 – #20) at  $\theta_{\text{lab}} = 7^\circ$ , gated on the deuteron group, are shown sorted together in Fig. 4.14. The low-channel (high-energy) side of each peak has a tail that is potentially smeared over other nearby peaks. This makes fitting peaks very challenging for yield measurements, when high resolution is required. However, Bayesian Monte Carlo techniques were implemented to obtain yield measurements with realistic uncertainties from these runs, as presented in Section 4.5.2.

### 4.5 Bayesian Peak Fitting and Target Oxidation

The energy loss of light, charged particles through a medium is a statistical process. Particles with the same initial energy will traverse the same length in the medium with a distribution of final energies. This phenomenon is known as energy straggling and was theoretically

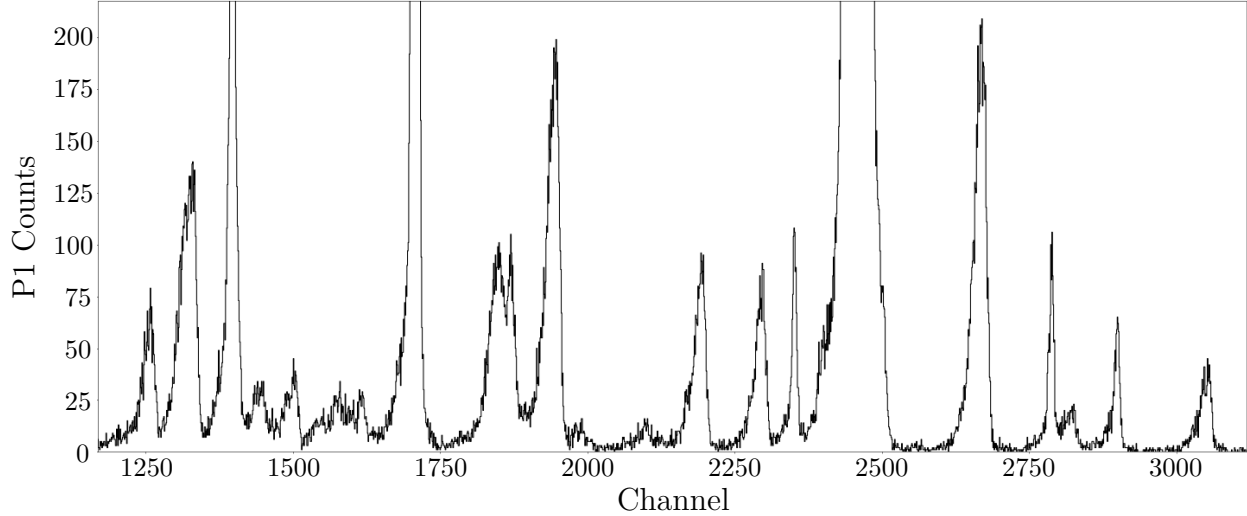


Figure 4.14: A histogram spectrum of the focal-plane P1 section at  $\theta_{\text{lab}} = 7^\circ$  with the KI #1 target, gated on the deuteron group. The peaks are clearly not gaussian because of the presence of high-energy (low-channel) tails, a result of oxidation in the KI #1 target.

described by Landau [Lan44]. Thin-film targets are ideal for high resolution spectral analysis because the energy loss distribution is approximately gaussian. Thick targets, however, alter the energy loss distribution in ways that present challenges to fitting peaks in a spectrum. Section 4.5.1 presents the Bayesian peak fitting procedure implemented in the analysis of the  $^{39}\text{K}(\text{He}^3, d)^{40}\text{Ca}$  experiment for the case of thin targets, and Section 4.5.2 presents a modified procedure for the case of thick targets, resulting from target oxidation which produces tails in the energy loss distribution.

### 4.5.1 Bayesian Peak Fitting

Transfer reaction analysis requires precise experimental cross section measurements for each relevant excited state of the residual nucleus. Each cross section is proportional to the yield of the transfer reaction populating the given excited state. An essential ingredient in the yield measurement, described in more detail in Section 4.6, is the number of counts of ejectile particles measured by the focal-plane detector. Each count contributes to a peak along the focal-plane spectrum corresponding to the given excited state with a finite width. The peaks are distinguished by their excitation energies, which are determined through an energy calibration based on their relative centroid positions along the focal-plane, as is done in Section 4.7.1. A typical transfer reaction spectrum will include many such peaks, as well as peaks from reactions in the target not necessarily of interest, known as contaminants. As mentioned in the introduction of this section, excited state peaks are typically gaussian-

distributed, assuming a thin-film target is used. The spectrum will also include background counts, represented by a straight line. A precise determination of the number of counts in a given peak, in the simplest case, is therefore done by fitting a gaussian with a background line.

The target for the  $^{39}\text{K}(^3\text{He}, d)^{40}\text{Ca}$  experiment was natural potassium iodine on a natural carbon film backing. The most prominent contaminants were from  $(^3\text{He}, d)$  reactions on  $^{12}\text{C}$ ,  $^{13}\text{C}$ ,  $^{14}\text{N}$ , and  $^{16}\text{O}$ , producing excited states from the residual nuclei  $^{13}\text{N}$ ,  $^{14}\text{N}$ ,  $^{15}\text{O}$ , and  $^{17}\text{F}$ , respectively. The chosen magnetic field of the Enge Split-Pole Spectrograph was such that deuterons from  $(^3\text{He}, d)$  reactions with iodine were not at all present along the focal-plane, and deuterons from  $^{41}\text{K}(^3\text{He}, d)$  were only minimally present. However, given the presence of the many other contaminants, and to distinguish doublets, triplets, and other multiplets, it was deemed necessary to use a more sophisticated technique to fit the peaks from this experiment than a simple chi-squared minimization. Bayesian Monte Carlo sampling was a natural choice, considering its realistic uncertainty handling and flexibility when dealing with non-gaussian fits, presented in Section 4.5.2. I used the `BayeSpec` [Lon18a] graphical user interface (GUI), along with custom Bayesian sampling routines described below, to acquire fits to the  $^{39}\text{K}(^3\text{He}, d)^{40}\text{Ca}$  data.

Most peaks from transfer reactions on a thin-film target are gaussian-distributed,

$$f(x; A, \mu, \sigma) = A \exp\left(-\frac{(x - \mu)^2}{2\sigma^2}\right), \quad (4.2)$$

where  $A$  is the peak intensity,  $\mu$  is its mean, and  $\sigma$  is its standard deviation. Bayesian sampling can be used to optimize these 3 parameters to match the focal-plane data if appropriate prior distributions are known. In this case, each prior distribution is approximately normal,  $\mathcal{N}(\mu_0, \sigma_0^2)$ , with its own mean  $\mu_0$  and standard deviation  $\sigma_0$ . Posterior distributions can then be computed from these priors to achieve parameter values with statistically realistic uncertainties that match the data. These more realistic uncertainties make it possible to handle difficult fitting scenarios that would normally cause problems for chi-square minimizations, such as distinguishing peaks in a multiplet with appropriate uncertainties.

Prior means  $\mu_0$  for  $A$  and  $\mu$  are particularly simple to obtain if the peak apex is visible. Even if it is not visible, as in the case of a multiplet, a guess can be made for each peak apex location,  $(x, y)$ , based on the curvature of their sum, where  $x$  is the mean guess and  $y$  is the intensity guess. Each guess is established by selecting a point using the `BayeSpec` GUI. The prior standard deviations  $\sigma_0$  for  $A$  and  $\mu$  are given constant values conservative enough for sampling to be successful in even the most uncertain cases. These can be adjusted by the user, but are typically left as their defaults, listed below.

The prior mean  $\mu_0$  and standard deviation  $\sigma_0$  for  $\sigma$  are ideally given constant values for a given reaction representative of most peaks from that reaction in focal-plane spectra. This is because energy loss is nearly equivalent for peaks with similar excitation energies from the same reaction, but it is not equivalent for peaks from different reactions. Therefore, peaks from each reaction should ideally have a shared  $\sigma$  prior and a shared  $\sigma$  posterior in a single fit if multiple peaks are fit simultaneously. In practice, a single  $\sigma$  prior can be used for different reactions if it is conservative enough for sampling to be successful, but the  $\sigma$  posteriors should remain different for different reactions.

A background line must also be included in the model, where its intensity  $y_{\text{bg}}$  and slope  $m_{\text{bg}}$  have their own  $\mathcal{N}(\mu_0, \sigma_0^2)$  priors. Put together, the prior distributions for gaussian peaks on a background line in a typical focal-plane spectrum are

$$\begin{aligned} A_i &\sim \mathcal{N}(y_i, 10.0^2) \\ \mu_i &\sim \mathcal{N}(x_i, 1.0^2) \\ \sigma &\sim \mathcal{N}(5.0, 1.0^2) \\ y_{\text{bg}} &\sim \mathcal{N}(\max(1, \min(d)), 0.1^2) \\ m_{\text{bg}} &\sim \mathcal{N}(0, 0.01), \end{aligned} \tag{4.3}$$

where  $\sigma$  is a constant prior for all reactions, but it can easily be adjusted by the user for different reactions if needed, and  $d$  refers to the focal-plane data in the specified fit range. The prior for  $m_{\text{bg}}$  can also be adjusted if the background line is clearly not horizontal. The model function to be fit is

$$f(x; A, \mu, \sigma, y_{\text{bg}}, m_{\text{bg}}) = \sum_i^N A_i \exp \left( -\frac{(x - \mu_i)^2}{2\sigma_j^2} \right) + \left( y_{\text{bg}} + m_{\text{bg}}(x - \min(x)) \right), \tag{4.4}$$

where  $N$  is the total number of gaussian peaks to be fit and  $\sigma_j$  refers to the shared standard deviation for peaks from reaction  $j$ .

The posterior computation in the custom Bayesian sampling routine uses the `quap` function in R, part of the Bayesian `rethinking` package [McE13]. This function finds a quadratic approximation to each full posterior distribution at its mode. It is less sophisticated than Markov Chain Monte Carlo, but its relative simplicity makes it a more efficient option to use with a GUI. The model composed of Eqns. 4.3 and 4.4 is provided to `quap`, which returns the posterior quadratic approximations with built-in uncertainties. Samples from these posteriors are then used to compute the area of each gaussian, given by  $\sqrt{2\pi} \sigma_j A_i$ , along with their uncertainties. A small number of posterior samples are also used to graphically display the gaussian fits, with different colors representing different reactions.

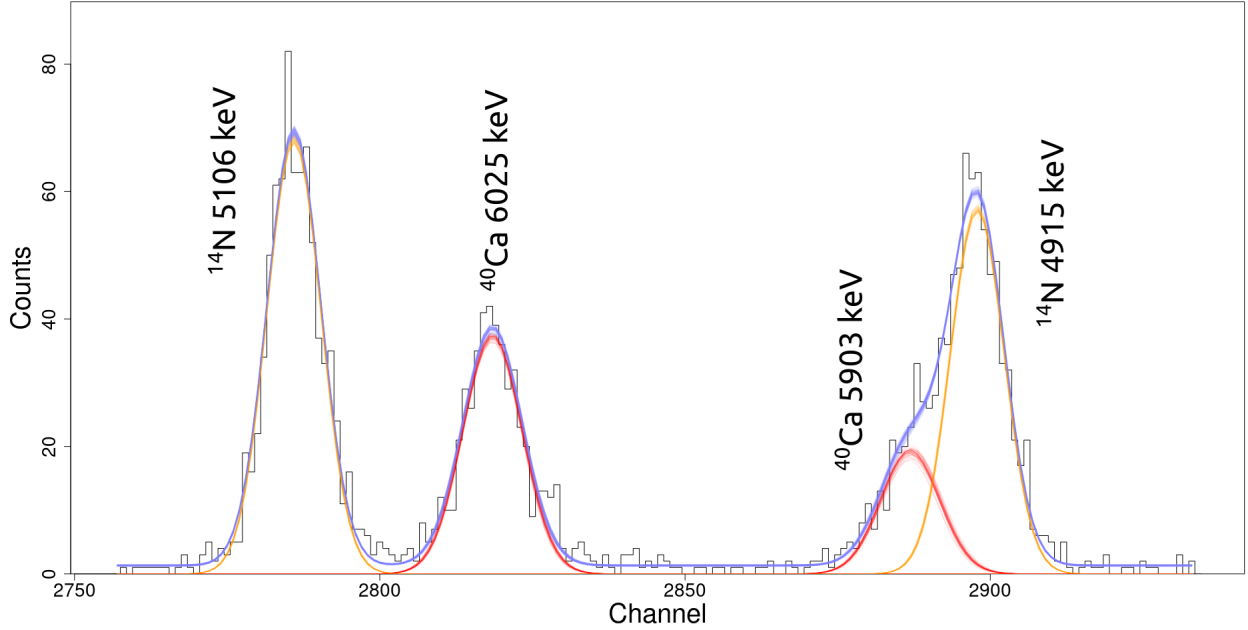


Figure 4.15: A Bayesian multi-gaussian fit with BayeSpec for the  $^{40}\text{Ca}$  excited states (in red) 6025 keV and 5903 keV from  $^{39}\text{K}(\text{He}, d)^{40}\text{Ca}$  and the  $^{14}\text{N}$  excited states (in orange) 5106 keV and 4915 keV from  $^{13}\text{C}(\text{He}, d)^{14}\text{N}$  at  $\theta_{\text{lab}} = 5^\circ$ . In red and orange are 50 random samples of the gaussian distributions from the  $\sigma$ ,  $\mu$ , and  $A$  posteriors for each peak. The  $^{40}\text{Ca}$  peaks share an identical  $\sigma$  posterior, while the  $^{14}\text{N}$  peaks share their own as well. In blue are the sums of the peaks plus the background line for each of those 50 samples.

Figure 4.15 shows an example of this Bayesian fitting procedure for a  $^{39}\text{K}(\text{He}, d)^{40}\text{Ca}$  focal-plane spectrum at  $\theta_{\text{lab}} = 5^\circ$ . Excited states of  $^{40}\text{Ca}$  are shown in red and  $^{14}\text{N}$  excited state contaminants are shown in orange. In blue is the sum of the gaussians and the background line, given by Eqn. 4.4. Each gaussian, as well as the blue curve, consists of 50 individual curves that were sampled from the posteriors to represent the uncertainties. The reason it is useful to combine these 4 peaks into one fit in this example is to better resolve the 5903 keV  $^{40}\text{Ca}$  state in red from the 4915 keV  $^{14}\text{N}$  state in orange in the double gaussian on the right side of the spectrum. The addition of the 6025 keV  $^{40}\text{Ca}$  peak in red and the 5106 keV  $^{14}\text{N}$  peak in orange on the left constrains the  $\sigma$  posteriors for the double gaussian. While this may seem like a minor correction, and it is minor in the present example, it is crucial in situations where the double gaussian or multiplet is otherwise impossible to resolve.

#### 4.5.2 Fitting Peaks with Target Oxidation

Potassium iodine is hygroscopic, meaning it easily absorbs moisture from the environment. When exposed to atmospheric pressure, the salt slowly oxidizes, forming potassium carbonate

and molecular iodine. This oxidation increases the thickness of thin-film targets. The probability of particles traversing the target with large final energies is decreased, introducing a high energy tail in the ejected particle spectrum. The Landau distribution describes this energy loss, but it is computationally challenging to implement. An approximation that has been found to fit oxidized-target spectra well is the exponentially-modified gaussian (EMG) distribution [Bab16]. The power of the EMG approximation is that its area calculation is the exact same as that of a gaussian distribution,  $\sqrt{2\pi}\sigma A$ , where  $\sigma$  and  $A$  are parameters of both gaussians and EMGs, but they have slightly different definitions as it will become clear below. This makes it very simple to determine the number of counts for EMG distributions, unlike Landau distributions, where the full area integral must be calculated.

The probability density function (PDF) of an EMG distribution  $f$  is a convolution of exponential  $g$  and gaussian  $h$  PDFs,

$$\begin{aligned} f(x; \sigma, \lambda, \mu, A) &= (g * h)(x) = \int_{-\infty}^{\infty} g(x')h(x - x') dx' \\ &= \int_0^{\infty} \lambda \exp(-\lambda x') A \exp\left(-\frac{1}{2}\left(\frac{x - x' - \mu}{\sigma}\right)^2\right) dx' \\ &= A \sigma \lambda \sqrt{\frac{\pi}{2}} \exp\left(\frac{1}{2}(\sigma\lambda)^2 - (x - \mu)\lambda\right) \operatorname{erfc}\left(\frac{1}{\sqrt{2}}\left(\sigma\lambda - \frac{x - \mu}{\sigma}\right)\right), \end{aligned} \quad (4.5)$$

where  $\lambda$  is the exponential-component rate,  $\mu$ ,  $\sigma$ , and  $A$  are the gaussian-component mean, standard deviation, and peak intensity, respectively, and  $\operatorname{erfc}$  is the complimentary error function, defined as  $\operatorname{erfc} z = 1 - \operatorname{erf} z$  for the complex variable  $z$ , where  $\operatorname{erf}$  is the error function,

$$\operatorname{erf} z = \frac{2}{\sqrt{\pi}} \int_0^z \exp(-t^2) dt. \quad (4.6)$$

The standard EMG distribution, as a function of  $x$ , has a high- $x$  tail. Since the focal-plane position spectrum channel number is inversely related to energy, the EMG must be modified to have a low- $x$  tail. This is done by simply replacing  $x - \mu$  with  $\mu - x$  to reflect the standard EMG distribution about its gaussian-component mean,  $\mu$ . The following discussion of EMG distributions assumes this reflection has been performed.

Previously it was shown for non-oxidized targets that the Bayesian fitting procedure for a gaussian peak requires gaussian mean  $\mu$  and peak intensity  $A$  priors. The means of these priors are provided by the user when selecting an estimate at the peak apex with the **BayeSpec** GUI. However, this presents a problem when extending the procedure to EMG fits. An EMG is defined by the  $\mu$  and  $A$  parameters of its gaussian component, not the mean and peak intensity of the EMG itself. To obtain reasonable priors for the  $\mu$  and  $A$  parameters, they must be derived from the attributes of the EMG peak apex, where the user selects. This

apex defines the mode  $x_m$  and peak intensity  $y_m$  of the EMG, which can both be calculated by determining the coordinates where the derivative of the PDF is equal to zero. These are

$$\begin{aligned} x_m &= \mu - \sigma^2 \lambda + \sqrt{2} \sigma z, \\ y_m &= A \exp \left( -\frac{1}{2} \left( \frac{\mu - x_m}{\sigma} \right)^2 \right), \end{aligned} \quad (4.7)$$

where  $z$  is defined such that

$$\exp(z^2) \operatorname{erfc}(z) = \sqrt{\frac{2}{\pi}} \frac{1}{\sigma \lambda}, \quad (4.8)$$

which can be solved numerically. With  $x_m$  and  $y_m$  provided by the user,  $\mu$  and  $A$  become

$$\mu(\sigma, \lambda) = x_m + \sigma^2 \lambda - \sqrt{2} \sigma z, \quad (4.9)$$

$$A(\sigma, \lambda) = y_m \exp \left( \frac{1}{2} \left( \frac{\mu - x_m}{\sigma} \right)^2 \right). \quad (4.10)$$

The priors would be fully determined if  $\sigma$  and  $\lambda$ , the parameters related to the EMG width and skewness, can be constrained. Fortunately, for a given transfer reaction observed in a focal-plane spectrum, there is little variation between these properties, much like the gaussian  $\sigma$  parameter of Section 4.5.1. From a sample of EMG fits for  $^{39}\text{K}(^{3}\text{He}, d)^{40}\text{Ca}$  peaks, reasonable priors for  $\sigma$  and  $\lambda$  were determined to be

$$\sigma \sim \mathcal{N}(5.0, 1.0^2), \quad (4.11)$$

$$\lambda \sim \mathcal{N}(0.09, 0.02^2), \quad (4.12)$$

where these are also usually sufficient for other reactions. Priors for Eqns. 4.9 and 4.10 can then be constructed by sampling from Eqns. 4.11 and 4.12. The resulting prior distributions for  $\mu - x_m$  and  $A/y_m$  are shown in Figure 4.16 in black after taking 10,000 samples from Eqns. 4.11 and 4.12. The gaussian approximations (blue) were constructed from the mean and standard deviation of the  $\mu - x_m$  and  $A/y_m$  samples, while the lognormal approximations (red) were similarly constructed from the mean and standard deviation of the natural logarithm of those samples. Note that the priors are not gaussian. In fact, the prior for  $A/y_m$  is neither gaussian nor lognormal. However, a lognormal approximation suffices for both in practice and is preferable to the actual distributions, which are either non-analytical or at least exceedingly complicated. The Bayesian quadratic approximation function, `quap`, used with `BayeSpec` requires named prior distributions, forbidding the use of non-analytical distributions. The lognormal approximations also correctly prevent negative sample values and are therefore taken as the priors for  $\mu$  and  $A$ .

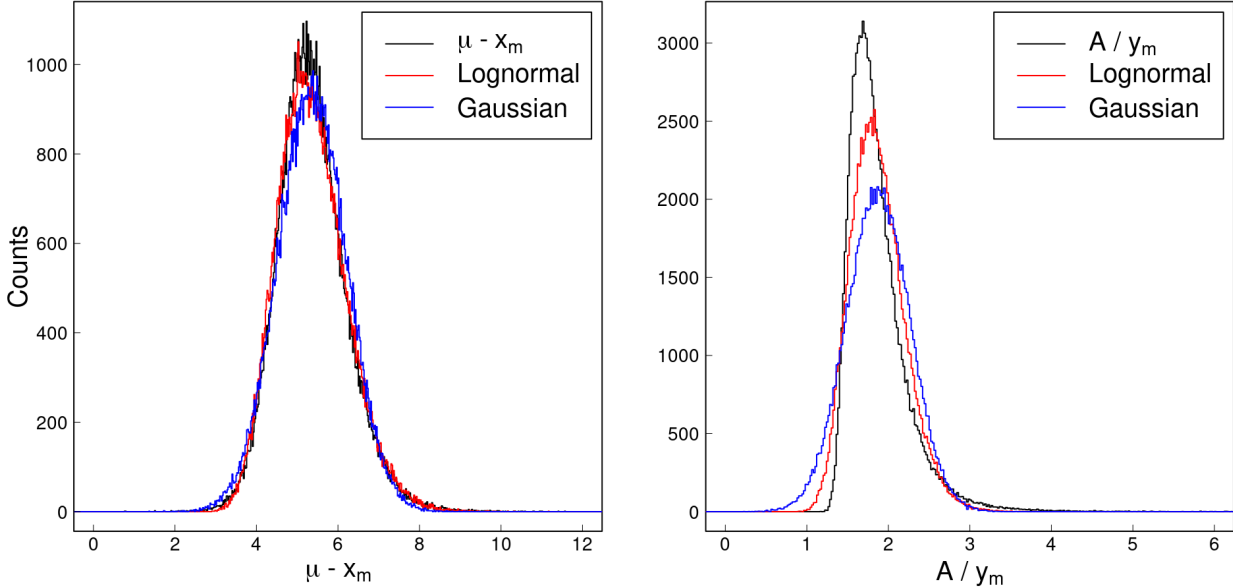


Figure 4.16: The constructed priors for  $\mu - x_m$  (left) and  $A/y_m$  (right) from 10,000 samples of the  $\sigma$  and  $\lambda$  priors of Eqns. 4.11 and 4.12. The gaussian (blue) approximations were derived from the mean and standard deviation of the samples. The lognormal (red) approximations were derived from the mean and standard deviation of the natural logarithm of those samples.

As in Section 4.5.1, once the priors have been determined, the quadratic approximations to the posteriors are computed with `quap`, and the fit is constructed from samples of the EMG distribution with those posteriors. An example of this Bayesian EMG fitting method is shown in Figure 4.17, where the 6285 keV  ${}^{40}\text{Ca}$  state from  ${}^{39}\text{K}({}^3\text{He}, d){}^{40}\text{Ca}$  at  $\theta_{\text{lab}} = 5^\circ$  is fit with an EMG distribution because the potassium iodine target for this run (KI #1) had undergone oxidation. The closely-packed blue lines are 50 representative samples of the EMG posteriors, plus that of the background line, while the green lines are the corresponding gaussian components of those EMG samples with mean  $\mu$ , standard deviation  $\sigma$ , and peak intensity  $A$ . The new mode and peak intensity from Eqn 4.7, obtained by sampling from the posteriors, are shown by the black lines, where the solid line represents its mean and the dashed lines represent its standard deviation. Note that the  $(x_m, y_m)$  coordinate lies along its gaussian component, a ubiquitous property of EMG distributions. The number of counts in the EMG distribution is simply equivalent to the area of its gaussian component,  $\sqrt{2\pi} \sigma A$ , constructed by sampling from the  $\sigma$  and  $A$  posteriors.

Figure 4.18 shows how powerful this method can be for high resolution spectral analysis with an oxidized target. The same focal-plane spectrum as Figure 4.17 is shown here, but it is focused on a region with multiple peaks. The blue summed fit consists of 5 EMG distributions, shown individually by the red and orange lines, and a small, virtually horizontal background

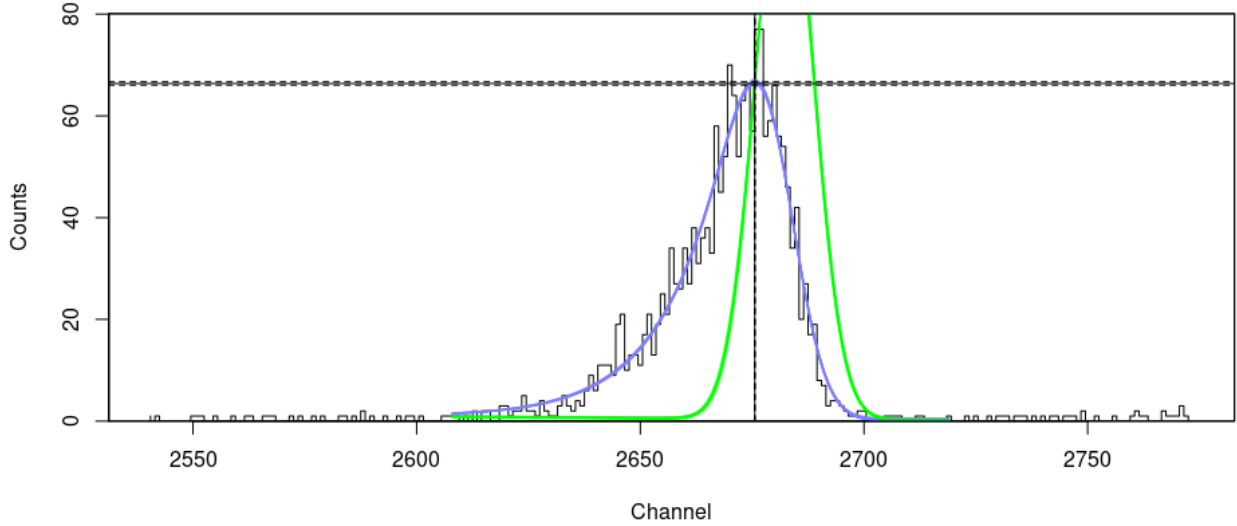


Figure 4.17: A Bayesian exponentially-modified gaussian fit with BayeSpec for the 6285 keV  $^{40}\text{Ca}$  state from  $^{39}\text{K}({}^3\text{He}, d)^{40}\text{Ca}$  at  $\theta_{\text{lab}} = 5^\circ$  with an oxidized potassium iodine target (KI #1). In blue are 50 random samples of the exponentially-modified gaussian distribution from the  $\sigma$ ,  $\lambda$ ,  $\mu$ , and  $A$  posteriors, plus the background line. In green are the gaussian components of the exponentially-modified gaussian samples. The new mode and peak intensity are represented by the black lines, where the solid line represents their mean and the dashed lines represent their standard deviation.

line. As before, each distribution shows 50 lines drawn from samples of the EMG posteriors. From a simple energy calibration, the red peaks were found to be  $^{40}\text{Ca}$  excited states with excitation energies 7694 keV, 7658 keV, 7623 keV, and 7532 keV, from left to right, and the orange peak corresponds to the  $^{14}\text{N}$  6446 keV excited state. Because we expect energy loss to be nearly equivalent for peaks with similar energies from the same reaction, the  $\sigma$  and  $\lambda$  width and skewness parameter posteriors are fixed between the  $^{40}\text{Ca}$  peaks, while the  $^{14}\text{N}$  peak has its own  $\sigma$  and  $\lambda$  posteriors. The custom Bayesian sampling routines for both gaussian and EMG fits can be used for a simultaneous fit of any number of peaks from up to 3 different reactions at present, and this could easily be extended to any number of reactions when the need arises.

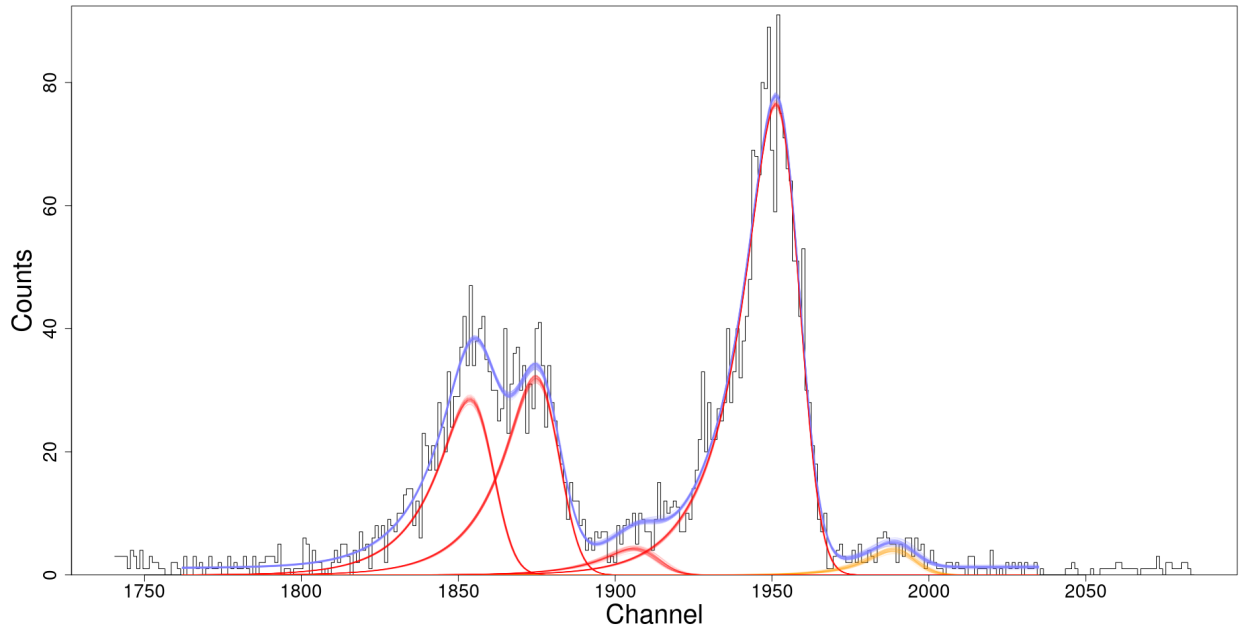


Figure 4.18: A Bayesian exponentially-modified gaussian fit with BayeSpec for the  $^{40}\text{Ca}$  excited states (left to right, in red) 7694 keV, 7658 keV, 7623 keV, and 7532 keV from  $^{39}\text{K}(\text{He}^3, d)^{40}\text{Ca}$  and the  $^{14}\text{N}$  excited state (in orange) 6446 keV from  $^{13}\text{C}(\text{He}^3, d)^{14}\text{N}$  at  $\theta_{\text{lab}} = 5^\circ$  with an oxidized potassium iodine target (KI #1). In red and orange are 50 random samples of the exponentially-modified gaussian distributions from the  $\sigma$ ,  $\lambda$ ,  $\mu$ , and  $A$  posteriors for each peak. The  $^{40}\text{Ca}$  peaks share identical  $\sigma$  and  $\lambda$  posteriors, whereas the  $^{14}\text{N}$  peak has its own. In blue are the sums of the peaks plus the background line for each of those 50 samples.

## 4.6 Cross Sections

An essential ingredient in the calculation of thermonuclear reaction rates is the nuclear reaction cross section  $\sigma$ , introduced in Section 2.3. The reaction cross section is an imaginary, effective area around the target nucleus where the reaction proceeds with a probability of unity if an incident particle passes through it. It is therefore a measure of the probability for a reaction to occur, varying with the incident particle energy. The cross section is closely related to the yield  $Y$  of the reaction

$$Y = \frac{N_R}{N_b}, \quad (4.13)$$

where  $N_R$  is the total number of reactions and  $N_b$  is the total number of incident particles. The total number of reactions  $N_R$  that occur is related to the number of counts  $N_c$ , or the area, of a given peak in a detector. However, this peak count is affected by the deadtime  $t_{\text{dead}}$  of the data acquisition system. To correct for the deadtime, and therefore get an accurate measure of the number of reactions, the livetime  $t_{\text{live}} = 1 - t_{\text{dead}}$  is used as in

$$N_R = \frac{N_c}{t_{\text{live}}}. \quad (4.14)$$

The total number of incident particles  $N_b$  is

$$N_b = \frac{q}{Z_p e}, \quad (4.15)$$

where  $q$  is the total charge deposited by the incident particles,  $Z_p$  is the unit charge of the incident particles, and  $e$  is the electronic charge ( $1.6 \times 10^{-19}$  C). The total charge  $q$  is derived from the beam-integrated current (BCI) scalar value collected for each pulse during a given run. The BCI has an associated  $\text{BCI}_{\text{scale}}$  setting that determines the scale of the deposited charge, which can be adjusted on the beam current readout module. For the  $^{39}\text{K}(^3\text{He}, d)^{40}\text{Ca}$  experiment, the  $\text{BCI}_{\text{scale}}$  setting was  $10^{-10}$  C/pulse. The number of incident particles  $N_b$  is therefore

$$N_b = \frac{\text{BCI} \times \text{BCI}_{\text{scale}}}{Z_p e}. \quad (4.16)$$

As described in Section 4.6.1, the conversion between the yield and the cross section depends on the target thickness  $\Delta E$  (in energy units) and the stopping power  $\mathcal{E} = -(1/N_t)dE/dx$  (in units of eV cm<sup>2</sup>/atom), where  $N_t$  denotes the number density of target nuclei.

A measurement of the total cross section or total yield would require the full  $4\pi$  sr solid angle coverage of detectors around the target to ensure that no emitted particles from the

reaction are missed. Since this is usually not feasible, the alternative is the measurement of a differential cross section  $d\sigma/d\Omega_\theta$  or differential yield  $dY/d\Omega_\theta$  from a detector covering a solid angle  $\Omega$  collecting the particles ejected at an angle  $\theta$  from the incident beam. The differential cross section can be measured at several angles to determine the angular distribution of the reaction. In the case of charged-particle reactions, such as  $^{39}\text{K}(^3\text{He}, d)^{40}\text{Ca}$ , each excited state of the recoil nucleus  $^{40}\text{Ca}$  has its own angular distribution that depends theoretically on the single-particle quantum numbers associated with the quantum mechanical selection rules for the transition, presented in Section 4.7.4.

#### 4.6.1 Yield to Cross Section Conversion

For thin targets, where the cross section  $\sigma$  and stopping power  $\mathcal{E}$  are approximately constant over the target thickness  $\Delta E$ , the yield  $Y$  is proportional to  $\sigma$ , with a proportionality constant  $n_X = \Delta E / \mathcal{E}$  representing the number of active target nuclei per  $\text{cm}^2$  in the target compound  $\text{X}_a\text{Y}_b$  [Ili15a]. The term *active nuclei* in this sense means the nuclei of interest X in the target, whereas the term *inactive nuclei* refers to the nuclei not of interest Y in the target. The number of inactive target nuclei per unit area is defined as  $n_Y$ , and the ratio  $n_Y/n_X$  is equivalent to the target molecule stoichiometry,  $b/a$ . For compound targets, the effective stopping power  $\mathcal{E}_{\text{eff}} = \mathcal{E}_X + n_Y \mathcal{E}_Y / n_X$  must be used. The same proportionality constant

$$n_X = \frac{\Delta E}{\mathcal{E}_{\text{eff}}} \quad (4.17)$$

also applies to the differential yield and differential cross section. Additionally, as some of the energy of the incident particles  $E_0$  is lost in the target, the cross section is evaluated at an effective, reduced energy  $E_{\text{eff}} = E_0 - \Delta E/2$ . The conversion between the differential yield and differential cross section therefore becomes

$$\left[ \frac{dY(E_0)}{d\Omega} \right]_\theta = n_X \left[ \frac{d\sigma(E_{\text{eff}})}{d\Omega} \right]_\theta. \quad (4.18)$$

The number of active nuclei per  $\text{cm}^2$ ,  $n_X$ , can also be expressed in a form more tractable for experiments in the lab system as [Rol88, Set11]<sup>1</sup>

$$n_X = \frac{\nu N_A \Delta x}{A_{t,\text{mol}}} \quad [\text{in cm}^{-2}], \quad (4.19)$$

where  $\nu$  is the number of X atoms per molecule in the target material,  $N_A$  is Avogadro's

---

<sup>1</sup>The “yield”  $Y$  defined in Eqns. 3.30 and 3.31 of Ref. [Set11] is  $N_R$ , not  $N_R/N_b$ , even though it describes it as such in the text.

number ( $6.023 \times 10^{23}$  atoms/mole),  $\Delta x$  is the thickness of the target (in g/cm<sup>2</sup>), and  $A_{t,\text{mol}}$  is the molecular mass of the target material (in grams).

Combining everything, the differential cross section in units of mb/sr, where  $1 \text{ b} = 10^{-24} \text{ cm}^{-2}$ , measured in the lab system is calculated as

$$\left[ \frac{d\sigma}{d\Omega} \right]_\theta = \frac{N_c Z_p A_{t,\text{mol}}}{(3.75 \times 10^9) \Omega t_{\text{live}} \text{BCI} \times \text{BCI}_{\text{scale}} \nu \Delta x} \quad [\text{in mb/sr}], \quad (4.20)$$

where the solid angle  $\Omega$  is in units of msr, all other variables are defined as before, and the factor  $e/N_A$  has been evaluated and converged into the numerical factor in the denominator.

### 4.6.2 Rutherford Scattering

For elastic scattering cross section measurements, it is typical to report the cross section as a ratio to the theoretical Rutherford scattering cross section at the same angle. Theoretical elastic scattering cross sections from optical model potentials (OMPs) are also typically given in terms of the Rutherford ratio, depending on the nuclear reaction code. In the coupled-reaction channels code Fresco [Tho06] for example, the Rutherford ratio is the default output of the elastic scattering cross section.

In the center-of-mass system, the Rutherford scattering cross section is [Ili15a]

$$\begin{aligned} \left[ \frac{d\sigma}{d\Omega} \right]_\theta^{\text{Ruth}} &= \left( \frac{Z_p Z_t e^2}{4E_{\text{c.m.}}} \right)^2 \frac{1}{\sin^4(\theta_{\text{c.m.}}/2)} \\ &= 1.296 \left( \frac{Z_p Z_t}{E_{\text{c.m.}}} \right)^2 \frac{1}{\sin^4(\theta_{\text{c.m.}}/2)} \quad [\text{in mb/sr}], \end{aligned} \quad (4.21)$$

where  $Z_p$  is the unit charge of the incident particles, as before,  $Z_t$  is the unit charge of the active target nuclei,  $E_{\text{c.m.}}$  is the total kinetic energy in the center-of-mass system, in units of MeV, and  $\theta_{\text{c.m.}}$  is the angle measured in the center-of-mass system. The elastic scattering cross section measured in the lab system must first be converted to the center-of-mass system before taking the ratio to Rutherford scattering. This conversion is described in Section 4.6.3.

### 4.6.3 Cross Sections in the Center-of-Mass System

The incident beam energy  $E_{\text{lab}}$ , scattering angle  $\theta_{\text{lab}}$ , and the differential cross section itself  $d\sigma/d\Omega_{\theta_{\text{lab}}}$  must be converted to the center-of-mass frame to apply the Rutherford ratio and to compare with theoretical differential cross sections, which are usually given in the center-of-mass frame.

The conversion from the incident beam energy in the lab system  $E_{\text{lab}}$  to the total kinetic energy in the center-of-mass system  $E_{\text{c.m.}}$  is [Ili15a]

$$E_{\text{c.m.}} = E_{\text{lab}} \frac{A_t}{A_t + A_p}, \quad (4.22)$$

where  $A_t$  and  $A_p$  are the nuclear masses of the active target nucleus and the incident particle nucleus, respectively. However, mass evaluations typically report atomic masses, not nuclear masses. In general, the nuclear masses  $A_{\text{Nuc}}$  can be calculated from the reported atomic masses  $A_{\text{Atom}}$  as [Wan21]

$$A_{\text{Nuc}} = A_{\text{Atom}} - Z m_e + B_e(Z), \quad (4.23)$$

where  $Z$  is the unit charge of the nucleus,  $m_e$  is the electron mass ( $548579.909065(16) \times 10^{-9}$  g/mole [Hua21]), and  $B_e$  is the electron binding energy, found from Ref. [Hua21] to be calculated as

$$B_e(Z) = 14.4381 Z^{2.39} + 1.55468 \times 10^{-8} Z^{5.35} \text{ eV}. \quad (4.24)$$

The lab angle  $\theta_{\text{lab}}$  can be converted to the center-of-mass angle  $\theta_{\text{c.m.}}$  using the kinematics relation [Ili15a]

$$\cos \theta_{\text{lab}} = \frac{\gamma + \cos \theta_{\text{c.m.}}}{\sqrt{1 + \gamma^2 + 2\gamma \cos \theta_{\text{c.m.}}}}, \quad (4.25)$$

where the  $\gamma$  parameter is defined as

$$\gamma = \sqrt{\frac{A_p A_e E_{\text{lab}}}{A_r (A_e + A_r) Q + A_r (A_r + A_e - A_p) E_{\text{lab}}}}, \quad (4.26)$$

with  $A_e$  and  $A_r$  representing the nuclear masses of the ejected particle and recoil nucleus, respectively, and  $Q$  representing the  $Q$ -value of the reaction. For elastic scattering,  $A_e = A_p$ ,  $A_r = A_t$ , and  $Q = 0$ , so that  $\gamma = A_p/A_t$ . Eqn. 4.25 can be solved numerically or it can be rewritten as a quadratic equation for  $\theta_{\text{c.m.}}$ , using the positive solution for forward scattering.

The differential cross section is defined such that the same number of ejected particles cross the solid angle  $d\Omega_{\text{lab}}$  in the direction  $\theta_{\text{lab}}$  as those crossing the solid angle  $d\Omega_{\text{c.m.}}$  in the direction  $\theta_{\text{c.m.}}$ . That is,

$$\left( \frac{d\sigma}{d\Omega} \right)_{\theta_{\text{lab}}}^{\text{lab}} d\Omega_{\text{lab}} = \left( \frac{d\sigma}{d\Omega} \right)_{\theta_{\text{c.m.}}}^{\text{c.m.}} d\Omega_{\text{c.m.}}. \quad (4.27)$$

Assuming the cross section does not depend on the azimuthal angle, the conversion between the lab and center-of-mass systems is therefore

$$\frac{(d\sigma/d\Omega)_{\theta_{\text{c.m.}}}^{\text{c.m.}}}{(d\sigma/d\Omega)_{\theta_{\text{lab}}}^{\text{lab}}} = \frac{d\Omega_{\text{lab}}}{d\Omega_{\text{c.m.}}} = \frac{d(\cos \theta_{\text{lab}})}{d(\cos \theta_{\text{c.m.}})} = \frac{1 + \gamma \cos \theta_{\text{c.m.}}}{(1 + \gamma^2 + 2\gamma \cos \theta_{\text{c.m.}})^{3/2}}. \quad (4.28)$$

#### 4.6.4 Si Detector Normalization

As mentioned in Section 4.4.4, a Si detector telescope was used to measure the  $^{39}\text{K}(^3\text{He}, ^3\text{He})^{39}\text{K}$  elastic scattering differential cross section at a constant  $\theta_{\text{lab}} = 45^\circ$ , while the focal-plane detector was simultaneously measuring the differential cross sections of both  $^{39}\text{K}(^3\text{He}, ^3\text{He})^{39}\text{K}$  and  $^{39}\text{K}(^3\text{He}, d)^{40}\text{Ca}$  over multiple  $\theta_{\text{lab}}$  angles. The Si detector elastic scattering cross section was used as a normalization to correct for systematic uncertainties associated with unknown target effects during the focal-plane measurements. Although this is a relative measurement, an absolute scale can be established by comparing to optical model predictions, described in Section 4.6.5.

The reason the relative measurement is effective is due to the conversion factor  $n_X$  between the yield and cross section in Eqn. 4.18. Since  $n_X$  only depends on the target properties, taking a relative cross section is equivalent to taking a relative yield, where the target properties cancel out. Because of the angular dependence, however, each differential yield (or equivalently, each differential cross section) must first be converted into the center-of-mass system before taking the ratio. The final form of the differential cross-section ratio  $R$  in the center-of-mass system becomes

$$R \equiv \frac{(d\sigma/d\Omega_{\text{FP}})_{\theta_{\text{c.m.}}}^{\text{FP}}}{(d\sigma/d\Omega_{\text{Si}})_{\theta_{\text{Si}}}^{\text{Si}}} = \frac{N_c^{\text{FP}} \Omega_{\text{Si}}}{\Omega_{\text{FP}} N_c^{\text{Si}}} \frac{1 + \gamma \cos \theta_{\text{c.m.}}}{(1 + \gamma^2 + 2\gamma \cos \theta_{\text{c.m.}})^{3/2}} \frac{(1 + \gamma^2 + 2\gamma \cos \theta_{\text{Si}})^{3/2}}{1 + \gamma \cos \theta_{\text{Si}}}, \quad (4.29)$$

where  $\theta_{\text{c.m.}}$  is the angle for the focal plane measurement,  $\theta_{\text{Si}} = 48.14^\circ$  is the center-of-mass angle for the Si measurement ( $\theta_{\text{lab}} = 45^\circ$ ),  $\Omega_{\text{Si}} = 4.23(4)$  msr, and  $\Omega_{\text{FP}} = 1.00(4)$  msr for all runs of the transfer reaction and at angles  $\theta_{\text{lab}} \leq 35^\circ$  for elastic scattering; otherwise,  $\Omega_{\text{FP}} = 0.50(4)$  msr for elastic scattering. Note that the only experimental quantities required with a relative measurement are the number of detector counts  $N_c$  and the solid angle  $\Omega$  that each detector covers, in addition to the quantities making up the center-of-mass conversion. The  $u_R$  uncertainty is found to be

$$u_R = R \sqrt{\left(\frac{u_{N_c}}{N_c}\right)_{\text{FP}}^2 + \left(\frac{u_\Omega}{\Omega}\right)_{\text{FP}}^2 + \left(\frac{u_{N_c}}{N_c}\right)_{\text{Si}}^2 + \left(\frac{u_\Omega}{\Omega}\right)_{\text{Si}}^2}, \quad (4.30)$$

where the uncertainties in the angle measurement and  $\gamma$  are sufficiently small to be neglected.

Due to the presence of energy shifts in the  $^{39}\text{K}(^3\text{He}, d)^{40}\text{Ca}$  experiment (see Section 4.4.3), the runs usually could not all be sorted together at a given scattering angle. Therefore, there were multiple relative cross sections that needed to be calculated at these angles, one per sort group, and a method of averaging these measurements was necessary. A weighted average over each sort group  $i$  at a given angle was deemed appropriate, where the weight is given in

terms of the individual relative cross section uncertainties  $u_R$ , as in

$$\bar{R} = \frac{\sum_i^n R_i / u_{R,i}^2}{\sum_i^n 1 / u_{R,i}^2}, \quad (4.31)$$

for  $n$  total sort groups at the given angle. This ensures that the more precise measurements are weighted more. The uncertainty in this weighted average is then

$$u_{\bar{R}} = \sqrt{\frac{1}{\sum_i^n 1 / u_{R,i}^2}}. \quad (4.32)$$

In calculating the individual relative cross section uncertainties  $u_R$ , it was clear that an additional scatter uncertainty  $u_s$  was required to accurately account for the variations from the average  $R$ . The goal was to apply the same fractional scatter uncertainty for all measurements of a given angle, based on the typical deviation from the average  $R$  over all  $^{40}\text{Ca}$  states. An example of this is depicted in Fig. 4.19, where the variations from the average  $R$ , normalized to unity, at  $\theta_{\text{lab}} = 13^\circ$  are shown over all sort groups and for all  $^{40}\text{Ca}$  states, up to  $E_x = 8935$  keV. Each color represents a different  $^{40}\text{Ca}$  state. It is clear that the variations from the average are typically no more than about 10%, which is also true for the other angles. The variation from the average  $R$  is written as

$$\text{var} = \frac{R}{R_{\text{avg}}}, \quad (4.33)$$

where each fractional deviation is found from

$$f_{\text{dev}} = |\text{var} - 1|. \quad (4.34)$$

The average of these fractional deviations  $f_{\text{dev, avg}}$  over all the  $^{40}\text{Ca}$  states and all sort groups for a given angle is used as the fractional uncertainty applied to the additional scatter,

$$u_s = f_{\text{dev, avg}} R. \quad (4.35)$$

In cases where only one sort group was needed for an angle, the fractional uncertainty was instead obtained by taking  $f_{\text{dev, avg}}$  for each sort group and  $^{40}\text{Ca}$  state over all angles.

For sort groups where an oxidized target (KI #1) was used, it was determined that the uncertainty was still underestimated, based on the tension between measurements at the same angle with targets that were not oxidized. An additional  $f_{\text{ox}} = 20\%$  scatter was added in these cases to account for any unknown variability and to apply more weight to measurements

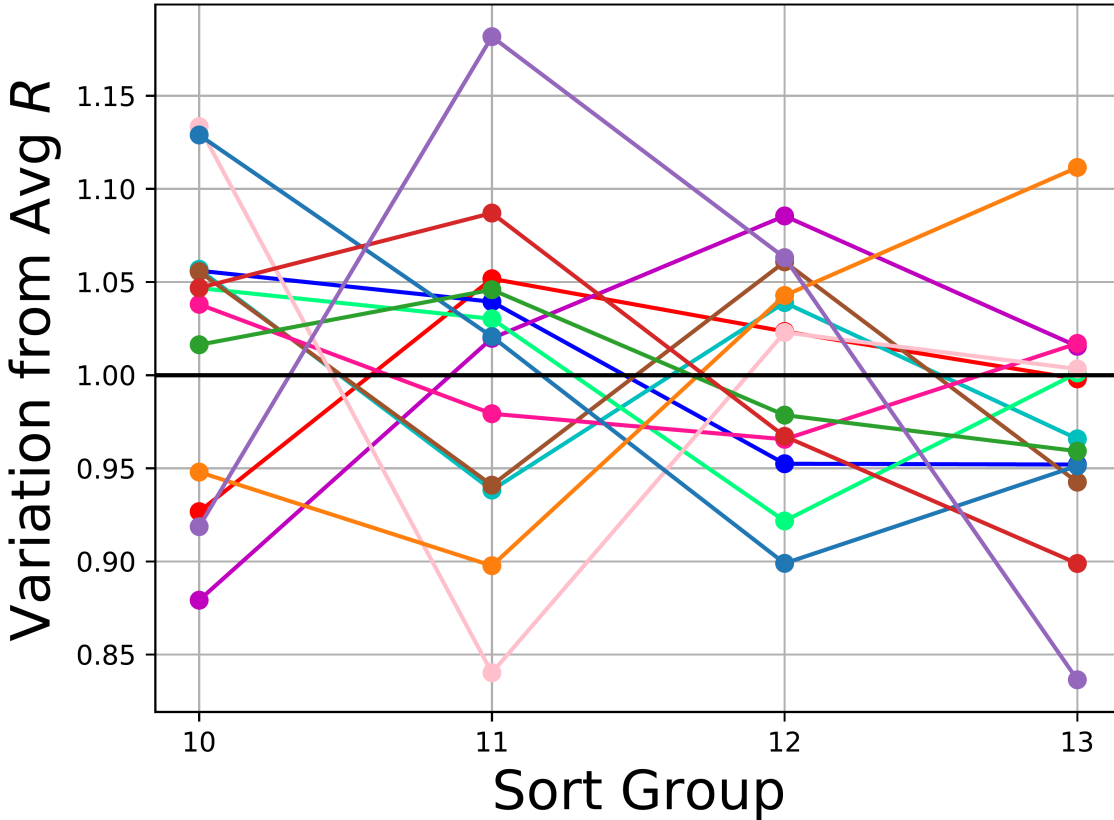


Figure 4.19: The variations from the average differential cross-section ratio  $R$ , normalized to unity, for each sort group over all  $^{40}\text{Ca}$  states measured at  $\theta_{\text{lab}} = 13^\circ$ . The colored lines correspond to each  $^{40}\text{Ca}$  state up to  $E_x = 8935$  keV. The variations are typically within 10% of the average, which is true for the other angles as well. The average deviation for a given angle is used as an additional scatter uncertainty, as described in the text.

with non-oxidized targets. The resulting uncertainty in each  $R$  measurement with the added scatter is thus

$$u'_R^2 = u_R^2 + u_s^2 + u_{\text{ox}}^2 = u_R^2 + (f_{\text{dev, avg}}^2 + f_{\text{ox}}^2) R^2, \quad (4.36)$$

where  $f_{\text{dev, avg}}$  covers all angles in cases where only one sort group was needed for an angle and  $f_{\text{ox}} = 0$  for non-oxidized targets.

#### 4.6.5 Optical Model Normalization

An absolute scale for the relative transfer differential cross section is established by applying a normalization factor  $N_{\text{ES}}$  obtained from the comparison between the relative elastic scattering differential cross section and the absolute differential cross section from a global  $^3\text{He}$  optical model potential (OMP) for  $^{39}\text{K}$  (see Section 2.4.1). The parameters of a global OMP are

Table 4.2: Global optical model potential parameters for  $^{39}\text{K} + ^3\text{He}$  at  $E_{\text{lab}} = 21$  MeV from Ref. [Lia09].

$V_r$	$r_r$	$a_r$	$W_v$	$r_v$	$a_v$	$W_s$
117.881	1.178	0.768	-0.646	1.415	0.847	20.665
$r_s$	$a_s$	$V_{so}$	$r_{so}$	$a_{so}$	$W_{so}$	$r_c$
1.198	0.852	2.083	0.738	0.946	-1.159	1.289

found through an optimization procedure, fitting them to an exhaustive list of experimental elastic scattering data for several target nuclei. Both the elastic scattering and global OMP cross sections are given in terms of a ratio to Rutherford scattering, which is theoretically unity at  $\theta_{\text{c.m.}} = 0^\circ$ .

The global  $^3\text{He}$  OMP of Ref. [Lia09] was chosen as the reference for the absolute scale. This potential includes real and imaginary volume terms, an imaginary surface term, real and imaginary spin-orbit terms, and a Coulomb potential, where the Woods-Saxon form factor  $f_i(r)$  and its derivative are used, as described in Section 2.4.1. A total of 148 sets of elastic scattering data for 52 target nuclei were used in the parametrization. The potential parameters are expressed as functions of beam energy and target mass. For  $^{39}\text{K} + ^3\text{He}$  at  $E_{\text{lab}} = 21$  MeV, the potential parameters of Ref. [Lia09] are given in Table 4.2, which are defined in the same manner as in Section 2.4.1.

The nuclear reaction code **Fresco** [Tho88, Tho06] was used to calculate the  $^{39}\text{K}(^3\text{He}, ^3\text{He})^{39}\text{K}$  differential cross section shown in Fig. 4.20 using the OMP parameters in Table 4.2 at  $E_{\text{lab}} = 21$  MeV. This differential cross section, represented as the black curve, was calculated in steps of  $1^\circ$  from  $\theta_{\text{c.m.}} = 0^\circ - 80^\circ$ . The present experimental differential cross section is shown in red at the angles  $\theta_{\text{lab}} = 15^\circ - 55^\circ$  in steps of  $5^\circ$ , and  $59^\circ$ , converted to  $\theta_{\text{c.m.}}$ . The experimental points have been corrected for the presence of  $^{41}\text{K}$  in all of the elastic scattering peaks of the Si spectra and only at  $\theta_{\text{lab}} < 40^\circ$  in the focal-plane P1 spectra, described in Section 4.4.4. Both the data and the model are given in terms of the ratio to Rutherford scattering. The difference in scale is attributed to the relative measurement of the focal-plane and the Si detectors.

The elastic scattering scale factor  $N_{\text{ES}}$  was calculated by taking the average ratio between each experimental point and the global model,

$$N_{\text{ES}} = \frac{1}{N} \sum_{i=1}^N \frac{R_{\text{ES},i}}{(d\sigma/d\Omega_{\text{ES,global}})_i}, \quad (4.37)$$

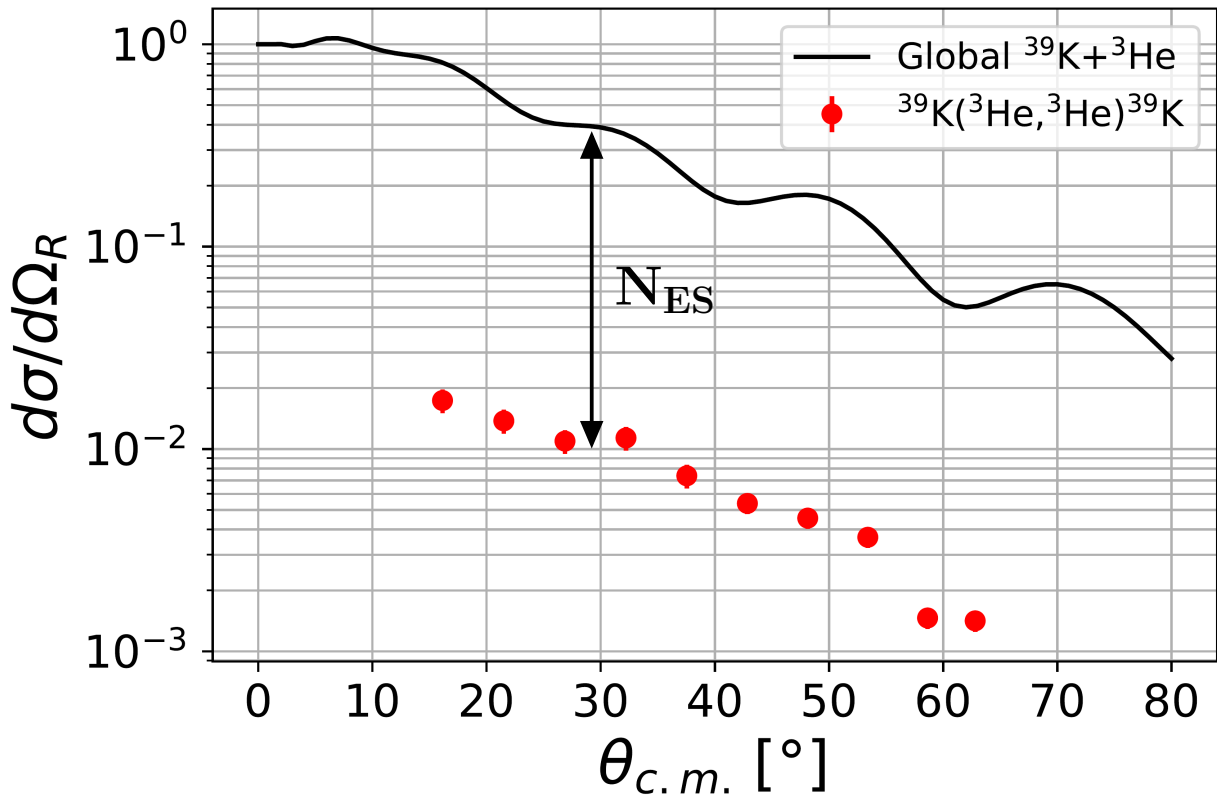


Figure 4.20: The differential cross-section, as a ratio to Rutherford scattering, of the global  ${}^3\text{He}$  optical model potential of Ref. [Lia09] for  ${}^{39}\text{K}$  (black line) and that of the present relative  ${}^{39}\text{K}({}^3\text{He}, {}^3\text{He}){}^{39}\text{K}$  measurements (red data). The scaling factor  $N_{\text{ES}}$  is illustrated, which is also applied to the transfer data to establish an absolute scale.

where  $R_{\text{ES},i}$  is defined by Eqn. 4.29 for the simultaneous  ${}^{39}\text{K}({}^3\text{He}, {}^3\text{He}){}^{39}\text{K}$  measurements of the focal-plane and Si detectors,  $(d\sigma/d\Omega_{\text{ES,global}})_i$  is the global OMP differential cross section evaluated at the experimental angle  $\theta_{\text{c.m.,}i}$ , and  $N$  is the number of experimental points. Since the global OMP differential cross section is not continuous, its value at each experimental center-of-mass angle must be interpolated. This is performed by cubic spline interpolation, where each pair of neighboring  $d\sigma/d\Omega_{\text{ES,global}}$  points defines a polynomial that ensures its first and second derivatives at each point are equal to that of neighboring polynomials. After interpolating the  $N$  points, the scale factor becomes  $N_{\text{ES}} = 0.0277(11) \approx 1/36$ . Fig. 4.21 shows the global model scaled by  $N_{\text{ES}}$  to match the data. No  $\chi^2$ -minimization or Bayesian Monte Carlo algorithm has been performed on the OMP potential parameters. The global  ${}^3\text{He}$  OMP parameters themselves sufficiently reproduce the angular distribution of the experimental points. However, the OMP parameters give rise to large systematic uncertainties in the spectroscopic factor calculations for the transfer reaction, as demonstrated in Section 4.7.4.

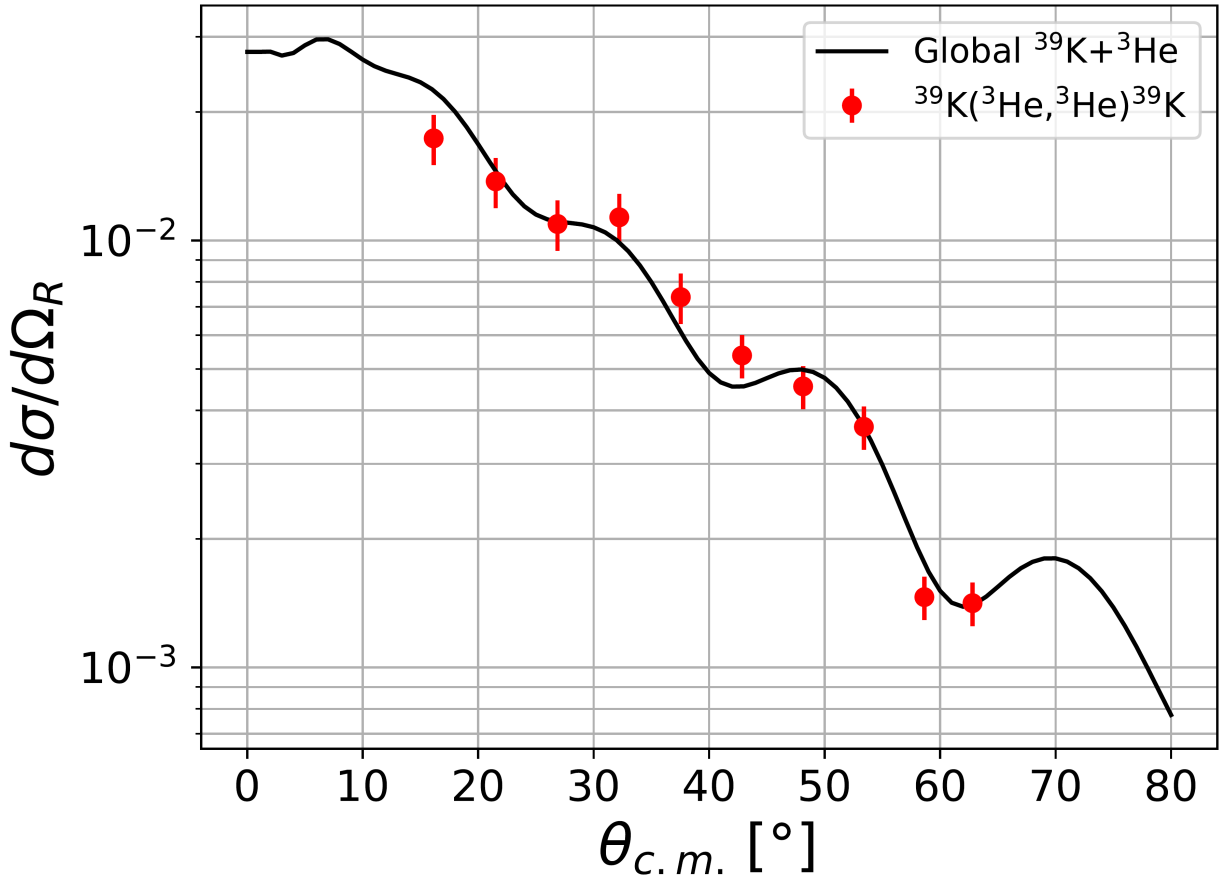


Figure 4.21: The same as Fig. 4.20, except the differential cross-section of the global  ${}^3\text{He}$  optical model potential has been scaled by  $N_{\text{ES}}$  to match the experimental measurements, as described in the text.

The same  $N_{\text{ES}}$  normalization is applied to the transfer differential cross sections, since they were also measured relative to the elastic scattering of the Si detector. The ratio between this corrected  ${}^{39}\text{K}({}^3\text{He}, d){}^{40}\text{Ca}$  differential cross section and that of an appropriate distorted-wave Born approximation (DWBA) model is the spectroscopic factor  $C^2S$  (see Sections 2.3.1 and 2.4.2). This ratio is performed in the exact same way as the global OMP normalization, including the cubic spline interpolation. The transfer differential cross sections will be presented in Section 4.7.2.

## 4.7 $^{39}\text{K}(\text{He}^3, d)^{40}\text{Ca}$ Analysis

### 4.7.1 Energy Calibrations

The centroid positions  $\mu$  of the  $^{40}\text{Ca}$  states along the P1 focal-plane spectra were used to determine their excitation energies, given several known calibration states. These  $\mu$  were obtained with high precision through the Bayesian peak fitting procedure, detailed in Section 4.5. However, the centroid uncertainty obtained from the fit does not represent the true channel uncertainty. The fit underestimates the uncertainty, as it does not take into account scatter associated with the known focal-plane detector response. An additional scatter uncertainty of  $u_s \sim 0.6$  channels was added to rectify this, corresponding to roughly 1 keV in excitation energy. The new channel uncertainty associated with each centroid value is

$$u_{\text{ch}}^2 = u_\mu^2 + u_s^2. \quad (4.38)$$

The oxidized target fits were also not used in the energy calibration. It is not clear whether the mode of the exponentially-modified gaussian (EMG) fits properly represents their energies. The inconsistency between using gaussian means and EMG modes could cause problems. However, the only angles that have oxidized target data,  $\theta_{\text{lab}} = 5^\circ$  and  $7^\circ$ , also have data from a target that was not oxidized. The EMG fit area was still used for the yield determination because the total number of counts should not be affected by target oxidation. Scatter was added to these yields regardless to put more weight on those from non-oxidized targets in the weighted averages.

The  $^{40}\text{Ca}$  calibration states that were used in the energy calibration are highlighted in red in Fig. 4.22 for the  $\theta_{\text{lab}} = 5^\circ$  focal plane position spectrum. These are the 4491 keV, 5614 keV, 6025 keV, 7532 keV, 8425 keV, and 9454 keV  $^{40}\text{Ca}$  states. The energies are provided by the ENSDF evaluation of Ref. [Che17], except the 8425 keV state uses the more recent energy measurement of Ref. [Gri22]. Unfortunately, not all of these states were unobscured throughout the course of the experiment, which made it necessary to use alternative calibration states in those cases. In total, of the 13 sort groups with non-oxidized targets in the  $^{39}\text{K}(\text{He}^3, d)^{40}\text{Ca}$  experiment (see Section 4.4.3), an alternative calibration state had to be used for 4 of them. At both the  $\theta_{\text{lab}} = 5^\circ$  (sort group #3) and  $\theta_{\text{lab}} = 7^\circ$  (sort group #5) angles, the 8425 keV state was obscured by the first excited state from  $^{16}\text{O}(\text{He}^3, d)^{17}\text{F}$ . The alternative calibration state for these sort groups was the 8484 keV state, as it is closest in energy and was clearly resolved. Similarly, for both sort groups (#15 – #16) at  $\theta_{\text{lab}} = 20^\circ$ , the 9454 keV calibration state did not have enough counts to properly resolve it from the neighboring 9405 – 9432 keV multiplet. In these cases, the 9136 keV state was used as the alternative calibration state.

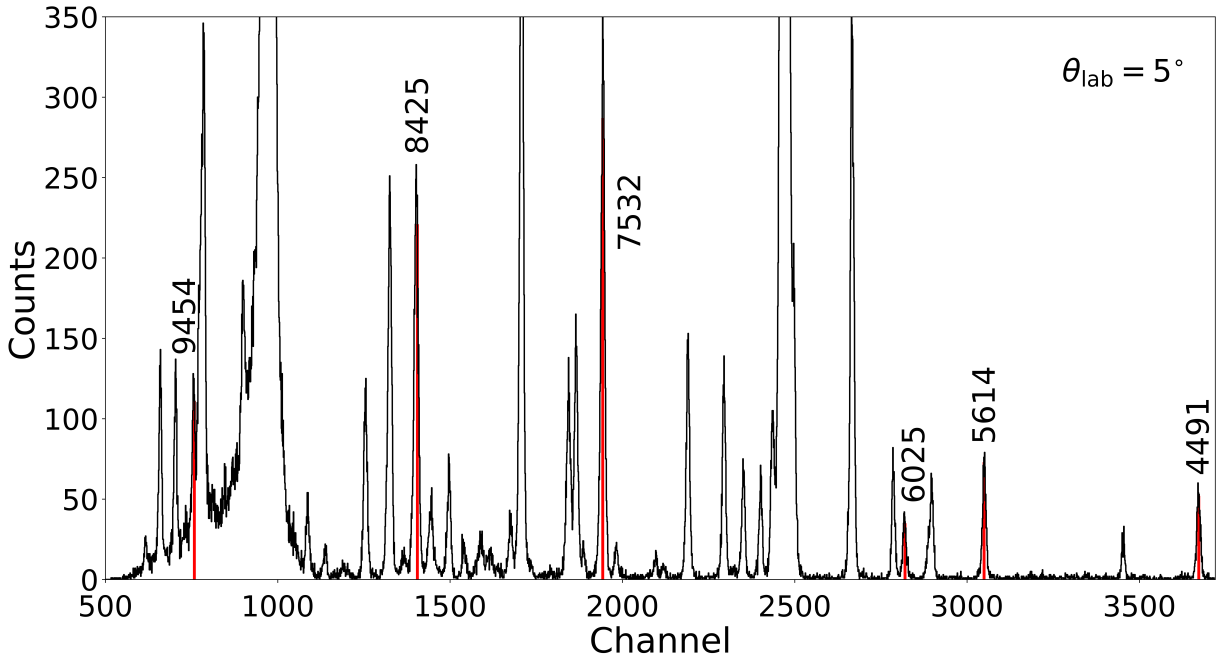


Figure 4.22: The calibration states for the MCMC energy calibration, represented by red vertical lines for the  $\theta_{\text{lab}} = 5^\circ$  focal plane position spectrum. Their ENSDF [Che17] energies are labeled in keV. The 8425 keV state uses the energy of the recent measurement from Ref. [Gri22] instead. The 8484 keV and 9136 keV alternative calibration states are used when the 8425 keV and 9454 keV states were obscured at  $\theta_{\text{lab}} = 5, 7^\circ$  and  $20^\circ$ , respectively. The  $^{17}\text{F}$  contaminant appears in exactly the same position as the 8425 keV state in the figure.

The closer 9538 keV state was determined to be too near the edge of the detector to have a reliable centroid and yield measurement. The 9227 keV state was also ruled out due to it being impossible to determine which of the 9226.69 keV or 9227.43 keV states, or both, from ENSDF it belongs to, as they both have a wide range of possible  $J^\pi$  assignments. It was still possible to report energies for these alternative calibration states over the sort groups where they were not involved in the calibration.

The energy calibration was performed with a quadratic fit that represents the magnetic rigidity  $B\rho$  of the Enge Split-Pole Spectrograph as a function of the focal-plane detector channels  $x_{\text{ch}}$ ,

$$B\rho = a + b_1 x_{\text{ch}} + b_2 x_{\text{ch}}^2. \quad (4.39)$$

The calibration uses  $x_{\text{ch}}$  and  $B\rho$  from the known calibration states to predict  $B\rho$  for all other states, known as test states. The excitation energies of the calibration states are first converted to  $B\rho$  by interpolation from the kinematics code `jrelkin` [Vis03]. After the calibration, the predicted  $B\rho$  are converted back to energy in the same manner, with uncertainties propagated

through both the calibration and the energy conversion.

Markov chain Monte Carlo (MCMC) fits were performed with Eqn 4.39 using the Hamiltonian Monte Carlo and Metropolis algorithms built into `rstan` [Tea11, Guo20]. This allowed for Bayesian statistical inference of the fit parameters from MCMC samples. The parameters, including an extra scatter parameter  $\sigma$  added in quadrature to each  $B\rho$  calibration state uncertainty, were given the prior distributions

$$\begin{aligned} a &\sim \mathcal{N}(0, 1^2), \\ b_1 &\sim \mathcal{N}(0, 1^2), \\ b_2 &\sim \mathcal{N}(0, 1^2), \\ \sigma &\sim \text{Cauchy}(0, 1^2). \end{aligned} \quad (4.40)$$

A total of  $5 \times 10^4$  iterations were performed for each of the four chains that are used by `rstan`. Samples were extracted from the last  $2.5 \times 10^4$  iterations, and the first half were used as warmup. Using the new posteriors,  $B\rho$  was sampled over the 4096 channels and converted to  $^{40}\text{Ca}$  excitation energy. Energy residuals from the median calibration line were also sampled over the 4096 channels.

The energy residuals for  $\theta_{\text{lab}} = 5^\circ$  (sort group #3) are shown in Fig. 4.23. The 68% ( $1\sigma$ ) and 95% ( $2\sigma$ ) confidence intervals from the MCMC samples are shown in dark and light shading, respectively, centered on the median calibration line. The red points represent the calibration states, and the black points represent the test states. Uncertainty bars shown for the test states are simply their input centroid uncertainties  $u_{\text{ch}}$  converted to energy from the fit,  $u_{\text{ch-to-E}}$ , added in quadrature with the ENSDF uncertainties. The uncertainties reported for each test state among each sort group are  $u_{\text{ch-to-E}}$  added in quadrature with half the  $1\sigma$  width from the fit at the given energy. That is,

$$u_E^2 = u_{\text{ch-to-E}}^2 + \left( \frac{u_{\text{MCMC,upper}} - u_{\text{MCMC,lower}}}{2} \right)^2, \quad (4.41)$$

where upper and lower refer to the 84th and 16th percentile of the MCMC samples, respectively.

The calibration was performed for every sort group, except for those where an oxidized target was used (sort groups #1, #2 and #4). Each test state therefore resulted in up to 13 reported energies, 1 for each sort group where the state was resolvable. Several averaging methods were attempted to obtain a final reported energy for each test state. A weighted average  $\bar{E}_{\text{wavg}}$  was the first attempt, where the weights were  $1/u_E^2$ , and the uncertainties were propagated through the weighted average. However, it was clear that for many test states, the scatter was not properly accounted for with the weighted average and its uncertainty.

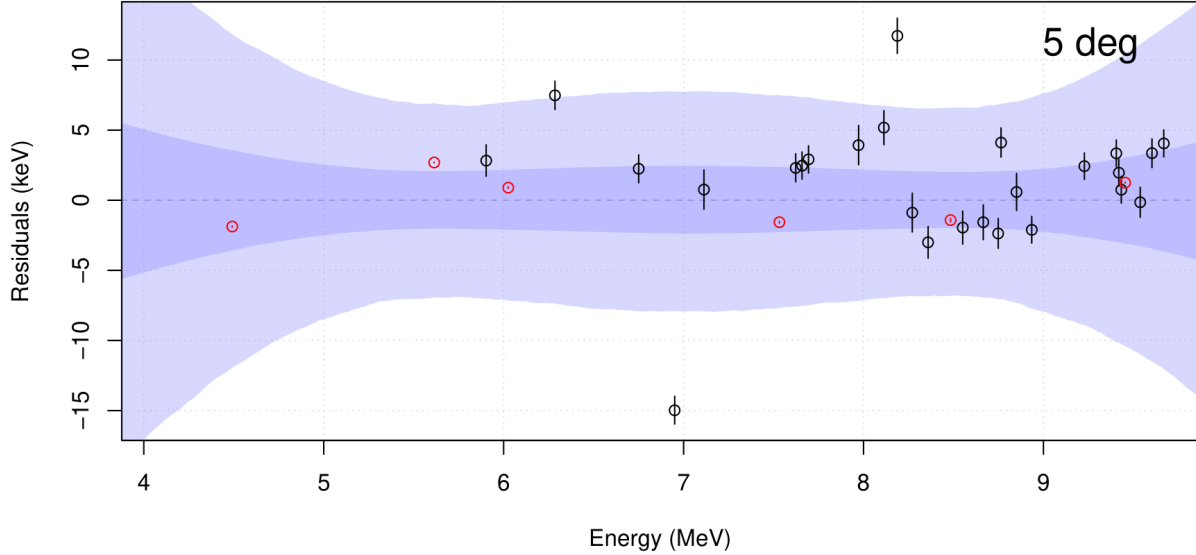


Figure 4.23: Residuals between the excitation energies predicted from the MCMC energy calibration and that of the median calibration line at  $\theta_{\text{lab}} = 5^\circ$  (sort group #3) for the calibration states (in red) and the test states (in black). The 68% ( $1\sigma$ ) and 95% ( $2\sigma$ ) confidence intervals for the fit are represented by the dark and light shading, respectively. See text for details.

The few sort groups with smaller uncertainties shifted the average unreasonably far from that of the other sort groups. A simple average  $\bar{E}$  was then attempted, which seemed to be better suited for the scatter. However, the uncertainty propagated through the simple average also did not reproduce the scatter appropriately. What finally captured the appropriate scatter was taking a simple average of the reported uncertainties. That is,

$$\bar{E} \pm u_{\bar{E}} = \frac{1}{N} \sum_i^N E_i \pm \frac{1}{N} \sum_i^N u_{E,i}, \quad (4.42)$$

was determined to be the appropriate final energy and uncertainty for each state.

To illustrate these different averaging methods, the resulting distribution of calibrated energies for the representative 8551 keV state is shown by the black data in Fig. 4.24. This is an example where the scatter was minimized, potentially due to its relatively large yield, but the different averaging methods are clearly distinguished. The black line represents the simple average, while the orange line represents the weighted average. The propagated uncertainty from each of these averages are the blue and orange bands, respectively. The green band

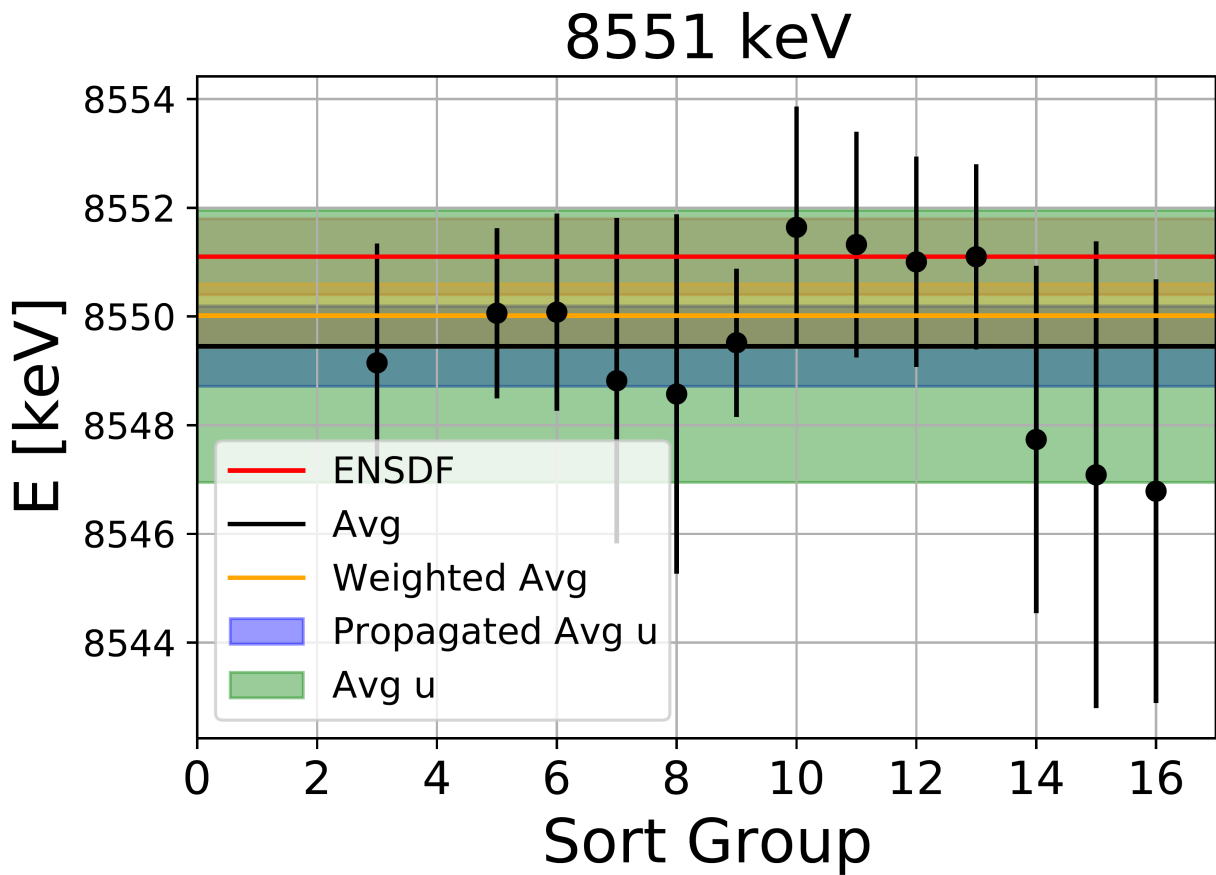


Figure 4.24: Excitation energies and their uncertainties of the 8551 keV state from the MCMC energy calibration for each sort group, excluding sort groups #1 and #2 that used an oxidized target. The ENSDF energy and its uncertainty are given as the red line and red band, respectively. A simple average and a weighted average of the energies are given by the black and orange lines, respectively. The uncertainty propagated from the simple average and from the weighted average are given by the blue and orange bands, respectively. The simple average of the MCMC uncertainties is represented by the green band, which best captures the range of the individual uncertainties for each state.

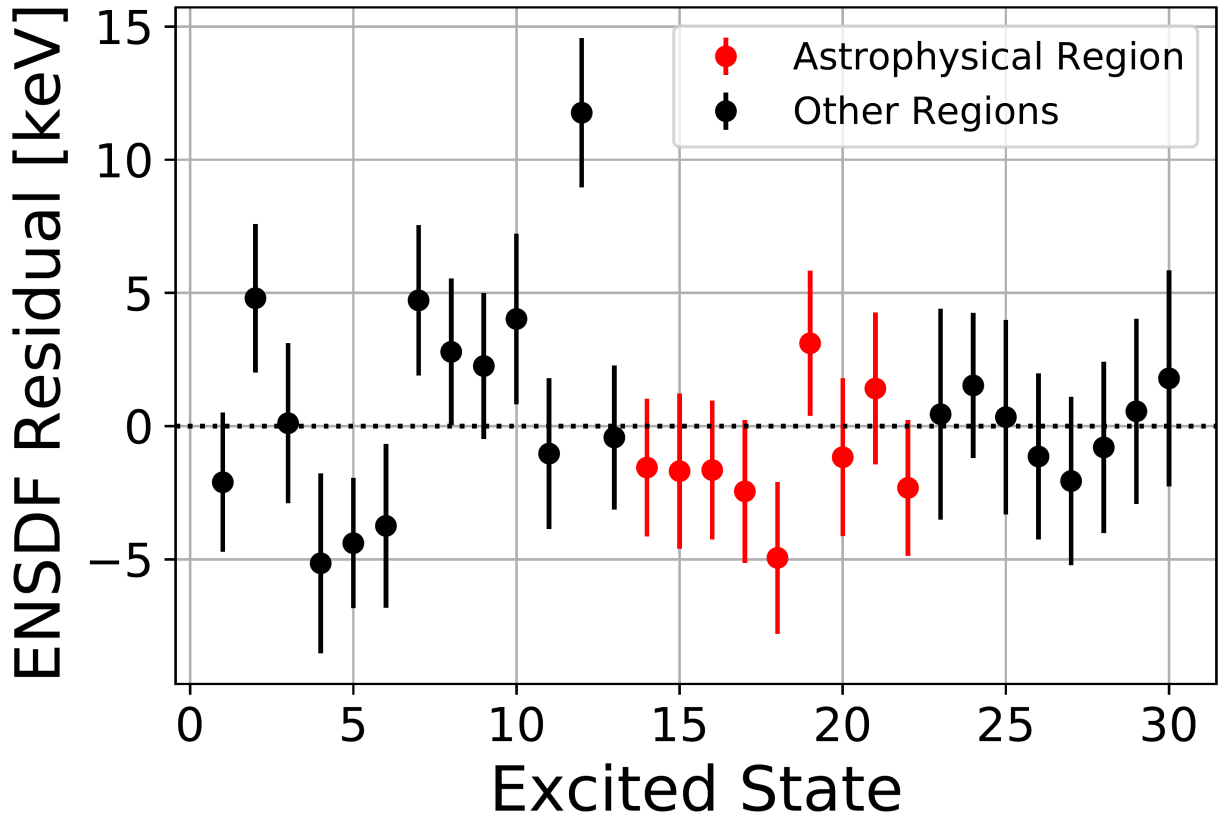


Figure 4.25: Residuals between the final reported energies for each state from the MCMC energy calibration and that of ENSDF [Che17]. The residuals and uncertainties for each state result from a simple average of the MCMC energies and uncertainties of each sort group, respectively. The residuals in red represent the astrophysical region, from 8359 keV to 8995 keV. The  $x$ -axis values correspond to the following states in keV; 1: 5903, 2: 6285, 3: 6582, 4: 6750, 5: 6950, 6: 7113, 7: 7623, 8: 7658, 9: 7694, 10: 7973, 11: 8113, 12: 8188, 13: 8271, 14: 8359, 15: 8484, 16: 8551, 17: 8665, 18: 8748, 19: 8764, 20: 8851, 21: 8935, 22: 8995, 23: 9092, 24: 9136, 25: 9227, 26: 9405, 27: 9419, 28: 9432, 29: 9538, 30: 9603.

shows the simple average uncertainty of Eqn. 4.42, coming from the black line. The energy from ENSDF is shown in red, with its uncertainty band also in red. Note that the blue band does not agree with ENSDF, and there is also tension between the orange band and ENSDF.

The final residuals between the energy-calibrated states using Eqn. 4.42 and their corresponding ENSDF state are shown in Fig. 4.25. It is clear that the typical energy uncertainty is in the range of 2 – 3 keV. The states highlighted in red are the ones that contribute to the  $^{39}\text{K}(p, \gamma)^{40}\text{Ca}$  reaction rate and are therefore of astrophysical interest. These range from 8359 keV to 8995 keV. The excited state labels are provided in the figure caption. There is decent agreement with ENSDF for most states at relatively high excitation energy, but there is considerable scatter at lower energies. In particular, the state that most disagrees with ENSDF is the 8188 keV state, which has a calibrated energy of 8199.3(27) keV, or a residual of 11.8(28) keV. This may correspond to the 8196 keV state in ENSDF instead, but there is a considerable lack of experimental evidence for this state. This hypothesis will be discussed further in Section 4.7.2.

The final energies from the MCMC calibration are reported in Table 4.3. Calibration states are shown in italics, except for the alternative calibration states 8484 keV and 9136 keV that were still able to have their energies determined. Cases where the observed state corresponds to an unresolvable doublet according to ENSDF are represented with a bracket around the doublet. The assigned  $J^\pi$  values from ENSDF are also given. Fig. 4.26 shows an energy calibrated focal plane spectrum of the proton-unbound  $^{40}\text{Ca}$  states labeled with their ENSDF [Che17] energies, where the proton separation energy  $S_p = 8328.18(2)$  keV [Wan21] is indicated by the red line.

Table 4.3: Excitation energies  $E_x$  determined through a Markov Chain Monte Carlo (MCMC) energy calibration for the  $^{40}\text{Ca}$  states observed in the present experiment. For comparison, the ENSDF [Che17] excitation energies and  $J^\pi$  values are also given, unless otherwise indicated. Brackets represent states from ENSDF too close in energy to resolve via the energy calibration alone. Calibration states are shown in italics.

$E_x^{\text{a}}$ [keV]	$E_x^{\text{b}}$ [keV]	$J^\pi$ <sup>a</sup>	$E_x^{\text{a}}$ [keV]	$E_x^{\text{b}}$ [keV]	$J^\pi$ <sup>a</sup>
4491.43(4)	<i>4491</i> <sup>c</sup>	$5^-$	8850.6(9)	8849.5(27)	$6^-, 7^-, 8^-$
5613.52(3)	<i>5614</i> <sup>c</sup>	$4^-$			
5902.63(7)	5900.5(26)	$1^-$	$\begin{cases} 8934.81(7) \\ 8938.4(9) \end{cases}$	8936.3(27)	$2^+$
6025.47(5)	<i>6025</i> <sup>c</sup>	$2^-$			$0^+$
6285.15(4)	6290.0(28)	$3^-$			
6582.47(10)	6582.6(30)	$3^-$	8994.5(11)	8992.2(25)	$(1^-, 2^+)$
6750.41(7)	6745.3(34)	$2^-$	9091.7(6)	9092.2(36)	$3^-$
6950.48(7)	6946.1(24)	$1^-$	9135.66(5)	9137.8(34) <sup>c</sup>	$2^-, 3^-$
$\begin{cases} 7113.1(10) \\ 7113.73(5) \end{cases}$	7109.4(29)	$1^-$	$\begin{cases} 9226.69(5) \\ 9227.43(7) \end{cases}$	9227.8(34)	$(1^-, 2, 3^-)$
		$4^-$			$(1, 2^+)$
7532.26(5)	<i>7532</i> <sup>c</sup>	$2^-$	$\begin{cases} 9404.85(19) \\ 9406.3(6) \end{cases}$	9403.7(31)	$2^-$
7623.11(8)	7627.8(28)	$(2^-, 3, 4^+)$			$0^+$
7658.23(5)	7661.0(28)	$4^-$			
7694.08(4)	7696.3(27)	$3^-$	$\begin{cases} 9412.3(2) \\ 9418.8(2) \end{cases}$	9416.7(32)	
7972.5	7976.5(30)	$3^-$			$3^-$
8113.2(5)	8112.2(28)	$1^-$			
8187.5(8)	8199.3(27)	$3, 4, 5^-$	$\begin{cases} 9429.11(5) \\ 9432.46(18) \end{cases}$	9431.7(32)	$(3, 4)^-$
8271(1)	8270.6(25)	$3^-$			$1^-$
8358.9(6)	8357.3(25)	$(0, 1, 2)^-$			
8424.35(31) <sup>d</sup>	<i>8425</i> <sup>c</sup>	$2^-$	9453.95(5)	<i>9454</i> <sup>c</sup>	$3^-$
8484.02(13)	8482.3(29) <sup>c</sup>	$(1^-, 2^-, 3^-)$	9537.8(5)	9538.4(34)	$1^-$
8551.1(7)	8549.5(25)	$5^-$			
8665.3(8)	8662.9(25)	$1^-$	$\begin{cases} 9603.0(4) \\ 9604.6(4) \end{cases}$	9605.1(40)	$3^-$
8748.59(19) <sup>d</sup>	8743.6(28)	$2^+$			$1^-$
8764.18(6)	8767.3(27)	$3^-$			

<sup>a</sup>From the ENSDF evaluation of Ref. [Che17], unless otherwise indicated.

<sup>b</sup>Present experiment.

<sup>c</sup>Level used as a calibration point for at least one angle in this work. See text for details.

<sup>d</sup>Energy from the nuclear resonance fluorescence measurement of Ref. [Gri22].

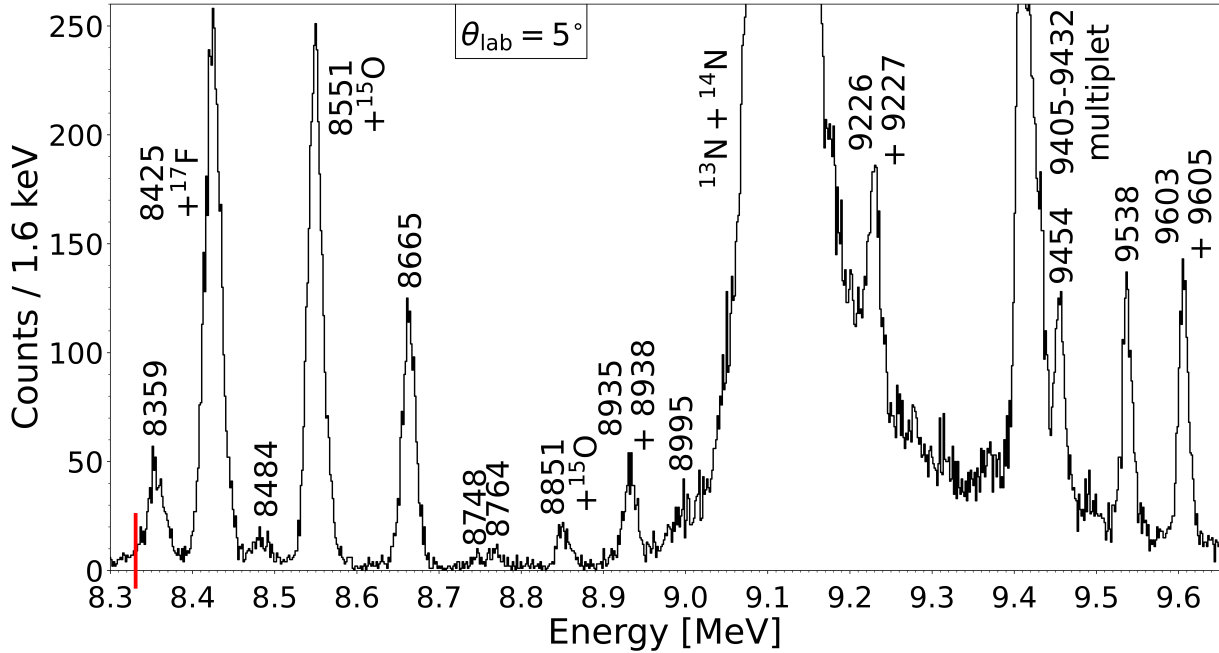


Figure 4.26: The energy-calibrated focal plane position spectrum, focused on the  $^{40}\text{Ca}$  states above the proton separation energy at  $\theta_{\text{lab}} = 5^\circ$  (sort group #3). The average width of the energy bins is approximately 1.6 keV in this region. The  $^{40}\text{Ca}$  states are labeled with their ENSDF [Che17] energies in keV, and contaminants at this angle are indicated. The red vertical line indicates the proton separation energy,  $S_p = 8328.18(2)$  keV from Ref. [Wan21].

### 4.7.2 DWBA Calculations

The  $^{39}\text{K}(\text{He}^3, d)^{40}\text{Ca}$  differential cross sections were normalized by the same amount  $N_{\text{ES}}$  as that of the focal plane  $^{39}\text{K}(\text{He}^3, \text{He})^{39}\text{K}$  measurements, since both were measured relative to the elastic scattering of the Si detector. The remaining normalization,

$$\frac{d\sigma}{d\Omega_{\text{Exp}}} = C^2 S \frac{d\sigma}{d\Omega_{\text{DWBA}}}, \quad (4.43)$$

between the scale-corrected transfer differential cross section  $d\sigma/d\Omega_{\text{Exp}}$  and that of an appropriate distorted-wave Born approximation (DWBA) model  $d\sigma/d\Omega_{\text{DWBA}}$  defines the spectroscopic factor  $C^2 S$ . The spectroscopic factor for  $^{39}\text{K}(\text{He}^3, d)^{40}\text{Ca}$  is broken into two parts, corresponding to the  $^{39}\text{K} + p$  and  $d + p$  overlaps (see Section 2.4.2),

$$C^2 S = C^2 S_{^{39}\text{K}+p} C^2 S_{d+p}. \quad (4.44)$$

The  $C^2S_{d+p}$  spectroscopic factor is frequently omitted in the literature, as it is a constant factor applied to all  $C^2S$  for  $(^3\text{He}, d)$  reactions. It can be approximated as  $A/2$  for  $A \leq 4$  nuclei [Sat83], which implies  $C^2S_{d+p} = 1.5$ . However, *ab-initio* calculations such as those from Ref. [Bri11] can be more precise, reducing systematic uncertainties associated with  $C^2S_{^{39}\text{K}+p}$ . Ref. [Bri11] calculates  $C^2S_{d+p} = 1.32(1)$ , which is adopted in the present analysis. The  $C^2S_{^{39}\text{K}+p}$  spectroscopic factor for proton-unbound states, when converted to a proton partial-width in Section 4.7.5, is a direct input in the  ${}^{39}\text{K}(p, \gamma){}^{40}\text{Ca}$  reaction rate. This is the main quantity of astrophysical interest in transfer reactions.

DWBA transfer reaction calculations require optical model potentials (OMPs) for both the incoming  ${}^{39}\text{K} + {}^3\text{He}$  and the outgoing  $d + {}^{40}\text{Ca}$  channels. The potential for the incoming channel is evaluated at the lab beam energy  $E_{\text{lab}}$ , whereas the outgoing channel potential is evaluated at  $E_{\text{lab}} - Q$ , where  $Q$  is the  $Q$ -value of the transfer reaction. The global  ${}^3\text{He}$  OMP of Ref. [Lia09] from the elastic scattering normalization is retained for the incoming channel. The parameters of this OMP were given in Table 4.2. For the outgoing channel, the global  $d$  OMP of Ref. [An06] is used in the present analysis, where the potential is defined in the exact same way as that of Ref. [Lia09].

The proton bound-state potential must also be specified for DWBA calculations of proton-bound  ${}^{40}\text{Ca}$  states. It consists of a real volume potential with a Woods-Saxon form and a Coulomb potential. The Woods-Saxon well depth  $V_r$  is automatically adjusted to reproduce the proton binding energy,

$$\text{BE}\left({}^{A-1}(X-1) + p\right) = S_p({}^AX) - E_x, \quad (4.45)$$

where  $S_p$  is the proton-separation energy of the compound nucleus  ${}^AX$ , and  $E_x$  is its excitation energy. However, many of the states observed in the present experiment, and indeed all of the states of astrophysical interest, are proton-unbound. In these cases, one could adjust the Woods-Saxon well depth until a resonance is formed at  $E_r$ . This is unfortunately not performed automatically in **Fresco** [Tho88, Tho06], the nuclear reaction code chosen for the present analysis. An alternative to this is to approximate the resonance scattering wave function as the wave function for a loosely-bound particle, with a binding energy of  $\lesssim 50$  keV. This is known as the weak binding approximation, and it has been shown to reproduce unbound calculations of  $C^2S$  to within 1% for states within about 500 keV of the particle threshold and 6% for states within about 1800 keV above the particle threshold [Kan16, Kah19]. The present analysis uses the weak binding approximation for unbound  ${}^{40}\text{Ca}$  states. The proton bound-state parameters, along with the global OMP parameters are summarized in Table 4.4.

Table 4.4: Global optical model potential parameters for  $^{39}\text{K} + ^3\text{He}$  and  $^{40}\text{Ca} + d$  and the proton bound-state parameters.

particle	$V_r$	$r_r$	$a_r$	$W_v$	$r_v$	$a_v$	$W_s$	$r_s$	$a_s$	$V_{so}$	$r_{so}$	$a_{so}$	$W_{so}$	$r_c$
$^3\text{He}$	117.881	1.178	0.768	-0.646	1.415	0.847	20.665	1.198	0.852	2.083	0.738	0.946	-1.159	1.289
$d$	91.120	1.150	0.762	2.234	1.334	0.513	10.274	1.378	0.743	3.557	0.972	1.011		1.303
$p$	$V_p^1$	1.250	0.650											1.250

Another factor that must be considered in DWBA calculations is the transferred-particle overlaps, in this case for  $^{39}\text{K} + p$  and  $d + p$ . Each overlap is specified by a single-particle state  $n\ell_j$  from the shell model with the quantum numbers  $n$ ,  $\ell$ , and  $j$  corresponding to the node, transferred orbital angular momentum, and total angular momentum ( $j = \ell \pm 1/2$ ), respectively (see Ref. [Kra87]). Only a select few single-particle states can be populated from a given transition, based on quantum-mechanical selection rules for angular momentum and parity (see Ref. [Ili15a]). For example, if the spin-parity  $J^\pi$  of the final  $^{40}\text{Ca}$  state is known, the possible  $n$ ,  $\ell$ , and  $j$  single-particle quantum numbers can be extracted from the selection rules. This can also be done for final states where  $J^\pi$  is narrowed down to a few possibilities. This extraction was performed for each excited state of  $^{40}\text{Ca}$  populated in the present experiment, given their known spin-parities, or spin-parity candidates, from the ENSDF evaluation of Ref. [Che17]. The  $d + p$  overlap was treated as constant for each DWBA calculation, since it was assumed that it occupied only the  $^3\text{He}$  ground state.

The nuclear reaction code **Fresco** [Tho88, Tho06] was used to calculate  $^{39}\text{K}(^3\text{He}, d)^{40}\text{Ca}$  DWBA differential cross sections using the zero-range (ZR) approximation introduced in Section 2.4.2. Calculations were performed for the allowed  $n\ell_j$  combinations of each excited state, based on their known  $J^\pi$  values from ENSDF. In cases where none of the angular distributions agreed with the experimental cross section, the  $n\ell_j$  combinations were expanded to account for different final  $J^\pi$  values. An example of the normalization procedure and the different  $n\ell_j$  combinations for the 7532 keV state is shown in Fig. 4.27. This state has a spin-parity of  $2^-$  from ENSDF, and therefore allows  $\ell = 1$  or  $\ell = 3$  orbital angular momenta from selection rules. The most likely single-particle states corresponding to these  $\ell$ -values are  $2p_{3/2}$  or  $2p_{1/2}$  for  $\ell = 1$  and  $1f_{7/2}$  or  $1f_{5/2}$  for  $\ell = 3$ , as they are the lowest energy transitions from the  $^{39}\text{K}$  ground state at  $1d_{3/2}$ . The higher  $n$ -values for a given  $\ell$  transition have a much greater transition energy and are therefore less likely. For that reason they are typically omitted in the literature. However, they were included in the analysis for completion and to test their effects. From Fig. 4.27, it is clear that the DWBA differential cross sections increase with increasing  $n$ . It can also be seen that the  $n$ - $\ell$  pairs produce very similar differential cross sections at low angles. This is especially true at angles below the first minimum, where the

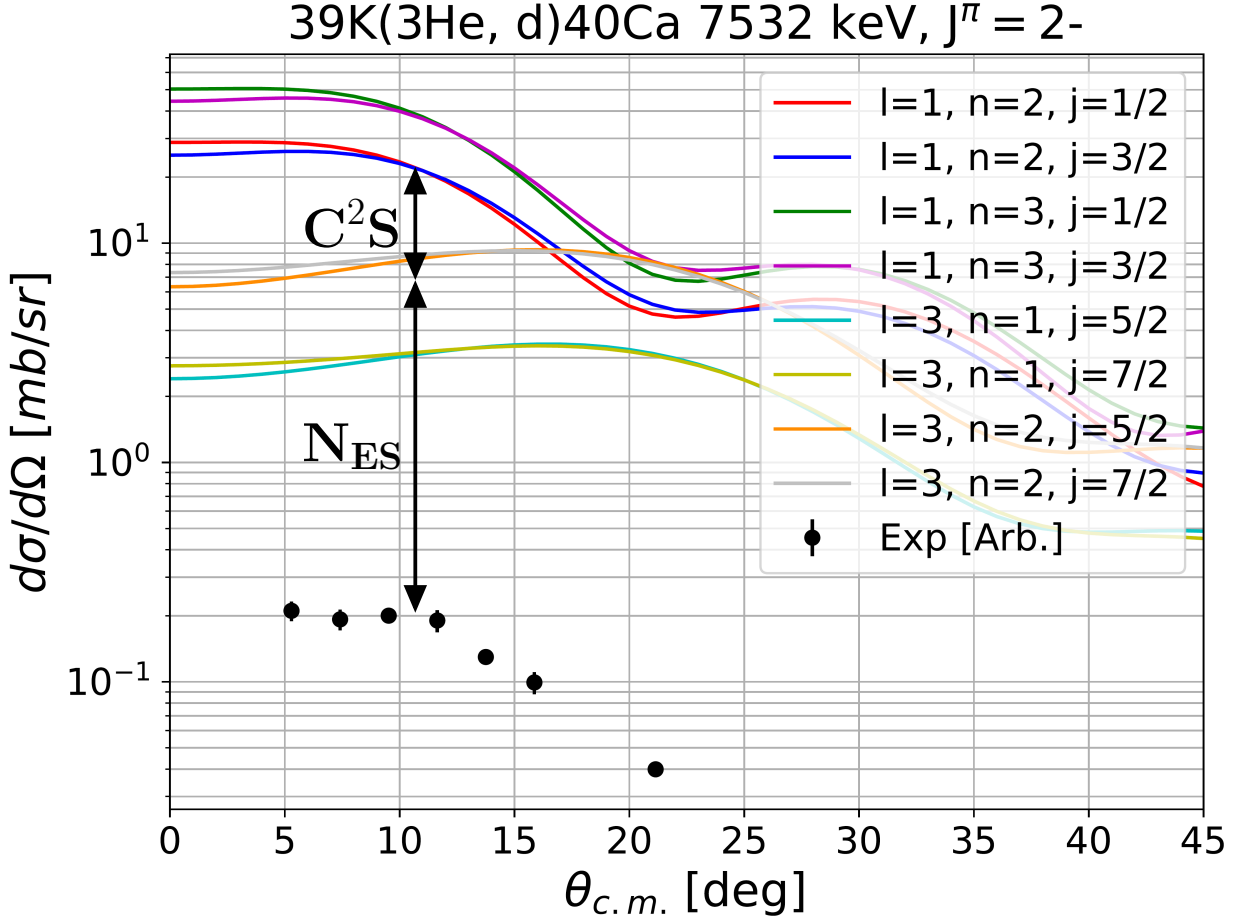


Figure 4.27: Normalization between the relative transfer differential cross section of the 7532 keV state and that of all possible DWBA models based on the current ENSDF  $J^\pi = 2^-$  assignment. The normalization  $N_{\text{ES}}$  between elastic scattering and the global  ${}^3\text{He}$  OMP is shown to scale, as is the  $C^2S$  normalization.

DWBA differential cross sections are most reliable. It is common during normalization to omit angles greater than the first DWBA minimum because that is roughly where the distorted-wave Born approximation loses validity. However, the present  ${}^{39}\text{K}({}^3\text{He}, d){}^{40}\text{Ca}$  experiment did not obtain data beyond the first minimum, so normalization was performed with all experimental points.

Fig. 4.28 shows the same differential cross sections as in Fig. 4.27, but the DWBA models have been scaled down to the experimental points to show all normalizations simultaneously. It is clear that the  $\ell = 1$  models match the angular distribution of the points. However, it is not possible to tell which of the  $\ell = 1$  models is the best match. As is done in the literature [Ers66, Set67, For70, Cag71, Fuc69], the present analysis chooses the  $n-j$  pair associated with

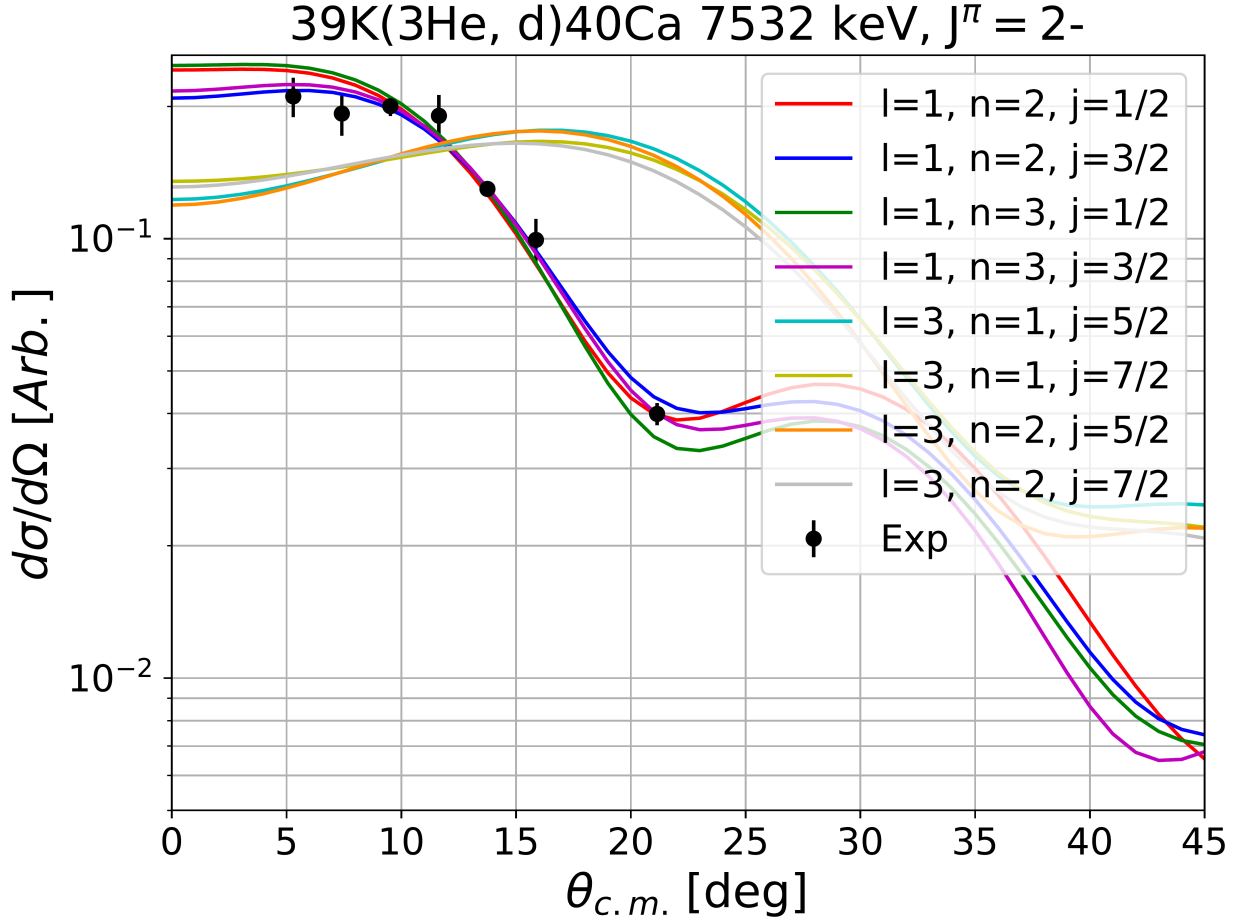


Figure 4.28: The DWBA models of Fig. 4.27 scaled down to the 7532 keV data to compare angular distributions. The  $l = 1$  models are a clear match for this state.

the lowest energy single-particle state, unless it is forbidden by selection rules. That is, unless they are forbidden, all  $\ell = 0$ ,  $\ell = 1$ ,  $\ell = 2$ , and  $\ell = 3$  distributions will be associated with  $3s_{1/2}$ ,  $2p_{3/2}$ ,  $2d_{5/2}$ , and  $1f_{7/2}$  single-particle states, respectively.

Finally, another transfer consideration comes from the fact that  $^{39}\text{K}$  has a non-zero ground state ( $J^\pi = 3/2^+$ ). It is possible in this case that more than one single-particle state contributes to the differential cross section, resulting in a mixed- $\ell$  angular distribution. Theoretically, all allowed  $\ell$  transitions can contribute, but it is usually impossible to distinguish between more than the two lowest  $\ell$  transitions. The differential cross section decreases with increasing  $\ell$ , making each larger  $\ell$  contribution more negligible [Hod71]. The mixed- $\ell$  angular distributions should then resemble a sum of two DWBA differential cross sections,

$$\frac{d\sigma}{d\Omega}_{\text{Exp}} = C^2 S_{\ell_1} \frac{d\sigma}{d\Omega}_{\text{DWBA}, \ell_1} + C^2 S_{\ell_2} \frac{d\sigma}{d\Omega}_{\text{DWBA}, \ell_2}. \quad (4.46)$$

The individual spectroscopic factors are given the common parameter  $\alpha$  which determines their fractional contributions, as in

$$C^2 S_{\ell_1} = \alpha C^2 S, \quad (4.47)$$

$$C^2 S_{\ell_2} = (1 - \alpha) C^2 S, \quad (4.48)$$

where  $C^2 S$  represents the joint spectroscopic factor. A  $\chi^2$ -minimization is performed in mixed- $\ell$  cases to determine the  $\alpha$  and  $C^2 S$  parameters, and the individual  $C^2 S_{\ell_1}$  and  $C^2 S_{\ell_2}$  are then reported. Their statistical uncertainties are obtained from the variance-covariance matrix elements added in quadrature to the  $d\sigma/d\Omega_{\text{Exp}}$  uncertainties.

### 4.7.3 Angular Distribution Results

Figs. 4.29–4.33 show the angular distributions extracted for each  $^{40}\text{Ca}$  state observed in the  $^{39}\text{K}(^{3}\text{He}, d)^{40}\text{Ca}$  experiment, with a few exceptions. The states observed above 9227 keV (9405–9603 keV) did not match any DWBA prescription. The experimental differential cross sections for these states rapidly decreased as a function of angle faster than even the lowest possible  $\ell$  transition. This is likely due to these peaks being too near the edge of the focal plane detector, which is exacerbated with increasing angle. The detector efficiency is significantly reduced at the fringes, which makes yield measurements unreliable. Another factor could be the breakdown of the weak binding approximation in DWBA models for states with energies this high above the proton separation energy, albeit likely to a lesser degree, considering the good agreement with the nearby 9227 keV differential cross section. Energies were still extracted for states up to 9603 keV with relatively small residuals from ENSDF [Che17] because detector efficiency does not affect centroid position, and DWBA calculations are not used in the energy calibration. Fig. 4.33 focuses on the proton-unbound  $^{40}\text{Ca}$  states of astrophysical interest ( $E_x = 8359$ –8851 keV), which are below the lowest directly measured  $^{39}\text{K}(p, \gamma)^{40}\text{Ca}$  resonance at  $E_x = 8935$  keV ( $E_r^{\text{c.m.}} = 606$  keV). These are the states that are updated in the new reaction rate calculation, shown in Section 4.8.

The angular distribution of each state is described in detail in the following discussion, where each excited state energy is labeled by its ENSDF [Che17] energy for clarity. For proton-unbound states, the resonance energy  $E_r^{\text{c.m.}}$  is also provided based on the energy calibration of the present analysis. Spectroscopic factors are compared to literature in Section 4.7.4, and the proton partial-widths of the states of astrophysical interest are discussed in Section 4.7.5.

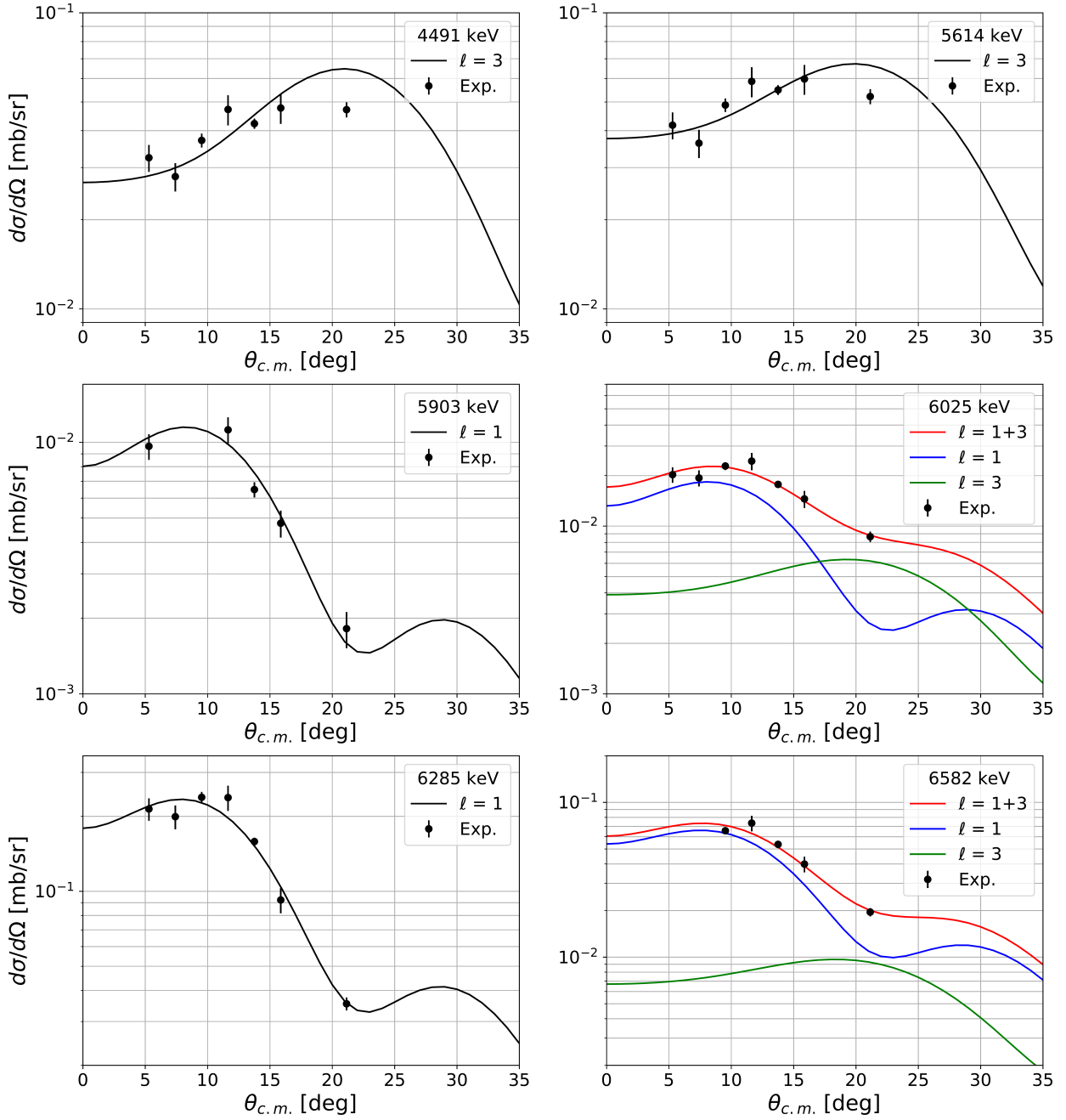


Figure 4.29: Differential cross sections for 4491 keV through 6582 keV. See text for details.

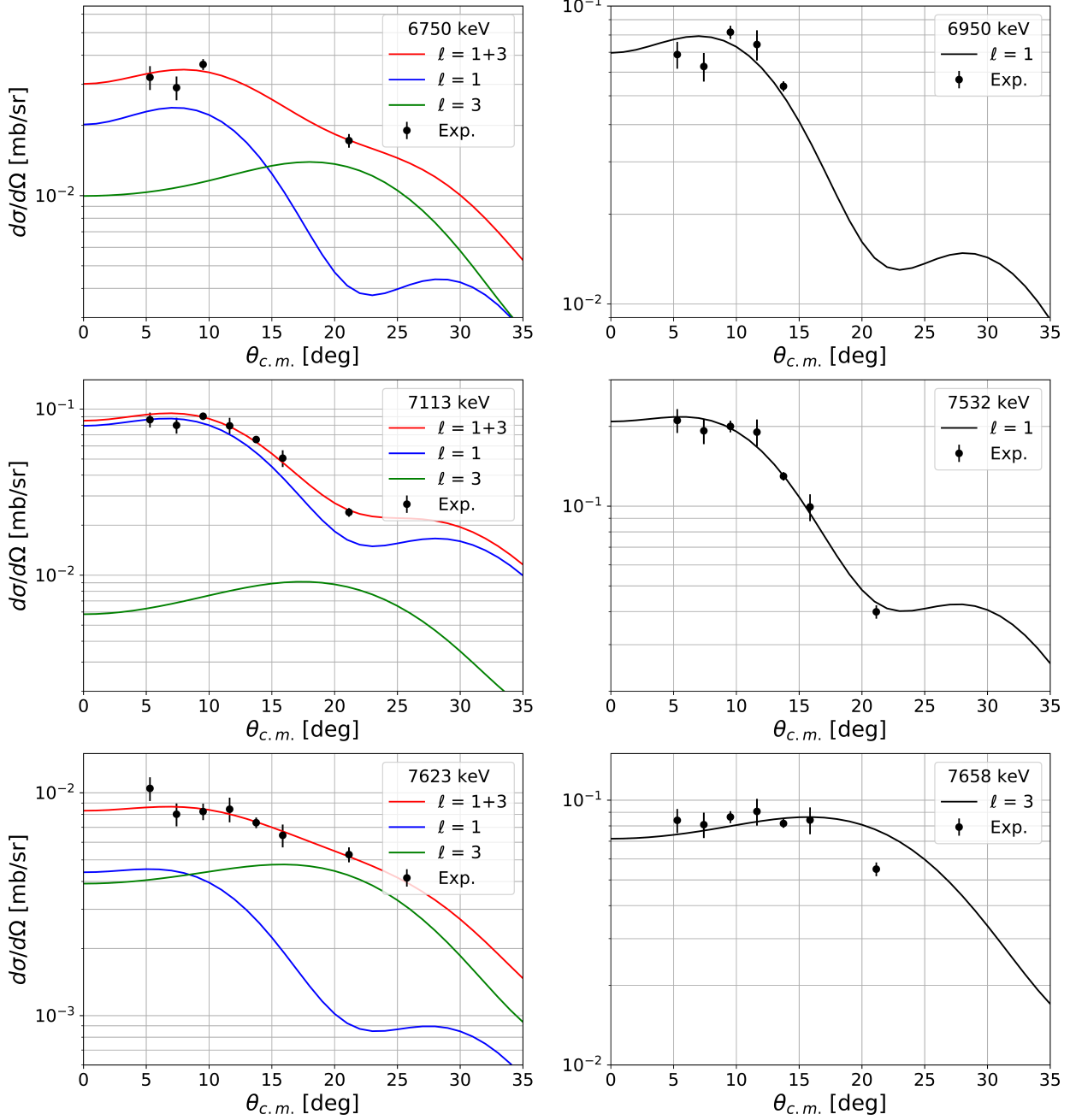


Figure 4.30: Differential cross sections for 6750 keV through 7658 keV. See text for details.

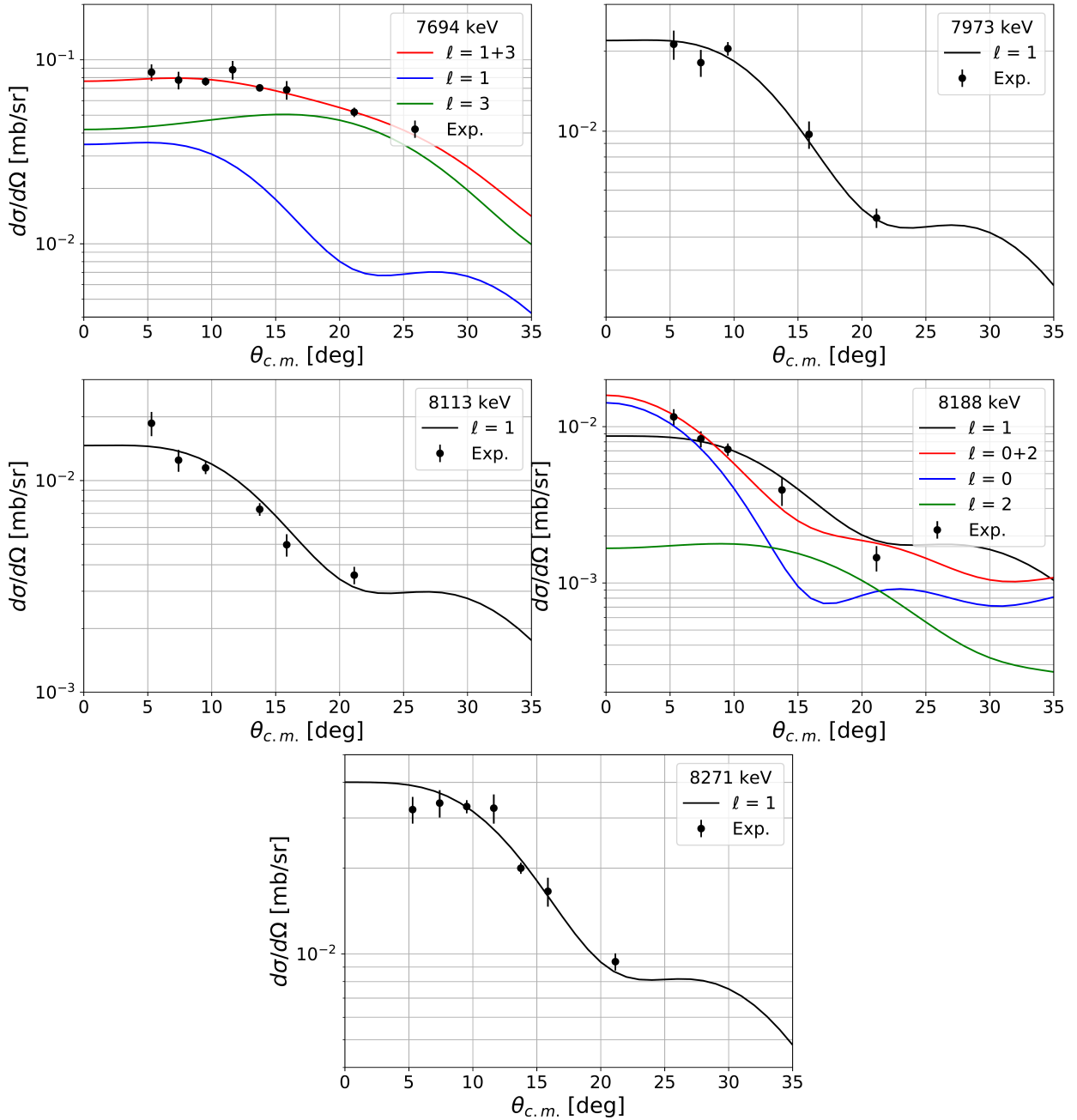


Figure 4.31: Differential cross sections for 7694 keV through 8271 keV. See text for details.

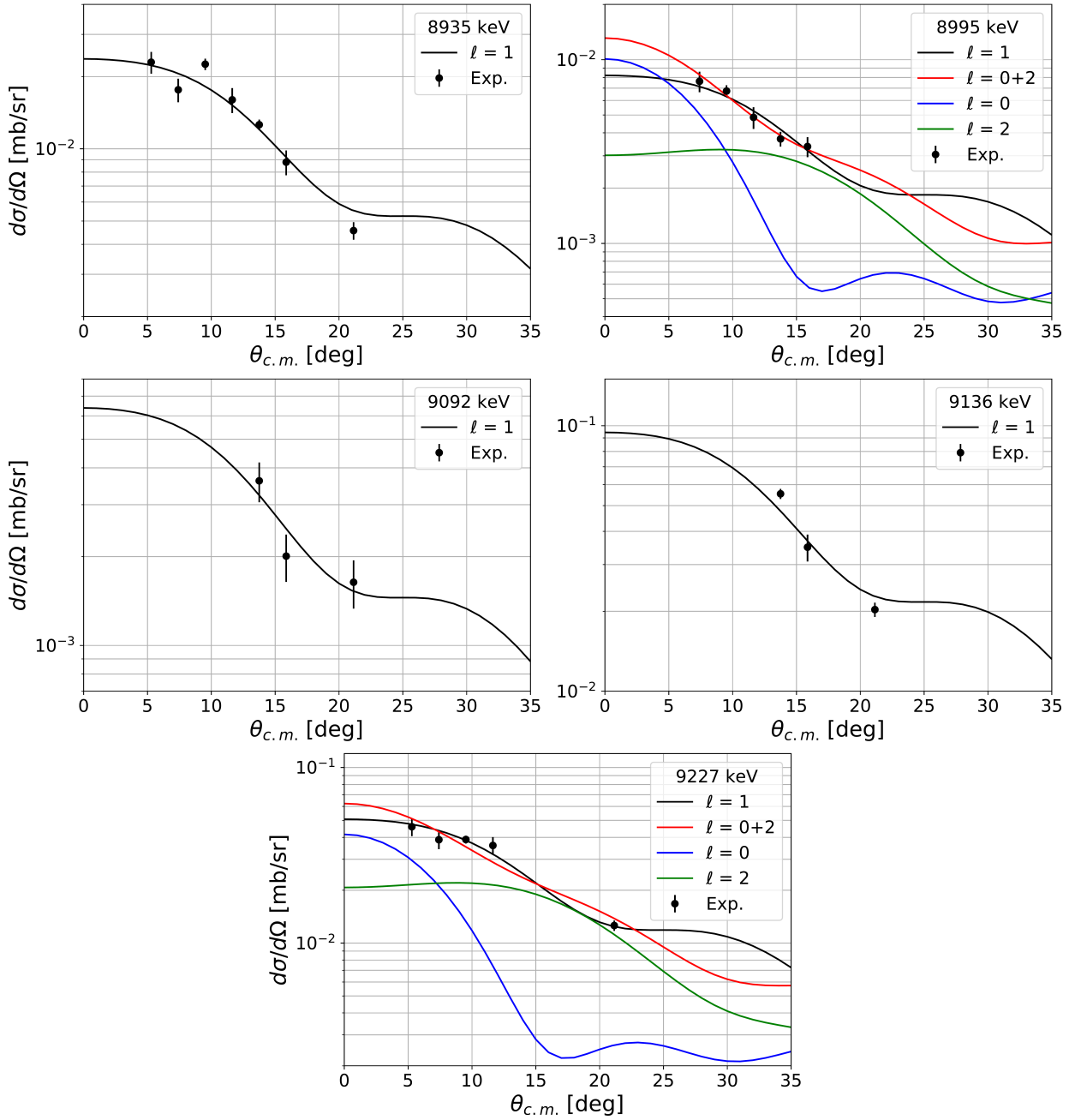


Figure 4.32: Differential cross sections for 8935 keV through 9227 keV. See text for details.

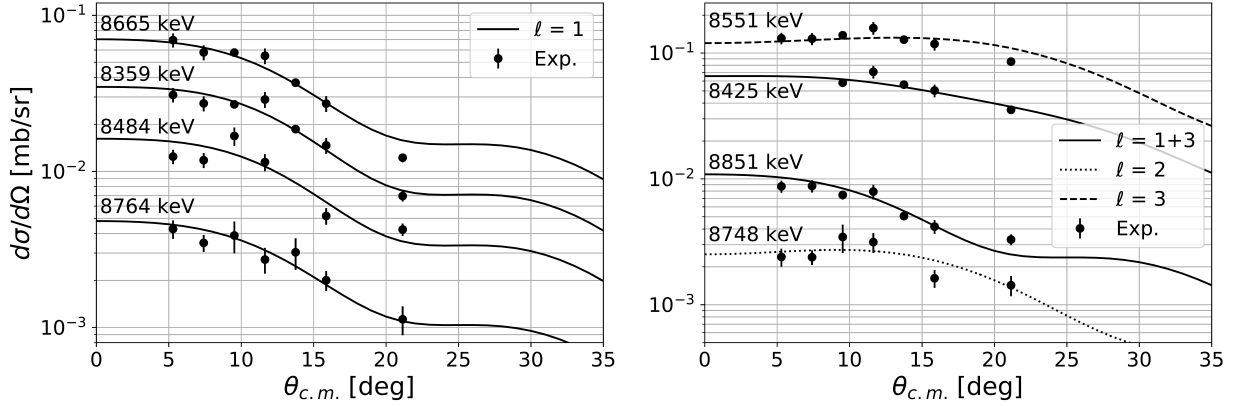


Figure 4.33: Differential cross-sections of proton-unbound  $^{40}\text{Ca}$  states observed in the present experiment below the lowest directly measured ( $p, \gamma$ ) resonance at 8935 keV. The left panel shows the  $\ell = 1$  distributions, while the right panel shows all other distributions.

**$E_x = 4491$  keV:** The spin-parity of this state is assigned  $J^\pi = 5^-$  by ENSDF [Che17], and its angular distribution is assigned  $\ell = 3$  from the present analysis. This is in agreement with all of the  $(^3\text{He}, d)$  measurements from Refs. [Ers66, Set67, For70, Cag71] and the only  $(d, n)$  measurement of Ref. [Fuc69] in the literature.

**$E_x = 5614$  keV:** The spin-parity of this state is assigned  $J^\pi = 4^-$  by ENSDF. Its angular distribution is assigned  $\ell = 3$  from the present analysis, in agreement with the literature [Ers66, Set67, For70, Cag71, Fuc69].

**$E_x = 5903$  keV:** The spin-parity of this state is assigned  $J^\pi = 1^-$  by ENSDF. Its angular distribution is assigned  $\ell = 1$  from the present analysis, despite it being obscured by the 4915 keV  $^{14}\text{N}$  contaminant at  $\theta_{\text{lab}} = 7^\circ$  and  $9^\circ$ . This is in agreement with Refs. [Ers66, Set67, Cag71] but in disagreement with  $(d, n)$  [Fuc69], where  $\ell = 1 + 3$  is assigned. It was not resolved by Ref. [For70].

**$E_x = 6025$  keV:** The spin-parity of this state is assigned  $J^\pi = 2^-$  by ENSDF, and its angular distribution is assigned  $\ell = 1 + 3$  from the present analysis. This is in agreement with Refs. [Ers66, Set67] and  $(d, n)$  [Fuc69], but in disagreement with Ref. [Cag71], where  $\ell = 3$  is assigned. It was not resolved by Ref. [For70].

**$E_x = 6285$  keV:** The spin-parity of this state is assigned  $J^\pi = 3^-$  by ENSDF, and its angular distribution is assigned  $\ell = 1$  from the present analysis. This is in agreement with Refs. [Ers66, For70, Cag71], but in disagreement with Ref. [Set67] and  $(d, n)$  [Fuc69] where  $\ell = 1 + 3$  is assigned.

**$E_x = 6582$  keV:** The spin-parity of this state is assigned  $J^\pi = 3^-$  by ENSDF, and its angular distribution is assigned  $\ell = 1 + 3$  from the present analysis, with most of the contribution from  $\ell = 1$ . It is obscured by the  $^{13}\text{N}$  ground state at  $\theta_{\text{lab}} \leq 7^\circ$ . This is in

agreement with  $(d, n)$  [Fuc69], but in disagreement with  $(^3\text{He}, d)$  [Ers66, Set67, For70, Cag71], which assign it purely  $\ell = 1$ .

**$E_x = 6750 \text{ keV}$ :** The spin-parity of this state is assigned  $J^\pi = 2^-$  by ENSDF, and its angular distribution is assigned  $\ell = 1 + 3$  from the present analysis. It is obscured by the  $^{13}\text{N}$  ground state at  $\theta_{\text{lab}} = 11^\circ, 13^\circ$ , and  $15^\circ$ . This state is widely disputed in the literature. It is in agreement with  $(d, n)$  [Fuc69], but Refs. [Ers66, Set67, For70] assign it  $\ell = 1$ , and Ref. [Cag71] assigns it  $\ell = 3$ .

**$E_x = 6950 \text{ keV}$ :** The spin-parity of this state is assigned  $J^\pi = 1^-$  by ENSDF, and its angular distribution is assigned  $\ell = 1$  from the present analysis. It is obscured by the 5834 keV  $^{14}\text{N}$  state at  $\theta_{\text{lab}} = 15^\circ$  and  $20^\circ$ . The energy residuals are about 13 keV lower than ENSDF at  $\theta_{\text{lab}} = 5^\circ$  and  $7^\circ$ , which makes these measurements questionable, but the remaining angles show only a 2 keV residual from ENSDF. Even among the other angles alone, however, the angular distribution is clearly  $\ell = 1$  and not  $\ell = 3$ . This assignment is in agreement with  $(^3\text{He}, d)$  [Ers66, Set67, For70, Cag71], but in disagreement with  $(d, n)$  [Fuc69] where  $\ell = 1 + 3$  is assigned.

**$E_x = 7113 \text{ keV}$ :** In ENSDF, the 7113.1(10) keV and 7113.73(5) keV states have spin-parities of  $J^\pi = 1^-$  and  $J^\pi = 4^-$ , respectively. The present energy calibration yielded a state at 7109.4(29) keV, within the uncertainty of the  $1^-$  state, but not the  $4^-$  state. An angular distribution of  $\ell = 1 + 3$  is assigned in the present analysis, with the main contribution from  $\ell = 1$ . This is impossible for a  $4^-$  state, where only  $\ell = 3$  and/or  $\ell = 5$  can be observed. Both of these measurements indicate that this corresponds with the 7113.1(10) keV  $1^-$  state, with possibly a small contribution from the 7113.73(5) keV  $4^-$  state at  $\ell = 3$ . This assignment is in agreement with  $(d, n)$  [Fuc69], but in disagreement with  $(^3\text{He}, d)$  [Ers66, Set67, For70, Cag71], where purely  $\ell = 1$  is assigned. This was the highest energy state measured by Ref. [For70], so this reference is omitted from the remaining discussion.

**$E_x = 7532 \text{ keV}$ :** The spin-parity of this state is assigned  $J^\pi = 2^-$  by ENSDF, and its angular distribution is assigned  $\ell = 1$  from the present analysis. This is in agreement with Refs. [Ers66, Cag71], but in disagreement with Ref. [Set67] and  $(d, n)$  [Fuc69] where  $\ell = 1 + 3$  is assigned.

**$E_x = 7623 \text{ keV}$ :** The spin-parity of this state is assigned  $J^\pi = (2^-, 3, 4^+)$  by ENSDF and was not resolved by  $(^3\text{He}, d)$  [Ers66, Set67, Cag71] or  $(d, n)$  [Fuc69]. This experiment has resolved this state for the first time through proton-transfer. Its angular distribution is assigned  $\ell = 1 + 3$  in the present analysis. This implies a  $J^\pi$  assignment of  $1^-, 2^-, 3^-$ . Comparing with ENSDF, the  $J^\pi = 3^+$  and  $4^+$  assignments can be ruled out with this measurement.

**$E_x = 7658 \text{ keV}$ :** The spin-parity of this state is assigned  $J^\pi = 4^-$  by ENSDF, and its

angular distribution is assigned  $\ell = 3$  in the present analysis, in agreement with the literature [Ers66, Set67, Cag71, Fuc69].

**$E_x = 7694$  keV:** The spin-parity of this state is assigned  $J^\pi = 3^-$  by ENSDF, and its angular distribution is assigned  $\ell = 1+3$  in the present analysis. This state is disputed across the literature. The present assignment is in agreement with Ref. [Ers66], but in disagreement with Refs. [Set67, Cag71] and  $(d, n)$  [Fuc69], where  $\ell = 3$  and  $\ell = 1$  are assigned, respectively.

**$E_x = 7973$  keV:** The spin-parity of this state is assigned  $J^\pi = (\text{LE } 3)^-$  by ENSDF based only on  $(d, n)$  [Fuc69]. It was not resolved by  $(^3\text{He}, d)$  [Ers66, Set67, Cag71]. This state was obscured in this experiment by the  $^{17}\text{F}$  ground state at  $\theta_{\text{lab}} = 11^\circ$  and  $13^\circ$ . The present analysis assigns  $\ell = 1$ , in agreement with  $(d, n)$ . This experiment alone suggests  $J^\pi = 0^-, 1^-, 2^-, 3^-$ .

**$E_x = 8113$  keV:** The spin-parity of this state is assigned  $J^\pi = 1^-$  by ENSDF, and it was not resolved by  $(^3\text{He}, d)$  [Ers66, Set67, Cag71]. The present analysis assigns  $\ell = 1$ , in disagreement with  $(d, n)$  [Fuc69], where  $\ell = 1+3$  is assigned. However, Ref. [Fuc69] observes a doublet at 8113 keV and 8135 keV, which is not observed in the present experiment. The presence of the 6859 keV  $^{15}\text{O}$  contaminant complicates matters because it overlaps with where the 8135 keV state is expected, making this state impossible to resolve. The 7029 keV  $^{14}\text{N}$  and 6793 keV  $^{15}\text{O}$  contaminants obscure the  $\theta_{\text{lab}} = 11^\circ$  measurement.

**$E_x = 8188$  keV ( $E_x = 8196$  keV):** The spin-parity of the 8188 keV state is assigned  $J^\pi = (3, 4, 5^-)$  in ENSDF, and it was not resolved by  $(^3\text{He}, d)$  [Ers66, Set67, Cag71]. No spectroscopic factor was reported from  $(d, n)$  [Fuc69] for a state observed at 8186 keV, but it was assigned a  $\ell = 0$  transition nonetheless. This would imply  $J^\pi = 1^+, 2^+$ , which conflicts with ENSDF. The present energy calibration found a state at 8199.3(27) keV, or a residual from the 8188 keV state of 11.8(28) keV. There is in fact a state at 8196 keV reported in ENSDF, but it has only been observed in  $(p, t)$  [Set74, Set77] and  $(p, p')$  [Nol75], and no official  $J^\pi$  assignment has been made. However, the  $(p, t)$  measurement of Ref. [Set77] makes a weak assignment of  $\ell = (2)$  for this state, which for  $(p, t)$  implies  $J^\pi = (0, 1)^+$ . In the present experiment, there is ambiguity in the angular momentum between  $\ell = 0+2$  and  $\ell = 1$ , with the  $\ell = 0+2$  transition being slightly more favorable. The spin-parities would be  $J^\pi = 0^+, 1^+$  for the former transition and  $J^\pi = 0^-, 1^-, 2^-, 3^-$  for the latter. It is possible that the  $(d, n)$  [Fuc69] assignment of  $\ell = 0$  applies to the 8196 keV state, a 10 keV residual, which would be more in alignment with the present measurement and Refs. [Set74, Set77, Nol75]. This may even be likely, considering that Ref. [Fuc69] also determined the energy of a nearby state to be 8371 keV, which is interpreted by ENSDF as coinciding with the 8359 keV state, a 12 keV residual. Observation of this state in the present experiment was obscured at  $\theta_{\text{lab}} = 11^\circ$  by the 6859 keV  $^{15}\text{O}$  state and at  $15^\circ$  by the 7029 keV  $^{14}\text{N}$  and 6793 keV  $^{15}\text{O}$  states.

**$E_x = 8271$  keV:** The spin-parity of this state is assigned  $J^\pi = (\text{LE } 3)^-$  by ENSDF, and it was not resolved by  $(^3\text{He}, d)$  [Ers66, Set67, Cag71]. The present analysis assigns  $\ell = 1$ , in agreement with  $(d, n)$  [Fuc69]. These experiments alone suggest  $J^\pi = 0^-, 1^-, 2^-, 3^-$ .

**$E_x = 8359$  keV;  $E_r^{\text{c.m.}} = 29$  keV:** This is the lowest energy proton-unbound state observed in the present experiment. The spin-parity of this state is assigned  $J^\pi = (0, 1, 2)^-$  in ENSDF, and it was not resolved by  $(^3\text{He}, d)$  [Ers66, Set67, Cag71]. The present analysis assigns  $\ell = 1$ , in agreement with  $(d, n)$  [Fuc69]. The recent  ${}^{39}\text{K}(p, \gamma){}^{40}\text{Ca}$  reaction rate evaluation from Ref. [Lon18b] did not use the  $(d, n)$  [Fuc69]  $C^2S$  measurement for a state at 8371 keV in their analysis because of the 12 keV energy discrepancy with ENSDF. This state was instead assigned a proton partial-width upper limit in the reaction rate calculation which the present work now replaces.

**$E_x = 8425$  keV;  $E_r^{\text{c.m.}} = 96$  keV:** The spin-parity of this state is assigned  $J^\pi = 2^-$  in ENSDF, and it has also since been confirmed via NRF [Gri22]. The present work assigns  $\ell = 1 + 3$ , in agreement with  $(d, n)$  [Fuc69], but in disagreement with  $(^3\text{He}, d)$  [Ers66, Set67, Cag71], where  $\ell = 3$  is assigned. Ref. [Lon18b] uses the  $(^3\text{He}, d)$   $C^2S$  measurement of Ref. [Cag71] in their reaction rate calculation. This state was obscured in the present experiment at  $\theta_{\text{lab}} = 5^\circ$  and  $7^\circ$  by the  ${}^{17}\text{F}$  first excited state.

**$E_x = 8484$  keV;  $E_r^{\text{c.m.}} = 154$  keV:** This weakly-populated state has not been observed in  $(^3\text{He}, d)$  [Ers66, Set67, Cag71] or  $(d, n)$  [Fuc69]. It has therefore been resolved for the first time in  ${}^{39}\text{K} + p$  from this experiment because the lowest energy resonance resolved by  $(p, \gamma)$  [Kik90, Che81, Lee66] is for  $E_r^{\text{c.m.}} = 606$  keV. Its spin-parity is assigned  $J^\pi = (1^-, 2^-, 3^-)$  in ENSDF. The present work assigns  $\ell = 1$  in support of the ENSDF  $J^\pi$  assignment. This measurement replaces the proton partial-width upper limit of Ref. [Lon18b] in the reaction rate calculation. This state was obscured in the present experiment at  $\theta_{\text{lab}} = 13^\circ$  by the  ${}^{17}\text{F}$  first excited state.

**$E_x = 8551$  keV;  $E_r^{\text{c.m.}} = 221$  keV:** The spin-parity of this state is assigned  $J^\pi = 5^-$  in ENSDF. The present work assigns  $\ell = 3$ , in agreement with  $(^3\text{He}, d)$  [Ers66, Set67, Cag71] and  $(d, n)$  [Fuc69].

**$E_x = 8665$  keV;  $E_r^{\text{c.m.}} = 335$  keV:** The spin-parity of this state is assigned  $J^\pi = 1^-$  in ENSDF, and it was not resolved by  $(^3\text{He}, d)$  [Ers66, Set67, Cag71]. The present work assigns  $\ell = 1$  in agreement with  $(d, n)$  [Fuc69].

**$E_x = 8748$  keV;  $E_r^{\text{c.m.}} = 415$  keV:** This weakly-populated state was observed in  $(d, n)$  [Fuc69] as part of an unresolved doublet with the 8764 keV state, but no  $\ell$  assignments were made. Neither state was resolved in  $(^3\text{He}, d)$  [Ers66, Set67, Cag71] or  $(p, \gamma)$  [Kik90, Che81, Lee66], but they have been resolved in the present experiment, making this the first time they have been resolved in  ${}^{39}\text{K} + p$  altogether. The spin-parity of the 8748 keV state

is assigned  $J^\pi = 2^+$  in ENSDF and has since been confirmed by NRF [Gri22]. The present work assigns  $\ell = 2$  in support of the ENSDF  $J^\pi$  assignment. This measurement replaces the proton partial-width upper limit of Ref. [Lon18b] in the reaction rate calculation. The statistics were not sufficient to obtain fits for  $\theta_{\text{lab}} = 13^\circ$  for this state.

**$E_x = 8764 \text{ keV}; E_r^{\text{c.m.}} = 439 \text{ keV}$ :** This state is part of a doublet with 8748 keV and was not resolved in  $(^3\text{He}, d)$  [Ers66, Set67, Cag71],  $(d, n)$  [Fuc69], or  $(p, \gamma)$  [Kik90, Che81, Lee66]. Its spin-parity is assigned  $J^\pi = 3^-$  in ENSDF, and the present work assigns  $\ell = 1$ , in support of this assignment. This experiment is therefore the first to resolve this state for  ${}^{39}\text{K} + p$ , and its measurement replaces the proton partial-width upper limit of Ref. [Lon18b] in the reaction rate calculation.

**$E_x = 8851 \text{ keV}; E_r^{\text{c.m.}} = 521 \text{ keV}$ :** The spin-parity of this state is assigned  $J^\pi = 6^-, 7^-, 8^-$  in ENSDF based on  $(p, p')$  [Gru72]. It was observed in  $(d, n)$  [Fuc69] with no  $\ell$  assignment determined, and it was not resolved by  $(^3\text{He}, d)$  [Ers66, Set67, Cag71] or  $(p, \gamma)$  [Kik90, Che81, Lee66]. The present experiment assigns  $\ell = 1 + 3$ , making its resolution a first for  ${}^{39}\text{K} + p$ . The  $\ell$  assignment suggests  $J^\pi = (1, 2, 3)^-$ , in stark disagreement with ENSDF. The upper limit from Ref. [Lon18b] for this state uses the ENSDF  $J^\pi$  assignment in the reaction rate calculation. For this reason, the  $(2J + 1)\Gamma_p$  value from this work is about 2 orders of magnitude larger than the upper limit, as shown in Table 4.7.

**$E_x = 8935 \text{ keV}; E_r^{\text{c.m.}} = 608 \text{ keV}$ :** In ENSDF, the 8934.81(7) keV and 8938.4(9) keV states have spin-parities of  $J^\pi = 2^+$  and  $J^\pi = 0^+$ , respectively. The 8934.81(7) keV state is the lowest energy proton-unbound state measured by the direct  $(p, \gamma)$  [Kik90] experiment, and they do not observe the 8938.4(9) keV state. The present energy calibration yielded a state at 8936.3(27) keV, within the uncertainty of both states. Neither state is resolved by  $(^3\text{He}, d)$  [Ers66, Set67, Cag71]. The present analysis assigns  $\ell = 1$ , in agreement with the 8931 keV assignment from  $(d, n)$  [Fuc69], and this joins Ref. [Fuc69] in disagreement with ENSDF. These measurements imply  $J^\pi = 0^-, 1^-, 2^-, 3^-$ . It is worth noting that a  $\ell = 0 + 2$  assignment was considered in the present analysis, which would imply  $J^\pi = 1^+, 2^+$ , in agreement with  $(p, \gamma)$  [Kik90]. However, the  $\ell = 1$  transition is significantly more likely.

**$E_x = 8995 \text{ keV}; E_r^{\text{c.m.}} = 664 \text{ keV}$ :** The spin-parity of this state is assigned  $J^\pi = (1^-, 2^+)$  in ENSDF, and it was not resolved by  $(^3\text{He}, d)$  [Ers66, Set67, Cag71] or  $(d, n)$  [Fuc69]. The angular momentum assignment in the present analysis is ambiguous between  $\ell = 0 + 2$  and  $\ell = 1$ , which does not narrow down the  $J^\pi$  assignment. Higher angle measurements of  $\theta_{\text{lab}} \geq 30^\circ$  could resolve the angular momentum. The state was obscured at  $\theta_{\text{lab}} = 5^\circ$  by the  ${}^{13}\text{N}$  first excited state, and the statistics were insufficient at  $\theta_{\text{lab}} = 20^\circ$ .

**$E_x = 9092 \text{ keV}; E_r^{\text{c.m.}} = 764 \text{ keV}$ :** The spin-parity of this state is assigned  $J^\pi = 3^-$  in ENSDF, and it was not resolved by  $(^3\text{He}, d)$  [Ers66, Set67, Cag71] or  $(d, n)$  [Fuc69]. The

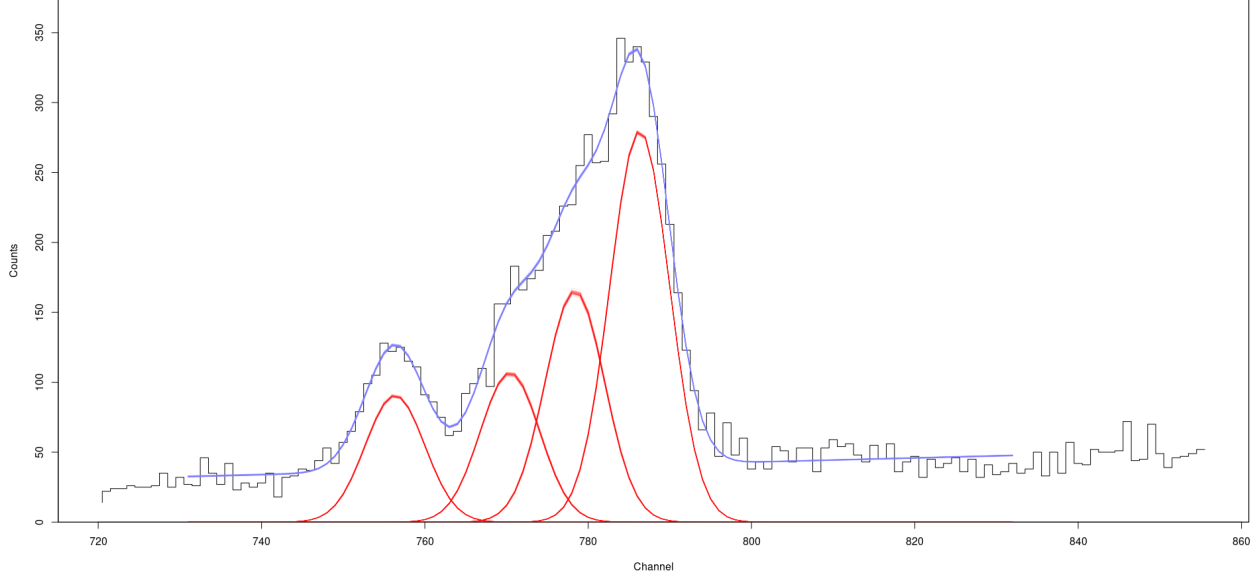


Figure 4.34: A Bayesian Monte Carlo fit for the 9405–9432 keV multiplet at  $\theta_{\text{lab}} = 5^\circ$ , including the clearly distinguishable 9454 keV state. The multiplet is fit with 3 peaks in this experiment, with calibrated energies of 9403.7(31) keV, 9416.7(32) keV, and 9431.7(32) keV. This is better resolution than  $(d, n)$  [Fuc69] was able to achieve, where only 2 peaks in the multiplet were fit at energies of 9408 keV and 9431 keV.

present analysis assigns  $\ell = 1$ , despite the state being obscured at  $\theta_{\text{lab}} = 5\text{--}11^\circ$  by the  $^{13}\text{N}$  first excited state. This is in agreement with the  $J^\pi$  assignment.

**$E_x = 9136 \text{ keV}; E_r^{\text{c.m.}} = 810 \text{ keV}$ :** The spin-parity of this state is assigned  $J^\pi = 2^-, 3^-$  in ENSDF, and it was not resolved by  $(^3\text{He}, d)$  [Ers66, Set67, Cag71]. The present analysis assigns  $\ell = 1$ , in agreement with  $(d, n)$  [Fuc69], despite the state being obscured at  $\theta_{\text{lab}} = 5\text{--}11^\circ$  by the  $^{13}\text{N}$  first excited state. This is in agreement with the  $J^\pi$  assignment.

**$E_x = 9227 \text{ keV}; E_r^{\text{c.m.}} = 900 \text{ keV}$ :** In ENSDF, the 9226.69(5) keV and 9227.43(7) keV states have spin-parities of  $J^\pi = (1^-, 2, 3^-)$  and  $J^\pi = (1, 2^+)$ , respectively. The present energy calibration yielded a state at 9227.8(34) keV, within the uncertainty of both states. Neither state is resolved by  $(^3\text{He}, d)$  [Ers66, Set67, Cag71]. The angular momentum assignment in the present analysis is ambiguous between  $\ell = 0 + 2$  and  $\ell = 1$ , which does not narrow down the  $J^\pi$  assignment in either case. The  $(d, n)$  measurement of Ref. [Fuc69] unambiguously assigns  $\ell = 1$ . The state was obscured at  $\theta_{\text{lab}} = 13^\circ$  and  $15^\circ$  by the  $^{13}\text{N}$  first excited state.

**$E_x = 9405 - 9432 \text{ keV Multiplet}$ :** This multiplet consists of the states 9405 keV ( $J^\pi = 2^-$ ), 9406 keV ( $J^\pi = 0^+$ ), 9412 keV (no  $J^\pi$  assignment), 9419 keV ( $J^\pi = 3^-$ ), 9429 keV ( $J^\pi = (3, 4)^-$ ), and 9432 keV ( $J^\pi = 1^-$ ) in ENSDF. Even though these individual states are unresolvable at the energy resolution attainable with the focal plane detector, it was possible

Table 4.5: The states resolved in the present experiment for the first time in the indicated regimes. Parentheses denote ambiguous  $\ell$  assignments.

New for ${}^{39}\text{K}({}^3\text{He}, d){}^{40}\text{Ca}$	New for ${}^{39}\text{K}$ Proton-Transfer	New for ${}^{39}\text{K} + p$
7623 keV	7623 keV	
7973 keV		
8113 keV		
(8188 keV)	(8188 keV)	
8271 keV		
8359 keV		
8484 keV	8484 keV	8484 keV
8665 keV		
8748 keV	8748 keV	8748 keV
8764 keV	8764 keV	8764 keV
8851 keV	8851 keV	8851 keV
8935 keV		
(8995 keV)	(8995 keV)	
9092 keV	9092 keV	
9136 keV		
(9227 keV)		

to consistently fit 3 peaks in this region with the Bayesian Monte Carlo procedure of Section 4.5, as shown in Fig. 4.34. From the present energy calibration, the peaks result in energies of 9403.7(31) keV, 9416.7(32) keV, and 9431.7(32) keV. These can likely be assigned as 3 separate doublets from the 6 ENSDF states, 9405+9406 keV, 9412+9419 keV, and 9429+9432 keV. The  $(d, n)$  measurement of Ref. [Fuc69] obtained fits for only 2 peaks in this region, at 9408 keV and 9431 keV. Attempting fits with 2 peaks in this region resulted in much worse agreement with the present data. Angular distributions were not obtained for these states in the present analysis, or for any higher energy states, since the focal plane detector efficiency at the high energy fringe resulted in dramatic yield loss over increasing angle.

To summarize the results of this section, the present experiment has unambiguously resolved 13 new states in  ${}^{39}\text{K}({}^3\text{He}, d){}^{40}\text{Ca}$ , 6 new states in  ${}^{39}\text{K}$  proton-transfer, and 4 new states in  ${}^{39}\text{K} + p$  altogether. Table 4.5 lists the states that are newly resolved in these regimes. States in parentheses were given an ambiguous  $\ell$  assignment in the present experiment.

#### 4.7.4 Spectroscopic Factors

Spectroscopic factors  $C^2 S_{39\text{K}+p}$  for each state were extracted from Eqns. 4.43 and 4.46, using the angular momentum assignments and DWBA calculations from the previous section.

These are summarized and compared with the  $(^3\text{He}, d)$  [Ers66, Set67, For70, Cag71] and  $(d, n)$  [Fuc69] measurements in the literature in Table 4.6. Doublets unresolved in the present analysis are given brackets around their ENSDF [Che17] energies. Ambiguous  $\ell$  assignments are also indicated with brackets. In mixed- $\ell$  or disputed- $\ell$  cases, each  $\ell$ -component is shown in parentheses on separate rows, where the lowest  $\ell$  is always the first row.

The  $J^\pi$  values shown in the table were used in the present DWBA models to calculate  $C^2S$ . They were also used to convert the other measurements from their reported  $(2J+1)C^2S$  values to  $C^2S$  for consistency, since their chosen  $J^\pi$  sometimes differed. The  $J^\pi$  values that differ from ENDSF are indicated. This difference is usually an arbitrary choice of the lowest appropriate ENDSF  $J^\pi$  value that is consistent with the present  $\ell$ -assignment. However, the choice sometimes genuinely conflicts with the ENDSF assignment, as is the case for the 8188 keV  $1^+$  ambiguity, 8851 keV, and the 8935+8938 keV doublet.

The statistical uncertainty of  $C^2S$  for the present experiment is also given in the table. An additional 30% systematic uncertainty in  $C^2S$  is assumed, which is typical of  $(^3\text{He}, d)$  reactions in the literature [End77]. The main contribution to this systematic uncertainty is the choice of OMP parameters, especially for the  ${}^3\text{He} + {}^{39}\text{K}$  incoming channel. This is due to the fact that the  ${}^{39}\text{K}(^3\text{He}, d){}^{40}\text{Ca}$  differential cross section was normalized to the  ${}^3\text{He} + {}^{39}\text{K}$  OMP prediction. The OMP parameters for the  $d + {}^{40}\text{Ca}$  outgoing channel also contribute to the systematic uncertainty, albeit to a lesser degree. For example, the  ${}^{23}\text{Na}(^3\text{He}, d){}^{24}\text{Mg}$  measurement of Ref. [Hal04] varied the choice of OMP parameters within a reasonable range. They found a 26% uncertainty associated with the  ${}^3\text{He}$  parameters alone and a 11% uncertainty associated with the  $d$  parameters alone. Added in quadrature, this is a 28% uncertainty from the choice of OMP parameters, which agrees with the historical scatter between  $(^3\text{He}, d)$  measurements of  $C^2S$  [End77].

Table 4.6: Spectroscopic factors compared with Refs. [Ers66, Set67, For70, Cag71, Fuc69].

$E_x^a$	$J^\pi$ <sup>b</sup>	$\ell$ <sup>b</sup>	$C^2 S_{^{39}\text{K}+p}$ <sup>b</sup>	[Ers66]	[Set67]	[For70]	[Cag71] <sup>c</sup>	[Fuc69]
4491	5 <sup>-</sup>	3	0.454(25)	0.609	0.382	0.364	0.418	0.340
5614	4 <sup>-</sup>	3	0.461(25)	0.656	0.389	0.378	0.389	0.470
5903	1 <sup>-</sup>	1	0.019(1)	0.037	0.025		0.015	0.027 (1) $<0.067$ (3)
6025	2 <sup>-</sup>	1 + 3	0.018(1) (1) 0.072(6) (3)	0.027 (1) 0.180 (3)	0.020 (1) 0.100 (3)		0.105	0.030 (1) 0.096 (3)
6285	3 <sup>-</sup>	1	0.167(9)	0.357	0.200 (1)	0.307	0.150	0.246 (1) $<0.171$ (3)
6582	3 <sup>-</sup>	1 + 3	0.047(3) (1) 0.069(9) (3)	0.114	0.086	0.107	0.060	0.080 (1) $<0.114$ (3)
6750	2 <sup>-</sup>	1 + 3	0.024(2) (1) 0.135(11) (3)	0.100	0.096	0.094		0.027 (1) 0.264 (3)
6950	1 <sup>-</sup>	1	0.134(8)	0.275	0.200	0.215	0.080	0.227 (1) $<0.267$ (3)
7113	1 <sup>-</sup>	1 + 3	0.150(8) (1) 0.132(23) (3)	0.317	0.257	0.233	0.257	0.240 (1) $<0.133$ (3)
7532	2 <sup>-</sup>	1	0.227(12)	0.436	0.150 (1) 0.400 (3)		0.095	0.392 (1) $<0.080$ (3)
7623	2 <sup>-d</sup>	1 + 3	0.005(1) (1) 0.037(3) (3)					
7658	4 <sup>-</sup>	3	0.375(20)	0.483	0.306		0.306	0.345
7694	3 <sup>-</sup>	1 + 3	0.027(4) (1) 0.279(20) (3)	$<0.057$ (1) 0.584 (3)	0.414		0.393	0.029
7973	3 <sup>-</sup>	1	0.017(1)					0.023
8113	1 <sup>-</sup>	1	0.026(2)					0.033 (1) 0.160 (3)
8188	3 <sup>-d</sup>	1	0.007(1)					
	1 <sup>+e</sup>	0 + 2	0.017(2) (0) 0.006(1) (2)					
8271	3 <sup>-</sup>	1	0.031(2)					0.046
8359	0 <sup>-d</sup>	1	0.191(11)					0.320
8425	2 <sup>-</sup>	1 + 3	0.037(6) (1) 0.246(21) (3)	0.320	0.500		0.280	0.008 (1) 0.288 (3)
8484	1 <sup>-d</sup>	1	0.031(2)					
8551	5 <sup>-</sup>	3	0.416(23)	0.591	0.455		0.418	0.356
8665	1 <sup>-</sup>	1	0.148(8)					0.187
8748	2 <sup>+</sup>	2	0.004(1)					
8764	3 <sup>-</sup>	1	0.005(1)					
8851	2 <sup>-e</sup>	1 + 3	0.011(1) (1) 0.011(1) (3)					
8935	1 <sup>-e</sup>	1	0.057(3)					0.147
8938								

Table 4.6: (continued)

$E_x^a$	$J^\pi^b$	$\ell^b$	$C^2 S_{^{39}\text{K}+p}^b$	[Ers66]	[Set67]	[For70]	[Cag71] <sup>c</sup>	[Fuc69]
8995	$1^-$	$1$	0.020(1)					
	$2^+$	$\begin{cases} 0 + 2 \\ \phantom{0 + } 2 \end{cases}$	0.006(1) (0) 0.006(1) (2)					
9092	$3^-$	1	0.007(1)					
9136	$2^{-d}$	1	0.152(9)				0.136	
{9226.69	$1^{-d}$	1	0.143(9)				0.213	
{9227.43	$1^{+d}$	$\begin{cases} 0 + 2 \\ \phantom{0 + } 2 \end{cases}$	0.048(6) (0) 0.071(6) (2)					

<sup>a</sup>From the ENSDF evaluation of Ref. [Che17]. Energy is given in keV.

<sup>b</sup>Present experiment. Statistical uncertainties are given. A 30% systematic uncertainty is assumed.

<sup>c</sup>Using the modified DWBA results of Ref. [Cag71].

<sup>d</sup>The lowest appropriate  $J^\pi$  from the ENSDF assignment possibilities.

<sup>e</sup>Differs from the ENSDF  $J^\pi$  assignment altogether.

#### 4.7.5 Proton Partial Widths and Resonance Energies

The proton partial widths  $\Gamma_p$  are small for the low proton energies  $E_r$  considered in this work,  $\Gamma_p \ll E_r$ . Therefore, the  $^{39}\text{K}(p, \gamma)^{40}\text{Ca}$  cross-section is considered to be dominated by narrow resonances, and the reaction rate can be calculated with Eqn. 2.16. The nonresonant contributions and interference effects are expected to be negligible for this reaction [Lon18b]. Proton partial widths are calculated using Eqn. 2.17, given the spectroscopic factors  $C^2 S$  obtained in the previous section. The penetration factor  $P(E)$  is easily computed from Eqn. 2.18 once the center-of-mass resonance energies  $E_r^{\text{c.m.}}$  have been determined. These energies are calculated from the measured excitation energies  $E_x$  in this work using the  $^{40}\text{Ca}$  proton separation energy  $S_p = 8328.18(2)$  keV from Ref. [Wan21].

The final factor to consider in the  $\Gamma_p$  calculation is the dimensionless single particle reduced width  $\theta_{\text{sp}}$ , calculated from Eqn. 2.19 as  $\theta_{\text{sp}} = R |u_{\text{sp}}(R)|^2 / 2$ . The channel number  $R$  is defined as

$$R = r_0(A_t^{1/3} + A_p^{1/3}) \text{ fm}, \quad (4.49)$$

where the standard choice of  $r_0 = 1.25$  fm is made here,  $A_t$  is the target ( $^{39}\text{K}$ ) mass, and  $A_p$  is the proton mass.  $u_{\text{sp}}$  is the single-particle radial wavefunction. As mentioned in Section 2.3.2, we use the weak binding approximation for this analysis, which assumes that unbound states are weakly bound by  $\lesssim 50$  keV. The channel radius  $R$  is chosen such that the wavefunctions for the bound state and unbound state at  $R$  are equivalent [Har23]. Therefore,  $u_{\text{sp}}(R)$  can be treated as the bound state radial wavefunction evaluated at  $R$ , which can be obtained from

Table 4.7: Center-of-mass resonance energies  $E_r$ , angular momentum assignments, and proton partial-widths obtained for proton-unbound  $^{40}\text{Ca}$  states in this experiment. The total proton partial-width uncertainty is reported, including a 30% systematic uncertainty. The last column shows proton partial-width upper limits calculated by Ref. [Lon18b].

$E_x^a$ [keV]	$E_r^b$ [keV]	$J^\pi{}^a$	$J^\pi{}^b$	$l^b$	$(2J+1)\Gamma_p^b$ [eV]	$(2J+1)\Gamma_{p,UL}$ [eV]
8358.9(6)	29.1(25)	$(0, 1, 2)^-$	$(0, 1, 2, 3)^-$	1	$2.62(80) \times 10^{-38}$	$5.88 \times 10^{-36}$
8424.35(31) <sup>cd</sup>	96.17(31) <sup>c</sup>	$2^-$	$(1, 2, 3)^-$	$1 + 3$	$5.4(18) \times 10^{-17}$ (1) $3.9(12) \times 10^{-19}$ (3)	$1.47 \times 10^{-15}$
8484.02(13) <sup>d</sup>	154.1(29)	$(1^-, 2^-, 3^-)$	$(0, 1, 2, 3)^-$	1	$8.1(25) \times 10^{-12}$	$1.16 \times 10^{-9}$
8551.1(7)	221.3(25)	$5^-$	$(1 - 5)^-$	3	$1.33(40) \times 10^{-9}$	$6.60 \times 10^{-9}$
8665.3(8)	334.7(26)	$1^-$	$(0, 1, 2, 3)^-$	1	$1.56(48) \times 10^{-4}$	$1.10 \times 10^{-3}$
8748.59(19) <sup>c</sup>	415.4(28)	$2^+$	$(0 - 4)^+$	2	$1.82(57) \times 10^{-5}$	$1.81 \times 10^{-1}$
8764.18(6)	439.1(27)	$3^-$	$(0, 1, 2, 3)^-$	1	$7.1(22) \times 10^{-4}$	$1.20 \times 10^{-1}$
8850.6(9)	521.2(28)	$6^-, 7^-, 8^-$	$(1, 2, 3)^-$	$1 + 3$	$1.10(34) \times 10^{-2}$ (1) $2.13(65) \times 10^{-5}$ (3)	$1.86 \times 10^{-4}$
$\begin{cases} 8934.81(7) \\ 8938.4(9) \end{cases}$	608.1(27)	$2^+$	$(0, 1, 2, 3)^-$	1	$2.31(77) \times 10^{-1}$	$2.07 \times 10^1$
		$0^+$				$1.28 \times 10^{-1}$
8994.5(11)	664.0(25)	$(1^-, 2^+)$	$\begin{cases} (0, 1, 2, 3)^- \\ (1, 2)^+ \end{cases}$	1	$2.30(77) \times 10^{-1}$	
				$0 + 2$	$4.7(16) \times 10^{-1}$ (0) $1.20(40) \times 10^{-2}$ (2)	
9091.7(6)	764.0(36)	$3^-$		1	$8.2(28) \times 10^{-1}$	
9135.66(5) <sup>d</sup>	809.6(34)	$(2, 3)^-$	$(0, 1, 2, 3)^-$	1	$2.33(78) \times 10^1$	
$\begin{cases} 9226.69(5) \\ 9227.43(7) \end{cases}$	899.6(34)	$(1^-, 2, 3^-)$	$\begin{cases} (0, 1, 2, 3)^- \\ (1, 2)^+ \end{cases}$	1	$3.7(12) \times 10^1$	
		$(1, 2^+)$		$0 + 2$	$5.1(18) \times 10^1$ (0) $2.27(77) \times 10^0$ (2)	

<sup>a</sup>From ENSDF [Che17], unless otherwise indicated.

<sup>b</sup>From the present experiment, unless otherwise indicated.

<sup>c</sup>From Ref. [Gri22].

<sup>d</sup>Level used as a calibration point for at least one angle in this work. See text.

**Fresco.** Both the spectroscopic factor  $C^2S$  and  $\theta_{\text{sp}}$  are obtained for unbound states using the weak binding approximation. It has been shown that  $C^2S$  decreases with binding energy at roughly the same rate as  $\theta_{\text{sp}}$  increases [Har23], making their product largely independent of energy. Therefore, no extrapolation to specific resonance energies is required.

The systematic uncertainty of  $\Gamma_p$  has been extensively studied in other works (e.g. Ref. [Hal04]). The largest contributor to this uncertainty comes from the choice of OMP parameters and is inherited from  $C^2S$ . The systematic uncertainty from the bound state parameters is expected to be low for  $\Gamma_p$ , since the two factors  $C^2S$  and  $\theta_{\text{sp}}$  have opposing bound-state potential dependence. Hence, to a good approximation, the systematic uncertainty of  $\Gamma_p$  can be treated as being derived entirely from  $C^2S$ . Therefore, the choice of a 30% systematic uncertainty applies in this work to both  $C^2S$  and  $\Gamma_p$ .

The proton partial widths in terms of  $(2J+1)\Gamma_p$  and the center-of-mass resonance

energies  $E_r^{\text{c.m.}}$  are summarized in Table 4.7. The ENSDF [Che17] excitation energies are given for reference, unless otherwise indicated. Doublets are indicated with brackets over the individual states. Brackets are also given to indicate ambiguous  $\ell$  assignments. In mixed- $\ell$  cases, each component is given in parentheses next to the  $(2J+1)\Gamma_p$  value. The full range of  $J^\pi$  possibilities determined from the  $l$ -assignments of the present work is also provided. The  $(2J+1)\Gamma_p$  upper limit calculations from Ref. [Lon18b] are given in the last column.

For the remainder of this chapter, unbound states will be referred to solely as resonances, and the corresponding center-of-mass resonance energy will be used to identify them.

## 4.8 New $^{39}\text{K}(p, \gamma)^{40}\text{Ca}$ Reaction Rate

### 4.8.1 The Reaction Rate

The Monte Carlo reaction rate code, `RatesMC` [Lon10, Lon23], was used to calculate a new  $^{39}\text{K}(p, \gamma)^{40}\text{Ca}$  reaction rate probability density from the resonance energies and proton partial-widths reported in the previous section. Among the resonances extracted in the  $^{39}\text{K}({}^3\text{He}, d)^{40}\text{Ca}$  experiment, only those that do not already have a directly measured  $^{39}\text{K}(p, \gamma)^{40}\text{Ca}$  resonance strength  $\omega\gamma$  from Refs. [Kik90, Che81, Lee66] were modified from the most recent reaction rate evaluation of Ref. [Lon18b]. That is, the only resonance strengths and resonance energies that were updated from those in Ref. [Lon18b] are below the 608 keV (606 keV ENSDF energy) resonance. Otherwise, the  $\omega\gamma$  expectation values and variances of the  $^{39}\text{K}(p, \gamma)^{40}\text{Ca}$  experiments [Kik90, Che81, Lee66] are adopted from Ref. [Lon18b].

The new reaction rate as a function of temperature is compared with that of Ref. [Lon18b] in Fig. 4.35. The solid line and blue band represent the median, recommended rate and the  $1\sigma$  confidence interval of this work, respectively. The dotted line and gray band represent that of Ref. [Lon18b], except with resonance energies calculated using  $S_p = 8328.18(2)$  keV from Ref. [Wan21] for consistency, but with marginal effect. Both reaction rates are normalized to the median, recommended rate of Ref. [Lon18b]. As mentioned in Section 4.3.1, the large uncertainty in the reaction rate of Ref. [Lon18b], between about 50 MK and 200 MK, overlaps with most of the relevant temperatures that reproduce the Mg–K anticorrelation in the globular cluster NGC 2419. Ref. [Ili16] found this temperature range to be  $T \approx 80 - 260$  MK. Therefore, the new median, recommended rate is significantly larger at the lower end of this temperature range compared to the previous rate, peaking at a factor of thirteen at about 70 MK.

Fig. 4.36 shows a direct comparison of the uncertainty between the new rate and that of Ref. [Lon18b]. This plot is almost identical to that of Fig. 4.35, except now each reaction rate

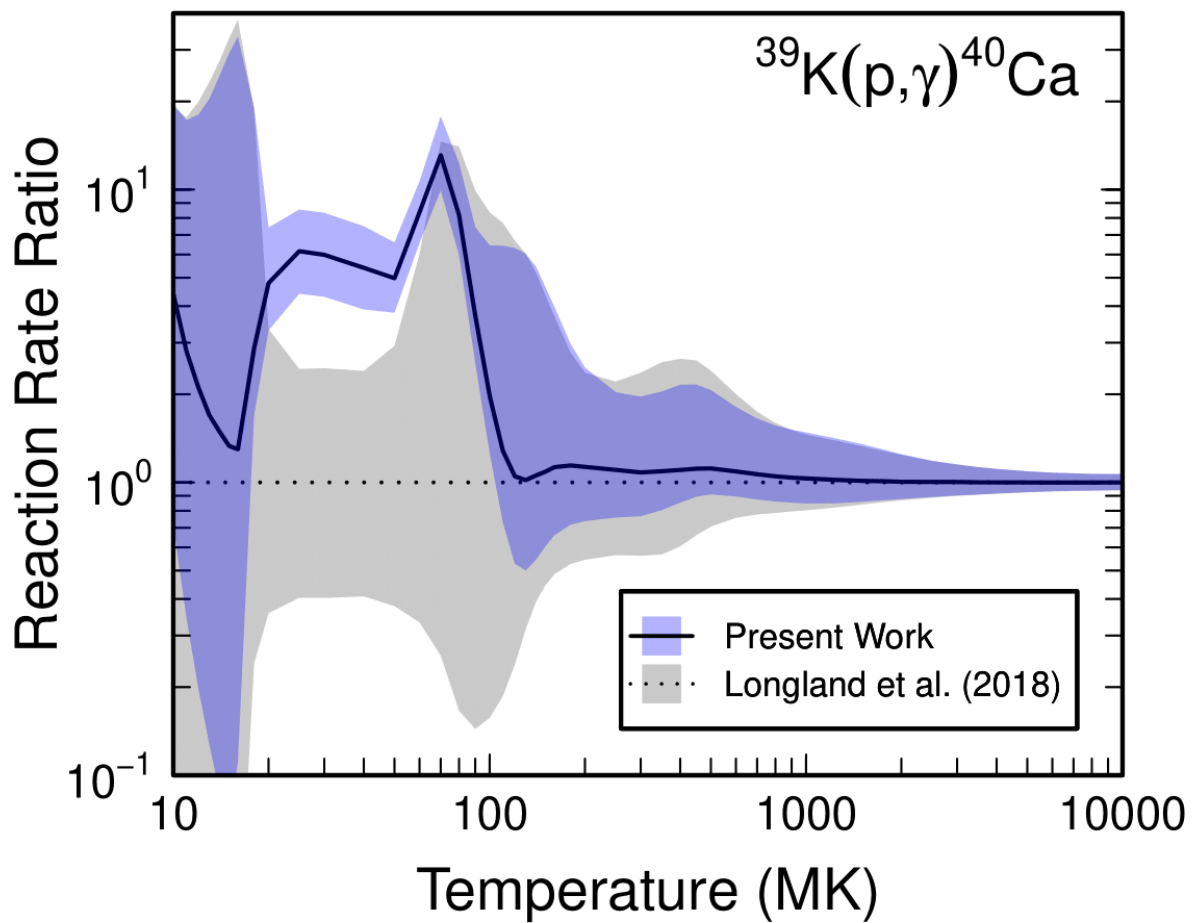


Figure 4.35: Comparison between the  $^{39}\text{K}(p,\gamma)^{40}\text{Ca}$  reaction rate using the proton partial-widths and resonance energies of the present experiment (solid line, blue band) and the most recent evaluation of Ref. [Lon18b] (dotted line, gray band). The reaction rate ratio is taken with respect to the median, recommended rate of Ref. [Lon18b] for both calculations. The  $1\sigma$  uncertainty bands are shown.

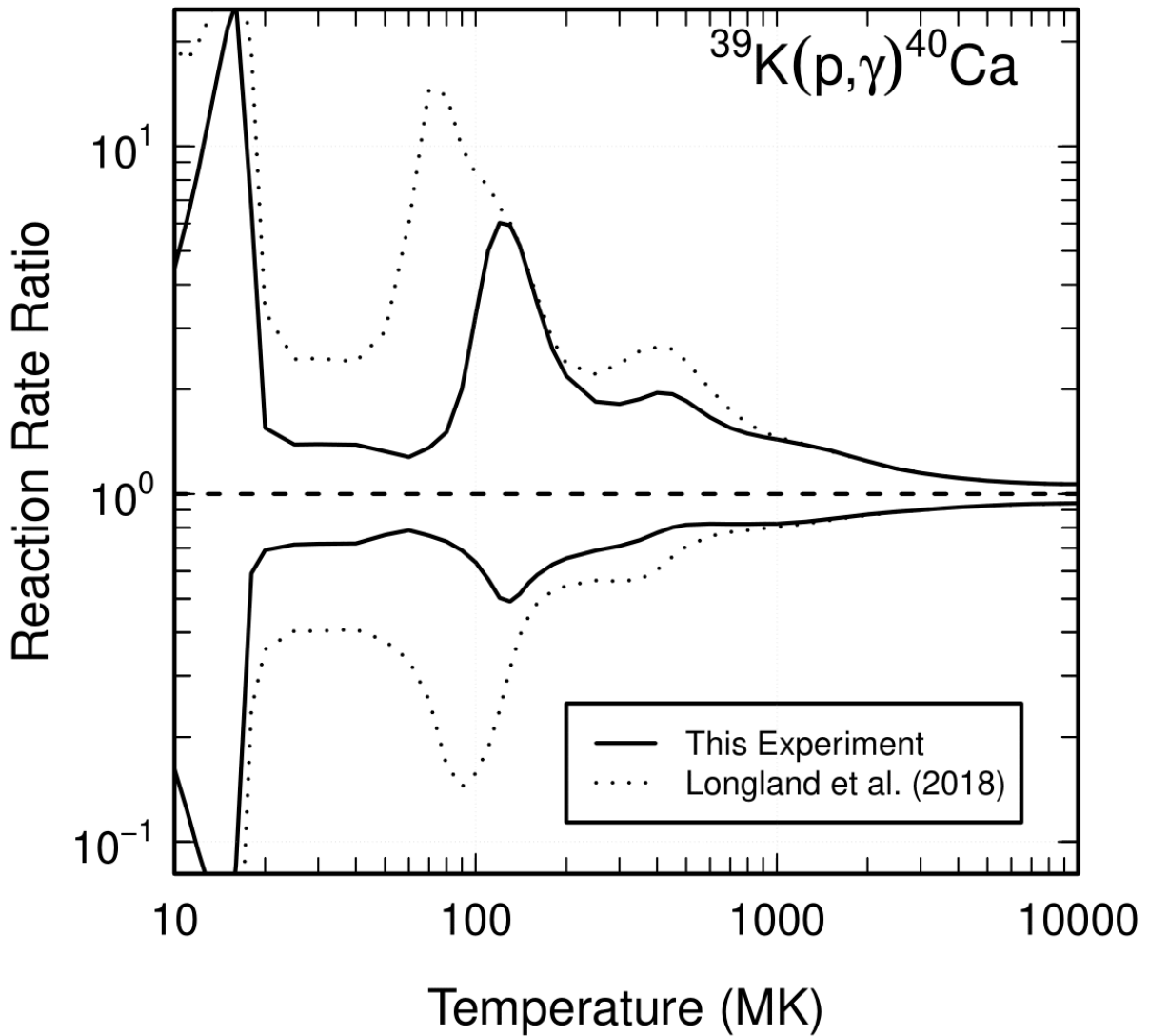


Figure 4.36: Comparison between the  $^{39}\text{K}(p, \gamma)^{40}\text{Ca}$  reaction rate uncertainty using the proton partial-widths and resonance energies of the present experiment (solid band) and the most recent evaluation of Ref. [Lon18b] (dotted band). Each reaction rate ratio is taken with respect to their own median, recommended rate. The  $1\sigma$  uncertainty bands are shown.

is normalized to its own median, recommended rate. The total width of the  $1\sigma$  uncertainty band is significantly reduced at the lower end of the astrophysically-important region, from a factor of 84 at 80 MK to just a factor of 2. This is a reduction of a factor of 42.

### 4.8.2 Resonance Contributions

Resolving the 154 keV resonance is mostly responsible for the increase in the reaction rate and decrease in its uncertainty between about 55 MK and 110 MK. Likewise, the new  $\ell = 1 + 3$  assignment of the 96 keV resonance, which has replaced the  $\ell = 3$  assignment of the  $(^3\text{He}, d)$  measurement of Ref. [Cag71] in this calculation, is mostly responsible for the increase in the rate and decrease in the uncertainty between about 20 MK and 55 MK. For this resonance, the  $(d, n)$  measurement of Ref. [Fuc69] is in agreement with the  $\ell = 1 + 3$  assignment. It is also important to note that using the previous  $\ell = 3$  assignment has a negligible impact on the significant results mentioned in the previous section at 70 MK and 80 MK. Therefore, the resolution of the 154 keV has made by far the largest impact of the reaction rate.

At less than 20 MK, the rate increase is a result of the replacement of the 29 keV proton partial width upper limit in Ref. [Lon18b]. The smaller rate increase and uncertainty reduction at temperatures higher than 110 MK are caused by a combination of the 335 keV, 415 keV, 439 keV, and 521 keV resonances. The latter three of these resonances have replaced proton partial width upper limits in Ref. [Lon18b]. The 221 keV resonance has not made a significant impact on the new rate because the previous  $C^2S$  value from Ref. [Cag71] is almost identical to the one obtained here. It was also found that the resonance energies calculated in this work have a negligible effect on the reaction rate compared to the proton partial-widths.

Fig. 4.37 illustrates the individual contributions from each resonance to the new  ${}^{39}\text{K}(p, \gamma){}^{40}\text{Ca}$  reaction rate. A value of unity means that the given resonance contributes 100% to the reaction rate at that temperature. The labels at the top of the figure represent the center-of-mass resonance energies in keV and are located directly above each resonance. Resonances with a shaded, finite width are measured and show their  $1\sigma$  uncertainty bands. Some measured resonances are represented with hatched lines instead for visible clarity. Upper limit resonances are shown with a single, dashed line at their 84th percentile value. The black, dotted line consists of all resonances that individually contribute less than 10% to the total reaction rate at their corresponding temperatures.

Compared with the previous contribution plot of Fig. 4.6, some key differences can be identified. Most importantly, the 154 keV resonance has been resolved, and its contribution dominates between about 55 MK and 110 MK. It has led to several additional constraints on the contribution of nearby resonances. For example, the 96 keV resonance contribution

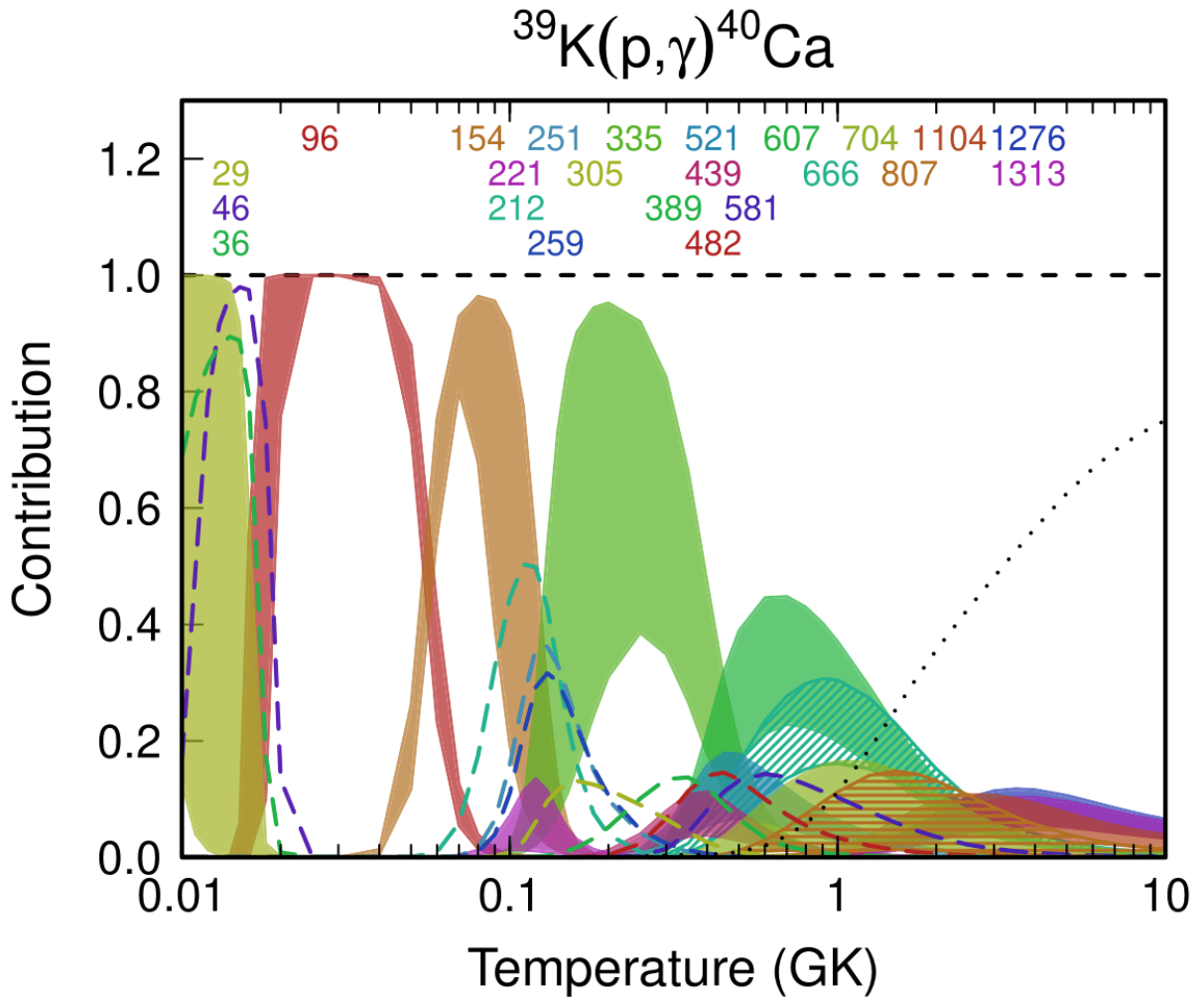


Figure 4.37: Individual resonance contributions to the  $^{39}\text{K}(p,\gamma)^{40}\text{Ca}$  reaction rate, where a value of 1.0 implies that the given resonance contributes 100% to the reaction rate at that temperature. The labels correspond to center-of-mass resonance energies in keV. Resonances with shading or hatched lines have been measured and are shown with their  $1\sigma$  uncertainty bands. Resonances with a single, dashed line are upper limit calculations and show their 84%  $1\sigma$  value, for clarity. The resonances displayed are those that individually account for at least 10% of the total reaction rate at their corresponding temperatures. The remaining summed resonance contributions are represented by the dotted line.

uncertainty is significantly constrained. The 221 keV resonance is also much smaller than it was previously. Finally, the 212 keV upper limit resonance has also been significantly reduced. The 335 keV resonance still dominates in the region between about 110 MK and 400 MK, and its lower 16th percentile value has increased slightly compared to the previous rate from the resolution of the 415 keV, 439 keV, and 521 keV resonances. The 415 keV resonance is not shown, as it contributes less than 10% to the reaction rate.

## 4.9 New Constraints for the Mg–K Anticorrelation

A nuclear reaction network was used to investigate the effect the new  $^{39}\text{K}(p, \gamma)^{40}\text{Ca}$  reaction rate has on potassium abundance in hydrogen-burning environments. New conditions are obtained for the hydrogen-burning temperatures  $T$  and densities  $\rho$  which reproduce the Mg-K anticorrelation observed in the globular cluster NGC 2419.  $T$ - $\rho$  conditions that no longer reproduce the anticorrelation with the new rate are also obtained.

The strategy to reproduce the Mg-K anticorrelation is similar to that of Ref. [Ili16]. A single network calculation is performed for a given  $T$ - $\rho$  condition, and the final  $X(\text{K})$  and  $X(\text{Mg})$  mass fractions are obtained. The mass fractions are subsequently mixed with varying amounts of pristine matter. This mixing is described by Eqn. 1.5, where one part of processed matter (final mass fractions) is diluted with  $f$  parts of pristine matter (initial mass fractions). The values of  $f$  are varied to produce a range of  $[\text{K}/\text{Fe}]$  and  $[\text{Mg}/\text{Fe}]$  abundances. If this range of abundances follows the observed anticorrelation of Fig. 4.1, then the  $T$ - $\rho$  condition is considered a solution.

The hydrogen-burning reaction network consists of 213 nuclei from  $^1\text{H}$  to  $^{55}\text{Cr}$  and 2127 total reactions. Initial mass fractions are chosen such that  $X_{\text{init}}(^1\text{H}) = 0.754$ ,  $X_{\text{init}}(^4\text{He}) = 0.245$ , and the remaining 0.001 is distributed among the other nuclei according to their relative solar system abundances. A grid of network calculations is performed, each with constant temperature  $T$  and density  $\rho$ , terminating at a specified final hydrogen mass fraction  $X_{\text{last}}(^1\text{H})$ . The grid spans  $T = 5 - 300$  MK (in steps of 5 MK),  $\rho = 10^{-4} - 10^{11}$  g/cm<sup>3</sup> (in logarithmic steps, 10 per order of magnitude), and  $X_{\text{last}}(^1\text{H}) = 0.2 - 0.7$  (in steps of 0.1). For each network calculation, the final  $X(\text{K})$  and  $X(\text{Mg})$  are mixed by  $f = 1000, 100, 30, 10, 3, 1, 0.1, 0.05, 0.02$ , and 0, and the new diluted  $[\text{K}/\text{Fe}]$  and  $[\text{Mg}/\text{Fe}]$  abundances are obtained. Their path through the  $[\text{Mg}/\text{Fe}]$  vs.  $[\text{K}/\text{Fe}]$  plot of Fig. 4.1 is tracked to test for a match with the observed abundances. Specifically, a solution is obtained if the path enters the box defined by the points  $1.3 \text{ dex} < [\text{K}/\text{Fe}] < 2.0 \text{ dex}$  and  $-1.5 \text{ dex} < [\text{Mg}/\text{Fe}] < -0.8 \text{ dex}$ .

Fig. 4.38 shows the results of the grid search with a specific  $X_{\text{last}}(^1\text{H})$  value of 0.2. Only  $T$ - $\rho$  solutions to the Mg-K anticorrelation are shown in the plot. The gray points are solutions

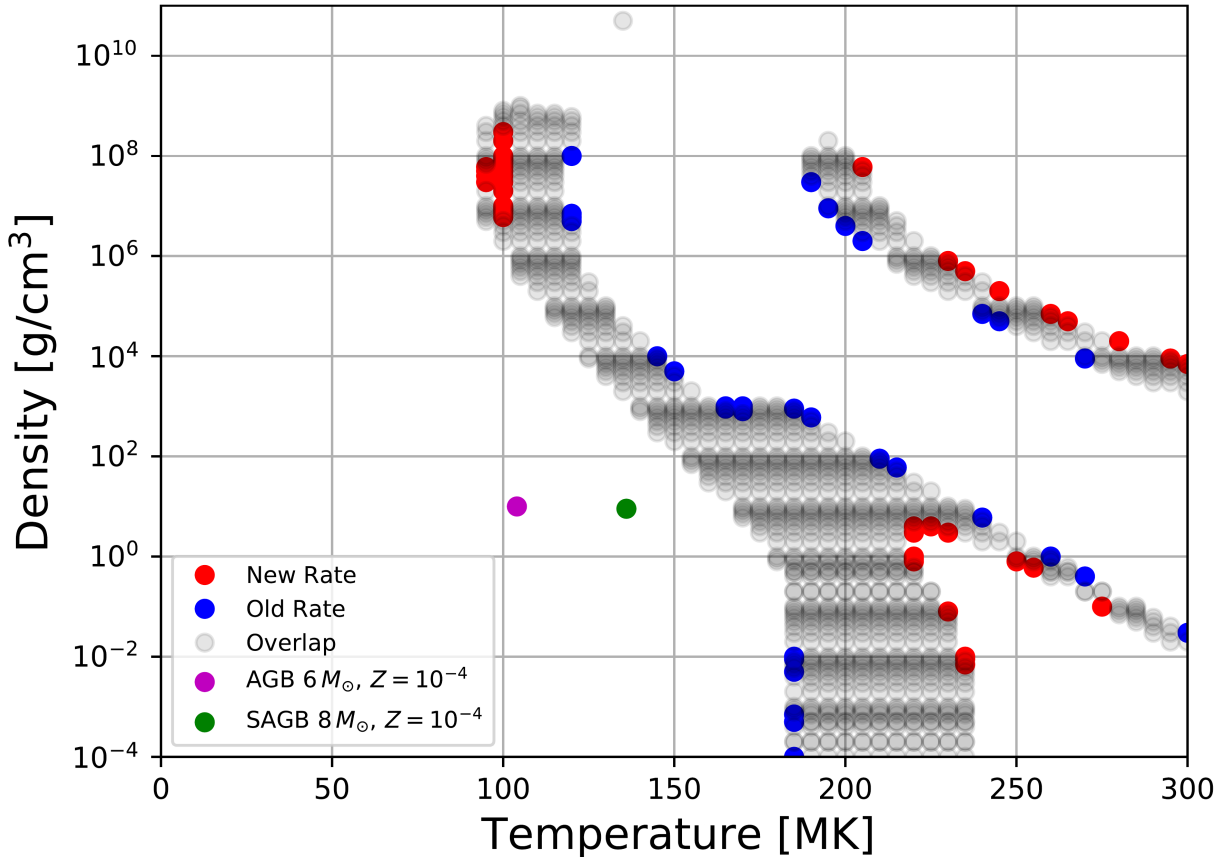


Figure 4.38: The  $T$ - $\rho$  conditions that match the observed Mg-K anticorrelation in the globular cluster NGC 2419, using both the new and previous  $^{39}\text{K}(p, \gamma)^{40}\text{Ca}$  reaction rates. Solutions for both rates are shown in gray as the overlap region, while solutions unique to one rate are indicated with red (new) or blue (old). An  $X_{\text{last}}(^1\text{H})$  value of 0.2 is used here.

for both the previous [Lon18b] and the new  $^{39}\text{K}(p, \gamma)^{40}\text{Ca}$  reaction rate. Red points are solutions with the new rate only, and blue points are no longer solutions with the new rate. The magenta point represents the maximum temperature,  $T = 104$  MK, of hot-bottom burning (HBB) in a  $6 M_{\odot}$  AGB star with metallicity  $Z = 10^{-4}$  and a typical density of  $10 \text{ g/cm}^3$  [Kar10]. Similarly, the green point represents the maximum temperature,  $T = 136$  MK, of HBB in an  $8 M_{\odot}$  SAGB star with metallicity  $Z = 10^{-4}$  and  $\rho = 9 \text{ g/cm}^3$  [Doh15].

Neither of these hydrogen-burning polluter star candidates reach a sufficient temperature of  $\gtrsim 150$  MK to be considered responsible for the Mg–K anticorrelation in NGC 2419. Because the new reaction rate does not introduce any new solutions on the left-hand side of the primary  $T$ - $\rho$  band, the likelihood for AGB or SAGB stars to be polluter star candidates for this globular cluster has not improved from the previous analysis of Ref. [Ili16]. The situation depicted by Fig. 4.3 remains the same. ONe and CO classical novae are the likely polluter candidates, as their  $T$ - $\rho$  evolution passes straight through the band. However, as mentioned in Section 4.2, AGB stellar model parameters are presently very uncertain, and adjusting these parameters could increase the HBB temperature of SAGB stars enough for them to be considered likely polluter star candidates [Ili16].

Fig. 4.38 still has several interesting features. There are two separate regions that describe the Mg–K anticorrelation in NGC 2419. The smaller band runs from 190 MK to more than 300 MK and from  $10^8 \text{ g/cm}^3$  to less than  $10^4 \text{ g/cm}^3$ . Meanwhile, the larger band spans 95 MK to at least 220 MK, where it diverges into two branches. This band spans most densities in the grid, from  $10^{-4} \text{ g/cm}^3$  up to about  $10^9 \text{ g/cm}^3$ . The distribution of red and blue points is also interesting. They are mostly associated with the outer edges of the bands, with no clear pattern for temperature or density. The sea of red points at 95 MK and 100 MK likely result from the 154 keV resonance acting to increase the rate at these temperatures. The reaction rate of Ref. [Lon18b] likely produces too much potassium here, while the new increased destruction rate reduces its abundance enough to match the observations.

This hypothesis is confirmed when analyzing Fig. 4.39. This plot shows the diluted [K/Fe] and [Mg/Fe] final abundances represented by crosses. Lines are drawn between each cross for clarity. The black crosses were obtained using the new  $^{39}\text{K}(p, \gamma)^{40}\text{Ca}$  reaction rate, while the gray crosses are from the previous rate of Ref. [Lon18b], tabulated in `Starlib` [Sal13]. The dashed box represents the conditions for acceptable values of  $T$ - $\rho$ , as the Mg–K anticorrelation is reproduced when the path enters roughly this box. This particular plot shows the specific scenario where the difference in the [K/Fe] abundances between the previous and new rate is maximized at the  $f = 0.02$  value, represented by the bottom-most crosses shown in the figure. The  $f = 0$  case is off-scale. This condition was found by ranking the [K/Fe] differences over the entire grid, including the  $X_{\text{last}}(^1\text{H})$  range. The maximum reduction of -0.23 dex (a factor

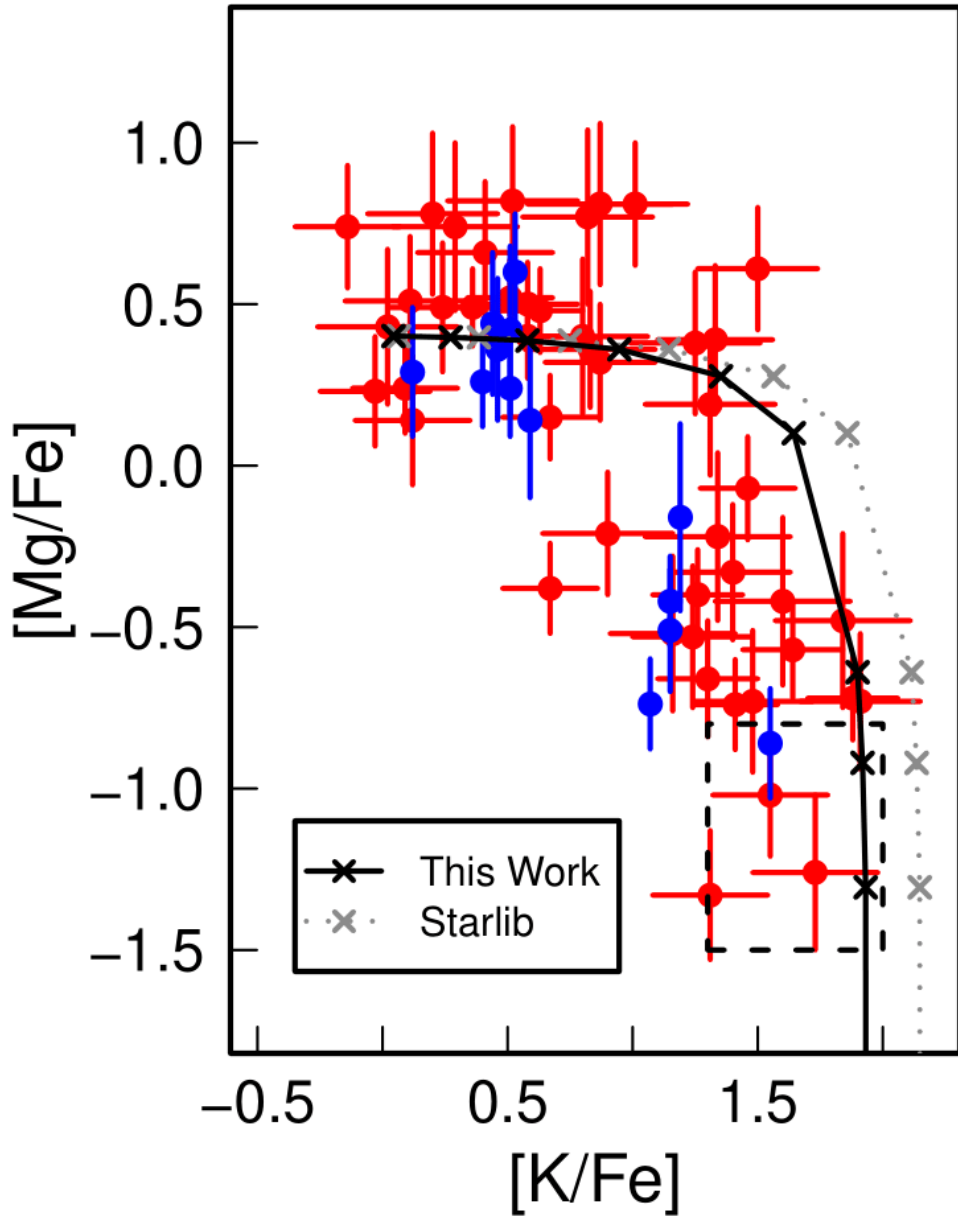


Figure 4.39: The maximum change in potassium abundance when using the new  ${}^{39}\text{K}(p, \gamma){}^{40}\text{Ca}$  reaction rate compared to that of Ref. [Lon18b]. All other reaction rates are provided by **Starlib** [Sal13]. A maximum decrease in [K/Fe] of 0.23 dex (a factor of 1.7 decrease) occurs at  $T = 100$  MK,  $\rho = 4 \times 10^7$  g/cm<sup>3</sup>, and  $X_{\text{last}}({}^1\text{H}) = 0.2$ . This configuration now reproduces the Mg–K anticorrelation in NGC 2419, whereas the rate of Ref. [Lon18b] does not.

of 1.7 decrease in abundance) occurs at the solution  $T = 100$  MK,  $\rho = 4 \times 10^7$  g/cm<sup>3</sup>, and  $X_{\text{last}}(^1\text{H}) = 0.2$ , which is exactly where the sea of red points was located in Fig. 4.38. Hence this maximum reduction in [K/Fe] is a direct result of the newly resolved 154 keV resonance.

## 4.10 Conclusions

New spectroscopic factors and proton partial widths have been extracted from the present  $^{39}\text{K}(^3\text{He}, d)^{40}\text{Ca}$  proton-transfer experiment. Among the states observed, 13 have been newly resolved for  $^{39}\text{K}(^3\text{He}, d)^{40}\text{Ca}$ , 6 have been newly resolved for  $^{39}\text{K}$  proton-transfer (including  $^{39}\text{K}(d, n)^{40}\text{Ca}$ ), and 4 have been newly resolved for  $^{39}\text{K} + p$  (including  $^{39}\text{K}(p, \gamma)^{40}\text{Ca}$ ). These latter 4 are the 154 keV, 415 keV, 439 keV, and 521 keV resonances, in terms of center-of-mass energy. Among these, the 154 keV resonance has by far the largest impact on the  $^{39}\text{K}(p, \gamma)^{40}\text{Ca}$  reaction rate, increasing it by a factor of 13 at about 70 MK from the most recent evaluation of Ref. [Lon18b]. The reduction in the total  $1\sigma$  width of the reaction rate uncertainty from this resonance is an even more significant result. At 80 MK, this width is reduced from a factor of 84 to a factor of 2. Another major impact on the reaction rate comes from the present  $\ell = 1 + 3$  assignment of the 96 keV resonance, in agreement with  $(d, n)$ . This replaced the  $\ell = 3$  assignment by Ref. [Cag71] in the previous reaction rate calculation. The rate is increased by as much as a factor of 6 at about 25 MK from this  $\ell = 1 + 3$  assignment. However, its effect is negligible above 55 MK compared to that of the 154 keV resonance.

The significant increase in the  $^{39}\text{K}(p, \gamma)^{40}\text{Ca}$  reaction rate below 110 MK has led to a decrease in [K/Fe] abundance from hydrogen-burning nuclear reaction networks by as much as 0.23 dex, or a factor of 1.7 at  $T = 100$  MK,  $\rho = 4 \times 10^7$  g/cm<sup>3</sup> and  $X_{\text{last}}(^1\text{H}) = 0.2$ . Several more  $T$ - $\rho$  conditions have been found to reproduce the Mg–K anticorrelation in NGC 2419 with the new reaction rate. Likewise, several  $T$ - $\rho$  conditions have been found to no longer reproduce the Mg–K anticorrelation. However, AGB and SAGB stars have not been found to be any more likely polluter star candidates than with the previous reaction rate.

The 335 keV resonance still contributes overwhelmingly to the reaction rate between about 110 MK and 400 MK, and several unknown resonances with only upper limit proton partial widths are distributed around it. These unknown resonances almost certainty contribute to the uncertainty in its resonance contribution, and continued focus should be placed on resolving them to further constrain the  $T$ - $\rho$  conditions for hydrogen burning in NGC 2419.

## CHAPTER

# 5

## DEVELOPMENT OF A NEW DIGITAL DATA ACQUISITION SYSTEM

### 5.1 Introduction

A new digital data acquisition system (DAQ) has been developed for use with the focal-plane detector package [Mar19] and Enge Split-Pole Spectrograph at the Triangle Universities Nuclear Laboratory (TUNL). A new digitizer will replace the traditional analog modules and analog-to-digital converter (ADC) that have been used for the focal-plane detector electronics at TUNL. This chapter serves to highlight the components of the upgraded system and my contributions to the development and testing of the DAQ, as well as a new GUI `EngeSpec`. The motivation for upgrading to a digital DAQ will be provided in Section 5.2. An overview of the CAEN V1730 digitizer will be given in Section 5.3. The custom frontend DAQ software will be presented in Section 5.4. Finally, Section 5.5 will highlight energy and timing resolution tests of the digital DAQ with  $^{152}\text{Eu}$  and  $^{60}\text{Co}$  radiation data using the `EngeSpec` GUI and its updated sort routine.

### 5.2 Background and Motivation

Nuclear physics experiments involving the detection of particles or  $\gamma$ -rays require a method of converting detected counts into numerical data. Fig. 5.1 illustrates the components of the traditional data acquisition system (DAQ). Detectors first convert each particle or  $\gamma$ -ray event

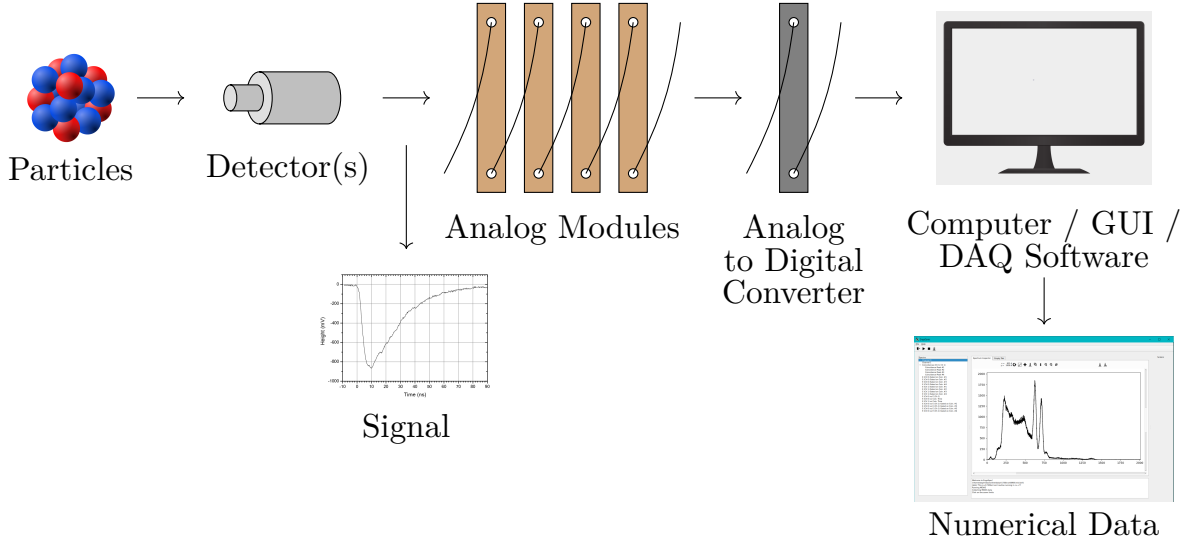


Figure 5.1: The traditional method of converting detected particles or  $\gamma$ -rays into numerical data using analog pulse-processing modules and an analog-to-digital converter (ADC).

into an analog electrical signal, or pulse. Pulse processing then alters the detector signal so as to reduce noise and amplify the pulse to sufficient levels for extraction. At this point, the energy and timing of the event can be determined by further processing. This processing is traditionally performed by a network of analog modules, where the processed pulse is then converted to a digital pulse via an analog-to-digital converter (ADC). The digital pulse can finally be read by a computer and collected by a DAQ software. The stored data can be visualized by a graphical user interface (GUI), which also sorts all of the data based on the corresponding detectors and observables and can perform several functions, such as curve fitting and gating.

The network of analog pulse-processing modules needed for nuclear physics experiments can be incredibly complex. Input and output cables connect modules together, and the vast number of cables can be cumbersome. Rearranging the network of modules between experiments amounts to physically altering the cable setup, which can lead to cable-mapping issues. The modules themselves also take up a significant amount of space. Hence, analog modules have an inherent portability problem.

A network of traditional analog modules can be replaced by a single digitizer, a module that performs the same pulse processing, but does so digitally after it samples the detector signals itself. Fig. 5.2 illustrates the new data acquisition method using a digitizer instead of analog modules and an ADC. Digitizers use firmware algorithms to emulate the functions of analog modules. Custom software is written by the user to perform specific functions that are needed for a given experiment. Changing the setup between experiments now amounts to

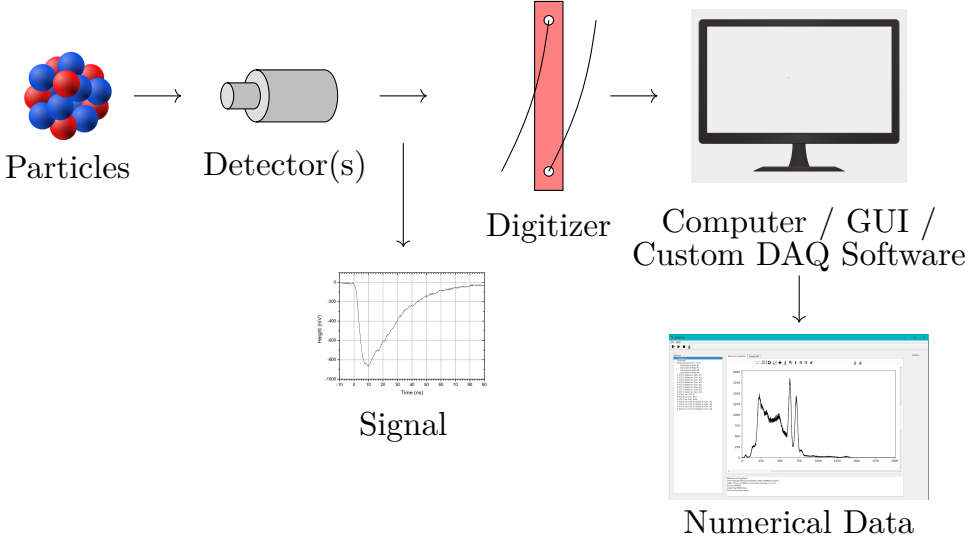


Figure 5.2: The new method of converting detected particles and  $\gamma$ -rays into numerical data with a digitizer, replacing analog modules and the need for an ADC.

altering existing code, rather than moving physical equipment.

At TUNL, the users of the Enge Split-Pole Spectrograph will replace the focal plane detector analog modules with the CAEN V1730 digitizer and its associated Digital Pulse Processing (DPP) firmware algorithms. Fig. 5.3 illustrates the difference between the traditional analog module setup versus the digitizer. Portability will be significantly improved, and a large amount of physical space will be freed up for other purposes. More importantly, the 14-bit digitizer will also provide enhanced energy and timing resolutions compared to the previous 12-bit ADC.

I led the development of a custom frontend DAQ software to accompany the digitizer, which uses MIDAS (Maximum Integrated Data Acquisition System) as the event-based DAQ. In order to visualize the data collected by the DAQ, I helped in the development of a GUI, called **EngeSpec**, that is connected with MIDAS to provide live data visualization during experiments. It also has an offline mode for analysis with previously stored data. **EngeSpec** has several data analysis tools like curve fitting for gaussian and double-gaussian peaks, peak area calculation, and gating functionality. A C++ sort routine, called **EngeSort**, used with the old GUI has been revamped from Java for use with **EngeSpec**. As before, it sorts the data by detector channel and by observable into each given histogram. However, I added trigger and coincidence logic to be used with live signals for the focal-plane detector package, something that was previously performed by analog modules. Note that this has not yet been commissioned as of this thesis, but tests with the new digital DAQ that are not specific to the focal plane detector have already been successful and are presented in Section 5.5.

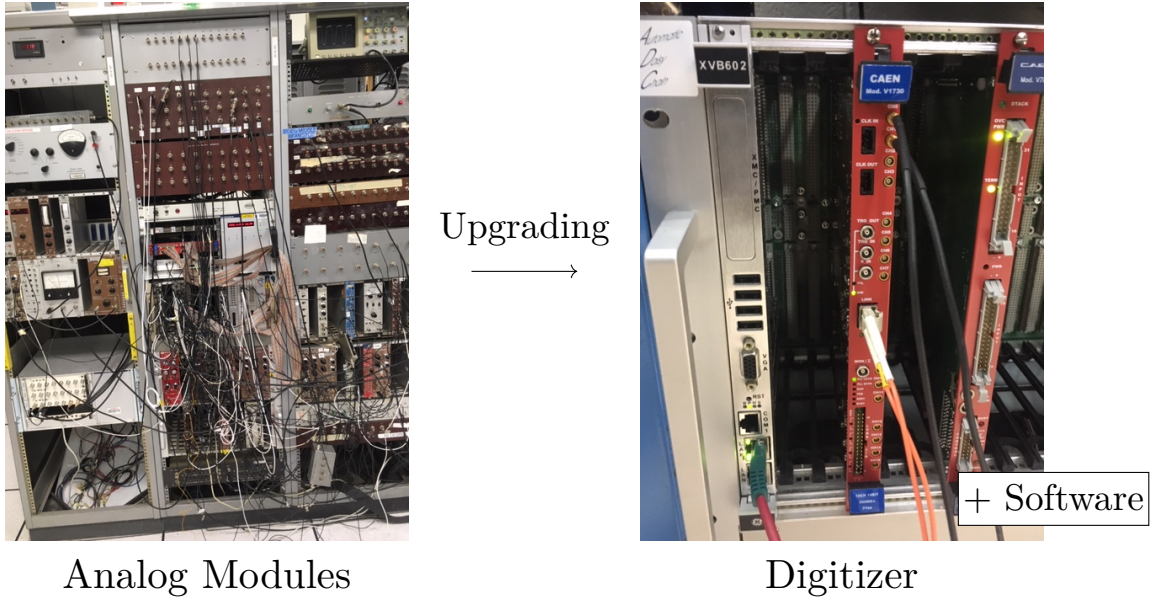


Figure 5.3: The CAEN V1730 Digitizer (pictured on the right), along with its associated DPP firmware and custom frontend DAQ software, is replacing the need for the unportable analog pulse-processing modules (pictured on the left) associated with the Enge focal-plane detector package at TUNL.

## 5.3 Overview of the CAEN V1730 Digitizer

This section provides a brief overview of how the CAEN V1730 digitizer functions, and the most important aspects of its Digital Pulse Processing (DPP) algorithms are discussed. Section 5.4 will then cover how to implement the algorithms via the frontend DAQ software. The version of the digitizer firmware we use is known as DPP-PSD, or Digital Pulse Processing for Pulse Shape Discrimination. The official CAEN DPP-PSD user manual is a comprehensive reference for details not covered in this chapter.

### 5.3.1 Digital Pulse-Processing Parameters

The V1730 digitizer is capable of sampling signals directly from detectors at a rate of 500 MS/s for each of its 16 input channels, corresponding to a time resolution of 2 ns per sample. Those samples are used by the DPP firmware in calculations of important quantities associated with a given signal, such as its baseline, energy, and time stamp. A typical sampled signal is shown in Fig. 5.4, where parameters used by the DPP algorithms are summarized. These parameters are all user-defined and depend on the shape of the detector signals. One can use an oscilloscope or any waveform display software, such as CoMPASS, to approximate the

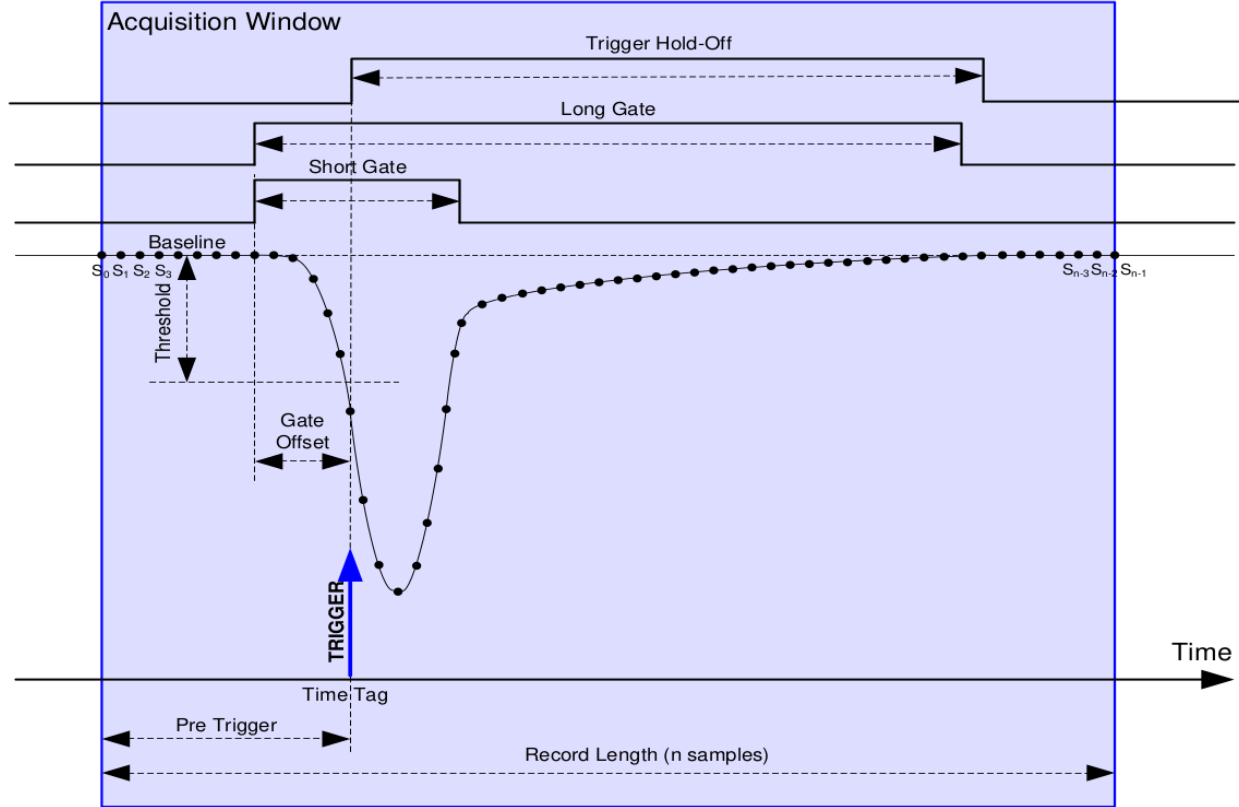


Figure 5.4: A signal sampled by the V1730 digitizer, summarizing the parameters used by the DPP algorithms. When the signal crosses the threshold value, the trigger fires, which primes the system for data acquisition.

parameters. For optimal resolution, it may be necessary to perform resolution tests for certain parameters over a range of values (see Section 5.5.1 for an example of this procedure).

A signal is triggered for data acquisition when it crosses the *threshold* voltage, which should be set high enough to filter out low-energy noise, but low enough not to miss signals. When the trigger fires, the signal is delayed by the *pre-trigger* width to prime for the energy calculation. Since the energy of a charged-particle event is proportional to the charge that it deposits, the digitizer calculates this charge, and therefore determines the (uncalibrated) energy, by integrating the signal voltage over time. The length of time used in the integration is a user-defined parameter known as the *long gate*, and the integrated charge (i.e. uncalibrated energy) is denoted by  $Q_{\text{Long}}$ . The energy integration begins a length of time before the trigger fires, known as the *gate offset*, which must be less than the pre-trigger width. The purpose of the gate offset is to include the portion of the signal before the trigger in the energy integration. After the trigger fires, all other triggers from the same channel are inhibited during the *trigger hold-off* width, which must last at least until the end of the long gate.

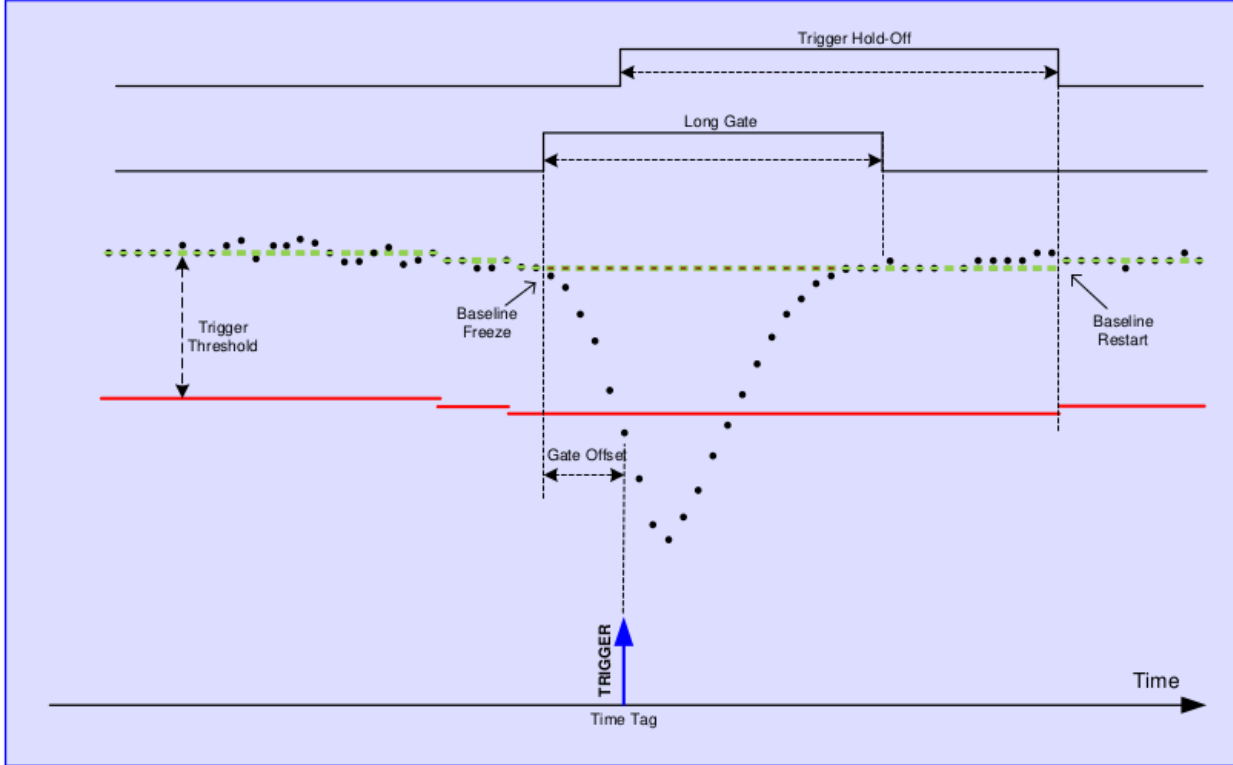


Figure 5.5: The dynamic baseline calculation using the mean value of a user-defined number of samples in a moving time window. The baseline freezes during the energy integration of a signal that has been triggered.

After this width, the channel can accept new triggers.

One of the most important quantities associated with the DPP algorithms is the baseline of the signal. The baseline is the reference value used for the energy calculation and to determine the threshold. This can either be a user-defined quantity, in which case it retains a fixed value, or the baseline can be dynamically calculated based on the average value of a user-defined number of samples during a moving time window. In the latter case, as shown in Fig. 5.5, the baseline freezes during energy integration, and the baseline calculation restarts after the trigger hold-off width, using the samples both before and after the freeze. This means the baseline calculation contributes almost no dead-time. Note that the threshold follows the baseline variations.

The *short gate* is a measure of the fast portion of the signal. This is used, in conjunction with the long gate, to discern between different types of particles, e.g. between gamma-rays and neutrons. The pulse shape discrimination (PSD) is a quantity that measures the ratio

between the area of the tail of the signal and the area of the total signal, i.e.

$$\text{PSD} = \frac{Q_{\text{Long}} - Q_{\text{Short}}}{Q_{\text{Long}}},$$

where  $Q_{\text{Long}}$  and  $Q_{\text{Short}}$  are the charge collected in the long gate and short gate during charge integration, respectively. Neutron events tend to have a distinctly higher PSD than gamma-ray events because they have larger tails. The option to collect the PSD for each event is currently not available in our frontend software, as we have other means of particle discrimination through post-processing.

The only parameter yet to be discussed in Fig. 5.4, the *record length*, is not used by our digitizer. The V1730 only operates in List mode, where the event data is stored, but the samples themselves are not. Some other CAEN digitizers can operate in Waveform mode, where the samples in the record length that make up the *acquisition window* are stored to visualize the signals and the baseline with the appropriate CAEN software. However, the reduced amount of data transferred in List mode compared to Waveform mode keeps the dead-time of the system very low during runs.

### 5.3.2 Time Stamp Determination

By default, the timing of events in the DPP firmware is performed by *leading edge discrimination* (LED), where a time stamp is given to each event the moment it crosses the trigger threshold. However, threshold triggering on the leading edge of signals causes well-known issues with timing, known as *time walk*. Two signals exactly coincident, but with different amplitudes, will register different time tags using LED mode because the leading edge of the larger signal rises sooner.

A more precise way of determining signal time is by using *constant fraction discrimination* (CFD), which can be enabled by the DAQ user instead of LED mode. This method assigns the time stamp to the moment the signal amplitude reaches a constant fraction of its total amplitude, allowing for timing to be independent of signal amplitude. As in traditional analog CFD modules, the digitizer takes the input signal and produces two new signals, one attenuated by a factor  $f$  of the total amplitude and the other inverted and delayed by a time  $d$ . The two signals are summed together to form a bipolar pulse with a single *zero-crossing*, which is taken as the time stamp of the event. Because of the finite sampling resolution of the digitizer, the exact zero-crossing location will always be located somewhere between two samples of the signal. The DPP firmware, by default, assigns the sample before the zero-crossing as the time stamp of the event, called the *coarse time stamp*. This is usually sufficient, but for more precise timing it is also possible to assign the time stamp as the

interpolated zero-crossing. The width between the coarse time stamp and the interpolated zero-crossing is called the *fine time stamp*. If the user enables zero-crossing interpolation, the data for each event will take up more memory. Note that in the case of CFD mode, the threshold trigger serves the purpose of priming the system for CFD implementation rather than assigning a time stamp.

The time stamp for LED mode and the coarse time stamp for CFD mode are both referred to as the *trigger time tag* in the DPP firmware, a 31-bit unsigned integer that has units equal to the time resolution of the digitizer, 2 ns. In CFD mode, the fine time stamp is a 10-bit unsigned integer, meaning the interpolated zero-crossing time stamp is a 41-bit unsigned integer (with a maximum value of  $2^{31}$ ). The trigger time tag is stored by default, but the fine time stamp can be retrieved separately. Both the interpolated zero-crossing time stamp and the trigger time tag roll back to zero once they reach their maximum value of  $2^{31}$ , or  $2 \times 2^{31}$  ns  $\approx 4.295$  s. It is also possible to extend the rollback of the time stamps by an extra 16-bits by enabling the *extended time stamp*.

### 5.3.3 Event Readout Format

Each of the 16 V1730 digitizer channels uses RAM to temporarily store event data. This memory is divided into *memory buffers*, or *aggregates*, that each contain data for up to 1023 events. The number of events per aggregate is programmable, but we have set this number to its maximum of 1023 as to optimize readout bandwidth. The drawback of this is that events are not available for readout until all 1023 events have been stored in an aggregate, unless the run is stopped before an aggregate becomes full. The total number of aggregates contained in the RAM is also programmable, but we have set this number to 8 due to the large size of each aggregate. The RAM for each aggregate is cleared after all aggregates have been read to make room for upcoming events.

In reality, there are two types of aggregates for the V1730 memory organization. *Channel aggregates* are what have been described so far, but there are also *board aggregates*. Each channel aggregate is shared by two consecutive channels, i.e. channel 0 and channel 1, channel 2 and channel 3, etc. The sample of all channel aggregates is a board aggregate. The sample of all board aggregates is called the *data block*. Since there are 16 channels in the V1730, there are up to 8 channel aggregates that comprise a board aggregate. If a channel aggregate contains no data, it is not included in the board aggregate. When data readout is performed, each successive channel aggregate is read at a time in a given board aggregate, and each successive board aggregate is read from the data block via a *block transfer*.

31	30	29	28	27	26	25	24	23	22	21	20	19	18	17	16	15	14	13	12	11	10	9	8	7	6	5	4	3	2	1	0	BIT	
1	CHANNEL AGGREGATE SIZE (in lwords)																																
DT	EQ	ET	EE	ES	EX	AP	DP2	DP1	NUM SAMPLES WAVE/8		SIZE																						
CH	TRIGGER TIME TAG																												FORMAT				
DP2 <sub>0</sub> DP1 <sub>1</sub>	S <sub>1</sub>															DP2 <sub>0</sub> DP1 <sub>0</sub>	S <sub>0</sub>																
DP2 <sub>3</sub> DP1 <sub>3</sub>	S <sub>3</sub>															DP2 <sub>2</sub> DP1 <sub>2</sub>	S <sub>2</sub>																
DP2 <sub>n-1</sub> DP1 <sub>n1</sub>	S <sub>n-1</sub>															DP2 <sub>n2</sub> DP1 <sub>n2</sub>	S <sub>n-2</sub>																
CH	EXTRAS																																
DP2 <sub>0</sub> DP1 <sub>1</sub>	S <sub>1</sub>															DP2 <sub>0</sub> DP1 <sub>0</sub>	S <sub>0</sub>																
DP2 <sub>3</sub> DP1 <sub>3</sub>	S <sub>3</sub>															DP2 <sub>2</sub> DP1 <sub>2</sub>	S <sub>2</sub>																
DP2 <sub>n-1</sub> DP1 <sub>n1</sub>	S <sub>n-1</sub>															DP2 <sub>n2</sub> DP1 <sub>n2</sub>	S <sub>n-2</sub>																
CH	EXTRAS																																
Q <sub>LONG</sub>	PUR															Q <sub>SHORT</sub>	PUR																

Figure 5.6: The data format for the first two events in a channel aggregate. Each memory location is 32-bits and is accessed during readout. Individual samples are not saved by our digitizer, so every 32-bit line that contains a sample,  $S_1$ ,  $S_2$ , etc., is omitted. Each event therefore contains up to three memory locations. The channel aggregate itself has a header consisting of the first two memory locations, SIZE and FORMAT.

### Channel Aggregate Event Format

The channel aggregates are formatted for readout as in Fig. 5.6. Each line represents a *memory location*, consisting of a 32-bit integer (each bit is either a 0 or 1). Note that only 2 events are shown, and a full channel aggregate will contain 1023 events. The first two memory locations, SIZE and FORMAT, comprise the channel aggregate *header*, which is common to all events in the aggregate. Beyond the header is data for each event in the aggregate. Our V1730 digitizer does not save individual samples, so every memory location that contains a sample,  $S_1$ ,  $S_2$ , etc., does not appear for readout. Therefore, each event contains a maximum of 3 memory locations. These are the trigger time tag, EXTRAS, and the charges from the long and short gates,  $Q_{\text{Long}}$  and  $Q_{\text{Short}}$ , respectively. EXTRAS contains extra information associated with CFD zero crossing interpolation. It is therefore omitted by default, unless the user has enabled CFD zero crossing interpolation. Note that if CFD mode is enabled, the trigger time tag is the coarse time stamp, associated with the sample before the zero crossing by default.

Not every bit in Fig. 5.6 will be discussed here. See the CAEN DPP-PSD manual for

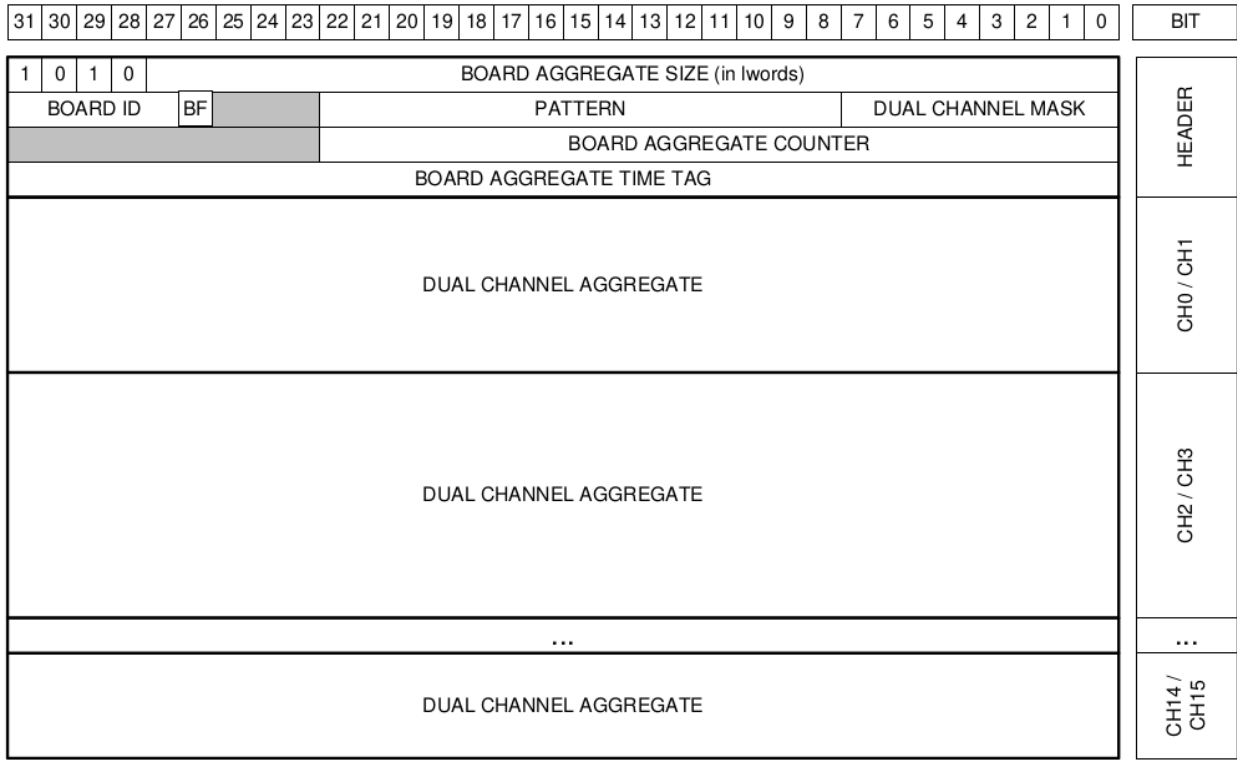


Figure 5.7: The data format for a board aggregate, consisting of up to 8 channel aggregates and 4 memory locations making up the header. Each memory location is 32-bits and is accessed during readout.

detailed information. However, the data most frequently accessed are as follows (from top to bottom in Fig. 5.6). In the SIZE memory location, the CHANNEL AGGREGATE SIZE is the number of memory locations that are contained in the given channel aggregate, including itself and FORMAT. This can be useful for debugging and determining how many events are contained in the aggregate. In the FORMAT memory location, EX contains 3 bits that the user inputs (through functions in the frontend DAQ) to specify what the EXTRAS memory location outputs. If all 3 of these bits are 0, the EXTRAS memory location is omitted. In the event memory locations, CH specifies which channel the event came from in the couple (0 for even or 1 for odd). PUR is a flag that detects events whose energy was not evaluated correctly, e.g. from pile-up or event saturation.

### Board Aggregate Event Format

The board aggregates are formatted for readout as in Fig. 5.7. Each board aggregate contains up to 8 channel aggregates and has 4 memory locations making up the header. Each channel aggregate that has data contributes all of its memory locations to the board aggregate in the

order shown in Fig. 5.7. Channel aggregates with no data do not contribute to the board aggregate.

Again, only the most important values in the board aggregate will be discussed here. The BOARD AGGREGATE SIZE is analogous to the CHANNEL AGGREGATE SIZE in that it is the total number of memory locations contained in the board aggregate, including all of the memory locations in the channel aggregates that comprise it. The DUAL CHANNEL MASK corresponds to the channel couples participating to the board aggregate. THE BOARD AGGREGATE COUNTER gives the current board aggregate count. The BOARD AGGREGATE TIME TAG gives the time that the board aggregate was created. This is not a physical quantity, but can be useful for debugging.

## 5.4 Frontend DAQ Software

The CAEN V1730 digitizer firmware uses Digital Pulse Processing (DPP) algorithms, which are implemented in the Field-Programmable Gate Array (FPGA) of the digitizer board. The DPP algorithms and settings can therefore be programmed by the user. This is performed by accessing and writing values to 32-bit wide *registers*, which have distinct hexadecimal addresses. For example, setting the width of the long gate for channel 0 amounts to writing the long gate value (as a 16-bit integer) into the Long Gate Width register specific to channel 0, which has the address 0x1058. All of the registers that the user can access are documented in the official V1730 DPP-PSD Registers manual. Some of the most important registers will be highlighted in the next section, which can easily be adjusted with the use of a settings file.

An important aspect of our custom DAQ software is to provide a simple way of changing user-defined settings (DPP parameters) without the user having to manually keep track of register values. In the DAQ software, the different settings are implemented via C++ functions writing the given parameter values into the appropriate register when executed. The function definitions are stored in the C file v1730DPP.c, while the functions are executed in the frontend C++ file fev1730-DPP.cxx. Almost all settings the user would ever need to specify are listed in the settings file, settings-DPP.dat, shown in Fig. 5.8, allowing for quick changes to be made. This file is read, and the settings are applied, by the frontend file. Therefore, the frontend file must be executed with each change to the settings file. Any additional, less common settings can be added to the settings file at any point with ease.

```

{0,1}      ## Enable Channels (0-15) e.g. --> {0,1,2,3}
700       ## Long gate (ns)
400       ## Short gate (ns)
110       ## Gate offset (ns)
0         ## Trigger Hold-Off (ns, multiple of 8 - If too low, automatically adjusts to lowest)
0         ## Pre Trigger (ns, multiple of 8, must be > Gate Offset - If too low, automatically adjusts to lowest)
1         ## Gain (0-5)
1         ## negSignals (1=yes, 0=no)
32767    ## DC Offset (in DAC LSB Units)
3         ## Trigger threshold (in mV)
40        ## CFD Delay (ns)
75        ## CFD Fraction (%)

0         ## Dynamic Range (0 = 2 Vpp, 1 = 0.5 Vpp)
2         ## Input Smoothing (0 = disabled, 1 = input pulse averaged over 2 samples, 2 = 4, 3 = 8, 4 = 16)
3         ## Mean Baseline Calc (0 = fixed baseline, 1 = use 16 samples, 2 = 64, 3 = 256, 4 = 1024)
0         ## Fixed Baseline (in mV, 0 = disabled, Mean Baseline Calc must be 0 if enabled)
0         ## Baseline Calc Restart after Long Gate (0 = disabled (default), 1 = enabled)
1         ## Trigger Mode (0 = LED mode, 1 = CFD mode)
0         ## Trigger Counting Mode (0 = only accepted self-triggers (default), 1 = all self-triggers)
0         ## Trigger Pile Up (0 = disabled (default), 1 = enabled)
0         ## Detect Signals with Opposite Polarity (0 = enabled (default), 1 = disabled)
0         ## Charge Zero Suppression Threshold (in LSB, 0 = disabled (default), cuts Q_Long < Q_thresh)

```

Figure 5.8: The settings file, settings-DPP.dat, where the most common user-defined DPP parameters are adjusted. It is unlikely any other internal setting is needed, but implementing new V1730 register settings has been made simple.

## 5.5 Testing the Digital Data Acquisition System

I performed the initial tests on the digital DAQ and DPP settings by measuring both the energy resolution and timing resolution using NaI(Tl) scintillation detectors. Note that a commissioning experiment has yet to take place for the new digital DAQ at the Enge Split-Pole Spectrograph using the focal plane detector package. However, these initial tests proved insightful in the development of the sort routine that will be implemented for the focal plane detector signals when the commissioning experiment takes place. This section showcases the results of the resolution tests, where optimal DPP settings were determined, and several features that were added to the `EngeSpec` sort routine.

### 5.5.1 Energy Resolution Tests with $^{152}\text{Eu}$

The extraction and analysis of the integrated charge  $Q_{long}$  is one of the most important goals in testing the DAQ because it represents the energy deposited in the detector.  $Q_{long}$  is extracted from its memory location in each event collected over all channel aggregates and board aggregates, with reference to Figs. 5.6 and 5.7, respectively. The energy spectrum is then obtained by sorting the event data in the `EngeSpec` sort routine and incrementing a histogram with  $Q_{long}$  values. In the present test, the radioisotope  $^{152}\text{Eu}$  was used along with a NaI(Tl) scintillator to analyze the  $\gamma$ -ray energies resulting from  $\beta$ -decay. The  $^{152}\text{Eu}$   $\gamma$ -ray spectrum, incremented by the raw  $Q_{long}$  values, is represented in Fig. 5.9. Four calibration

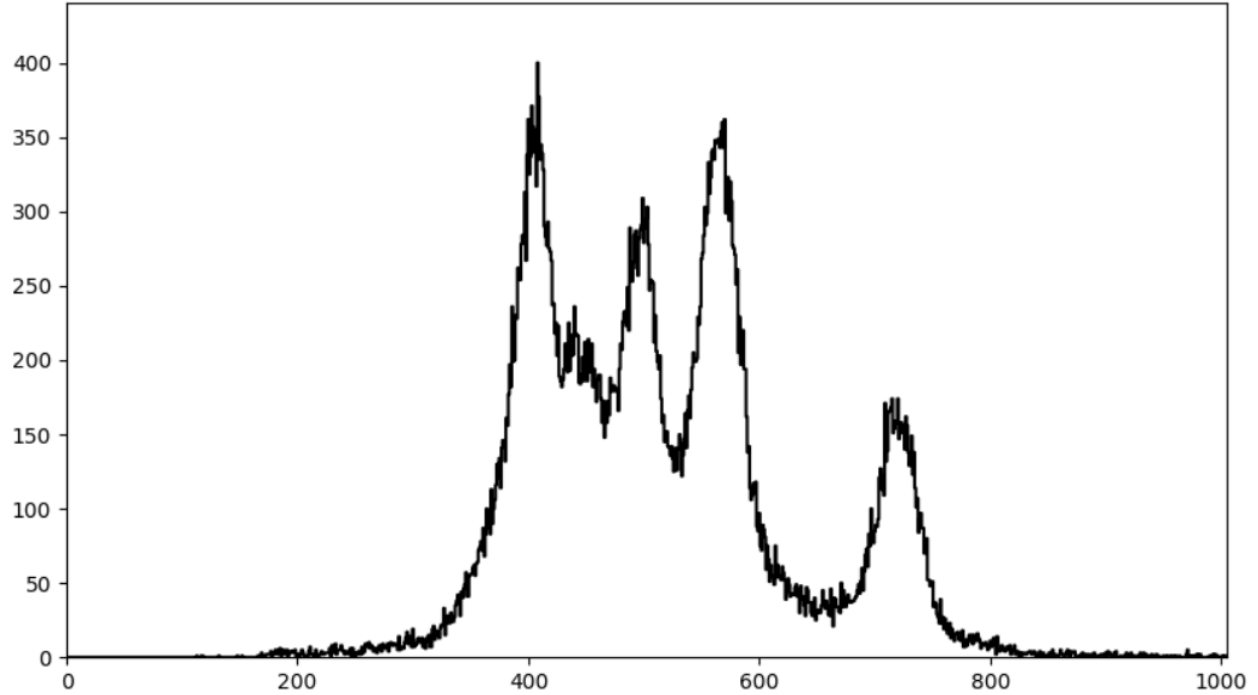


Figure 5.9: The  $^{152}\text{Eu}$   $\gamma$ -ray spectrum as a result of  $\beta$ -decay. The raw  $Q_{long}$  value is given on the  $x$ -axis and the number of counts in each bin is given on the  $y$ -axis. The largest four  $\gamma$ -ray peaks are shown, where the right-most one is the 1408 keV peak used for the energy resolution analysis.

peaks are clearly visible. The right-most peak corresponds with the 1408.013(3) keV state [Bé07], which will be the focus of the resolution tests, since it is the most isolated.

To measure the energy resolution, the full-width at half max (FWHM) and the centroid of the 1408 keV calibration state was determined by fitting a gaussian distribution plus a background line in the EngeSpec GUI. An energy calibration was performed with the other  $^{152}\text{Eu}$  calibration states, and the resulting energy distribution was used to calculate the relative resolution  $R$  as a percentage

$$R = 100 \times \text{FWHM}_E / E_c \text{ [in \%]}, \quad (5.1)$$

where  $\text{FWHM}_E$  is in terms of calibrated energy and  $E_c$  is the calibrated peak energy.

The impact of the DPP parameters on the resolution was tested by varying a single DPP parameter and calculating the new resolution for each step. This was first performed for the long gate parameter, since this has the most direct link to  $Q_{long}$ , as it defines the gate for energy integration. Similarly, the gate offset parameter was varied next, since this also plays a role in the energy integration before the trigger fires. The results of the resolution

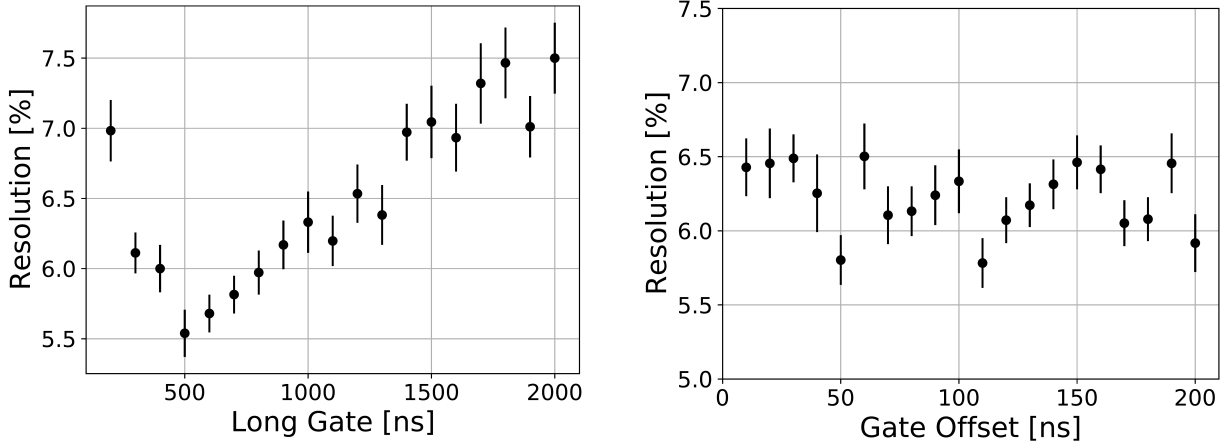


Figure 5.10: Resolution tests of the long gate (left) and gate offset (right) DPP parameters for the 1408 keV  $^{152}\text{Eu}$  calibration state.

tests for these parameters are given in Fig. 5.10. The long gate shows a clear minimum (i.e. best) resolution of about 5.5% for 500 ns. This corresponds to the true size of the signals when analyzed with an oscilloscope. The sharp rise as gate sizes become smaller than this makes physical sense, as the integration range begins to stop before reaching the end of the signal. However, the steady rise at gate sizes larger than the signal itself is interesting. One would think that a larger integration range would not play a significant role, considering the additional contribution to the charge should be negligible. It appears this is not the case, however. The likely scenario is that the baseline for the signal is slightly unparallel to the true, virtual baseline, so that more and more charge is accumulated at large gate size. The conclusion is that the raw signals should always be investigated with an oscilloscope and the long gate adjusted accordingly before scientific runs.

The resolution distribution for the gate offset parameter is more complicated and perhaps less insightful. There are two minima, at 50 ns and 110 ns, but the distribution rises abruptly on either side. This likely indicates that the resolution is not sensitive to this parameter, and the plot only shows statistical scatter. The quick fall time in the oscilloscope signals for this radiation source is likely the reason the gate offset has little impact.

These resolution tests were performed for many of the other parameters listed in Table 5.8 as well, and there were minor improvements. They will not be described here for brevity, but the optimum parameters were found to be gain = 1, mean baseline calculation = 3, and input smoothing = 2. The trigger threshold did not have a clear minimum, and no other parameters were tested.

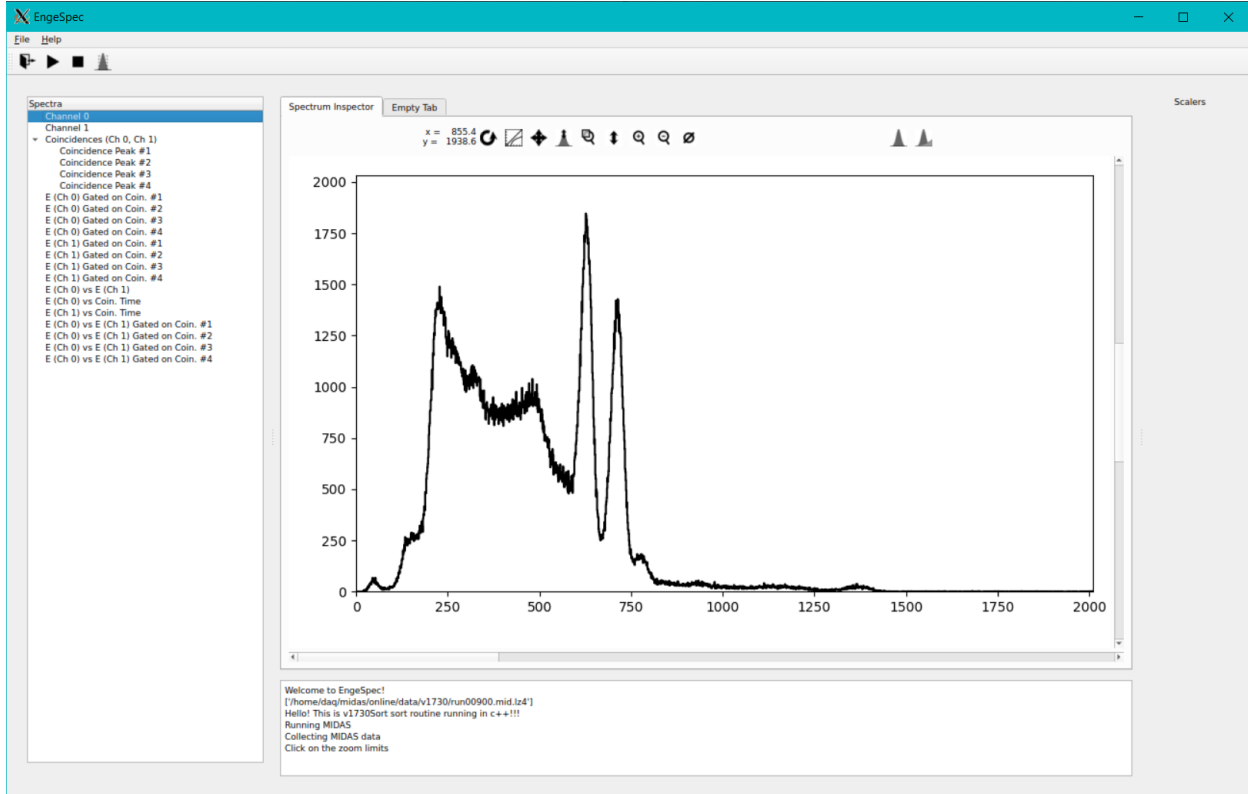


Figure 5.11: The  $^{60}\text{Co}$   $\gamma$ -ray spectrum shown with the `EngeSpec` GUI.

### 5.5.2 Timing Resolution Tests with $^{60}\text{Co}$

The timing resolution for the digital DAQ was tested by measuring coincidences. For this purpose, two NaI(Tl) scintillation detectors were needed. A  $^{60}\text{Co}$  source was used this time because of its simplicity, and no energy calibration was needed. The  $\gamma$ -ray distribution for one of the detectors is shown in Fig. 5.11, where the full `EngeSpec` GUI is shown. The 1332 keV and 1173 keV peaks are clearly visible. Coincidences between the two detectors are handled entirely by the `EngeSpec` sort routine. The development of the coincidence feature in `EngeSpec` is detailed in Section 5.5.3.

At the beginning of these tests, the default time stamp determination had been set to leading edge discrimination (LED), or LED mode, described in Section 5.3.2. Unsurprisingly, the timing resolution was clearly impacted as a result. Fig. 5.12 shows a histogram of the coincidences obtained with LED mode, where the  $x$ -axis spans the channels 0 to 8196, and the time differences have been scaled so that  $\Delta t = 0$  corresponds to channel 4096. The trigger time tags themselves have a resolution of 2 ns, so each channel in the histogram represents 2 ns. The coincidence fit is found to have a FWHM of 10.7 ns. The base of the peak appears to be broad and is contributing to the width. Using constant fraction discrimination (CFD)

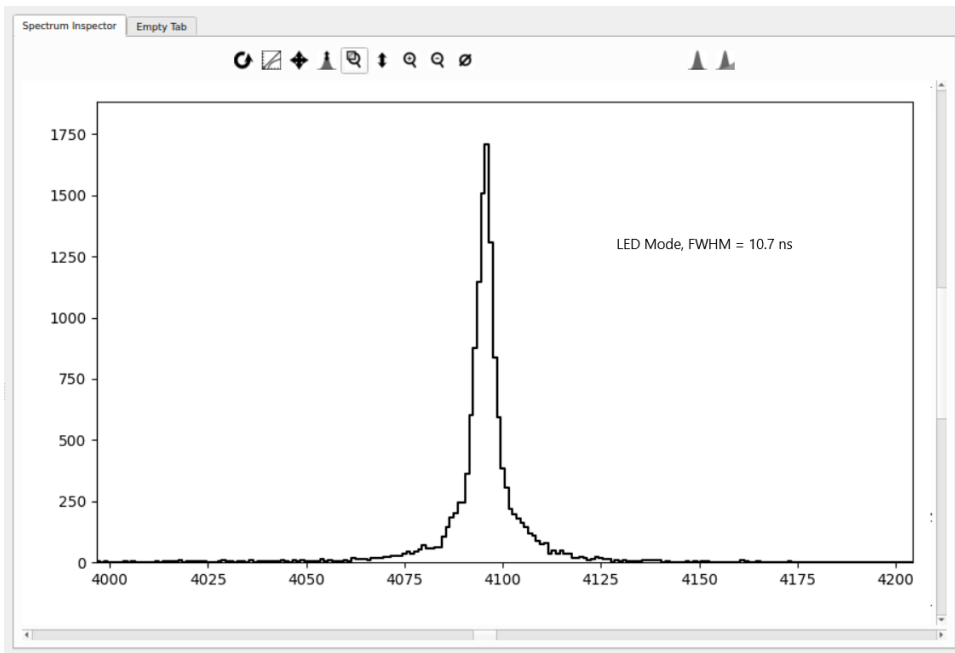


Figure 5.12: The coincidence histogram using the LED time stamp determination mode. The channels on the  $x$ -axis span from 0 to 8196, where the  $\Delta t = 0$  condition has been shifted to the center, at channel 4096. The FWHM is found to be 10.7 ns for this case.

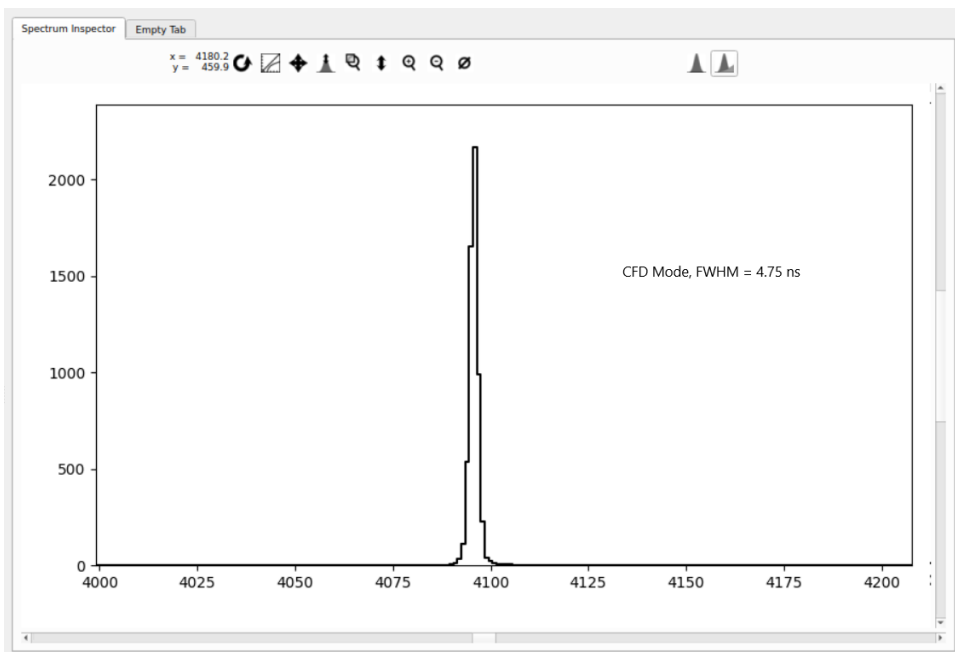


Figure 5.13: The coincidence histogram using the CFD time stamp determination mode. The FWHM is 4.75 ns for this case.

mode), the result significantly narrows. This is seen in Fig. 5.13, where the FWHM is 4.75 ns. Hence, the timing resolution for the digital DAQ using CFD mode is over twice as good as that of LED mode.

### 5.5.3 Development of Coincidence Logic in EngeSpec

Acquiring coincidences in the previous section required the use of two detectors, but it also required new developments in the `EngeSpec` sort routine. The individual  $Q_{long}$  and trigger time tag data for each detector needed to be collected and sorted separately. At the time of this test, the software infrastructure for multiple simultaneous channels was not yet developed. The way the CAEN V1730 digitizer couples adjacent channels in its channel aggregate memory structure made this a difficult task. However, this was resolved, and the implementation was rapidly extended to all 16 channels simultaneously. The infrastructure for obtaining coincidences also had to be developed. This is traditionally handled by analog modules, but the `EngeSpec` sort routine can now handle coincidences entirely on its own.

There are currently two versions, in terms of coincidence development, of the `EngeSpec` sort routine. The first attempt was for the above case where 2 and only 2 channels are in coincidence. In this case, coincidence candidates must occur consecutively between the 2 channels. In other words, a flag is raised if two events from the same channel are collected consecutively. Furthermore, they must have a sufficiently small timetag difference such that they fit in the coincidence histogram, with the range specified by the user. This is not very sophisticated, but it clearly served the purpose for the timing resolution test, as this was the version that was used.

The second version came later, where coincidence logic was developed with the focal plane detector electronics in mind. In this updated case, a coincidence window is opened when an event is collected from the specified triggering channel, where the total time for the window is user-defined. Coincidences are achieved only if an event from a different channel is collected within that window. The relative times are kept track of with the trigger time tag data for each event.

## 5.6 Conclusions

A digital data acquisition system has been developed at the Triangle Universities Nuclear Laboratory that will replace the traditional analog module system for the focal plane detector package used with the Enge Split-Pole Spectrograph. The CAEN V1730 digitizer is the main component of the new system. Its digital pulse processing algorithms emulate the effects

of analog modules, and frontend software has been developed to write user-defined settings to their associated registry addresses on the digitizer board. A settings file is read by the frontend software for ease of access to the registries. A system in which extraction and sorting of the important quantities associated with each detector event, such as its energy and time tag, has also been developed.

Initial tests were performed on the resolution of these quantities using radioisotopes with NaI(Tl) detectors. An energy resolution of 5.5% has been determined with a  $^{152}\text{Eu}$  source when the long gate parameter responsible for charge integration is optimized. A timing resolution of 4.75 ns (FWHM) has also been determined through coincidence studies with a  $^{60}\text{Co}$  source and two NaI(Tl) detectors when constant fraction discrimination is enabled over leading edge discrimination. As a result of the timing resolution test, significant progress was made in the development of coincidence logic in the sort routine of the graphical user interface *EngeSpec*. A sort routine appropriate for signals from the focal plane detector package at the Enge Split-Pole Spectrograph has been developed as a result, which handles coincidence and triggering logic. This system will soon be commissioned at TUNL.

## CHAPTER

# 6

## SUMMARY AND CONCLUSIONS

Key reaction rates correlated with enhanced rubidium abundance in the s-process have been determined in this thesis through Monte Carlo sampling of the reaction rate probability densities. The rates of the  $^{86}\text{Rb}(n, \gamma)^{87}\text{Rb}$ ,  $^{13}\text{N}(n, p)^{13}\text{C}$ , and  $^{14}\text{N}(n, p)^{14}\text{C}$  reactions were found to be the most correlated with the ratio of rubidium abundance to nearby s-process elements. This ratio is an indicator of s-process branching activation associated with the neutron source  $^{22}\text{Ne}(\alpha, n)^{25}\text{Mg}$  occurring during thermal pulses, which is expected to be activated for massive O-rich AGB stars. The discrepancy between observed and theoretical rubidium abundance, known as the “rubidium problem”, was investigated, and the rate uncertainties of the relevant reactions were found to not play a role in this discrepancy.

The Mg–K anticorrelation in the globular cluster NGC 2419 was investigated by experimentally constraining the rate of the key potassium-destruction reaction  $^{39}\text{K}(p, \gamma)^{40}\text{Ca}$ . This constraint was established through the first-ever resolution of key  $^{39}\text{K} + p$  resonances in the proton-transfer reaction  $^{39}\text{K}(^3\text{He}, d)^{40}\text{Ca}$  performed at the Triangle Universities Nuclear Laboratory (TUNL) with the Enge Split-Pole Spectrograph. The resonances at 154 keV, 415 keV, 439 keV, and 521 keV were resolved for the first time, and new proton partial widths were calculated from their measured angular distributions. The impact on the  $^{39}\text{K}(p, \gamma)^{40}\text{Ca}$  reaction rate from these new resonances, as well as that of the many other resonances resolved in this experiment, was found to be significant. A large increase in the previously calculated rate was found for  $T \lesssim 110$  MK, due primarily to the new resolution of the 154 keV resonance. The rate increased by as much as a factor of 13 at 70 MK, and its total  $1\sigma$  width decreased by as much as a factor of 42 at 80 MK. These massive constraints were tested in a nuclear reaction

network model reproducing the Mg–K anticorrelation in NGC 2419. The  $T$ - $\rho$  conditions of the hydrogen burning nucleosynthesis environment that reproduce the Mg–K anticorrelation were investigated through a grid search. Several  $T$ - $\rho$  solutions that were acceptable with the previously calculated reaction rate were found to no longer be acceptable, and vice versa. However, massive AGB and super-AGB stars were not found to be any more or less likely to be candidates for the Mg–K anticorrelation as a result of this new reaction rate.

In order to enhance future proton-transfer measurements at TUNL, a new digital data acquisition system (DAQ) was developed that will replace the traditional analog module system for the focal plane detector package at the Enge Split-Pole Spectrograph. Both frontend software and a sort routine were developed to extract energy and timing information from events collected by a new digitizer, the CAEN V1730. Initial tests were performed on the energy and timing resolution of the DAQ, and coincidence and triggering logic were developed for use with the focal plane detector. The commissioning of this DAQ will mark a new era for the Enge Split-Pole Spectrograph at TUNL.

## BIBLIOGRAPHY

- [An06] Haixia An and Chonghai Cai. “Global deuteron optical model potential for the energy range up to 183 MeV”. *Phys. Rev. C* **73**, 5 (2006).
- [Aud03] G. Audi et al. “The Nubase evaluation of nuclear and decay properties”. *Nuclear Physics A* **729**, 1 (2003). The 2003 NUBASE and Atomic Mass Evaluations.
- [Bab16] S. Babu and N. Badiger. “Measurement of Energy Loss Straggling of Relativistic Electrons in Thin Aluminum Foils”. *Acta Physica Polonica A* **129** (2016).
- [Bas66] R. H. Bassel. “Normalization of and Finite-Range Effects in  $(^3\text{He}, d)$  and  $(t, d)$  Reactions”. *Phys. Rev.* **149**, 3 (1966).
- [Bé07] M.-M. Bé et al. *Update of X Ray and Gamma Ray Decay Data Standards for Detector Calibration and Other Applications*. Tech. rep. Vienna, Austria: International Atomic Energy Agency, 2007.
- [Bre36] G. Breit and E. Wigner. “Capture of Slow Neutrons”. *Phys. Rev.* **49**, 7 (1936).
- [Bri11] I. Brida, Steven C. Pieper, and R. B. Wiringa. “Quantum Monte Carlo calculations of spectroscopic overlaps in  $A \leq 7$  nuclei”. *Phys. Rev. C* **84**, 2 (2011).
- [Bur57] E. Margaret Burbidge et al. “Synthesis of the Elements in Stars”. *Rev. Mod. Phys.* **29**, 4 (1957).
- [Bus99] M. Busso, R. Gallino, and G. J. Wasserburg. “Nucleosynthesis in Asymptotic Giant Branch Stars: Relevance for Galactic Enrichment and Solar System Formation”. *Annual Review of Astronomy and Astrophysics* **37**, 1 (1999).
- [Cag71] M.E. Cage et al. “The  ${}^{39}\text{K}(^3\text{He}, {}^3\text{He}){}^{39}\text{K}$  and  ${}^{39}\text{K}(^3\text{He}, d){}^{40}\text{Ca}$  reactions at 29.3 MeV”. *Nuclear Physics A* **162**, 3 (1971).
- [Cam57] A. G. W. Cameron. “NUCLEAR REACTIONS IN STARS AND NUCLEOGENESIS”. *Publications of the Astronomical Society of the Pacific* **69**, 408 (1957).
- [Car07] B. Carroll and D. Ostlie. *An Introduction to Modern Astrophysics*. 2nd ed. Pearson Education Inc., publishing as Addison-Wesley, 2007.
- [Car09] Carretta, E. et al. “Na-O anticorrelation and HB\*\*\* - VIII. Proton-capture elements and metallicities in 17 globular clusters from UVES spectra”. *A&A* **505**, 1 (2009).
- [Car10] Carretta, E. et al. “Properties of stellar generations in globular clusters and relations with global parameters”. *A&A* **516** (2010).

- [Che17] Jun Chen. “Nuclear Data Sheets for A=40”. *Nuclear Data Sheets* **140** (2017).
- [Che81] C.-W. Cheng et al. “Hydrogen burning of  $^{39}\text{K}$  in explosive oxygen burning”. *Canadian Journal of Physics* **59**, 2 (1981).
- [Cla61] D.D Clayton et al. “Neutron capture chains in heavy element synthesis”. *Annals of Physics* **12**, 3 (1961).
- [Coc14] Alain Coc, Jean-Philippe Uzan, and Elisabeth Vangioni. “Standard big bang nucleosynthesis and primordial CNO abundances after Planck”. *Journal of Cosmology and Astroparticle Physics* **2014**, 10 (2014).
- [Coh04] Judith G. Cohen. “Palomar 12 as a Part of the Sagittarius Stream: The Evidence from Abundance Ratios\*”. *The Astronomical Journal* **127**, 3 (2004).
- [Coh12] Judith G. Cohen and Evan N. Kirby. “The Bizarre Chemical Inventory of NGC 2419, An Extreme Outer Halo Globular Cluster”. *The Astrophysical Journal* **760**, 86 (2012).
- [Cov06] Thomas M. Cover and Joy A. Thomas. *Elements of Information Theory*. Vol. Second edition. A Wiley-Interscience Publication. Wiley-Interscience, 2006.
- [Den89] P. A. Denisenkov and S. N. Denisenkova. “Possible Explanation of the Correlation Between Nitrogen and Sodium Over Abundances for Red Giants in Globular Clusters”. *Astronomicheskij Tsirkulyar* **1538** (1989).
- [Der17] J. R. Dermigny and C. Iliadis. “Sensitivity to Thermonuclear Reaction Rates in Modeling the Abundance Anomalies of NGC 2419”. *The Astrophysical Journal* **848**, 1 (2017).
- [Doh15] Carolyn L. Doherty et al. “Super- and massive AGB stars - IV. Final fates - initial-to-final mass relation”. *Monthly Notices of the Royal Astronomical Society* **446**, 3 (2015).
- [End77] P. M. Endt. “Spectroscopic factors for single-nucleon transfer in the  $A = 21\text{--}44$  region”. *Atomic Data and Nuclear Data Tables* **19**, 1 (1977).
- [Erc10] Annibale D’Ercole et al. “Abundance patterns of multiple populations in globular clusters: a chemical evolution model based on yields from AGB ejecta”. *Monthly Notices of the Royal Astronomical Society* **407**, 2 (2010).
- [Erc11] Annibale D’Ercole, Francesca D’Antona, and Enrico Vesperini. “Formation of multiple populations in globular clusters: constraints on the dilution by pristine gas”. *Monthly Notices of the Royal Astronomical Society* **415**, 2 (2011).

- [Erc12] Annibale D’Ercole et al. “The role of super-asymptotic giant branch ejecta in the abundance patterns of multiple populations in globular clusters”. *Monthly Notices of the Royal Astronomical Society* **423**, 2 (2012).
- [Ers66] John R. Erskine. “Energy-Level Structure of  $^{40}\text{Ca}$  as Observed with the  $^{39}\text{K}(^3\text{He}, d)$   $^{40}\text{Ca}$  Reaction”. *Phys. Rev.* **149**, 3 (1966).
- [For70] J. S. Forster et al. “Proton stripping to particle-hole states in  $^{40}\text{Ca}$  and  $^{42}\text{Ca}$ ”. *Nuclear Physics A* **150**, 1 (1970).
- [Fuc69] H. Fuchs, K. Grabisch, and G. Röschert. “Investigation of states in  $^{40}\text{Ca}$  by the  $^{39}\text{K}(d, n)$  reaction”. *Nuclear Physics A* **129**, 3 (1969).
- [Gar06] D. A. García-Hernández et al. “Rubidium-Rich Asymptotic Giant Branch Stars”. *Science* **314**, 5806 (2006).
- [Gar07] D. A. García-Hernández et al. “Lithium and zirconium abundances in massive Galactic O-rich AGB stars \*\*\*”. *A&A* **462**, 2 (2007).
- [Gar09] D. A. García-Hernández et al. “Rb-RICH ASYMPTOTIC GIANT BRANCH STARS IN THE MAGELLANIC CLOUDS”. *The Astrophysical Journal* **705**, 1 (2009).
- [Gra04] Raffaele Gratton, Christopher Sneden, and Eugenio Carretta. “Abundance Variations within Globular Clusters”. *Annual Review of Astronomy and Astrophysics* **42**, 1 (2004).
- [Gra12] Raffaele G. Gratton, Eugenio Carretta, and Angela Bragaglia. “Multiple populations in globular clusters”. *The Astronomy and Astrophysics Review* **20**, 1 (2012).
- [Gra19] Raffaele Gratton et al. “What is a globular cluster? An observational perspective”. *The Astronomy and Astrophysics Review* **27**, 1 (2019).
- [Gri22] D. Gribble et al. “Investigation of  $^{11}\text{B}$  and  $^{40}\text{Ca}$  levels at 8–9 MeV by nuclear resonance fluorescence”. *Phys. Rev. C* **106**, 1 (2022).
- [Gru72] C. R. Gruhn et al. “Energy Dependence of Proton Inelastic Scattering from  $^{40}\text{Ca}$ ”. *Phys. Rev. C* **6**, 3 (1972).
- [Guo20] J. Guo et al. “RStan”, v2.26.23. <https://github.com/stan-dev/rstan>. 2020.
- [Gus08] B. Gustafsson et al. “A grid of MARCS model atmospheres for late-type stars. I. Methods and general properties”. *A&A* **486**, 3 (2008).
- [Hab04] H. Habing and H. Olofsson. *Asymptotic Giant Branch Stars*. Springer-Verlag, 2004.

- [Hal04] S. E. Hale et al. “Investigation of the  $^{23}\text{Na}(p, \gamma)^{24}\text{Mg}$  and  $^{23}\text{Na}(p, \alpha)^{20}\text{Ne}$  reactions via ( $^3\text{He}, d$ ) spectroscopy”. *Phys. Rev. C* **70**, 4 (2004).
- [Ham21] Faïrouz Hammache and Nicolas de Séreville. *Transfer reactions as a Tool in Nuclear Astrophysics*. English. Copyright - © 2021. This work is published under <http://creativecommons.org/licenses/by-nc-nd/4.0/> (the “License”). Notwithstanding the ProQuest Terms and Conditions, you may use this content in accordance with the terms of the License; Last updated - 2023-03-20. 2021.
- [Har23] Djamila Sarah Harrouz. “Experimental study of the  $^{30}\text{Si}(p, \gamma)^{31}\text{P}$  reaction for understanding elemental anomalies in globular clusters”. PhD thesis. Université Paris-Saclay, 2023.
- [Hod71] P. Hodgson. *Nuclear reactions and nuclear structure*. International series of monographs on physics. Clarendon Press, 1971.
- [Hua21] W.J. Huang et al. “The AME 2020 atomic mass evaluation (I). Evaluation of input data, and adjustment procedures\*”. *Chinese Physics C* **45**, 3 (2021).
- [Ili15a] C. Iliadis. *Nuclear Physics of Stars*. 2nd ed. Wiley-VCH, 2015.
- [Ili15b] Christian Iliadis et al. “Statistical methods for thermonuclear reaction rates and nucleosynthesis simulations”. *Journal of Physics G: Nuclear and Particle Physics* **42**, 3 (2015).
- [Ili16] C. Iliadis et al. “ON POTASSIUM AND OTHER ABUNDANCE ANOMALIES OF RED GIANTS IN NGC 2419”. *The Astrophysical Journal* **818**, 1 (2016).
- [Ili20] Christian Iliadis and Alain Coc. “Thermonuclear Reaction Rates and Primordial Nucleosynthesis”. *The Astrophysical Journal* **901**, 2 (2020).
- [Ili97] C. Iliadis. “Proton single-particle reduced widths for unbound states”. *Nuclear Physics A* **618**, 1 (1997).
- [Kah19] D. Kahl et al. “Single-particle shell strengths near the doubly magic nucleus  $^{56}\text{Ni}$  and the  $^{56}\text{Ni}(p, \gamma)^{57}\text{Cu}$  reaction rate in explosive astrophysical burning”. *Physics Letters B* **797** (2019).
- [Kan16] A. Kankainen et al. “Angle-integrated measurements of the  $^{26}\text{Al}(d, n)^{27}\text{Si}$  reaction cross section: a probe of spectroscopic factors and astrophysical resonance strengths”. *Eur. Phys. J. A* **52** (2016).
- [Kar10] A. I. Karakas. “Updated stellar yields from asymptotic giant branch models”. *Monthly Notices of the Royal Astronomical Society* **403**, 3 (2010).

- [Kar12] Amanda I. Karakas, D. A. García-Hernández, and Maria Lugaro. “HEAVY ELEMENT NUCLEOSYNTHESIS IN THE BRIGHTEST GALACTIC ASYMPTOTIC GIANT BRANCH STARS”. *The Astrophysical Journal* **751**, 1 (2012).
- [Kar14] Amanda I. Karakas and John C. Lattanzio. “The Dawes Review 2: Nucleosynthesis and Stellar Yields of Low- and Intermediate-Mass Single Stars”. *PASA* **31**, e030 (2014).
- [Kar16] Amanda I. Karakas and Maria Lugaro. “STELLAR YIELDS FROM METAL-RICH ASYMPTOTIC GIANT BRANCH MODELS”. *The Astrophysical Journal* **825**, 1 (2016).
- [Kik90] S.W. Kikstra et al. “The  $^{40}\text{Ca}$  level scheme investigated with the  $^{39}\text{K}(p, \gamma)^{40}\text{Ca}$  reaction”. *Nuclear Physics A* **512**, 3 (1990).
- [Kra87] K. Krane. *Introductory Nuclear Physics*. Wiley, 1987.
- [Lan44] L. D. Landau. “On the Energy Loss of Fast Particles by Ionisation”. *J. Exp. Phys. (USSR)* **8** (1944).
- [Lan93] G. E. Langer, R. Hoffman, and C. Sneden. “SODIUM-OXYGEN ABUNDANCE ANTICORRELATIONS AND DEEP MIXING SCENARIOS FOR GLOBULAR CLUSTER GIANTS”. *Publications of the Astronomical Society of the Pacific* **105**, 685 (1993).
- [Lee66] H.P. Leenhouts and P.M. Endt. “Gamma decay of levels in  $^{40}\text{Ca}$  measured with the  $^{39}\text{K}(p, \gamma)^{40}\text{Ca}$  reaction”. *Physica* **32**, 2 (1966).
- [Lia09] Chun-Tian Liang, Xiao-Hua Li, and Chong-Hai Cai. “Global  $^3\text{He}$  optical model potential below 270 MeV”. *Journal of Physics G: Nuclear and Particle Physics* **36**, 8 (2009).
- [Lod09] K. Lodders, H. Palme, and H.-P. Gail. “Abundances of the elements in the Solar System”. In: *Group VI Astronomy and Astrophysics*. Ed. by J.E. Trümper. Vol. 4B. Springer-Verlag Berlin Heidelberg, 2009.
- [Lon10] R. Longland et al. “Charged-particle thermonuclear reaction rates: I. Monte Carlo method and statistical distributions”. *Nuclear Physics A* **841**, 1 (2010).
- [Lon12] Longland, R. “Recommendations for Monte Carlo nucleosynthesis sampling”. *A&A* **548**, A30 (2012).
- [Lon18a] R. Longland. “Analysis-BayeSpec”. Private GitHub Repository. 2018.
- [Lon18b] R. Longland, J. Dermigny, and C. Marshall. “Reaction rates for the  $^{39}\text{K}(p, \gamma)^{40}\text{Ca}$  reaction”. *Phys. Rev. C* **98**, 2 (2018).

- [Lon19] R. Longland. “DAQ-EngeSpec”. <https://github.com/TUNL-Enge/DAQ-EngeSpec>. 2019.
- [Lon23] R. Longland. “RatesMC”. <https://github.com/rlongland/RatesMC>. 2023.
- [Mar19] Caleb Marshall et al. “The Focal-Plane Detector Package on the TUNL Split-Pole Spectrograph”. *IEEE Transactions on Instrumentation and Measurement* **68**, 2 (2019).
- [McE13] R. McElreath. “rethinking”. <https://github.com/rmcelreath/rethinking>. 2013.
- [Muc12] A. Mucciarelli et al. “News from the Galactic suburbia: the chemical composition of the remote globular cluster NGC 2419”. *Monthly Notices of the Royal Astronomical Society* **426**, 4 (2012).
- [Muc15] Alessio Mucciarelli et al. “POTASSIUM: A NEW ACTOR ON THE GLOBULAR CLUSTER CHEMICAL EVOLUTION STAGE. THE CASE OF NGC 2808\*”. *The Astrophysical Journal* **801**, 1 (2015).
- [Muc17] Mucciarelli, A., Merle, T., and Bellazzini, M. “The potassium abundance in the globular clusters NGC 104, NGC 6752 and NGC 6809”. *A&A* **600** (2017).
- [Nol75] J. A. Nolen and R. J. Gleitsmann. “High-resolution study of  $^{40}\text{Ca}$  via inelastic proton scattering at 35 MeV”. *Phys. Rev. C* **11**, 4 (1975).
- [Per17] V. Pérez-Mesa et al. “Rubidium and zirconium abundances in massive Galactic asymptotic giant branch stars revisited”. *A&A* **606** (2017).
- [Pig16] M. Pignatari et al. “NUGRID STELLAR DATA SET. I. STELLAR YIELDS FROM H TO BI FOR STARS WITH METALLICITIES  $Z = 0.02$  and  $Z = 0.01$ ”. *The Astrophysical Journal Supplement Series* **225**, 2 (2016).
- [Por56] C. E. Porter and R. G. Thomas. “Fluctuations of Nuclear Reaction Widths”. *Phys. Rev.* **104**, 2 (1956).
- [Pra07] Nikos Prantzos, Corinne Charbonnel, and Christian Iliadis. “Light nuclei in galactic globular clusters: constraints on the self-enrichment scenario from nucleosynthesis”. *Astronomy and Astrophysics* **470** (2007).
- [Raa12] van Raai, M. A. et al. “Rubidium, zirconium, and lithium production in intermediate-mass asymptotic giant branch stars”. *A&A* **540** (2012).
- [Rau13] R. Raut et al. “Cross-Section Measurements of the  $^{86}\text{Kr}(\gamma, n)$  Reaction to Probe the  $s$ -Process Branching at  $^{85}\text{Kr}$ ”. *Phys. Rev. Lett.* **111**, 11 (2013).

- [Rei14] R. Reifarth. “Nuclear astrophysics of the *s* and *r*-process”. In: *Neutrons and Nuclei* (Fréjus, France). Joliot Curie School, 2014.
- [Rol88] C. Rolfs and W. Rodney. *Cauldrons in the Cosmos*. 1st ed. The University of Chicago Press, 1988.
- [Sal13] A. L. Sallaska et al. “STARLIB: A NEXT-GENERATION REACTION-RATE LIBRARY FOR NUCLEAR ASTROPHYSICS”. *The Astrophysical Journal Supplement Series* **207**, 1 (2013).
- [Sat83] G. Satchler. *Direct nuclear reactions*. Oxford University Press, 1983.
- [Sbo07] Sbordone, L. et al. “The exotic chemical composition of the Sagittarius dwarf spheroidal galaxy”. *A&A* **465**, 3 (2007).
- [See65] P A Seeger, W A Fowler, and D D Clayton. “NUCLEOSYNTHESIS OF HEAVY ELEMENTS BY NEUTRON CAPTURE”. *Astrophys. J., Suppl. Ser.* **11** (1965).
- [Set11] K. Setoodehnia. “Level Structure of  $^{30}\text{S}$  and the  $^{29}\text{P}(p, \gamma)^{30}\text{S}$  Reaction Rate”. PhD thesis. McMaster University, 2011.
- [Set67] Kamal K. Seth et al. “Study of Proton Particle-Hole States in  $^{40}\text{Ca}$  by the  $^{39}\text{K}({}^3\text{He}, d)^{40}\text{Ca}$  Reaction”. *Phys. Rev.* **164**, 4 (1967).
- [Set74] Kamal K. Seth et al. “Discovery of the Missing Two-Particle, Two-Hole  $0^+$  States in  $^{40}\text{Ca}$ ”. *Phys. Rev. Lett.* **33**, 4 (1974).
- [Set77] K. K. Seth et al. “( $p, t$ ) Reactions on  $^{41}\text{K}$ ,  $^{42}\text{Ca}$  and  $^{43}\text{Ca}$  and Core Excited States”. In: *Proc. Intern. Conf. Nuclear Structure*. Vol. 1. Tokyo, 1977.
- [Swa01] Kenneth B. Swartz, Dale W. Visser, and John M. Baris. “A Java-based data acquisition system for nuclear physics”. *Nuclear Instruments and Methods in Physics Research Section A: Accelerators, Spectrometers, Detectors and Associated Equipment* **463**, 1 (2001).
- [Swa02] K. Swartz, D. Visser, and J. Baris. “Jam-v3.1.3-Linux”. <http://jam-daq.sourceforge.net/>. 2002.
- [Tea11] Stan Development Team. “Stan Modeling Language Users Guide and Reference Manual”, v2.33. <https://mc-stan.org>. 2011.
- [Tho06] I. J. Thompson. “Fresco”. <https://github.com/I-Thompson/fresco>. 2006.
- [Tho88] Ian J. Thompson. “Coupled reaction channels calculations in nuclear physics”. *Computer Physics Reports* **7**, 4 (1988).

- [Ven12] Paolo Ventura et al. “SUPER-AGB–AGB EVOLUTION AND THE CHEMICAL INVENTORY IN NGC 2419”. *The Astrophysical Journal Letters* **761**, 2 (2012).
- [Vis03] D. Visser. “JRelKin”. <https://sourceforge.net/projects/nukesim-classes/>. 2003.
- [Wan21] Meng Wang et al. “The AME 2020 atomic mass evaluation (II). Tables, graphs and references\*”. *Chinese Physics C* **45**, 3 (2021).
- [Wei09] H. A. Weidenmüller and G. E. Mitchell. “Random matrices and chaos in nuclear physics: Nuclear structure”. *Rev. Mod. Phys.* **81**, 2 (2009).
- [Wil20] J. Wilhelmy et al. “Dipole response of  $^{87}\text{Rb}$  and its impact on the  $^{86}\text{Rb}(n, \gamma)^{87}\text{Rb}$  cross section”. *Phys. Rev. C* **102**, 4 (2020).
- [Yam94] T. Yamaya et al. “Cluster structure in  $^{40}\text{Ca}$  via the  $\alpha$ -transfer reaction”. *Nuclear Physics A* **573**, 1 (1994).
- [Zam14] Zamora, O. et al. “Circumstellar effects on the Rb abundances in O-rich AGB stars”. *A&A* **564** (2014).

## **APPENDIX**

APPENDIX

A

**S-PROCESS REACTION NETWORK  
INITIAL ABUNDANCES**

Table A.1: Initial abundances, in terms of mass fractions  $X_{\text{init}}$ , in the s-process reaction network model of Chapter 3. Relative solar system abundances from Ref. [Lod09] are applied to the remaining nuclei after modifications to  $^1\text{H}$ ,  $^4\text{He}$ ,  $^{12}\text{C}$ ,  $^{13}\text{C}$ ,  $^{14}\text{N}$ ,  $^{16}\text{O}$ , and  $^{56}\text{Fe}$ .

Nucleus	$X_{\text{init}}$	Nucleus	$X_{\text{init}}$	Nucleus	$X_{\text{init}}$	Nucleus	$X_{\text{init}}$
H 2	1.29E-05	AR 40	1.13E-08	ZN 66	3.06E-07	ZR 94	2.26E-09
HE 3	3.96E-05	K 39	1.75E-06	ZN 67	4.55E-08	ZR 96	3.71E-10
HE 4	7.50E-01	K 40	3.07E-09	ZN 68	2.12E-07	NB 93	9.29E-10
LI 6	3.23E-10	K 41	1.33E-07	ZN 70	7.17E-09	MO 92	4.36E-10
LI 7	4.61E-09	CA 40	3.00E-05	GA 69	1.94E-08	MO 94	2.81E-10
BE 9	7.06E-11	CA 42	2.10E-07	GA 71	1.33E-08	MO 95	4.92E-10
B 10	4.74E-10	CA 43	4.52E-08	GE 70	2.18E-08	MO 96	5.23E-10
B 11	2.13E-09	CA 44	7.10E-07	GE 72	2.92E-08	MO 97	3.04E-10
C 12	2.20E-01	CA 46	1.18E-09	GE 73	8.23E-09	MO 98	7.81E-10
C 13	1.00E-02	CA 48	6.95E-08	GE 74	3.91E-08	MO100	3.20E-10
N 14	1.00E-02	SC 45	1.98E-08	GE 76	8.28E-09	RU 96	1.22E-10
N 15	1.50E-06	TI 46	1.20E-07	AS 75	5.86E-09	RU 98	4.14E-11
O 16	3.00E-03	TI 47	1.11E-07	SE 74	5.69E-10	RU 99	2.88E-10
O 17	1.29E-06	TI 48	1.12E-06	SE 76	6.15E-09	RU100	2.87E-10
O 18	7.26E-06	TI 49	8.41E-08	SE 77	5.08E-09	RU101	3.93E-10
F 19	1.96E-07	TI 50	8.20E-08	SE 78	1.60E-08	RU102	7.34E-10
NE 20	7.84E-04	V 50	4.48E-10	SE 80	3.43E-08	RU104	4.42E-10
NE 21	1.97E-06	V 51	1.87E-07	SE 82	6.19E-09	RH103	4.88E-10
NE 22	6.34E-05	CR 50	3.65E-07	BR 79	5.50E-09	PD102	1.82E-11
NA 23	1.70E-05	CR 52	7.33E-06	BR 81	5.48E-09	PD104	2.02E-10
MG 24	2.49E-04	CR 53	8.42E-07	KR 78	2.00E-10	PD105	4.08E-10
MG 25	3.30E-05	CR 54	2.14E-07	KR 80	1.33E-09	PD106	5.04E-10
MG 26	3.76E-05	MN 55	6.50E-06	KR 82	6.84E-09	PD108	4.97E-10
AL 27	2.93E-05	FE 54	3.43E-05	KR 83	6.86E-09	PD110	2.24E-10
SI 28	3.31E-04	FE 56	5.00E-03	KR 84	3.42E-08	AG107	3.48E-10
SI 29	1.74E-05	FE 57	1.31E-05	KR 86	1.06E-08	AG109	3.30E-10
SI 30	1.19E-05	FE 58	1.78E-06	RB 85	5.58E-09	CD106	2.72E-11
P 31	3.30E-06	CO 59	1.78E-06	RB 87	2.35E-09	CD108	1.94E-11
S 32	1.64E-04	NI 58	2.48E-05	SR 84	1.40E-10	CD110	2.78E-10
S 33	1.34E-06	NI 60	9.92E-06	SR 86	2.53E-09	CD111	2.86E-10
S 34	7.75E-06	NI 61	4.37E-07	SR 87	1.78E-09	CD112	5.45E-10
S 36	3.32E-08	NI 62	1.41E-06	SR 88	2.16E-08	CD113	2.78E-10
CL 35	1.76E-06	NI 64	3.72E-07	Y 89	5.28E-09	CD114	6.60E-10
CL 37	5.93E-07	CU 63	3.02E-07	ZR 90	6.40E-09	IN113	1.16E-11
AR 36	3.62E-05	CU 65	1.39E-07	ZR 91	1.41E-09	IN115	2.50E-10
AR 38	6.96E-06	ZN 64	5.17E-07	ZR 92	2.18E-09	SN112	5.02E-11

Table A.1: (continued)

Nucleus	$X_{\text{init}}$	Nucleus	$X_{\text{init}}$	Nucleus	$X_{\text{init}}$	Nucleus	$X_{\text{init}}$
SN114	3.51E-11	CE136	3.48E-12	HO165	1.92E-10	OS189	2.66E-10
SN115	1.77E-11	CE138	5.30E-12	ER162	8.30E-13	OS190	4.36E-10
SN116	7.79E-10	CE140	1.87E-09	ER164	8.83E-12	OS192	6.84E-10
SN117	4.15E-10	CE142	2.38E-10	ER166	1.87E-10	IR191	6.12E-10
SN118	1.32E-09	PR141	3.11E-10	ER167	1.28E-10	IR193	1.04E-09
SN119	4.71E-10	ND142	4.20E-10	ER168	1.53E-10	PT190	4.87E-13
SN120	1.81E-09	ND143	1.89E-10	ER170	8.49E-11	PT192	2.46E-11
SN122	2.61E-10	ND144	3.75E-10	TM169	8.79E-11	PT194	1.04E-09
SB121	2.77E-10	ND145	1.39E-10	YB168	6.46E-13	PT195	1.08E-09
SB123	2.11E-10	ND146	2.75E-10	YB170	1.66E-11	PT196	8.09E-10
TE120	7.69E-12	ND148	9.29E-11	YB171	7.91E-11	PT198	2.31E-10
TE122	1.91E-10	ND150	9.22E-11	YB172	1.23E-10	AU197	4.92E-10
TE123	6.78E-11	SM144	1.48E-11	YB173	9.15E-11	HG196	2.51E-12
TE124	3.59E-10	SM147	7.72E-11	YB174	1.83E-10	HG198	1.17E-10
TE125	5.37E-10	SM148	5.69E-11	YB176	7.51E-11	HG199	1.96E-10
TE126	1.44E-09	SM149	7.06E-11	LU175	8.30E-11	HG200	2.72E-10
TE128	2.44E-09	SM150	3.84E-11	LU176	2.48E-12	HG201	1.55E-10
I 127	1.79E-09	SM152	1.38E-10	HF174	6.69E-13	HG202	3.55E-10
XE124	1.11E-11	SM154	1.18E-10	HF176	1.83E-11	HG204	8.10E-11
XE126	9.69E-12	EU151	9.11E-11	HF177	6.58E-11	TL203	1.40E-10
XE128	2.00E-10	EU153	1.01E-10	HF178	9.69E-11	TL205	3.39E-10
XE129	2.48E-09	GD152	1.36E-12	HF179	4.86E-11	PB204	1.73E-10
XE130	3.98E-10	GD154	1.54E-11	HF180	1.26E-10	PB206	1.62E-09
XE131	2.00E-09	GD155	1.06E-10	TA180	6.00E-15	PB207	1.80E-09
XE132	2.43E-09	GD156	1.47E-10	TA181	4.87E-11	PB208	5.19E-09
XE134	9.05E-10	GD157	1.13E-10	W 180	4.61E-13	BI209	3.70E-10
CS133	6.32E-10	GD158	1.81E-10	W 182	8.46E-11		
BA130	8.33E-12	GD160	1.61E-10	W 183	4.60E-11		
BA132	8.46E-12	TB159	1.29E-10	W 184	9.90E-11		
BA134	1.85E-10	DY156	4.00E-13	W 186	9.29E-11		
BA135	5.10E-10	DY158	8.10E-13	RE185	4.91E-11		
BA136	6.12E-10	DY160	1.93E-11	RE187	8.96E-11		
BA137	8.81E-10	DY161	1.57E-10	OS184	2.36E-13		
BA138	5.67E-09	DY162	2.13E-10	OS186	2.57E-11		
LA138	0.00E+00	DY163	2.10E-10	OS187	2.06E-11		
LA139	8.14E-10	DY164	2.40E-10	OS188	2.18E-10		